Annual Report 2012

Physik-Department

Lehrstuhl für Funktionelle Materialien

Technische Universität München

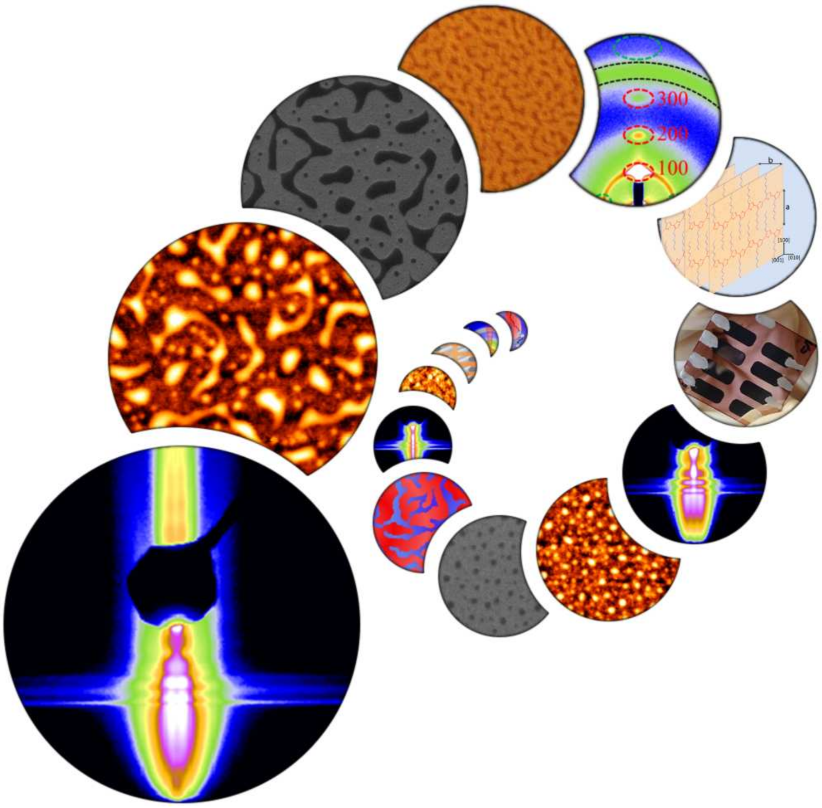

Prof. Dr. Winfried Petry
Chair of Functional Materials
Physik-Department

Deputy chairman for Prof. Dr. Petry:
Prof. Dr. Peter Müller-Buschbaum

Prof. Dr. Christine M. Papadakis

Physik-Department
Technische Universität München
James-Franck-Straße 1
85748 Garching

Secretaries: Marion Waletzki
Susanna Fink

Tel.: +49(0)89 289 12452
Fax: +49(0)89 289 12473

Email: peter.mueller-buschbaum@ph.tum.de
marion.waletzki@ph.tum.de
papadakis@ph.tum.de
http://www.functmat.ph.tum.de

Editor: Dr. Volker Körstgens

Cover-page picture:

The individual circular images are related to thin films of ternary blends consisting of poly(3-hexylthiophene) (P3HT), the fullerene derivate PCBM and poly(styrenesulfonate) (PSS).

1 Preface

It is a great pleasure to present in the name of the staff of the Chair of Functional Materials the annual report for the year 2012. It provides an overview of our teaching, research, and development activities. Our research activities are focused on functional materials and cover a broad range from soft matter physics to developments in methods and instrumentation. We examine the fundamental physics of material properties using mainly scattering methods (neutrons-, x-ray and light scattering). The general goal of our research is to explain the functional characteristics of soft condensed matter from the knowledge of the molecular dynamics and nanostructure.

In 2012, the chair activities covered the specific areas of water-based polymer systems, thin polymer films, polymer films for application in photovoltaics, polymer-hybrid systems, dynamics, and methodological and instrumental developments. The activities in the fields of polymer films for application in photovoltaics and polymer-hybrid systems have increased further. With 'TUM.solar' a keylab in the network of in the Bavarian Collaborative Research Project 'Solar Technologies go Hybrid' (SolTec) was established by Prof. Müller-Buschbaum. It bundles the research activities in the field of solar energy conversion and storage.

The in-house experiments available in the laboratories of the chair were supplemented by the lively activities at numerous large scale facilities, comprising synchrotron radiation and neutron scattering experiments. The complete renewal of the X-ray laboratory with the implementation of a new SAXS/WAXS instrument and reflectometer/diffractometer was one of the major activities concerning the developments in methods and instrumentation. The new SAXS/WAXS instrument allows for a very large range of length scales from small angle x-ray scattering (SAXS) to wide angle x-ray scattering (WAXS). Especially the scatter-less slits in combination with a micro-focus X-ray source and the powerful two-dimensional Pilatus 300k detector will enable exciting experiments.

In 2012, the Chair of Functional Materials comprised 11 fellows, 34 PhD students, 10 diploma students, 12 master students, 13 bachelor students, 6 student assistants and 9 administrative and technical staff members. 11 PhD theses were accomplished, moreover, 5 diploma and 7 master theses as well as 10 bachelor theses were finished. As all the years before, we had the pleasure to host several guests from abroad which stimulated a lively scientific atmosphere.

In general, all members of the chair were very active at conferences and workshops, participating with both talks and posters. Moreover, important conferences were organized by members of the chair: two Edgar-Lüscher Seminars were again organized, this year on the subjects 'Elekromobilität: Grundlagen und Konzepte' and 'Astrophysik'. The 2nd Colloquium of the Munich School of Engineering 'Energy Challenges Germany 2050' took place in Garching. Moreover, the 3rd TUM-HASYLAB colloquium 'The polymer metal interface' and a teaching series 'Medizinphysik' was organized in the framework of the 'Ferienakademie Sarntal'. For the chair, a very important event this year was the summer school at the Rudolfshütte in Austria – at an altitude of 2315 m, all members of the chair gave talks on general subjects from the field of polymer physics. Everybody enjoyed the extensive discussions in combination with a fascinating landscape a lot!

Regarding teaching activities of the chair, we offered general physics lectures for students of mechanical engineering (Müller-Buschbaum) and teachers for vocational schools (Papadakis). Specialized lectures comprised 'Polymer physics' (Müller-Buschbaum) and 'Nanostructured soft materials' (Papadakis). Prof. Papadakis acted again as a women's representative of the Physics Department. Moreover Prof. Müller-Buschbaum is heading the activities in the 'Network Renewable Energies (NRG)' in the Munich School of Engineering (MSE).

This annual report comprises a selection of the different research topics and projects carried out in the individual groups of the chair. It highlights the dedicated and successful research activities and collaborations with other groups and large scale facilities. We wish all chair members a fruitful continuation and a successful year 2013.

Peter Müller-Buschbaum and Christine Papadakis March 2013

Contents

2 Water based polymer systems

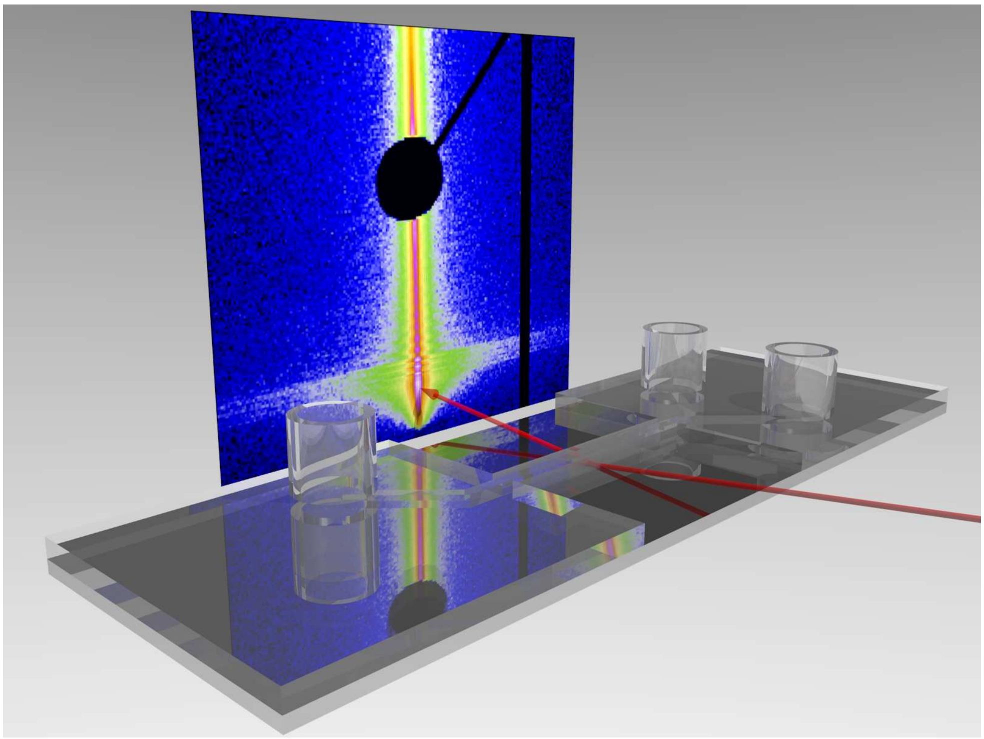

2.1 A comparison of the thermoresponsive switching behavior in thin films of cyclic and linear PNIPAM

D. Magerl, X.-P. Qiu[1], F. M. Winnik[1], P. Müller-Buschbaum

[1] Université de Montréal, Faculty of Pharmacy and Department of Chemistry, Montréal, Canada

Hydrogels are chemically or physically cross-linked polymers that build-up networks in which large amounts of water, i.e. more than the volume of the polymer, are stored. In thermoresponsive hydrogels this property is linked to the temperature in a way that the amount of stored water is controlled by the temperature. A promising and frequently investigated candidate of thermoresponsive hydrogels is poly(N-isopropylarylamide) (PNIPAM), which exhibits a lower critical solution temperature (LCST) at around 32 °C. As a consequence, the polymer can store water below its transition temperature and precipitates from water at higher temperatures, as shown in fig. 2.1a. However, investigations so far are mainly focused on thermoresponsive hydrogels in solution but the behavior of thin films of the polymer on silicon substrates in the presence of humid air is only covered in few studies [1]. Compared to volume samples, the thin film geometry reduces the possibility for swelling to one dimension as shown in fig. 2.1b. This geometry is much closer to applications such as sensors [2] and thus basic knowledge of the behavior of thin films in this geometry is very important.

In the present study we compare films of cyclic PNIPAM, i.e. the ends of the molecules are covalently bond to form a ring shaped molecule, with films of its linear counterpart. Both polymers were synthesized in the group of Prof. Winnik in a way that the linear polymer has end-groups which can be connected via so-called click chemistry to form the cyclic polymer [3]. Hence, the investigated linear PNIPAM is the precursor of the cyclic PNIPAM with exactly these end-groups. Thus, the difference between the two polymers is supposed to be very low, except for the linear and circular architecture.

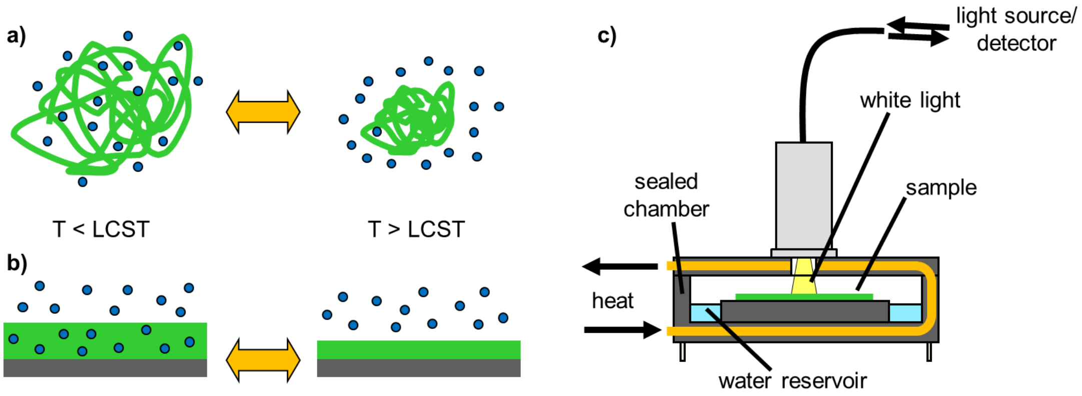

Figure 2.1:
Sketch of thermoresponsive switching from below to above the LCST a) in dilute solutions and b) in thin films. c) Schematic drawing of the sample chamber. The sample (center) is surrounded by a water reservoir. The chamber is temperature controlled and the white light interferometry is conducted through a window in the top of the chamber.

Films of different film thicknesses were prepared by spin-casting from solutions with different polymer concentrations. The solvent used was chloroform. Thickness measurements with white light interferometry were conducted to investigate the thermoresponsive switching behavior. This method ensures a fast and nondestructive measurement of the film thickness in the desired range. The instrument is a Filmetrics F20 Thin Film Analyzer (Filmetrics, San Diego, USA) that is mounted on a custom made sample chamber. The sample chamber consists of an elevated area for sample placement, surrounded by a reservoir, as shown in fig. 2.1c. In our case the reservoir is filled with water to ensure a high humidity atmosphere inside the chamber. The chamber is tightly sealed and its temperature is controlled by liquid from a heating bath pumped through the bottom and top of the sample chamber. The white light interferometry measurement is conducted through a glass window in the top of the chamber.

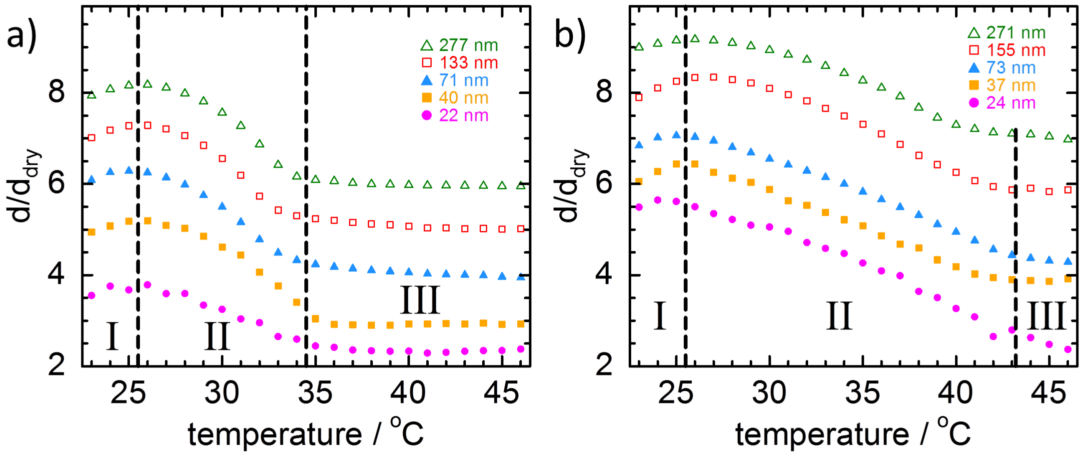

Figure 2.2:
Relative swelling amount (based on the dry film thickness) at different temperatures of a) linear and b) cyclic PNIPAM thin films of different film thicknesses. Different film thicknesses are shifted vertically for clarity.

At first the samples were kept at the initial temperature while the humidity inside the chamber was built up and the films increased their thickness due to water uptake. Then the chamber with the swollen film was heated in steps of 1 °C. At each of the steps the thickness was measured after equilibration of the film. The relative thickness change compared to the dry thickness for the initial films is plotted against the temperature in fig. 2.2 for the linear and cyclic PNIPAM thin films, respectively. Both graphs show three regions that are described as following: In the beginning the polymers are far away from the transition temperature and an increasing temperature leads to an increased saturated vapor pressure in the cell. Thus the number of available water molecules in the system is increased and the films increase their thickness even more (I). When approaching the transition temperature the films start to release the water molecules back into the surrounding vapor and therefore decrease their thickness (II). At some point the transition region is left and the films keep their thickness upon heating (III). However, there is still a small amount of water left in the films so that the thickness is above the dry thickness measured beforehand. Quite astonishing is the highly enlarged width of the transition region in the cyclic polymer compared to its linear counterpart. It increases from about 9 °C in the films of linear PNIPAM to about 18 °C in the films of cyclic PNIPAM. A similar behavior for these polymers is reported in aqueous solution [3]. This is explained by the reduced cooperativity effect in the cyclic polymer due to the steric hindrance in the ring shaped molecule. This cooperativity is responsible for the sharp transition region of PNIPAM compared to other thermoresponsive hydrogels. Reduction of the cooparativity effect therefore increases the transition region as clearly seen in both, solutions as well as thin films.

[1] W. Wang, E. Metwalli, J. Perlich, C. M. Papadakis, R. Cubitt, P. Müller-Buschbaum, *Macromolecules* **42**, 9041-9051 (2009)

[2] A. Richter, G. Paschew, S. Klatt, J. Lienig, K. F. Arndt, H. J. P. Adler, *Sensors* **8**, 561-581 (2008)

[3] X.-P. Qiu, F. Tanaka, F. M. Winnik, *Macromolecules* **40**, 7069-7071 (2007)

2.2 The swelling of thin hydrogel films: A kinetic micro-fluidics study

M. Philipp, V. Körstgens, C. Heller, Y. Yao, W. Wang, S. V. Roth[1], P. Müller-Buschbaum

[1] HASYLAB at DESY, Hamburg, Germany

The interaction of flowing liquids with polymer surfaces is poorly understood. Of particular interest are the molecular interactions and the resulting structural reorganizations in case of stimuli-responsive films and surfaces. Such systems can be switched by applying an external stimulus, like a variation of pH, ionic strength or temperature [1]. The observed sharp switching is in general related to phase transitions, like demixing transitions [1].

In the present study we address the interactions of water with a stimuli-responsive thin film made of poly(N-isopropylacrylamide) (PNIPAM) [2]. During the water uptake, the initially glassy PNIPAM film gets gel-like and the gained molecular mobility allows the film to undergo a structural reorganization. Well-defined experimental conditions for the water-film contact are guaranteed by making use of a micro-fluidics device. This device was specially designed to be combined with micro-focused grazing incidence small angle x-ray scattering (GISAXS) [3]. Hence, the kinetics of the structural reorganization during the water uptake of the hydrogel film, in particular in its initial stages, can be monitored by GISAXS.

For very smooth spin-coated polymer films, interface correlation [4] between the substrate/film and film/air interfaces may be installed during the spin-coating process [5]. In that case, part of the roughness spectrum of the substrate is replicated by that of the upper surface of the polymer film. As a consequence, the resulting in-plane morphology of the polymer film strongly depends on the underlying one. The smallest replicable in-plane length scale R_c is defined by the transition from a correlated to a statistically independent roughness spectrum of both film interfaces. R_c as well as the degree of roughness correlation are two parameters that allow quantifying the interface correlation. Interface correlation was observed for different glassy polymeric films, as for example polystyrene films, and arose from a frozen non-equilibrium state that developed during spin-coating [4]. Consequently, annealing of glassy films above the glass transition temperature may provoke the vanishing of interface correlation. This was proven to be true for thermal annealing [4]. In the present investigation, the annealing is provoked by lowering the glass transition temperature of the film below room temperature, due to the water uptake of the hydrophilic PNIPAM film.

The PNIPAM hompolymer (M_n = 20.5 kg/mol, PDI = 1.23) was purchased from PSS, Mainz. It was spin-coated out of a chloroform solution on pre-cleaned glass substrates. The resulting dry PNIPAM films are in the glassy state at room temperature (T_g is about 400 K). An as-prepared dry PNIPAM film was carefully placed within the micro-fluidics device and carefully aligned for the GISAXS investigation. With the micro-focused x-ray beam of 10 microns size offered at the P03 beamline at HASYLAB at DESY in Hamburg, the properties of the film can be probed within the micro-fluidics channel with a high spatial resolution of 50 microns step size. By changing the position of the footprint on the film within the channel, radiation damage of the film can be reduced during the kinetic swelling experiment, as for the acquisition of each GISAXS pattern a new position on the PNIPAM film can be selected. Before the beginning of the actual swelling experiment, the dry film was probed by GISAXS along the micro-fluidics channel in order to witness the structural homogeneity of the as-prepared PNIPAM film. The micro-fluidics experiment is accomplished under flow conditions: a laminar flow of water with a flow rate of 1 mm/s was chosen. The swelling kinetics of the hydrogel film is resolved with a time resolution of 1 s. As soon as the water flowed into the micro-fluidics channel, the acquisition of GISAXS patterns was started to resolve the kinetics of the water uptake of the film.

A preliminary analysis of the swelling of the PNIPAM film is shown in Fig. 2.3. From the measured 2D GISAXS patterns the information about the interface correlation is extracted

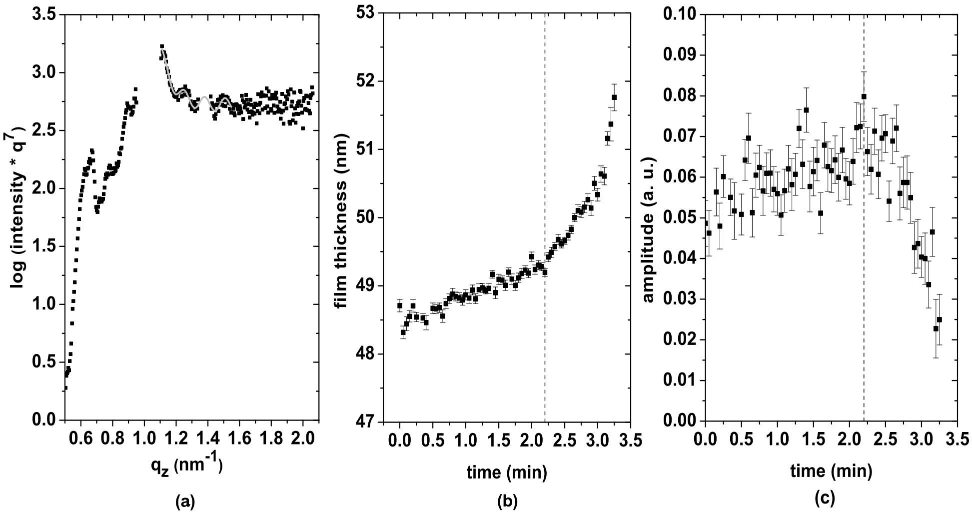

Figure 2.3:
(a) Representative detector cut of a 2D GISAXS pattern from the swelling PNIPAM film, fitted in the $Iq_z^7(q_z)$-representation. Temporal evolution of (b) the film thickness and (c) the amplitude of the sinus, representing the quality of the interface correlation.

from the detector cuts. Hence, the preliminary data evaluation concentrated on the temporal evolution of the detector cuts during the water uptake of the PNIPAM film. The detector cuts are fitted in the $log(Iq_z^7)(q_z)$-representation using as model the sum of a sinus term and an exponential decay (related to the intensity of the specular peak, which is partially shielded by a beam-stop). The sinus term describes the intensity streaks related to resonant diffuse scattering that occur parallel to the q_x-axis because of the interface correlation. The spacing of these fringes allows for estimating the distance between the correlated interfaces. The amplitude of the sinus term quantifies the quality of the interface correlation. The fit of a representative detector cut is shown in Fig. 2.3(a). In Fig. 2.3(b) the correspondingly determined film thickness versus time is depicted during the water uptake of the initially dry PNIPAM film. The vertical line represents a qualitative change in the swelling kinetics, which is related to the changeover from a glassy to a gel-like PNIPAM film. Fig. 2.3(c) quantifies the vanishing of interface correlation (amplitude of the sinus term), which occurs within the margin of error as soon as the film has become gel-like. The present investigation thus allows for the first time resolving the initial stages of the water uptake of a glassy hydrophilic film.

M.P. thanks the Fonds National de la Recherche (Luxembourg) for the receipt of a Marie Curie cofunded AFR Postdoc grant.

[1] M. A. Cole, N. H. Voelcker, H. Thissen, H. J. Griesser, *Biomaterials* **30**, 1827 (2009)

[2] M. Philipp, U. Müller, R. Aleksandrova, R. Sanctuary, P. Müller-Buschbaum, J. K. Krüger, *Soft Matter* **8**, 11387-11395 (2012)

[3] J.-F. Moulin, S. V. Roth, P. Müller-Buschbaum, *Rev. Sci. Instr.* **79**, 015109 (2008)

[4] P. Müller-Buschbaum, J. S. Gutmann, C. Lorenz, T. Schmitt, M. Stamm, *Macromolecules* **31**, 9265-9272 (1998)

[5] C. J. Lawrence, *Phys. Fluids* **31**, 2786-2795 (1988)

2.3 Kinetics of aggregation in thermoresponsive triblock copolymers – influence of concentration, start and target temperature

J. Adelsberger, A. Kulkarni, I. Grillo[1], M. Sharp[2], A. M. Bivigou Koumba[3], A. Laschewsky[3], P. Müller-Buschbaum, C. M. Papadakis

[1] Institut Laue-Langevin, Grenoble, France

[2] Institut für Werkstoffforschung, Helmholtz-Zentrum Geesthacht, Germany (now at ESS, Lund, Sweden)

[3] Institut für Chemie, Universität Potsdam, Potsdam, Germany

Thermoresponsive polymers have received increasing attention because they respond with a strong change of conformation and solubility to a small variation of temperature across their cloud point, i.e. they show lower critical solution temperature (LCST) behavior. A widely used LCST polymer is poly(N-isopropyl acrylamide) (PNIPAM) which has a cloud point of ≈ 32°C. The kinetics of the transition, such as the switching time and the reversibility, is of importance for many applications. We have investigated triblock copolymers consisting of a long hydrophilic PNIPAM middleblock and two short hydrophobic polystyrene (PS) endblocks. In aqueous solution, they form flower-like core-shell micelles or, above the critical gel concentration, micellar hydrogels. When heated above the LCST, the PNIPAM block becomes hydrophobic and releases water from the micellar shell, which consequently collapses. The collapsed micelles form large aggregates. These changes are reversible [1]. We have investigated the aggregation behavior in dependence on polymer concentration and on the start and target temperatures [2]. This way, we obtain information on the role of intermicellar bridging and on the role of the temperatures for the reversibility of the switching.

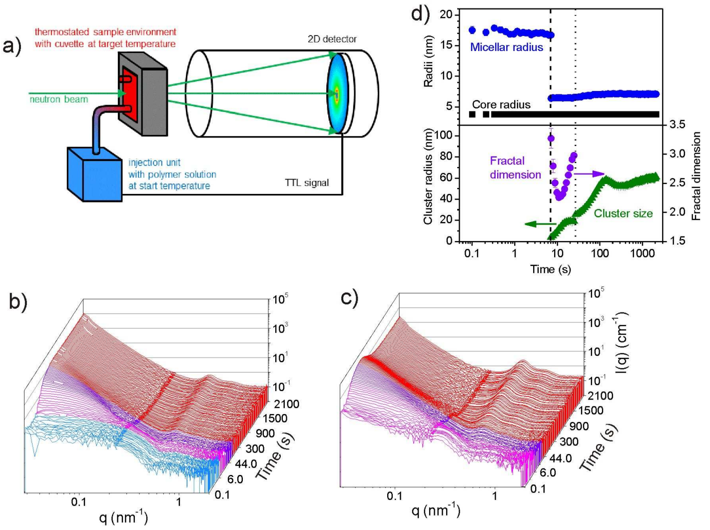

Figure 2.4:
(a) Scheme of the setup of the experiment. SANS curves at 50 mg/ml during a jump from 29.6°C to 34.6°C (b) and at 200 mg/ml during a jump from 20.0°C to 42.8°C (c). (d) Core radius and micellar radius and b) cluster radius and fractal dimension of the clusters from (b). The dashed line denotes the cloud point, the dotted line the end of the near-transition regime.

Time-resolved small-angle neutron scattering (SANS) experiments allowed us to investigate the kinetics of the collapse of the micellar shell and the cluster formation with an excellent time resolution (0.1 s) and gave information on a wide range of length scales. For that purpose, a stopped-flow apparatus was used at beamline D22 at ILL (figure 2.4a). The triblock copolymer solutions $P((S\text{-}d_8)_{11}\text{-}b\text{-}NIPAM_{220}\text{-}b\text{-}(S\text{-}d_8)_{11})$ at 20, 50 or 200 mg/ml in D_2O were kept in a reservoir at a temperature below the cloud point (20.0°C or 29.6°C). The target temperatures were chosen at 34.6°C or 42.8°C. To realize a fast temperature jump, the solution was injected into the preheated sample cell, and the time-resolved measurement was started. The curves were fitted using a model for spherical core-shell micelles together with different form and structure factors for their clusters [2].

The SANS curves during two jumps are shown in figure 2.4b and c. Four time regimes are distinguished by the appearance of forward scattering, its shape and the presence of a correlation peak. For high concentrations and high target temperatures, the first time regime below the cloud point is not resolved (figure 2.4c).

The most important results are compiled in figure 2.4d. In all cases, the micellar radius decreases very rapidly and relaxes to slightly higher values during the later stages after crossing the cloud point, whereas the radius of the PS cores stays constant. Right after the cloud point is passed, the collapsed micelles form small imperfect clusters with voids; thus, their correlation is of fractal type. Only later, the clusters are dense enough to be described by a liquid-like structure. The clusters grow first by attachment of additional micelles from solution; this process depends on the polymer concentration and thus the degree of intermicellar bridging. Eventually, the clusters grow by coagulation. Their final surface structure depends on the target temperature: For 34.6°C, a concentration gradient is present in the beginning which transforms into a rough cluster surface. For 42.8°C, the behavior is opposite.

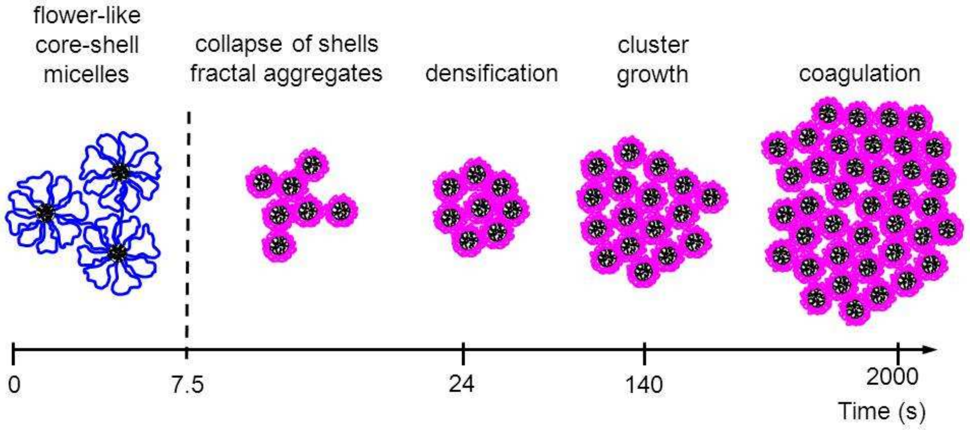

Figure 2.5: Scheme of cluster formation and growth for the four different regimes.

Thermoresponsive triblock copolymer solutions thus show a complex collapse and aggregation behavior (figure 2.5). From our results, we conclude that, in appliations where fast switching back is needed, prolonged heating above the cloud point should be avoided because then large aggregates form which dissolve only slowly. Moreover, we find that the behavior in the triblock copolymers is much more complex than the one in PNIPAM homopolymers [3].

This work is funded by the DFG within the project SPP1259 ”Intelligent Hydrogels”.

[1] A. Jain, A. Kulkarni, A. M. Bivigou Koumba, W. Wang, P. Busch, A. Laschewsky, P. Müller-Buschbaum, C. M. Papadakis, *Macromol. Symp.* **291-292**, 221-229 (2010). J. Adelsberger, A. Kulkarni, A. Jain, W. Wang, A. M. Bivigou-Koumba,P. Busch, V. Pipich, O. Holderer, T. Hellweg, A. Laschewsky, P. Müller-Buschbaum, C. M. Papadakis, *Macromolecules* **43**, 2490-2501 (2010)

[2] J. Adelsberger, E. Metwalli, A. Diethert, I. Grillo, A. M. Bivigou-Koumba, A. Laschewsky, P. Müller-Buschbaum, C. M. Papadakis, *Macromol. Rapid Commun.* **33**, 254-259 (2012). J. Adelsberger, I. Grillo, A. Kulkarni, M. Sharp, A.M. Bivigou-Koumba, A. Laschewsky, P. Müller-Buschbaum, C. M. Papadakis, *Soft Matter* **9**, 1685-1699 (2013)

[3] A. Meier-Koll, V. Pipich, P. Busch, C.M. Papadakis, P. Müller-Buschbaum, *Langmuir* **28**, 8791-8798 (2012)

2.4 Cononsolvency of PNIPAM and P(S-*b*-NIPAM) in aqueous solution

K. Kyriakos, M. Philipp, J. Adelsberger, S. Jaksch, A. Miasnikova[1], A. Laschewsky[1], I. Grillo[2], P. Müller-Buschbaum, C.M. Papadakis

[1] Institut für Chemie, Universität Potsdam, Germany
[2] Institut Laue-Langevin, Grenoble, France

Poly(N-isopropylacrylamide) (PNIPAM) and its thermoresponsive behavior in aqueous solutions have been widely studied. In water, this polymer exhibits lower critical solution temperature (LCST) behavior with $T_c = 32^o$C. When heated above T_c, the PNIPAM chains release the bound water and collapse, which results in a very sharp coil-to-globule transition. Recently, strong interest has arisen in the PNIPAM chain conformation in water upon addition of a second, water-miscible solvent, e.g. methanol (MeOH) [1]. Although both water and methanol are good solvents for PNIPAM, the addition of the latter induces a miscibility gap and subsequently a decrease of the T_c. This enhanced phase separation is known as cononsolvency. We report here on a time resolved small angle neutron scattering (SANS) experiment on two different PNIPAM systems; namely on a linear PNIPAM homopolymer and on an amphiphilic diblock P(S-*b*-NIPAM) system (PS stands for polystyrene). The latter system, when dissolved in H_2O, forms core-shell micelles below T_c. Aqueous solutions of both systems have been studied before with SANS experiments, focusing on the phase transition and the kinetics of the collapse of PNIPAM [2, 3]. In this work, the emphasis is on the kinetics of the conformational changes occurring upon the addition of methanol. Fully deuterated MeOH (*d*-MeOH) was added in various mixing ratios (i.e. 90:10, 85:15 and 80:20 v/v D_2O/*d*-MeOH) to solutions of PNIPAM or P(S-*b*-NIPAM)) in D_2O having an initial concentration of 20 mg/ml. To elucidate the kinetics of the collapse of the chain or the micellar shell, respectively, *d*-MeOH was added to the initial aqueous solutions using a stopped-flow set-up (Biologic SFM-300, dead time 0.25 ms) and the changes were followed using time-resolved SANS at the high flux small-angle neutron scattering instrument D22 at the Institut Laue-Langevin in Grenoble, France. The selected neutron wavelength was $\lambda = 8$ Å and the sample-to-detector distances (SDD) 4 m and 14.4 m. The use of fully deuterated solvents ensured a high contrast.

Figure 2.6a shows representative SANS curves of PNIPAM homopolymer for one mixing ratio (80:20 v/v) of D_2O:*d*-MeOH. The strong forward scattering indicates very large aggregates of collapsed PNIPAM chains. Moreover, in the high q-region, an additional small contribution is observed, most probably due to thermal fluctuations within the aggregates. For analysis, the sum of two contributions was used for the low and the high q-regions: a modified Porod model $I(q) = K/q^{\alpha}$, where K is the amplitude and α contains information on the surface of the cluster, and an Ornstein-Zernicke contribution $I(q) = I_{OZ}/(1+q^2\ \xi^{\ 2})$. The Porod amplitude ($K$) (Figure 2.6b) exhibits two distinctive regimes and indicates that the aggregation path depends on the content of *d*-MeOH. Namely the more methanol is present, the faster the aggregation. The exponent α (Figure 2.6c) increases over time due to the increase of the scattering length density (SLD) gradients at the surface of PNIPAM-rich domains, thus the interfaces of the aggregates with the solvent are becoming more PNIPAM-rich.

Figure 2.7a shows representative SANS curves of P(S-*b*-NIPAM) for one mixing ratio (80:20 v/v). The strong forward scattering, even in the first curves, indicates that the collapse has occurred already and small aggregates are already present in the probed volume. Later, a form factor fringe, appears and moves to lower q-values with time. Two different models were used for fitting: for the first stages, a Guinier-Porod model and, when the fringe becomes pronounced enough, polydisperse spheres with Gaussian size distribution was used. From both models the radius of the formed aggregates was extracted (Figure 2.7b). At intermediate times both models were used and demostrate the reliability of the results. During the first second, the radius is

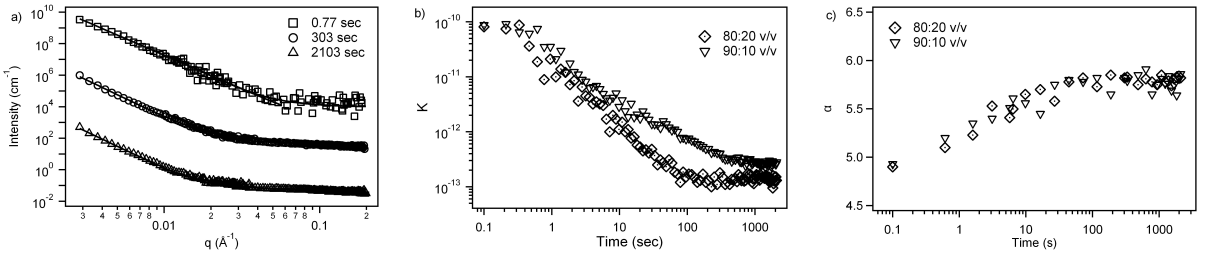

Figure 2.6: (a) Representative SANS curves of PNIPAM homopolymer for a mixing ratio D_2O:*d*-MeOH of 80:20 v/v for selected time frames. The lines are fitting curves to the open symbols. For clarity the curves were shifted vertically by a factor of 10^3 (303 sec) and 10^6 (0.77 sec). (b) Porod intensity (K) of the formed aggregates over time versus two mixing ratios, 80:20 v/v and 90:10 v/v. (c) Porod exponent α versus time for two mixing ratios 80:20 v/v and 90:10 v/v.

similar for all mixing ratios, but at later stage, the growth of the aggregates starts earlier and bigger radii are reached, when more *d*-MeOH is present.

To summarize, we studied the cononsolvency effect of a PNIPAM homopolymer and a P(S-*b*-NIPAM) diblock copolymer in D_2O, regarding the kinetics of the phase transition upon the addition of different amounts of the cononsolvent *d*-MeOH. As expected, the presence of the cononsolvent resulted in the very rapid collapse of the PNIPAM chains (faster than the dead time of the set up). The amount of *d*-MeOH affected the subsequent aggregation pathway of the collapsed PNIPAM chains or the collapsed P(S-*b*-NIPAM) micelles as well as the final aggregate radius.

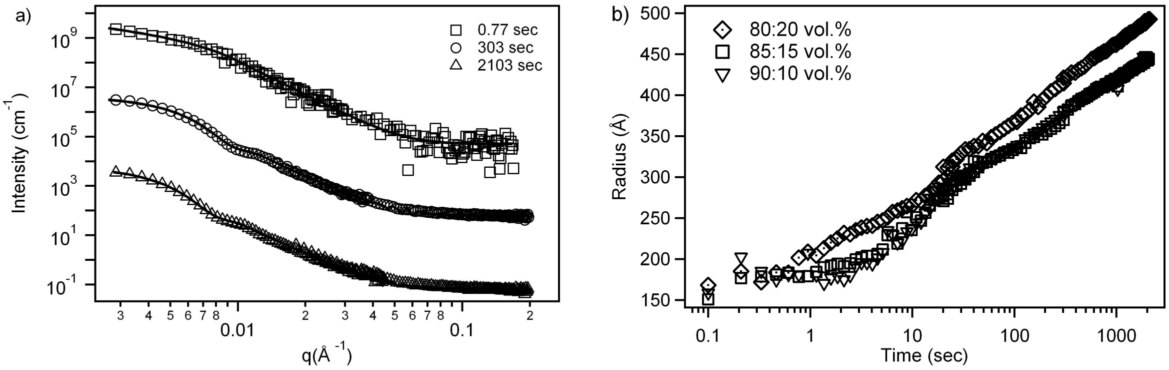

Figure 2.7: (a) Representative SANS curves of P(S-*b*-NIPAM) diblock for a mixing ratio D_2O:*d*-MeOH of 80:20 v/v for selected time frames. The lines are fitting curves to the open symbols. For clarity the curves were shifted vertically by a factor of 10^3 (303 sec) and 10^6 (0.77 sec). (b) Aggregrates radii over time for all three mixing ratios.

The project is supported by DFG within the priority program SPP1259 (Intelligente Hydrogele).

[1] F. Tanaka, T. Koga, H. Kojima, N. Xue, F. M. Winnik, *Macromolecules* **44**, 2978-2989 (2011)

[2] J. Adelsberger, I. Grillo, A. Kulkarni, M. Sharp, A. M. Bivigou-Koumba, A. Laschewksy, P. Müller-Buschbaum, C. M. Papadakis, *Soft Matter* **9**, 1685-1699 (2013)

[3] A. Meier-Koll, V. Pipich, P. Busch, P. Müller-Buschbaum, C. M. Papadakis, *Langmuir* **28**, 8791-8798 (2012)

2.5 Thermoresponsive hydrogels from symmetrical triblock copolymers poly(styrene-*b*-(methoxy diethylene glycol acrylate)-*b*-styrene)

G. De Paoli, A. Miasnikova[1], A. Laschewsky[1], P. Müller-Buschbaum, S. S. Funari[2], C. M. Papadakis

[1] Institut für Chemie, Universität Potsdam, Germany
[2] HASYLAB at DESY, Hamburg, Germany

Symmetrical amphiphilic block copolymers BAB with hydrophobic outer blocks B and a hydrophilic inner block A can form physical hydrogels under appropriate conditions. Above a critical concentration, a gel of bridged micelles is formed, and the mechanical properties result mainly from the proportion of active bridges. In this study, we describe the temperature-dependent gelation behvaior of a series of BAB symmetrical triblock copolymers, namely poly(styrene-*b*-methoxy diethylene glycol acrylate-*b*-styrene (PS-PMDEGA-PS) (Fig. 2.8) [1]. The inner PMDEGA block is thermo-responsive. The phase transition temperature of PMDEGA in aqueous solution varies between 35-45°C, i.e. in the most interesting physiological window. Moreover, PMDEGA cannot form self-consistent inter- and intra-molecular H-bonds. This presumably leads to transitions with virtually no hysteresis between the cooling and the heating cycles [2]. We were interested in the effects of the PMDEGA block onto the hydrogel mechanical properties. In particular, we investigated the influence of the inner block length on the gel formation. Moreover, we wanted to correlate the changes of the mechanical properties to the structural changes with temperature. For this purpose, we carried out temperature-resolved small-angle X-ray scattering (SAXS) experiments.

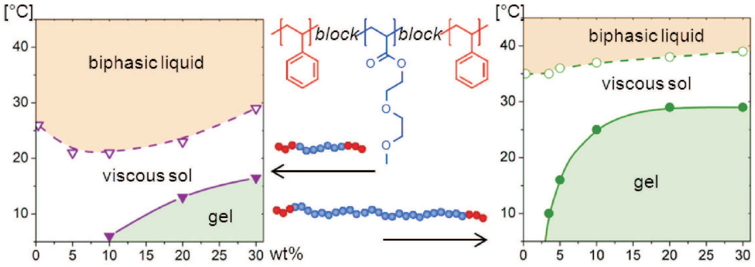

Figure 2.8:
Structure of PS-PMDEGA-PS and phase behavior as determined from turbidimetry and rheology.

Cloud points were determined by visual observation. Concentration-dependent sol-gel transitions were detected by the tube inversion test. SAXS experiments were performed at beamline A2 at HASYLAB/DESY. An X-ray beam with a wavelength $\lambda = 0.15$ nm was used. A 2D MarCCD detector was mounted at a distance of 3.24 m from the sample.

Representative scattering curves of PS_8-$PMDEGA_{452}$-PS_8 at 10 wt. % in water are displayed in Fig. 2.9. At low temperatures, a broad peak is present which is due to the correlation between the positions of the micelles. It becomes weaker upon heating to the cloud point, and, at the same time, the forward scattering increases. At high temperatures, the peak is shifted to higher q-values, indicating the collapse of the micellar network, and forward scattering becomes more intense. The decrease of the overall intensity above the cloud point is due to sedimentation of large clusters formed by collapsed micelles.

We attribute the peak to a liquid-like correlation between the PS cores with a close to hard-sphere interaction; thus a Percus-Yevick structure factor was used to model the correlation. The forward scattering was modeled using a Porod law describing large, homogeneous and smooth clusters formed by water-insoluble and bridged micelles. The X-ray scattering length density of PMDEGA differs strongly from the nearly equal ones of PS and H_2O, and the PS blocks are very short; thus, the scattering signal in PS-PMDEGA-PS is dominated by the scattering from the PMDEGA corona of the presumably formed core-shell micelles. We therefore modelled the

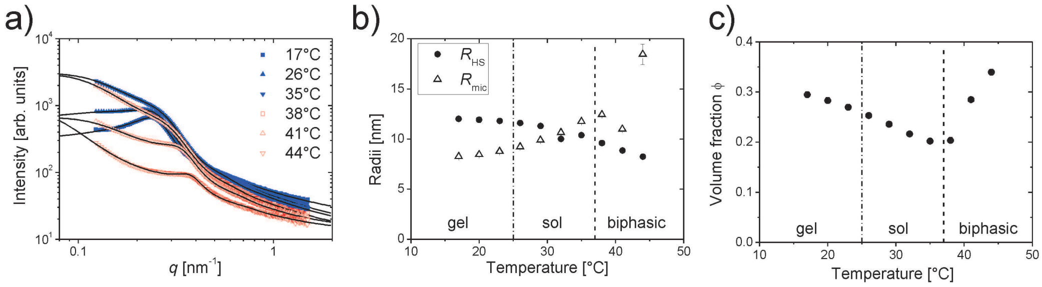

Figure 2.9:
(a) Temperature-resolved SAXS curves of PS_8-$PMDEGA_{452}$-PS_8 at 10 wt.% in water (symbols) together with model fits (lines). (b) Micellar radius, R_{mic}, and hard-sphere radius, R_{HS}. (c) Volume fraction of correlated micelles, ϕ.

micelles by homogeneous spheres. Fluctuations within the PMDEGA shells were taken into account by an Ornstein-Zernike structure factor.

Below the cloud point, R_{HS} decreases slightly as temperature is increased towards the cloud point, whereas the micellar radius, R_{mic} increases slightly (Fig. 2.9b), whereas the volume fraction of correlated micelles, ϕ, decreases slightly (Fig. 2.9c). The latter may be due to the fact that single micelles are released from loose aggregates of micelles. No change is observed at the gel point. Above the cloud point, R_{HS} continues decreasing, whereas R_{mic} slightly decreases and ϕ increases strongly. We conclude that the SAXS curves of PS_8-$PMDEGA_{452}$-PS_8 can be described by a model including spherical micelles with liquid-like correlation and a loose corona consisting of a solvent-swollen polymer matrix. Interestingly, discontinuities are neither observed at the gel point nor at the cloud point. The distance between the micelles keeps decreasing smoothly. Only the correlation between micelles decreases slightly below the cloud point, whereas it increases above. This makes an important difference of the thermo-responsive BAB triblock copolymer systems containing PMDEGA as switchable inner A block compared to the analogous system based on PNIPAM, which is widely used as model for thermo-responsive systems.

In this series of triblock copolymers BAB, based on PMDEGA as block A and bearing two short hydrophobic PS outer blocks B, which still allow direct dissolution in water, the behavior of the triblock copolymers is found to be dominated by the length of the thermo-responsive inner block. Two thermal transitions are observed, namely from gel to liquid at temperatures well below the cloud point, and from sol to phase separated liquid at the cloud point. This makes a marked difference to the behavior of analogous triblock copolymers containing PNIPAM as thermo-responsive inner block, for which gelling can be induced by heating close to the phase transition temperature. This exemplifies the importance of the chemical nature of the thermo-responsive block for controlling not only the phase transition temperature, but also the polymer-polymer interactions in the amphiphilic copolymers. The unusual temperature dependence of the hydrogels seems to be due to a decreasing number of micelle-bridging polymers. Though polystyrene is commonly believed to build kinetically frozen glassy micelle cores, the short PS_8 blocks studied seem to represent a good compromise for already providing sufficient hydrophobicity while still maintaining a certain mobility in aqueous self-organization.

This work is funded by DFG within the priority program "Intelligente Hydrogele".

[1] A. Miasnikova, A. Laschewsky, G. De Paoli, C. M. Papadakis, P. Müller-Buschbaum, S. S. Funari, *Langmuir* **28**, 4479-4490 (2012)

[2] A. Miasnikova, A. Laschewsky, *J. Polym. Sci. A: Polym. Chem.* **50**, 3313-3323 (2012)

2.6 Transition behavior of poly(styrene-*b*-monomethoxydiethylenglycol-acrylate-*b*-styrene) thick film prepared from water investigated by SAXS measurements

Q. Zhong, J. Adelsberger, M. Niedermeier, A. Golosova, A. M. Bivigou-Koumba[1],
A. Laschewsky[1], S. S. Funari[2], C. M. Papadakis, P. Müller-Buschbaum

[1] Institut für Chemie, Univesität Potsdam, Potsdam, Germany
[2] HASYLAB at DESY, Hamburg, Germany

During the last years, due to the large variety of applications, e.g. for drug delivery systems, [1] valves to control liquid transfer [2] or optical devices, [3] thermo-responsive hydrogels with a lower critical solution temperature (LCST) behavior attracted more and more interest. In our investigations, novel thermo-responsive hydrogel-forming polymers based on poly(methoxydiethylenglycol acrylate) (PMDEGA) are studied. PMDEGA shows a higher LCST (39 °C) as compared to the frequently investigated thermo-responsive polymer poly(N-isopropylacrylamide) (PNIPAM). [4] Similar to di-block or tri-block copolymers based on NIPAM, the hydrophilic monomer MDEGA can be polymerized with hydrophobic polystyrene blocks forming PMDEGA-based block copolymers. These block copolymers can give rise to thermo-responsive micelles, which self-assemble in solution. By solution casting, the core-shell micellar structure formed in aqueous solution is transferred into thick films on supports. The transition behavior upon crossing the LCST for films after exposure to water is probed by SAXS measurements, which were performed at beamline A2, HASYLAB at DESY in Hamburg, Germany.

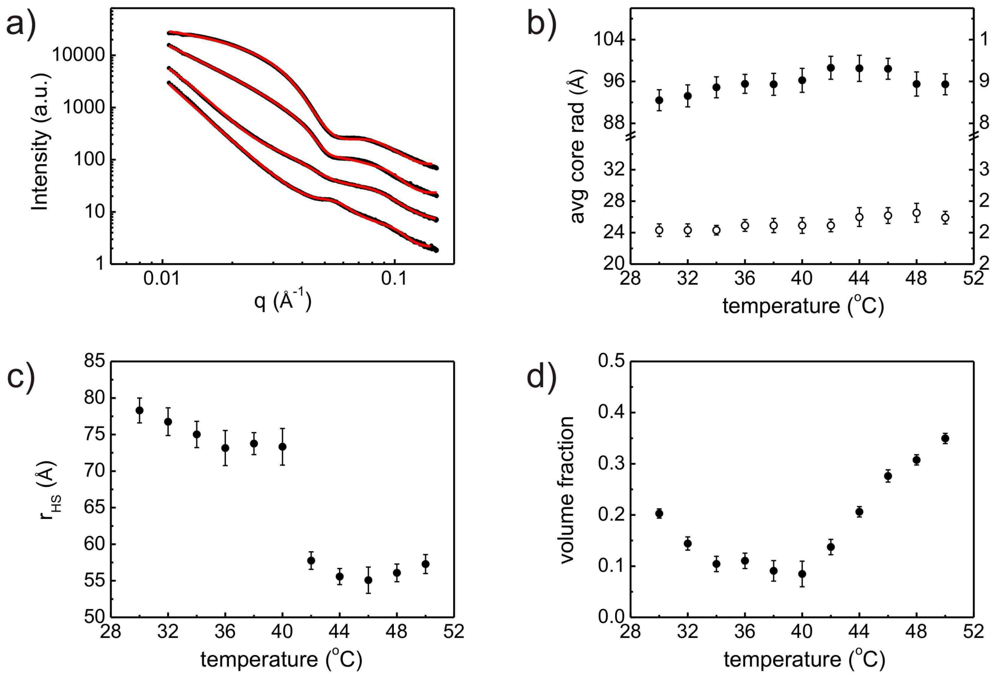

Figure 2.10:
a) Four representative SAXS scattering curves of thick films prepared from water and immersed in D_2O (black dots) shown together with the fits (red line) at 32 °C, 38 °C, 42 °C and 48 °C from top to bottom. b) Temperature-dependence of the core radius (open circle) and the micelle radius (solid circle) when the temperature increases from 30 °C to 50 °C. c) Temperature-dependence of the hard-sphere radius of the micelles. d) Temperature-dependence of the volume fraction of the micelles.

Fig. 2.10a shows four representative SAXS curves of thick films prepared from water at 32 °C, 38 °C, 42 °C and 48 °C in D_2O. It is obvious, that in the low q region, there is only a flat intensity plateau. This indicates that the large domains in the as-prepared film do no longer exist. As the PMDEGA chains start to absorb D_2O and swell, the micelles with swollen PMDEGA shell may rearrange themselves and the domain boundaries vanish. When the temperature increases above the transition temperature (40 - 42 °C), the collapsed micelles in the film prefer to aggregate, resulting in a reappearance of a strong forward scattering. Simultaneously, the correlation peak in the curves shifts from 0.042 $Å^{-1}$ to 0.055 $Å^{-1}$, which corresponds to a shrinkage of the intermicellar distance from 75 Å to 57 Å. It shows that the collapsed micelles tend to move closer towards each other. Note that the scattering curves change gradually when the temperature crosses the transition temperature, instead of undergoing a sudden change of the SAXS pattern. This finding compares well to our former observation, that PMDEGA homopolymer films exhibit a broad transition region. [4]

To gain the details of the collapse process of the swollen micelles, the scattering curves are fitted with a simple hard sphere core-shell model. Fig. 2.10b presents the core and micelle radii as extracted from these fit. As the core consists of the PS blocks, the radius of the core almost stays constant. Surprisingly, the radius of the micelle exhibits no shrinkage, even when the temperature is above the transition temperature. This behavior is similar to P(S-*b*-MDEGA-*b*-S) solutions investigated previously, and totally differs from the transition behavior of the PNIPAM based block polymer solutions. On the contrary, the hard-sphere radius (r_{HS}) shows a pronounced shrinkage when the temperature passes the transition temperature (see Fig. 2.10c). The value of r_{HS} drops from 74 Å at 34 °C (below the transition temperature) to 58 Å at 42 °C (above the transition temperature). It is noted that r_{HS} below the transition temperature is even smaller than the radius of the micelle, which may have two reasons. The first reason can be the bridge connections between the different micelles. They induce the diameter of the micelles obtained from the fits to be slightly larger than the real distance between the micelles because of overlap. The second reason could be that the hard-sphere structure factor is not a good model assumption any longer, because the micelles formed in the film may not have a well-defined spherical shape and exhibit size polydispersity. In addition, besides the data point at 30 °C, the volume fraction is constant before the temperature approaches the transition temperature (see Fig. 2.10d). When the temperature is above the transition temperature, the volume fraction gradually increases from 0.09 to 0.35. This indicates that the collapsed micelles start to pack densely in the film.

According to the fitting results from SAXS measurements, although the swollen PMDEGA shell does not exhibit a pronounced shrinkage when the temperature is raised above the transition temperature, the intermicellar distance abruptly decreases and the volume fraction gradually increases. These indicates that when the temperature crosses the transition temperature, the micelles switches from the swollen to collapsed state. The collapsed micelles have a tendency to aggregate to form large domains.

[1] D. C. Coughlan, F. P. Quilty, O. I. Corrigan, *J. Control. Release* **98**, 97-114 (2004)

[2] H. Iwata, M. Oodate, Y. Uyama, H. Amemiya, Y. Ikada, *J. Membr. Sci.* **55**, 119-130 (1991)

[3] S. Mias, J. Sudor, H. Camon, *Microsyst. Technol.* **14**, 747-751 (2008)

[4] Q. Zhong, W. N. Wang, J. Adelsberger, A. Golosova, A. M. Bivigou-Koumba, A. Laschewsky, S. S. Funari, J. Perlich, S. V. Roth, C. M. Papadakis, P. Müller-Buschbaum, *Colloid Polym. Sci.* **289**, 569-581 (2011)

2.7 Kinetics of the collapse transition of poly(2-oxazoline) gradient copolymers

S. Jaksch, K. Kyriakos, J. Zhang, I. Grillo[1], A. Schulz[2], R. Jordan[2], C. M. Papadakis

[1] Institut Laue-Langevin, Grenoble, France
[2] Professur für Makromolekulare Chemie, Department Chemie, TU Dresden

Thermoresponsive polymers in aqueous solution exhibit a reversible strong change in solubility and chain conformation when heated above their cloud point. Especially interesting polymers of this class of materials are poly(2-oxazoline)s (POx) whose behavior can be tuned from hydrophilic over thermoresponsive to hydrophobic by a pendant 2-substitution. By including hydrophobic moieties into a thermoresponsive copolymer, the cloud point can be tuned in a wide range [1]. Moreover they are non-toxic and biocompatible. These properties make them ideal candidates for medical applications such as drug delivery [2].

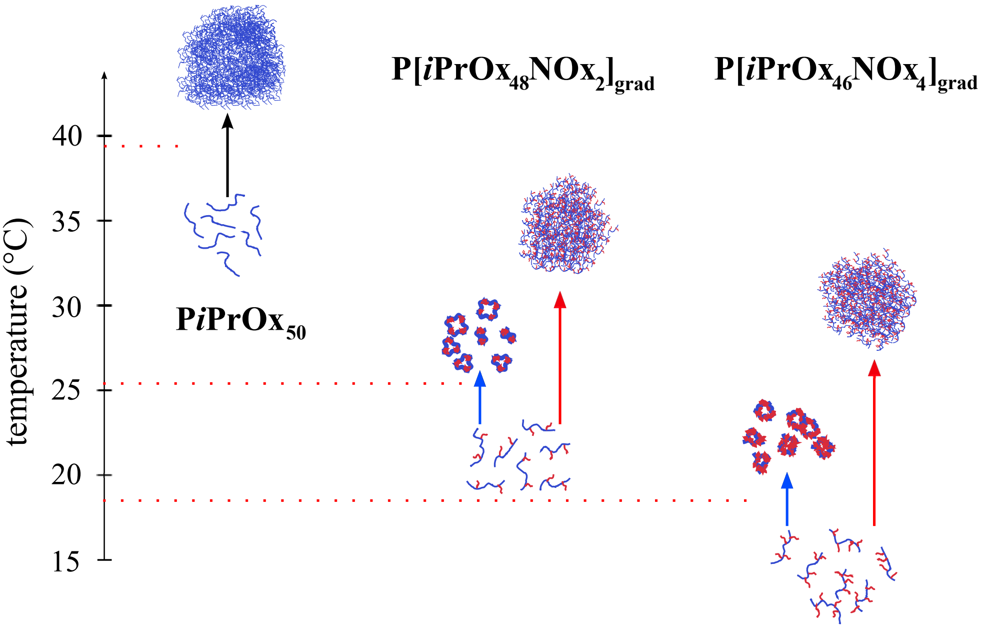

Figure 2.11: Phase diagram of P*i*PrOx$_{50}$, P[*i*PrOx$_{48}$-NOx$_2$]$_{grad}$ and P[*i*PrOx$_{46}$-NOx$_4$]$_{grad}$ in solution. Temperature quenches were performed along the arrows. Shallow and deep quenches are indicated by blue and red arrows, respectively. Both gradient copolymers show an intermediate and a high temperature regime.

We investigated the kinetics of the collapse transition of dilute aqueous solutions of the thermoresponsive poly(2-*iso*-propyl-2-oxazoline)$_{50}$ (P*i*PrOx$_{50}$) and the two gradient copolymers poly[(2-*iso*-propyl-2-oxazoline)-(2-n-nonyl-2-oxazoline)]$_{grad}$ P[*i*PrOx$_{48}$NOx$_2$]$_{grad}$ and P[*i*PrOx$_{46}$NOx$_4$]$_{grad}$, where two or four of the thermoresponsive units were replaced by hydrophobic moieties with a n-nonyl side group [3].
This substitution lowered the cloud point from 39.2°C for the homopolymer to 24.5°C and 17.7°C, respectively. Temperature-resolved small-angle neutron scattering (SANS) revealed a two-step behavior for the gradient copolymers when heated above their cloud point: In the intermediate regime just above the cloud point, small aggregates of only a few chains, already formed at temperatures slightly below the cloud point, dominate and only very few large aggregates are present. In contrast, in the high temperature regime, 5 K above, large aggregates dominate [1]. For the homopolymer, no intermediate regime is observed.

To investigate the stability of the intermediate regime, we used time-resolved SANS at the D22 beamline at the Institut Laue-Langevin, Grenoble, France, during temperature jumps across the cloud point into the intermediate (shallow quench) or into the high-temperature regime (deep quench). At this, we used a modified stopped-flow setup where we kept the solutions in a reservoir kept below the cloud point and then injected them into the preheated cuvette at the target temperature in the neutron beam (fig. 2.11). Simultaneously, SANS data acquisition was started with measurement times of 3 or 30 s for 1 h. To fit the data, we used a form factor of small fractals for the scattering of single chains and small aggregates. This way, we obtained the aggregate size, ξ, and the fractal dimension, D, which is related to the Flory exponent, ν via $\nu = 3/D + 2$ and thus allowed us to investigate the solvent quality. This fractal form factor was superimposed by a power law to account for the forward scattering due to large aggregates.

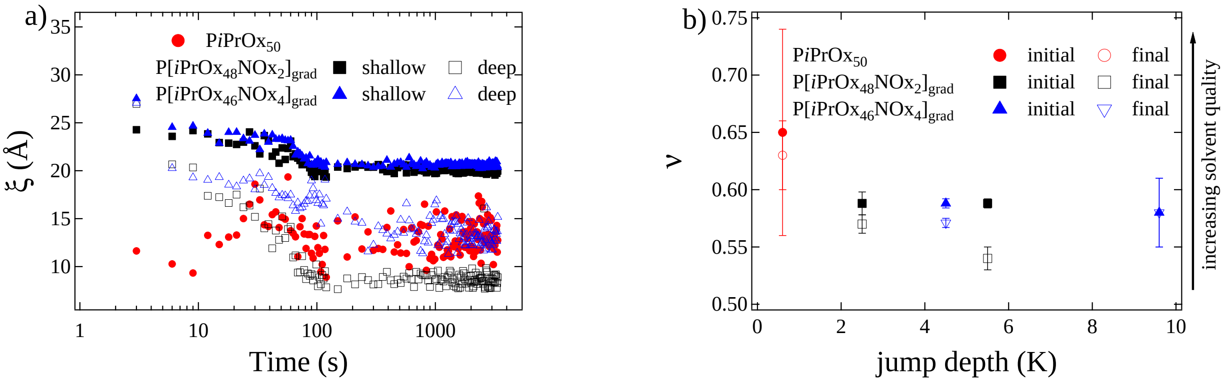

Figure 2.12: Results of the fits of a fractal form factor to the SANS curves for all temperature quenches. (a) Size of the small aggregates, ξ, as a function of time. (b) Initial and final values of the Flory exponent, ν.

Fig. 2.12 shows the results of the fits of the fractal form factor. After 100 s, the size of the small aggregates, ξ, is stable for the remaining time, i.e. the intermediate regime is stable and does not evolve into the high temperature regime (fig. 2.12a). Moreover, the shallow jumps always result in small aggregates with $\xi \approx 20$ Å, whereas these are smaller after the deep jumps, where $\xi = 8 - 15$ Å. Thus, deeper quenches lead to a more pronounced collapse. Regarding the solvent quality derived from the Flory exponent ν (fig. 2.12b), it is seen that, upon inclusion of hydrophobic moieties along the chain, ν and thus the solvent quality decrease, as expected for a thermoresponsive polymer. Interestingly, the quench depth and the number of NOx groups have no effect.

To conclude, the conformation of thermoresponsive polymers after the collapse depends on the chemical composition and the temperature above the cloud point. Gradient copolymers containing few hydrophobic moieties display a stable intermediate regime just above the cloud point.

This project is supported by the DFG within the project „Multicompartment systems based on poly(2-oxazolines)“ (Pa771/6-2).

[1] S. Salzinger, S. Huber, S. Jaksch, P. Busch, R. Jordan, C. M. Papadakis, *Colloid Polym. Sci.* **290**, 385-400 (2012)

[2] F. C. Gärtner, R. Luxenhofer, B. Blechert, R. Jordan, M. Essler, *J. Contr. Release* **119**, 291-300 (2007)

[3] S. Jaksch, K. Kyriakos, J. Zhang, I. Grillo, A. Schulz, R. Jordan, C. M. Papadakis, Kinetics of the Collapse Transition of Poly(2-oxazoline) investigated by time resolved SANS, in preparation

2.8 Structure and disintegration of nanoparticles from clinically relevant polymers

M. Dyakonova, A. Bogomolova[1], S. Filippov[1], A. Radulescu[2], C.M. Papadakis

[1] Institute of Macromolecular Chemistry, Prague, Czech Republic
[2] FRM II, Garching, Germany

Polymers based on water-soluble N-(2-hydroxypropyl methacrylamide) (HPMA) which carry both a cancer drug, namely doxorubicin (Dox), and a hydrophobic targeting group, namely cholesterol derivatives have been shown to be successful for tumor therapy, i.e. clinically relevant. Both groups are bound via pH-sensitive hydrazone bonds to the polymer backbone. The polymer is expected to form nanoparticles at the pH value of blood but to disintegrate in tumor where the pH value is low and to release both Dox and cholesterol.

In the present study, the polymers were investigated where Dox was bound to the backbone by a hydrazone bond, whereas cholesterol was bound either firmly or via hydrazone bond too. We focused on the dependence of the nanoparticle structure on the polymer architecture, the content of Dox and cholesterol and the pH value [1].

Scattering curves from SANS measurements of polymeric conjugates with Dox and without both containing 1.2 mol % of cholesterol in phosphate buffer at pH 7.4 and 5.0 are presented in figure 2.13. Model fitting at pH 7.4 manifests contributions from unimers and from ellipsoidal nanoparticles. The resulting radius of gyration of the unimers stays constant at 11 Å for all the conjugates. In contrast, the ellipsoids are more elongated and narrower for the conjugates containing Dox than for those without (main radius 42-47 Å vs. 36.1 Å and 2.5-3.9 Å vs. 4.5 Å).

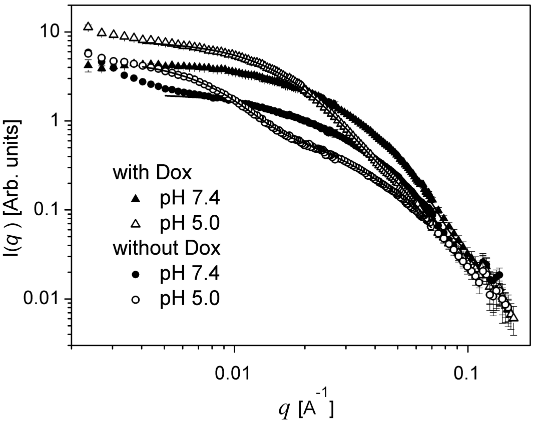

Figure 2.13:
Scattered intensity I(q) as a function of the momentum transfer q for conjugates with doxorubicin and without at pH 7.4 and 5.0 at room temperature. Solid lines represent fits.

Thus, at neutral pH values the most probable aggregation pattern of HPMA-Cholesterol nanoparticles is an ellipsoid composed of a cholesterol core and a shell of the hydrophilic HPMA copolymers. The same conjugates were exposed to acidic conditions (Figure 2.13) to study the disintegration behavior of the nanoparticles. Fitting of the SANS curves shows that ellipsoids and spheres are present simultaneously in solution. A possible explanation is that, after cleavage of the hydrazone bond, cholesterol moieties are released from the polymer backbone. Since they are highly hydrophobic, they phase-separate from the aqueous solution and crystallize, forming large spherical aggregates, which are located separately or are attached to the initial ellipsoids by hydrophobic interactions.

Fluorescence correlation spectroscopy (FCS) confirmed that the aggregation process is non-monotonous. Figure 2.14 shows the resulting hydrodynamic radii of the conjugate with 3.0 mol % of cholesterol as a function of conjugate concentration in PBS buffer at pH 7.4. The corresponding hydrodynamic radii increase with polymer concentration from 11.2 nm to 21.4 nm. FCS reveals a step-like increase of the hydrodynamic radius which indicates that existing nanoparticles associate rather than to grow continuously. The critical micelle concentration was determined at 1.7×10^{-2} mg·ml $^{-1}$ [1].

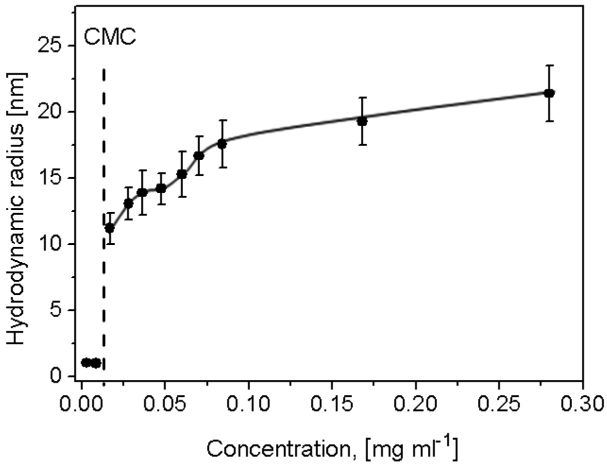

Figure 2.14:
Hydrodynamic radii of the conjugate with 3.0 mol % of cholesterol as a function of conjugate concentration.

By means of time-resolved SANS the kinetics of the structural changes was followed upon a rapid change in pH from a value corresponding to the one of blood (pH 7.4) and to the one of a tumor (pH 5.0). Model fitting of the scattering curves (Figure 2.15) proves that for a conjugate with Lev-cholesterol moieties, the structure of the aggregates alters from Gaussian chain state to the elongated ellipsoidal conformation within the first 57 minutes, and after 60 minutes it undergoes the drastic change to a spherical form. The kinetics is very slow, in the time range of minutes or slower.

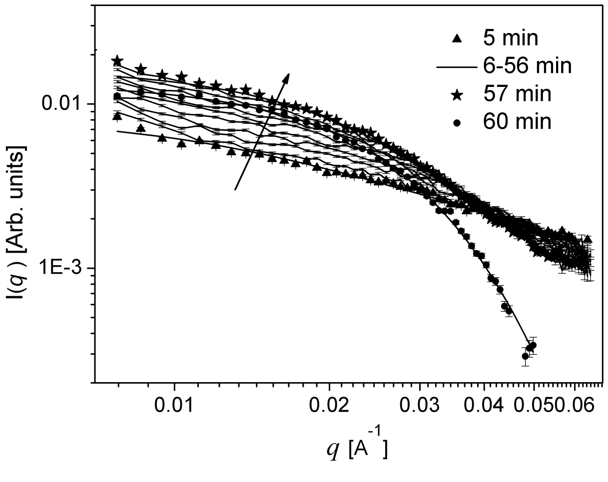

Figure 2.15:
Scattered intensity I(q) as a function of the scattering vector q for conjugate with Lev-cholesterol moieties at room temperature.

Thus, the observed conformational changes of the HPMA chains are in good agreement with the results obtained earlier [1] and give a direct proof of nanoparticle formation.

The project was carried out in terms of two year European Master program in Materials Science, MaMaSELF.

[1] S. K. Filippov, P. Chytil, P. V. Konarev, M. Dyakonova, C. M. Papadakis, A. Zhigunov, J. Plestil, P. Stepanek, T. Etrych, K. Ulbrich, D. I. Svergun, *Biomacromolecules* **13**, 2594-2604 (2012)

2.9 Molecularly imprinted conductive polymers for controlled trafficking of neurotransmitter at solid-liquid interfaces

N. Paul, M. Müller[1], A. Paul[2], E. Guenther[3], I. Lauermann[1], P. Müller-Buschbaum, M.Ch. Lux-Steiner[1]

[1] Helmholtz Zentrum für Materialen und Energie, Berlin, Germany
[2] Physics Department E21, TUM, Garching, Germany
[3] Natural and Medical Sciences Institute, Reutlingen, Germany

On entering the eye, light is converted by photoreceptor cells in the retina into electrical impulses which are sent to the brain via inter-neuronal communication in the inner retina. The inter-neuronal communication takes places via release and binding of neurotransmitters between the pre-synaptic neuron and the post-synaptic neuron. On arrival of nerve impulses, the neurotransmitters are released within milliseconds from the pre-synaptic neuron (e.g. photoreceptor cells) into the synaptic cleft where they diffuse in the synaptic fluid till they reach and bind to the postsynaptic membrane receptors. The nerve impulse is then transferred to the postsynaptic neuron. In some incurable diseases of the eye, like retinitis pigmentosa and age-related macular degeneration, the photoreceptor cells are specifically damaged whereas the rest of the visual network remains largely unaffected. These diseases lead to loss of vision and presently affect about 15 million people around the world.

Recently, we proposed a biochemistry based retinal implant using the retinal neurotransmitter, glutamate [1]. The aim of our envisaged device is the replacement of a degenerated photoreceptor by a neurotransmitter imprinted implant (n-MIP). Fig. 2.16 shows a schematic of the envisaged implant site and the proposed idea. Our intention is to regulate the glutamate concentration in the liquid with voltage applied to the n-MIP. In the rest state, when there is no voltage, there is some initial concentration of glutamate in the liquid. On application of a positive voltage to the n-MIP, the glutamate molecules are adsorbed on the n-MIP from the liquid, leading to decrease in glutamate concentration in the liquid. On removal of the voltage, the glutamate is released back into the liquid, leading to an increase in the glutamate concentration in the liquid. This process is expected to be reversible. The advantage would be the direct control of this ejection of neurotransmitters and therefore a specific access to the successional neurons. In this work, we demonstrate the proof of principle of this device with voltage by verifying the change in the concentration of glutamate in physiological solvents. [1]

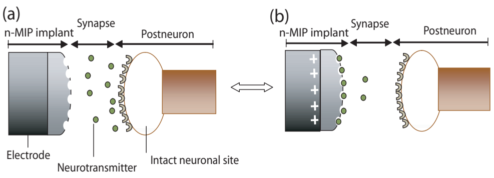

Figure 2.16:
Schematic diagram of the synaptic cleft and the proposed implant at the preneuron(photoreceptor) site showing the (a) rest state (without voltage stimulation) corresponding to an initial concentration (or release state) of the neurotransmitter in the synapse and (b) the active state (with voltage stimulation) corresponding to binding of the neurotransmitter to the n-MIP.

The infrared spectrum of glutamate-doped polypyrrole (Ppy) (n-MIP) is shown in Fig. 2.17. The absorption peaks of glutamate, normally observed at 1565 cm^{-1} and 1610 cm^{-1} are shifted slightly to lower frequencies due to accommodation of glutamate within the Ppy matrix. The peak at 1400 cm^{-1} has also decreased in intensity due to a reduced contribution from the symmetric stretching contribution of at least one of the carboxylate group due to its conversion into carbonyl group.

One way to investigate the adsorption/release of biomolecules at solid-liquid interface is to monitor the concentration of the biomolecules in the liquid using fluorescence spectroscopy.

In this technique, a fluorescent dye (which by itself does not have any fluorescence, e.g fluorescamine) is added to the liquid under investigation, and the resulting fluorescence intensity corresponds to the amount of biomolecules in the liquid. The n-MIP film was placed in contact with different solvents each containing 5 mM glutamate. Voltage steps were applied to the n-MIP film by an external power supply. During that time, a minute amount of the solution as extracted for analysis by fluorescence spectroscopy and labeled with fluorescamine. The intensity of the emitted fluorescence radiation quantifies the amount of glutamate molecules and accordingly their concentration.

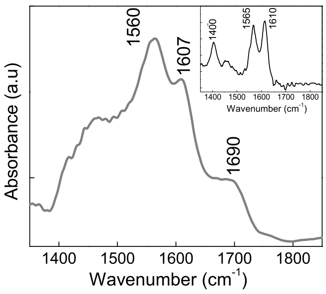

Figure 2.17:
An infrared difference spectrum of glutamate-doped Ppy film on a Si crystal / D_20 solution. There is no glutamate in the solution. The background spectrum was a clean Si crystal / D_20 solution. Inset shows IR spectrum of pure glutamate / D_20 solution.

For all three solvents, the trend of the curves in Fig. 2.18 shows a decrease in glutamate concentration for positive voltages and a increase (recovery to initial concentration) of glutamate in the solvent for zero or negative voltages. This can be interpreted as binding of the negatively charged glutamate molecule to the positively charged n-MIP electrode and its release from the uncharged (or negatively charged) n-MIP film due to electrostatic forces. The similarity of the binding/release property of the n-MIP to glutamate in solvents of phosphate buffer and Ringer's solution, in which other ions are also present, elucidate the specificity of the molecule for the n-MIP film. In all the solutions, the process seems completely reversible.

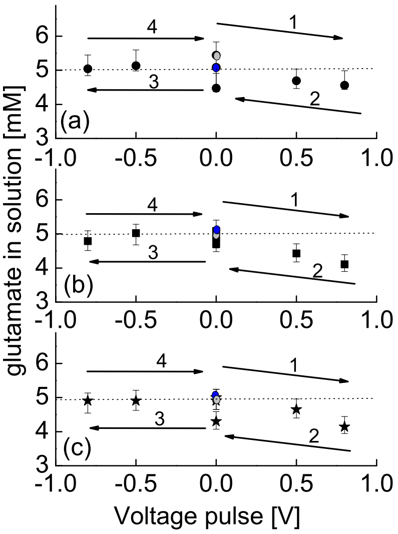

Figure 2.18:
Changes in glutamate concentration calculated from the fluorescence intensities as a result of voltages applied to the n-MIP/Si surface in (a) water (b) phosphate buffer and (c) Ringer's solution. The arrows define the sequence of the process.

[1] N. Paul, M. Müller, A. Paul, E. Guenther, I. Lauermann, P. Müller-Buschbaum, M.Ch. Lux-Steiner *Soft Matter* **9**, 1364 (2013)

3 Thin polymer films

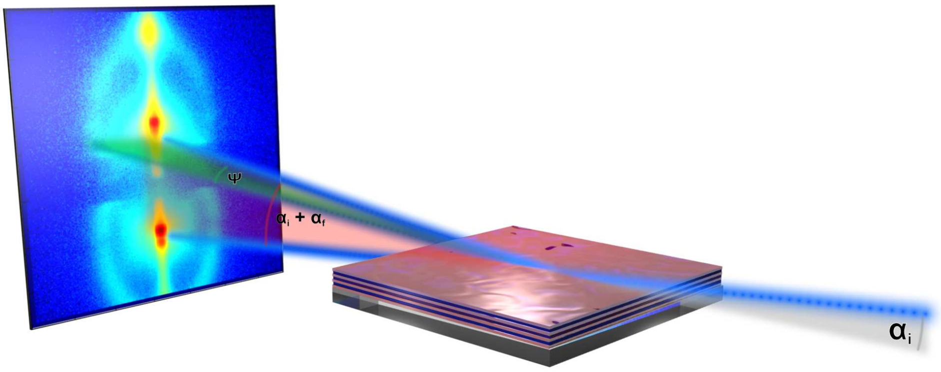

3.1 Identification of the conditions to improve the block copolymer thin film nanostructures by solvent vapor treatment

A. Sepe, D. Posselt[1], S. Jaksch, K. Swiatek[1], R. Steinacher, J. Zhang, J. Perlich[2], D.-M. Smilgies[3], C. M. Papadakis

[1] Roskilde University, IMFUFA, Denmark
[2] HASYLAB at DESY, Hamburg, Germany
[3] Cornell University, Ithaca, NY, USA

Nanostructured block copolymer thin films find a number of applications, especially as templates for structuring inorganic materials, which may be used as optical elements. At this, it is necessary to promote defect-free structures. However, the self-assembly process during film preparation introduces defects and multi-domain structures, especially during the often used, fast spin-coating process. A post-preparation technique to remove these defects is solvent vapor treatment. The solvent has two effects: It decreases the repulsive interaction between the two blocks, and it increases the mobility of the (glassy) blocks. However, it is unclear which conditions lead to defect-free structures, and very different conditions have been applied in the literature.

In the present work, we focus on the role of the conditions during swelling with solvent vapor and subsequent drying, in particular on the rate of swelling and the final degree of swelling of the film as well as on the rate of drying. In our previous studies, we have investigated the structural changes in block copolymer thin films during solvent vapor induced swelling of lamellae-forming poly(styrene-*b*-butadiene) (P(S-*b*-B)) employing in-situ, real-time grazing-incidence small-angle X-ray scattering (GISAXS) [1]. This copolymer features a glassy PS block and a rubbery PB block. We used saturated vapor or a stepwise increasing vapor pressure. It was found that the lamellar not only swells uniaxially but also reorganizes and additional lamellae form to accommodate the swollen chains. For technical reasons, the drying process was not followed due to technical reasons.

The goals of the present work are (i) to swell the films with CHX vapor at a low swelling rate such that they are always close to thermodynamic equilibrium and form a well-ordered structure in the swollen state, (ii) to follow the processes during drying and (iii) to identify conditions under which the highest order would be achieved. To reach these goals, a new gas handling system has been designed in which the vapor pressure of CHX can be increased and decreased continuously.

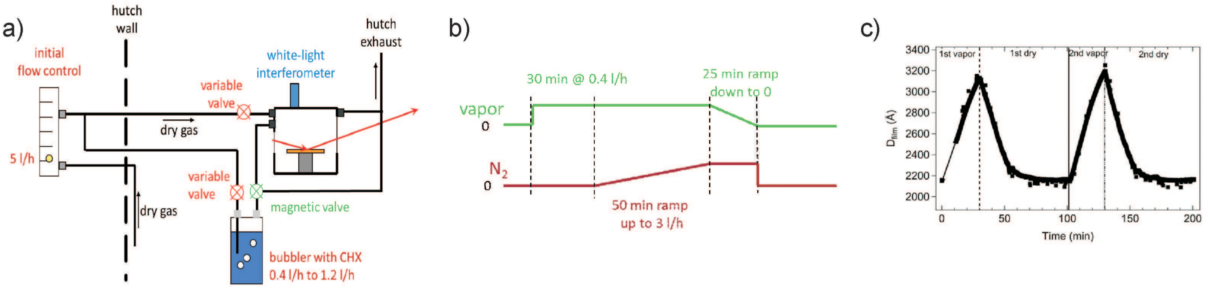

Figure 3.1:
(a) Schematics of the set-up for vapor treatment and drying employed for in-situ measurements at beamline BW4. (b) Protocol used for swelling and drying which was carried out twice. (c) Corresponding film thickness profile as determined using in-situ white-light interferometry.

The setup is show in Fig. 3.1a. Two variable valves allowed us to set the flow rate of both CHX vapor and dry N_2 with high precision. Moreover, we installed two dedicated lines for N_2 and

CHX, respectively, into the sample cell which hampers backflow of vapor/N_2 into the other line. The swelling was accomplished by letting N_2 gas flow through the bubbler containing liquid CHX at a flow rate of 0.4 l/h (Fig. 3.1b). The subsequent drying process was carried out by keeping the vapor flow rate constant at 0.4 l/h and, at the same time, increasing the flow rate of N_2 gas step by step from zero to 3 l/h within 50 min. To dry the film completely, the CHX vapor flow was decreased step by step to zero which took 25 min. The film which was subject to this treatment had been prepared from lamella-forming poly(styrene-*b*-butadiene) having a molar mass of 28.0 kg/mol by spin-coating of acid-cleaned Si wafers from toluene solution. GISAXS experiments were carried out at beamline BW4 at HASYLAB, DESY. Images were taken continuously every 30 s throughout the whole treatment at an incident angle $\alpha_i = 0.18°$.

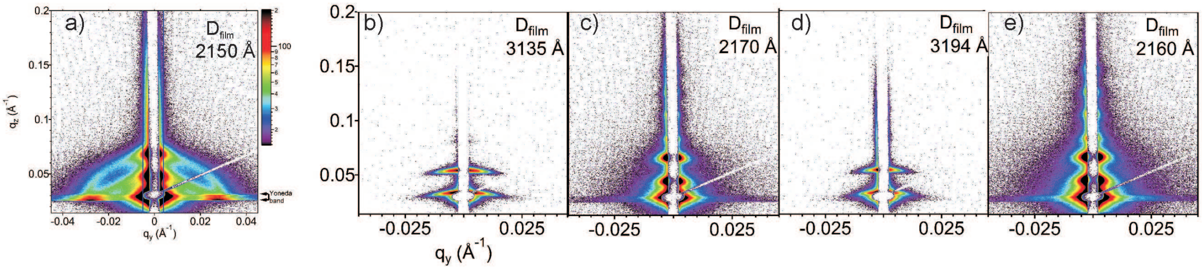

Figure 3.2:
2D GISAXS images of the as-prepared film (a), of the fully swollen film (b) and the dried film (c) during the first cycle and during the second cycle (d,e). The actual film thicknesses are given in the images.

The setup and the protocol used resulted in a linear and reproducible increase and decrease of the film thickness (Fig. 3.1c). The GISAXS image of the as-prepared film features a pair of diffuse Bragg sheets (DBSs) (Fig. 3.2a) indicating that the parallel lamellar orientation prevails. However, diffuse Debye-Scherrer rings are present as well indicating that a part of the sample consists of randomly oriented lamellae. The GISAXS image of the swollen film shows a pair of well-defined first-order DBSs, the rings have vanished (Fig. 3.2b). Their slight bending downwards has previously been attributed to the reorganization of the lamellar stack [2]. After the first drying (Fig. 3.2c), DBSs up to third order are present indicating that the correlation between the lamellar interfaces and their orientational order have improved significantly compared to the as-prepared state. These changes are reproduced during the second cycle (Fig. 3.2d,e).

In comparison with our previous studies [1,2], we conclude that the lamellar order can be significantly improved by means of solvent vapor treatment. Sufficiently slow swelling, a sufficiently high maximum degree of swelling and sufficiently slow drying result in the best structures. The restructuring of the lamellar stack is possible only (i) if the glass transition of PS is crossed by the solvent vapor uptake, (ii) if the interfacial tension between PS and PB is reduced sufficiently and (iii) if the drying is slow enough to preserve the lamellar stack formed in the vapor-swollen state. At this, the combination of in-situ film thickness measurements and GISAXS measurements give a wealth of information which help to identify the relevant parameters.

This project was funded by the International Graduate School ”Materials Science of Complex Interfaces” (CompInt).

[1] D. Posselt, Z. Di, A. Sepe, D.-M. Smilgies, C. M. Papadakis, Proceedings from International Workshop on Soft Matter Physics & Complex Flows, eds.: Jon Otto Fossum and Elisabeth Bouchaud, May 22 - 25, 2012, Svolvær, Lofoten, Norway, accepted

[2] C. M. Papadakis, Z. Di, D. Posselt, D.-M. Smilgies, *Langmuir* **24**, 13815-13818 (2008)

3.2 Structural evolution of perpendicular lamellae in diblock copolymer thin films during solvent vapor treatment

J. Zhang, A. Sepe, X. Shen, J. Perlich[1], D. Posselt[2], D.-M. Smilgies[3], C. M. Papadakis

[1] HASYLAB at DESY, Hamburg, Germany
[2] Roskilde University, IMFUFA, Denmark
[3] Cornell University, Ithaca, NY, USA

The structural rearrangements in block copolymer thin films have attracted considerable interest since vapor treatment is frequently used for annealing defects hampering applications. In-situ, real-time grazing-incidence small-angle X-ray scattering (GISAXS) is a very powerful method to determine the structural changes of block copolymer thin films with high time resolution and statistical relevance [1].

In the present work, we focus on poly(styrene-*b*-butadiene) (P(S-*b*-B)) diblock copolymers having a molar mass of 216 kg/mol which shown perpendicular lamellar orientation. Compared with parallel lamellae, perpendicular lamellae have severe geometrical constraints because the normal of the lamellar interfaces lies in the film plane and changes of the lamellar thickness are not easily accommodated. To investigate the structural changes during vapor treatment and drying, two different incident angles, one below and one above the critical angle of the polymer, were used in the GISAXS experiments. This way, we could discriminate surface-near order from the one in the bulk of the film. Cyclohexane was used to treat the samples; it is a good solvent for PB and a theta solvent for PS. Time-resolved GISAXS was performed at beamline BW4, HASYLAB at DESY. VIS interferometry was used to determine the film thickness during the vapor treatment. The time resolutions of GISAXS and VIS interferometry are 30 s and 1 s, respectively.

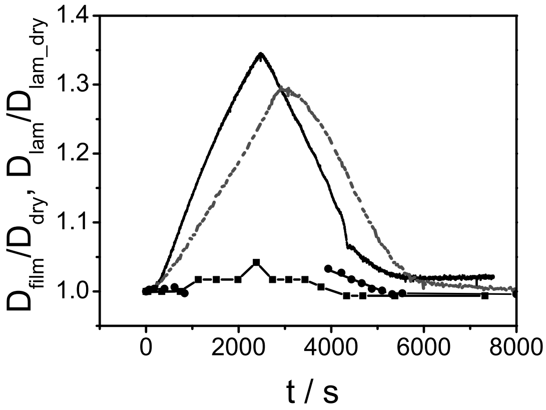

Figure 3.3:
Reduced film thickness (black solid and grey dashed lines for $\alpha_i = 0.18°$ and $\alpha_i = 0.10°$, respectively) and reduced lamellar thickness (squares and circles for $\alpha_i = 0.18°$ and $\alpha_i = 0.10°$, respectively) as a function of treatment time. In the latter dataset, missing data are due to very weak BRs.

Fig. 3.3 shows the film thickness behavior during swelling and drying of the polymer films obtained in-situ using white-light interferometry for two films whose initial film thickness was 1600 Å. With maximum degrees of swelling of 1.35 and 1.30, respectively, the behavior was thus quite reproducible. The presence of solvent in the microphase-separated, lamellar morphology not only lowers T_g but also screens the repulsive interaction between the PS and the PB blocks. In the absence of solvent, $\chi N = 190$; the diblock copolymer is deep in the strong-segregation regime. For a non-selective solvent, χN of the copolymer is decreased to $\chi_{eff} N$ with $\chi_{eff} = \phi\chi$ where ϕ is the volume fraction of polymer, calculated by $\phi = D_{dry}/D_{film}$, where D_{dry} and D_{film} are the film thicknesses of the as-prepared film and during vapor treatment, respectively. Using this assumption in spite of the slight selectivity of CHX, $\chi_{eff} N$ is estimated to decrease to 138 and 148 during the swelling, respectively, which is still significantly higher than 30; i.e., the block copolymer remains in the strong-segregation regime [2].

The variation of D_{lam} was obtained by following the peak positions of the Bragg rods (BRs) in the 2D GISAXS images. The reduced lamellar thicknesses, defined as the ratio of the D_{lam}

values during the swelling and drying to the values of the as-prepared films, are plotted in Fig. 3.3. Comparing with the behavior of the film thickness, we conclude that the swelling of the film is one-dimensional along the normal of the film surface, which is due to the geometrical confinement.

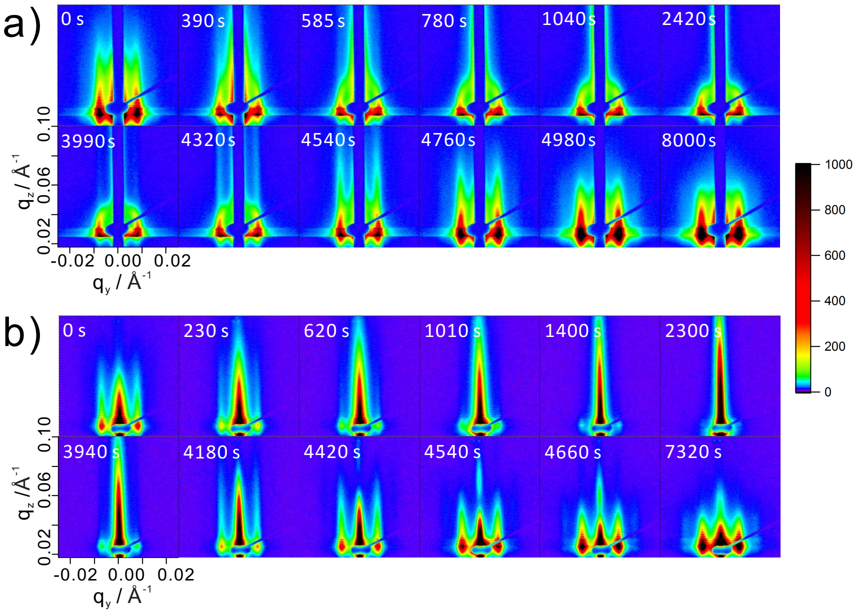

Figure 3.4:
Two-dimensional GISAXS images before and during vapor treatment (upper row) and during drying (lower row) of the thin P(S-*b*-B) film. The times after the start of the vapor treatment are indicated.

At $\alpha_i = 0.18°$, the scattering signal is an average over the entire film thickness. The BRs bent inwards during the swelling (Fig. 3.4a top). We attribute this bending to tilting of the lamellae away from the purely perpendicular orientation. During drying, the straight BRs reappeared (Fig. 3.4a bottom) in such a way that, initially, they were very long along q_z with very weak intensity; then, their intensity increased while their length decreased. Thus, we propose that the purely perpendicular orientation is lost due to the solvent uptake during swelling, while it is reinstalled during drying. At the end of the drying, the BRs became short again. At $\alpha_i = 0.10°$, during swelling (Fig. 3.4b, top row) the intensity of the BRs became weaker and weaker, which may be attributed to a loss of lamellar order near the film surface. During drying, a modulation appeared in-plane, i.e. at $q_y = 0$. Both the narrow and elongated DBRs and the modulation appeared during the drying are due to the the protrusion of one block at the film surface. Since the solvent is slightly selective for the PB domains, the PS domains are more quickly depleted of the solvent and turn solid earlier than the PB domains. This means a characteristic time is passed after which there is practically no solvent left in the PS domains, while the PB domains are still swollen with solvent. Further evaporation leads to a collapse of the swollen PB domains to a level below the interface of the already rigid PS domains. This way, the protrusion structure is formed during drying.

This project is funded by DFG (Pa771/10-1).

[1] Z. Di, D. Posselt, D.-M. Smilgies, R. Li, M. Rauscher, I. I. Potemkin, C. M. Papadakis, *Macromolecules* **45**, 5185-5195 (2012)

[2] C. M. Papadakis, K. Almdal, K. Mortensen, D. Posselt, *Europhys. Lett.* **36**, 289-294 (1996).

3.3 Randomly oriented lamellae rearrangements in diblock copolymer thin film during solvent vapor treatment

J. Zhang, S. Jaksch, K. Kyriakos, J. Perlich[1], D. Posselt[2], D.-M. Smilgies[3], C. M. Papadakis

[1] HASYLAB at DESY, Hamburg, Germany
[2] Roskilde University, IMFUFA, Denmark
[3] Cornell University, Ithaca, NY, USA

Well-ordered structures formed by self-assembly of diblock copolymer have attracted increasing interest due to their potential applications, such as the preparation of nanoporous films, nanostructured templates, ultrahigh-density data storage media, and biosensors [1]. However, the thin film preparation by solvent-casting or spin-coating does not necessarily lead to the equilibrium structure. Often, only short-ranged order is observed in the self-assembled structures, which hampers many applications. Methods to bring the samples into their equilibrium states and to reduce the number of defects are thus highly desirable. Vapor treatment with solvents is a commonly used technique to anneal defects in block copolymer thin films. The solvent vapor swells the film and effectively lowers the glass transition temperature (T_g) of blocks; meanwhile it affects the interactions between blocks (χ_{eff}) and the relative volume fractions. The mentioned parameters all depend on the selectivity of the solvent [2].

In the present work, thin films of lamellar poly(styrene-*b*-butadiene) (P(S-*b*-B)) diblock copolymers having a molar mass of 28 kg/mol were studied to elucidate the mechanisms of structural changes induced by solvent vapor treatment. As in our previous studies, the thin films feature parallel lamellae with respect to the substrate [3]. Cyclohexane (CHX) which is slightly selective for the PB block was used to treat films. In addition to ex-situ atomic force microscopy (AFM) to investigate the film surfaces, time-resolved in-situ grazing-incidence small-angle X-ray scattering (GISAXS) at beamline BW4, HASYLAB at DESY, together with VIS interferometry were used. The time resolutions of GISAXS and VIS interferometry are 30 s and 1 s, respectively.

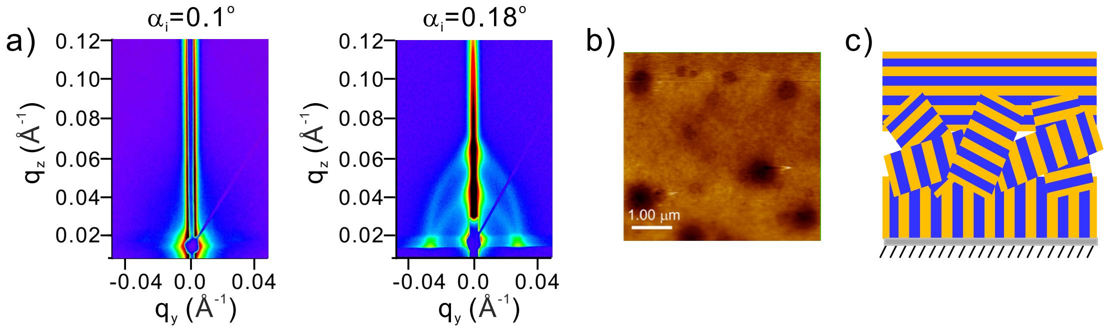

Figure 3.5:
(a) 2D GISAXS patterns of an as-prepared film measured at 0.1° (left) and 0.18° (right). (b) AFM image of an as-prepared film which shows terraces. (c) Sketch of the inner structure of the as-prepared thin film.

Firstly, the inner structures of the as-prepared film were determined using different incident angles by GISAXS. Fig. 3.5a shows the 2D GISAXS patterns of the as-prepared film at 0.1° and 0.18°. The penetration depth of the X-ray beam is 140 Å and larger than 10^5 Å for the used polymer at 0.1° and 0.18°, respectively, the scattering is thus surface-sensitive or is averaged over the entire film thickness. At 0.18°, the GISAXS image shows a distorted Debye-Scherrer ring, i.e. the lamellae have a random orientation in the thin film. The lamellar thickness is 168 Å, as determined from the position of the diffuse Bragg sheet at $q_z = 0$. However, at 0.1°, the

GISAXS image shows no structural feature, i.e. near the surface, there are no perpendicular lamellae. Since the penetration depth is smaller than the lamellar thickness, no diffuse Bragg sheets appear at $q_y = 0$. To verify the conclusion, the surface structures were determined by AFM (Fig. 3.5b). The terraces confirm the presence of parallel lamellae at film surface. Based on these results, the inner structure of the as-prepared film is given by the sketch (Fig. 3.5c).

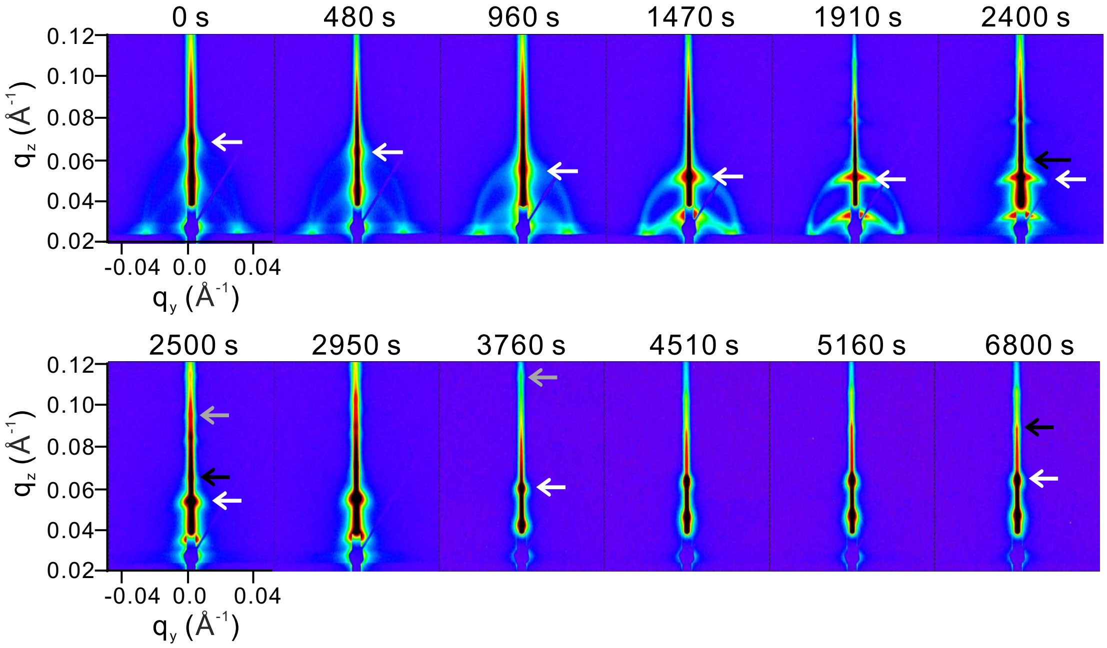

Figure 3.6:
2D GISAXS images of the thin film during vapor treatment (upper row) and drying (bottom row). The times after the beginning of the vapor treatment are indicated. Deswelling was started after 2400 s. The white, black and grey arrows point to the first, second and third order of Bragg peak, respectively.

Fig. 3.6 shows representative two-dimensional GISAXS images of the thin film during vapor treatment and drying. During swelling, firstly, the position of first order Bragg sheet moves rapidly to lower q_z values till 1470 s and is almost constant afterwards. This means that, initially, the parallel lamellae swell due to the solvent uptake, which results in a more stretched polymer chain conformation causing an entropy loss. Then, the lamellae reorganize to lower the free energy of the system. Secondly, a second-order diffuse Bragg sheet (marked by the black arrow) appears at the end of swelling, i.e. the lamellae become asymmetric, as expected for a selective solvent. Thirdly, the perpendicular lamellae vanish at the end of the swelling. During drying, the asymmetry vanishes but reappears, as evident from the vanishing and reappearance of the second-order diffuse Bragg sheet. After drying, the 2D GISAXS image shows only diffuse Bragg sheets, indicating that only parallel lamellae remain. The lamellar stacking has thus been improved during vapor treatment. We have shown that the behavior during swelling and drying follows a complex pathway.

This project is funded by DFG (Pa771/10-1).

[1] J. Albert, T. H. Epps III, *Mater. Today* **13**, 24-33 (2010)

[2] Z. Di, D. Posselt, D-M. Smilgies, C. M. Papadakis, *Macromolecules* **43**, 418-427 (2010)

[3] P. Busch, D. Posselt, D-M. Smilgies, B. Rheinländer, F. Kremer, C. M. Papadakis, *Macromolecules* **36**, 8717-8727 (2003)

3.4 GISAXS simulation of lamellar structures

X. Shen, M. Rauscher[1], J. Zhang, C.M. Papadakis

[1] MPI für Intelligente Systeme, Stuttgart, Germany

Self-organized thin films represent an interesting class of mesoscopically structured materials, because they undergo spontaneous microphase separation into ordered structures, such as lamellae, cylinders or spheres [1-2]. Meanwhile, grazing-incidence small-angle X-ray scattering (GISAXS) is a rapidly developing technique for the investigation of thin films of nanostructured block copolymers [3]. Busch *et al.* (2006) derived general expressions for the diffuse scattering cross section of X-rays from two model cases in the framework of the distorted-wave Born approximation (DWBA), namely lamellar films where the lamellar interfaces are infinitely large, are perfectly smooth and are purely perpendicular or parallel to the substrate surface [4].

The aim of the present work is, among others, to calculate the diffuse scattering cross-section from thin films from perpendicular lamellae having a realistic domain structure. The software is based on above-mentioned simple cases. It calculates the in-plane and out-of-plane structure factors and combines them to give 2D GISAXS images. The in-plane structure factor is the Fourier transform of the in-plane density-density autocorrelation function, whereas the out-of-plane structure factor is related to the density distribution in the direction of the film normal.

A realistic in-plane density distribution was obtained from an atomic force microscopy (AFM) image featuring the typical meandering lamellae (Fig. 3.7a). We have developed a procedure to translate such an AFM image into an in-plane structure factor $S(\mathbf{q}_{||})$. It involves the following steps: first, we converted the original AFM image (normally it is a color picture) by grayscaling, thresholding and edge-smoothing to an in-plane density distribution to a binary image (Fig. 3.7b). Then, we used fast Fourier transformation and circle intergration to obtain the in-plane structure factor $S(\mathbf{q}_{||})$ (Fig.3.7c). It features a broad peak on a decaying background with the peak position reflecting the lamellar thickness. The curve was parametrized by fitting a Porod law, $I \propto q^{-4}$, and a Lorentz function to describe the background and the peak, respectively. This function serves as the in-plane component of a 2D GISAXS image from thin films featuring perpendicular lamellae.

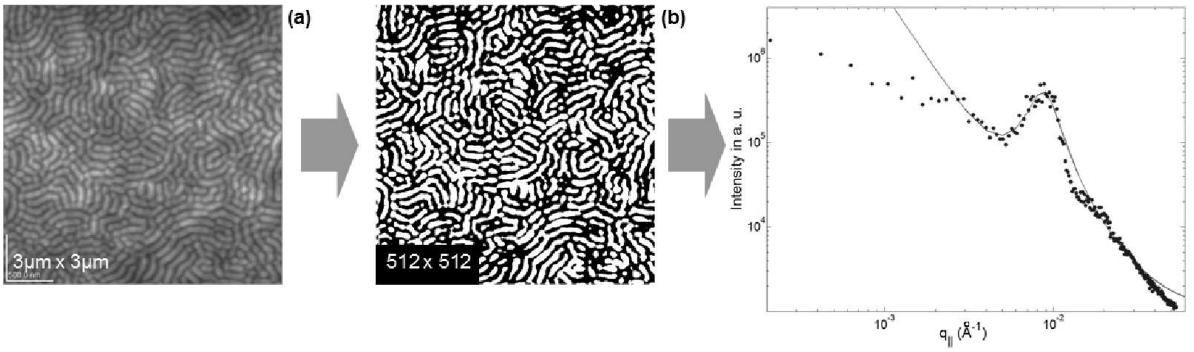

Figure 3.7:
(a) Experimental AFM image used for calculation of the in-plane density distribution. (b) Modified AFM image (see text). (c) Resulting in-plane structure factor (circles). The line is the parameterization, a combination of a Porod law and a Lorentz function.

For a thin film with the purely perpendicular lamellar orientation, the density along the film normal is homogeneous with a scattering length density being the average of the two blocks. The intensity profile along the film normal, q_z, was calculated following Ref. [4]. The resulting intensity features – apart from the Yoneda peaks of the polymer film and the substrate – fringes reflecting the film thickness: Their period is equal to $2\pi/D_{lam}$ (Fig.3.8).

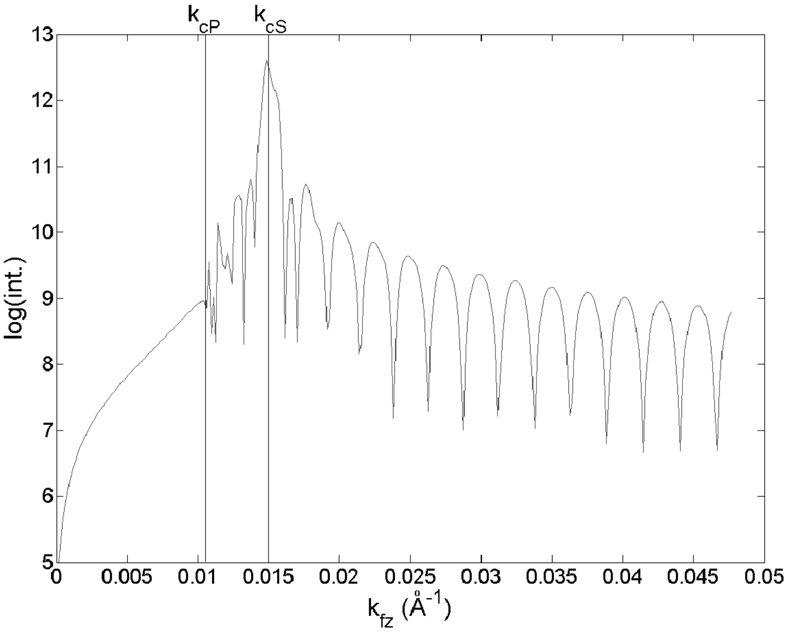

Figure 3.8:
Intensity profile along q_z calculated using the following parameters: X-ray wavelength $\lambda = 1.54$ Å, critical angles of polymer and substrate $\alpha_{cP} = 0.15°$ and $\alpha_{cs} = 0.23°$, film thickness $d_{film} =$ 2350Å, z-component of the incident wave vector $k_{iz} = -0.015$ Å^{-1}.

The 2D image which results from the factorization of the two contributions is shown in Fig. 3.9. It shows the fringes along q_z related to the film thickness as well as the Bragg rods. The new software allows us to model measured GISAXS images and in this way to determine domain sizes from the width of the Bragg rods.

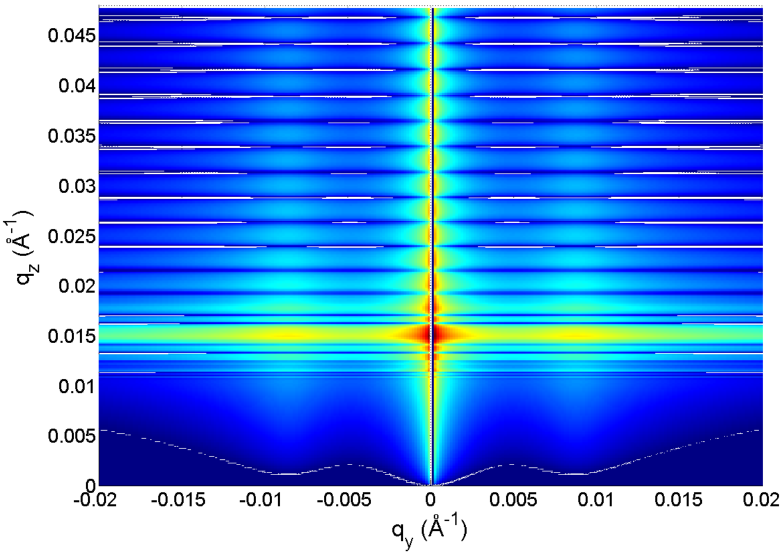

Figure 3.9:
2D simulated image combining in-plane structure factor $S(q_{||})$ and Intensity profile along q_z

[1] M. J. Fasolka, A.M. Mayes, *Annu. Rev. Mater. Res.* **31**, 323-355 (2001)

[2] F. S. Bates, *Science* **251**, 898-915 (1991)

[3] T. Xu, J. T. Goldbach, M. J. Misner, S. Kim, A. Gibaud, O. Gang, B. Ocko, K. W. Guarini, C. T. Black, C. J. Hawker, T. P. Russell, *Macromolecules* **37**, 2972-2977 (2004)

[4] P. Busch, M. Rauscher, D.-M. Smilgies, D. Posselt, C. M. Papadakis, *J. Appl. Crystallogr.* **39**, 433-442 (2006)

3.5 Depth-dependent morphology investigation of diblock copolymer films using TOF-GISANS

Y. Yao, E. Metwalli, J.-F. Moulin[1], M. Haese-Seiller[1], P. Müller-Buschbaum

[1] FRM II, Garching, Germany

Block copolymers with embedded nanoparticles mark one interesting class of hybrid nanocomposites. A well ordered polymer matrix is essential for producing well defined hybrid films. In the present work, we have investigated a well aligned, highly oriented polystyrene(deuterated)-block-polybuthyl methacrylate, symmetric lamellar copolymer, which can be used as structure directing matrix. Films with two different thicknesses (60 nm and 300 nm) were probed. After annealing the films show a perpendicular and a horizontal lamellar structure, respectively, corresponding to thin and thick films. The depth-dependent morphology of the micro-phase separation structure was observed with time-of-flight grazing incidence small angle neutron scattering (TOF-GISANS). In general, different neutron wavelengths λ are probing different depths of the investigated polymer film. With increasing neutron wavelength the penetration depth of the neutron beam decreases. As a consequence, for the long wavelengths a high surface sensitivity of the measurements is achieved.

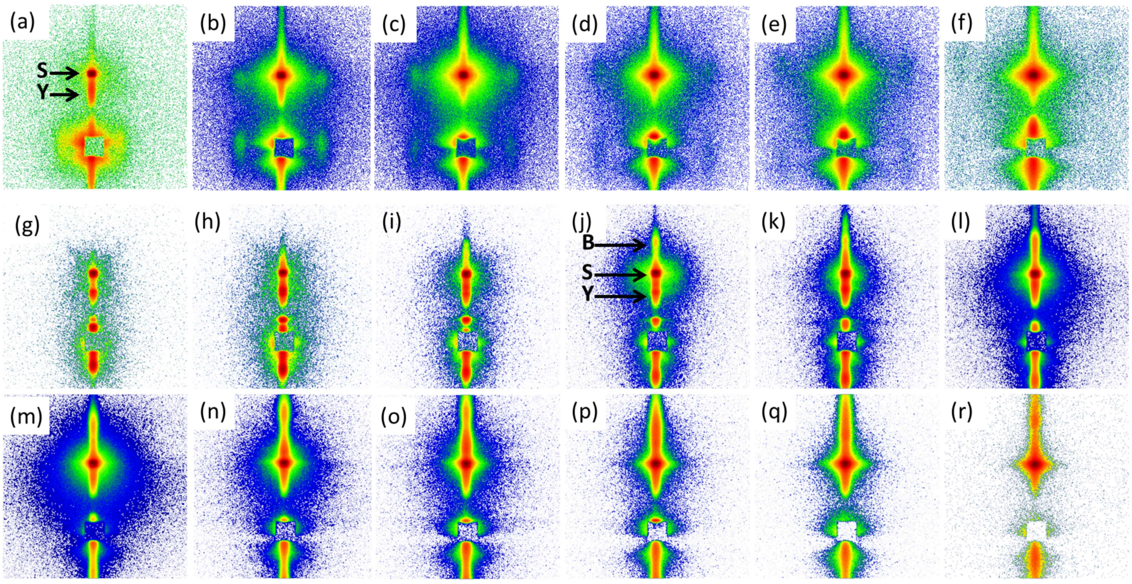

Figure 3.10:
(a) to (f) and (g) to (r) show 2D TOF-GISANS data measured simultaneously for the diblock copolymer with film thickness of 60 nm and 300 nm, respectively. The corresponding wavelengths increase along the image sequence with a range of the mean wavelength start at 0.229 nm and ending at 1.22 nm.

The diblock copolymer films were prepared by spin coating on Si substrates, which were cut into 70×70mm sized pieces and cleaned with an acid cleaning bath at 353 K. Two different film thicknesses were obtained by adjusting the spin coating parameters. To achieve an equilibrium morphology, all samples were annealing at 433K for 3 days under N_2 atmosphere. In all two-dimensional (2D) GISANS data the specular peak is observed almost at fixed position (in the middle of the image). As seen in Fig. 3.10 (a) to (f) a second characteristic feature, the so-called Yoneda peak, is present in the 2D GISANS data. It is located between the direct beam and the specular peak and moves along the (α_i+α_f) direction as the neutron wavelength increases. In addition, two side peaks are sitting symmetrically at the same height along both sides of the Yoneda peak, which originate from the highly ordered structure perpendicular to the sample surface. In contrast, in Fig. 3.10 (g) to (r) no obvious side peaks are visible, but the scattering patterns change significantly along the (α_i+α_f) direction. Above the specular peak, additional strong peaks appear which are first and second order Bragg diffraction peaks. These higher order Bragg peaks indicate multiply ordered layers parallel to the film surface. For further quantitative analysis the 2D data were cut in vertical and horizontal directions (with respect to the sample surface) to address structures along the surface normal and in-plane structures.

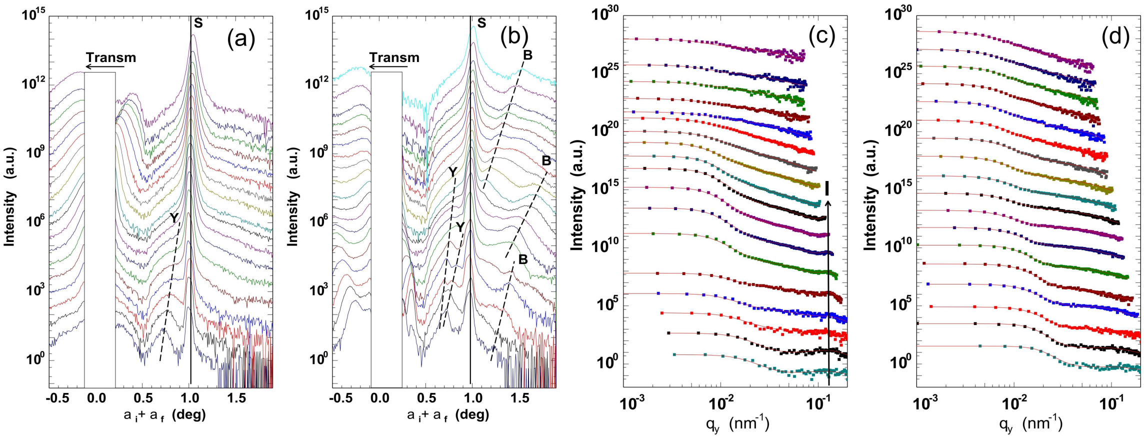

Figure 3.11:
(a) and (b), vertical line cuts of the 2D GISANS data as a function of the detector angle (α_i+α_f) for 60 nm and 300 nm film thickness, respectively. The position of the specular peak (S) is indicated by the solid line. The position of the Yoneda peak (Y) and Bragg peak (B) are indicated by the dash line, respectively. (c) and (d), horizontal line cuts of the 2D GISANS data as a function of the q_y value for 60 nm and 300 nm film thickness.

As seen in vertical cuts (Fig. 3.11 (a) and (b)) the Yoneda peak positions are approaching the specular peak positions with increasing wavelength. The critical angle of the investigated polymer is wavelength depending, following α_c=$\lambda(\rho/\pi)^{1/2}$. ρ denotes the scattering length density (SLD) of the specific polymer material. In case of a thin block copolymer film one mean Yoneda peak is observed (Fig. 3.11 (a)). In contrast, in Fig. 3.11 (b) two individual Yoneda peaks are found. One Yoneda peak originates from the substrate and one from the thick block copolymer film. Moreover, Bragg diffraction peaks appear above the specular peaks, which indicate the multiply ordered parallel layers. The Bragg peaks are positioned at

$$\sin\alpha_f = \left\{ \sin^2\alpha_{cp} + \left[\frac{m\lambda}{D} \pm \left(\sin^2\alpha_i - \sin^2\alpha_{cp}\right)^{1/2} \right]^2 \right\}^{1/2}$$

D denotes the periodic distance of the micro-phase separation structure of the block copolymer film. Horizontal line cuts (see Fig. 3.11 (c) and (d)) show the scattering intensity decayed firstly due to the presence of large and unresolved lateral structures. In case of the thin film sample a pronounced peak I appears in addition. This peak I indicates the lateral orientation of the micro-phase separation structure with a characteristic distance of 53 nm. In contrast, in the thick film such lateral structure is not present (see Fig. 3.11(d)) as the intensity shows a big shoulder only. In summary, the order of the micro-phase separation structure in the block copolymer film can be tuned from parallel to perpendicular orientation by changing the film thickness, as known for many block copolymers.

3.6 Evolution of the near surface composition of pressure sensitive adhesives

M. Schindler, R. A. Campbell [1], P. Müller-Buschbaum

[1] Institut Laue-Langevin, Grenoble, France

The formation of mechanical bonds between different kinds of materials using pressure-sensitive adhesives (PSAs) is still conquering new fields of application [1]. Their fast and permanent tack, the low force needed for bonding compared to the energy needed for the release, as well as the low weight of the joint or the nearly residual free removal from the adherent are just some of many important features of PSAs which make them -in many cases- superior to common techniques for the establishment of mechanical joints. Reasons for this are for example their comparably low costs or the fact that the structure of the joined parts does not need to be weakened compared to e.g. the use of screws. Very different classes of materials such as paper, glass, polymers and metal can not only be joint by common adhesives like epoxies, but also by PSAs [2]. PSAs also play a big role in medicine for the removable attachment of patches and sensors to the human skin. These features are all of macroscopic nature while the origin of the tackiness is found in the structure and the properties of the nanoscopic polymer chains of the adhesive. [3]

In the present investigation, the formation and evolution of enrichment layers in the near surface composition is studied, because the surface composition is crucial for the performance of any adhesive. The statistical copolymer poly(ethylhexylacrylate-stat-d-methylmethacrylate) (denoted P(EHA-20dMMA)) is used as a model system for pressure sensitive adhesives (PSAs). It consists of 80% ethylhexylacrylate and 20% deuterated methylmethacrylate. Changes in the near-surface composition were followed in-situ both, during solution casting and during humidity treatments. Solution casting of a film of this PSA on a silicon wafer, as well as its inner reorganization upon different post-treatments with different humidities were probed with in-situ neutron reflectivity (NR). Solution casting is the common technique to establish PSA films out of solution as the PSA film thickness needs to be typically in the micrometer regime. Due to operation of the films in different environments, the impact of different humidities is essential. Earlier measurements using X-ray reflectivity (XRR) have shown that the freshly cast film exhibits a MMA-enrichment at the surface. [4,5]. This enrichment results from the better solubility of the MMA component in the solvent toluene (used in solution casting), which drags MMA to the surface during evaporation. Unfortunately, due to radiation damage problems, XRR measurements can only be applied to dry and static samples. In-situ XRR measurements on wet PSA films are not feasible. Using a copolymer with a deuterated MMA component we achieved the necessary contrast to follow the establishment of enrichment layers in-situ with NR. The FIGARO time-of-flight reflectometer at the Institute Laue-Langevin (ILL), Grenoble, France, provided the necessary horizontal geometry for this in-situ NR experiment.

In the first part of the experiment, four adhesive films were cast simultaneously and followed during drying with in-situ NR. After the samples had dried, in the second part of the experiment, four different humidities were provided to probe their impact on the speed of the inner rearrangement in the PSA films. These environments of different polarity were realized by insertion of silica gel (providing <2% RH), saturated salt solutions of magnesium chloride, $MgCl_2$ (33% RH) and potassium chloride, NaCl (75.47% RH), and heavy water, D_2O (100% RH) into the four different compartments of a well-sealed chamber. Thus simultaneously, the four initially prepared PSA films were subjected to the four different environments. The reorganization was followed for 24 hours. The drying of a similar sample system was already successfully investigated by Diethert et al. [4]

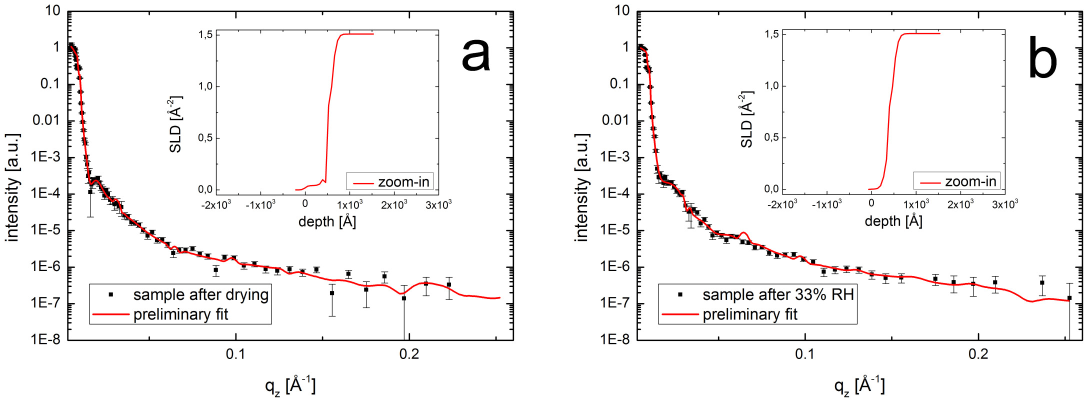

Figure 3.12:
a) Reflectivity measurement of the dry sample and the corresponding preliminary fit. The inset shows a zoom-in on the surface region in the resulting SLD profile. b) Reflectivity curve of the sample stored under 33% RH for 24h. The zoom-in on the surface region of the SLD profile shows a steep increase of SLD to the bulk value. Compared to the composition of the dry sample, this already indicates the diffusion of PMMA to the top surface.

Fig. 3.12a shows the NR curve of the finally dried sample which marks the end of the first part of the experiment. The data are shown together with a preliminary fit along with a zoom-in of the near surface region of the SLD profile. After a rough surface at approximately $1\mu m$ the bulk value is reached, which extends over 3 μm and ends in a narrow transition to the SLD of the silicon substrate. This dry state represents the starting point for the treatments with the four different humidities, where the low q_z-range at an angle of 0.621° was followed in-situ for 24 hours. Afterwards full NR measurements over an extended q_z-range were made. Fig. 3.12b exemplarily shows this full NR measurement for the sample treated with a relative humidity of 33%. From the inset it can be seen that the near surface region appears less rough with a steeper transition to the bulk value of the adhesive. This indicates a smoothening of the surface and a migration of the more polar component, PMMA, to the surface. For the higher relative humidities we expect even more prominent changes in the SLD profile, because one of the driving forces for the rearrangement was found to be the polarity of the environment. [3] The analysis of in-situ NR measurements is still in progress and will provide insights into the timescales of the inner rearrangement, which is of high relevance for the estimation and prediction of the durability of established adhesive bonds.

[1] P. Minghetti, F. Cilurzo, L. Tosi, A. Casiraghi, L. Montanari, *AAPS PharmSciTech* **4(8)**, 53-61 (2003)

[2] E. Maurer, S. Loi, D. Wulff, N. Willenbacher, P. Müller-Buschbaum, *Physica B* **357**, 144-47 (2005)

[3] A. Diethert, K. Ecker, Y. Peykova, N. Willenbacher, P. Müller-Buschbaum, *ACS Appl. Mater. Interfaces* **3**, 2012-2021 (2011)

[4] A. Diethert, E. Metwalli, R. Meier, Q. Zhong, R. A. Campbell, R. Cubitt, P. Müller-Buschbaum, *Soft Matter* **7**, 6648-6659 (2011)

[5] M. Schindler, A. Kriele, P. Müller-Buschbaum, *J. Adhes.* **88**, 684-698 (2012)

3.7 Mechanism analysis of symmetric adhesion of water-swelling polymer films

R. Iikubo, M. Schindler, P. Müller-Buschbaum

Commonly symmetric adhesion between polymer films is studied in case of hydrophobic polymers such as polybutadiene, polydimethylsiloxane or polystyrene and various discussions are based on the molecular level of how the following two behaviors are expressed: 1) enhanced mobility of the near-surface molecules in comparison to the bulk, 2) entanglement between the near-surface chains. On the other hand, the symmetric adhesion of polymer films, which swell in water and ubiquitously exist in our atmosphere, is less investigated, despite its technological importance and scientific interest. In the present study we focus on the influence of water on the internal reorganization and symmetric adhesive properties of adhesive films that include polymethymethacrylate (PMMA), which have been found to on of the polymer films which swell in water [1].

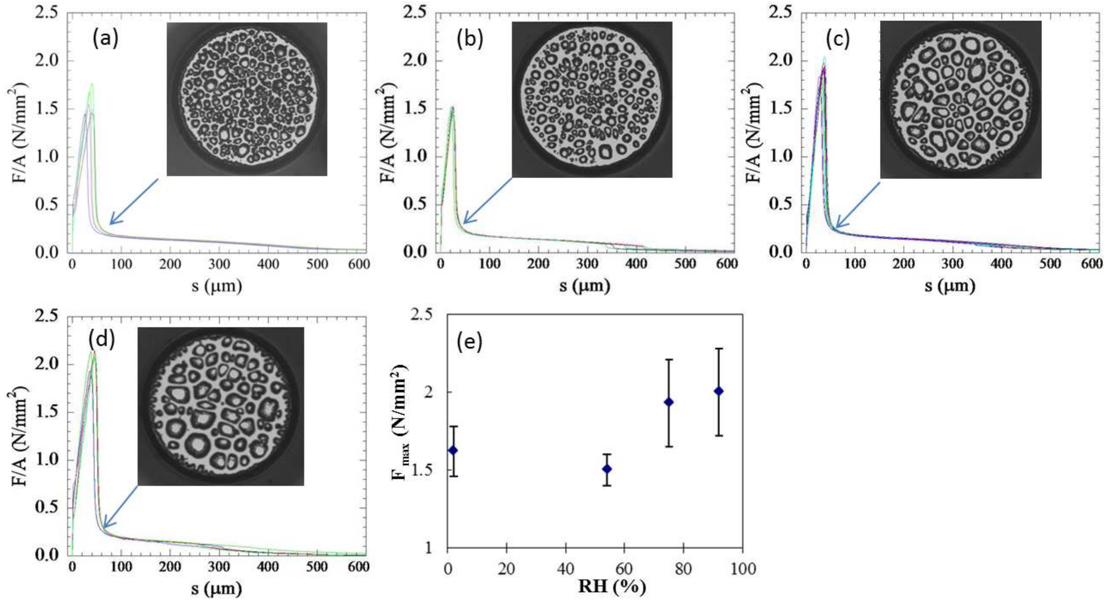

Figure 3.13:
(a)-(d) Force-distance curves together with an inset of the cavity morphology for samples prepared under (a) 2%RH, (b) 54%RH, (c) 75%RH and (d) 93%RH. (e) Force maximum as a function of RH.

The strength of an adhesive bond is affected by many different influences. Diethert et al. have shown that the statistical copolymer poly(ethylhexylacrylate-stat-methylmethacrylate) establishes an enrichment layer of methylmehacrylate (MMA) at the top surface, while the MMA content changes depending on the relative humidity, which severely affects the performance of the adhesive [2]. Tanaka et al. have shown the swelling behavior of PMMA films and their symmetric adhesion via water [3]. Taking these findings into account, it is strongly expected that a simple copolymer film composed of MMA as one comonomer is a valid model to understand the symmetric adhesion of copolymer films that swell in water. We used the statistical copolymer poly(ethylhexylacrylate-stat-methylmethacrylate), denoted P(EHA-stat-MMA), with a monomer composition of 80% ethylhexylacrylate (EHA) and 20% methylmethacrylate and a molecular weight of M_w = 150 k. We chose the well-established tack-measurement to address the adhesive properties before we investigate the symmetric adhesion test.

Fig. 3.13 shows force-distance curves together with an inset of the cavity morphology for the samples prepared under different relative humidity (RH), RH = 2%, 54%, 75% and 93%. The different conditions were achieved by storing the freshly cast samples in desiccators directly above saturated salt solutions. All experiments were performed at 16°C and a stainless steel punch was used for the tack test. As a result, we observe a tendency to increase the maximum force and to decrease the number of cavities for increasing RH.

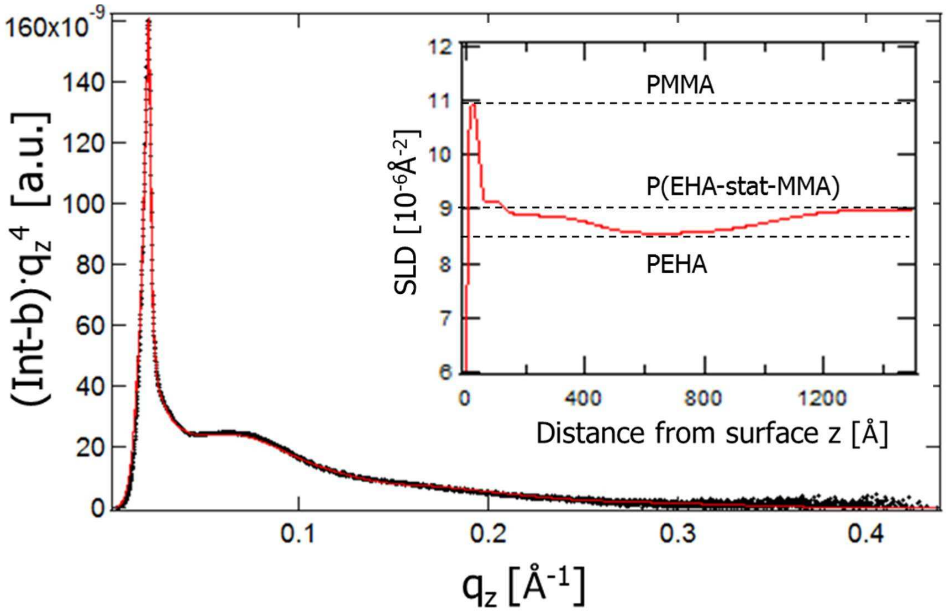

Figure 3.14:
XRR data (dots) and the corresponding fit (line) for the P(EHA-stat-MMA) film prepared under 2%RH. The SLD profile is shown in the inset.

The near-surface composition profile of P(EHA-stat-MMA) prepared under 2% RH, as extracted from x-ray reflectivity (XRR) measurements, is shown in Fig. 3.14. It shows that the polymer established an enrichment layer of PMMA with a thickness of 70 *Å*, followed by a transition to an enrichment layer of PEHA. A homogeneous bulk value is observed for a depth larger than 1200 *Å*. Compared to the result of Diethert et al. [2], the general tendency is similar, except for the surface PMMA concentration which appears higher (100%) than in their findings (50%). This difference originates from the difference in molecular weight (150 k versus 248 k). The shorter the polymer chains are, the higher is their mobility and as a result, PMMA diffuses more easily to the surface. The establishment of the surface enrichment layer takes place during the drying process, which also means that the shorter chains stay dissolved for a longer time, providing a higher mobility for longer. Further investigation of P(EHA-stat-MMA) prepared under different RH using XRR will be needed to explain the results of the tack measurement on the molecular level.

[1] B. Jing, J. Zhao, Y. Wang, X. Yi, H. L. Duan, *Langmuir* **26**, 7651-7655 (2010)

[2] A. Diethert, K. Ecker, Y. Peykova, N. Willenbacher, P. Müller-Buschbaum, *ACS Appl. Mater. Interfaces* **3**, 2012-2021 (2011)

[3] T. Date, M. Ishikawa, K. Hori, K. Tanaka, T. Nagamura, M. Iwahashi, T. Serizawa, *Chem. Lett.* **38**, 660-661 (2009)

3.8 Influence of imprinting processes on crystallinity of P3HT thin films

D. Moseguí González, C. M. Palumbiny, J. Perlich[1], P. Müller-Buschbaum

[1] HASYLAB at DESY, Hamburg, Germany

Controlling the morphology of the different layers composing organic solar cells (OSCs) through imprinting procedures has been found to be a promising pathway to achieve higher efficiencies. This improvement is caused by different effects such as scattering of the incoming light, reflection effects, enlarged interface between layers, improved charge carrier extraction or molecular orientation. [1] In particular, tuning the arrangement of the materials, which compose the active layer of the device, has been demonstrated to be a well suited method to strategically maximize the interface between the donor and acceptor polymers of an organic solar cell. Furthermore, the number of polymer dead ends (active regions not connected to an electrode and therefore acting as recombination centers) and therefore the rate of charge carrier recombination are minimized. In this regard, the interdigitated configuration between donor and acceptor polymers is the best choice in order to completely discard the presence of dead ends within the active layer of heterojunction solar cells (see Fig. 3.15).

Besides the minimization of charge carrier recombination through an enlarged interface with direct percolation pathways or light scattering effects the imprinting is known to have an influence on crystallinity of the conducting polymers in the active layer. Molecular reorientation of the conducting polymers as well as variation of the typical crystal sizes have an impact on the charge carrier extraction rate, the conductivity and thus on the final device performance. [2]

In the present investigation the effect of imprinting on P3HT crystallinity is presented. Grazing incidence wide angle x-ray scattering (GIWAXS) was carried out to determine the cristallinity.

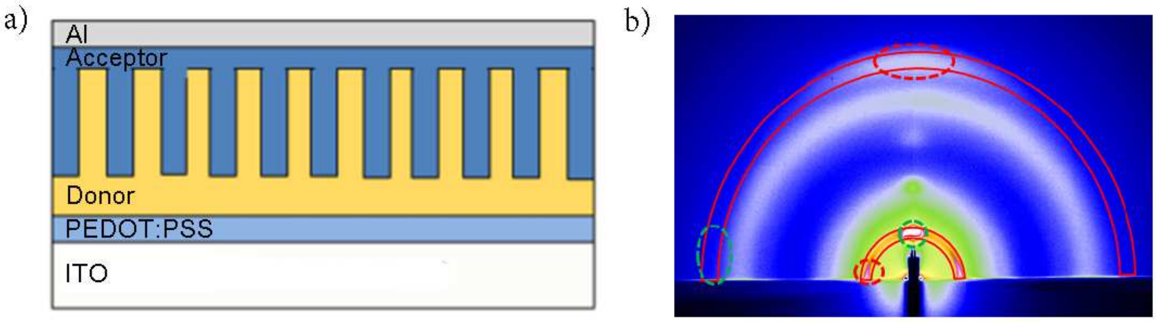

Figure 3.15:
a) Sketch of an ideal interdigitated configuration for an OSC. A large donor-acceptor interface and the ideal percolation pathways provide respectively a large exciton splitting and a low carriers recombination rates. b) Typical 2D GIWAXS data. For the case of P3HT the (so called) edge on and face on families are highlighted in green and red respectively (dashed circles). The red semicircles represent the cuts made on the pictures in order to compare different ratios of orientations.

We present a comparison between a patterned and a non patterned P3HT film for investigating the influence of imprinting on crystallinity of P3HT. On both GIWAXS data two tube cuts corresponding to the scattering signal in 100 and 010 directions are performed. The 100 and the 010 scattering signals correspond to the distances between the backbones and the stacking planes of P3HT, respectively (indicated in Fig. 3.15b). The signal coming from the "edge on" areas (green circles in Fig. 3.15b) is cause from a horizontal orientation of the backbones of P3HT with respect to the substrate whereas stacking planes are lying perpendicular to it. On the other hand the stacking planes parallel to the substrate give rise to the signal in the areas indicated for the red dashed circles in Fig. 3.15b. This orientation is known as "face on" orientation. The conductivity along stacking planes is better than along side chains of P3HT. Therefore the "face on" orientation is beneficial for the application in organic solar cells implying a better conductivity and thus an improved device performance.

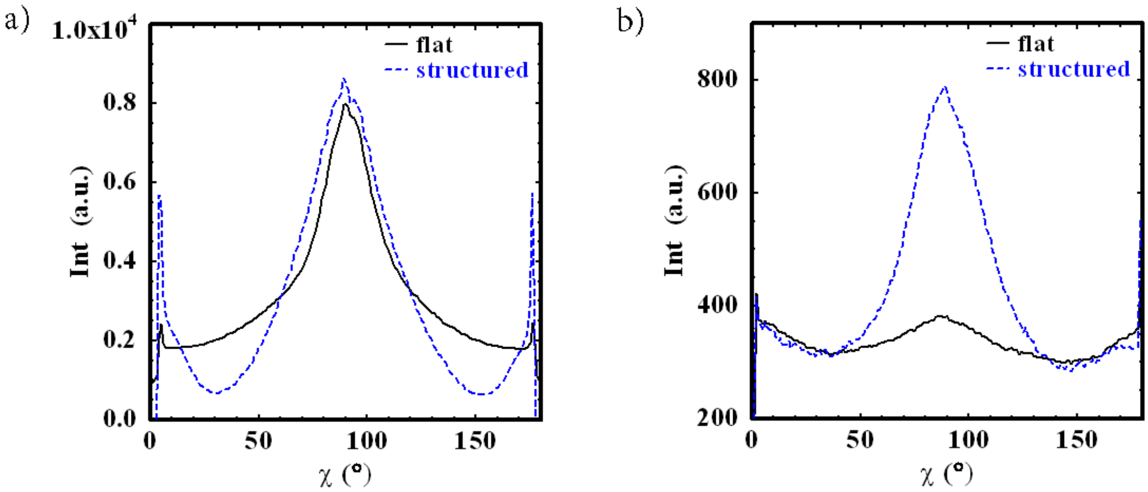

Figure 3.16:
a) Tube cuts in 100 direction for flat (solid line) and structured (dashed line) sample. The edge on orientation corresponds to the central feature and the face on orientation contributes to the signal on the sides. b) Tube cuts in 010 direction. Face on orientation gives rises to signal in the center of the diagram. The edge on orientation contributes to the sides.

The comparison of the scattering in the tube cuts in 100 direction shows that imprinting yields to a better defined orientation, both edge on and face on. The intensity due to edge on orientation is clearly lowered in favor of an improvement in the face on orientation (Fig. 3.16a). The signals in the tube cuts in 010 direction (Fig. 3.16b) confirm this improvement of face on orientation as the corresponding signal is increased by almost a factor two.

In the case of patterning via imprinting the re-orientation and crystallization of P3HT takes place within confined spaces, where the degree of freedom for molecular chains and crystal formation is reduced. This favorable re-arrangement is most likely induced by mechanical stress that the patterning implies.

The presented results open an interesting line of research towards a better understanding of the different agents composing organic electronic devices, as well as a remarkable improvement of electric properties of the active components.

[1] Y. Yang, K. Mielczarek, M. Aryal, A. A. Zakhidov, W. Hu, *ACS Nano* **5**, 7532-7538 (2011)

[2] H. Sirringhaus, P. J. Brown, R. H. Friend, M. M. Nielsen, K. Bechgaard, B. M. W. Langeveld-Voss, A. J. H. Spiering, R. A. J. Janssen, E. W. Meijer, P. Herwig, D. M. de Leeuw, *Nature* **401**, 685-688 (1999)

4 Polymer films for applications in photovoltaics

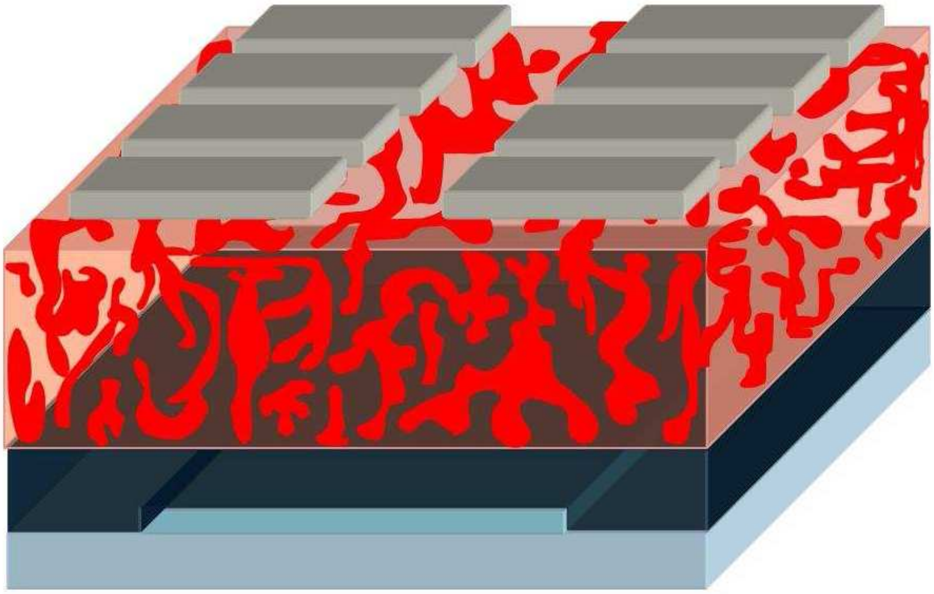

4.1 The effect of solvents in manipulating the nano-morphology in the PTB7:PC$_{70}$BM bulk heterojunction system

S. Guo, J. Perlich[1], P. Müller-Buschbaum

[1] HASYLAB at DESY, Hamburg, Germany

The efficiency of polymer-based solar cells has reached values above 10%, and thus has exceeded the threshold for commercial application. [1] In combination with the unique advantages such as being lightweight, flexible, and potentially low cost, polymer-based solar cells are among the most promising renewable energy sources. In the present investigation, the record setting system PTB7:PC$_{70}$BM in bulk heterojunction (BHJ) geometry are investigated. Due to the solution-based spin-coating procedure, it is quite intriguing to find out the ideal solvent which assists to optimize the morphology of the active layers during the self-assembly process. The active layer is spin-coated from a mixture of PTB7 and PC$_{70}$BM dissolved in different solvents such as chlorobenzene (CB), dichlorobenzene (DB), and trichlorobenzene (TB) without and with solvent additive 1,8- diiodooctane (DIO). Atomic force microscopy (AFM) is used to reveal the real space information of the active layer surfaces. In combination with the reciprocal space information obtained from grazing incidence small angle x-ray scattering (GISAXS) measurements, the whole morphology of the active layer is reconstructed. Consequently, the different morphologies formed from different solvents are determined and correlated with the corresponding solar cell device performance. As a result, the best solvent for PTB7:PC$_{70}$BM BHJ system can be identified.

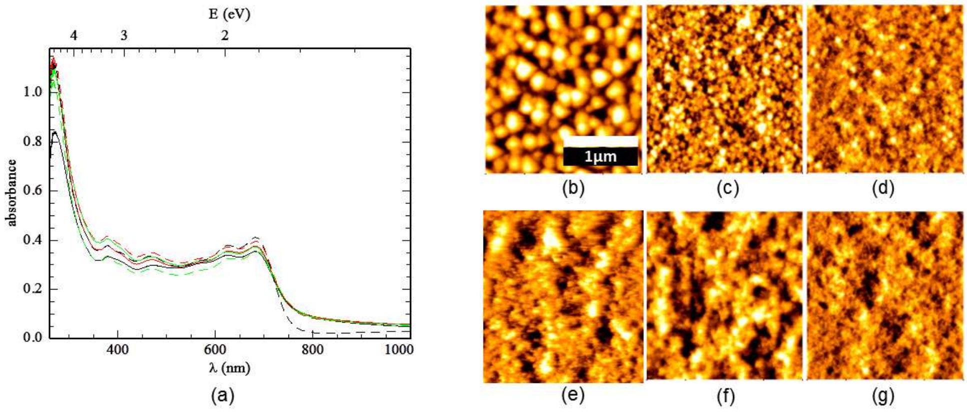

(a) (b) (c) (d) (e) (f) (g)

Figure 4.1:
(a) Absorption curves of PTB7:PCBM films made from different solvents: CB (black), DB (red) and TB (green), and solvent additive DIO included as indicated as dash lines. Six AFM topographic images of samples made from (a, d) CB, (b, e) DB and (c, f) TB without and with DIO.

Samples with similar thickness are prepared and examined by UV/Vis to allow for comparison among different solvents. In Figure 4.1a, the absorption curves are obtained from active layers spin-coated from solvents with different concentration. The dash lines represent data from samples with the solvent additive DIO. As seen from this figure, all the absorption curves follow a linear superposition of the corresponding individual spectra, implying that significant ground-state charge transfer does not occur in these films. [2]

The images in Figure 4.1b to 4.1g present the AFM images of all the investigated active layers. From the AFM measurements, not only the topography and the corresponding roughness information of the samples is obtained, but also the characteristic length scale of the surface structure is extracted via the power spectral density function (PSD). The PSD of the films is shown in Figure 4.2a. From all the topography images without DIO, one can observe aggregated $PC_{70}BM$ clusters. The cluster size on the film surface decreases with increasing the boiling point of used solvent from chlorobenzene to trichlorobenzene. This is due to the increasing relaxation time of the polymer backbone introduced by decreasing the solvent evaporation rate. With DIO added, all the well distributed $PC_{70}BM$ clusters are interrupted, and again, for the film made out of tricholorobenzene, the smallest structure size is observed.

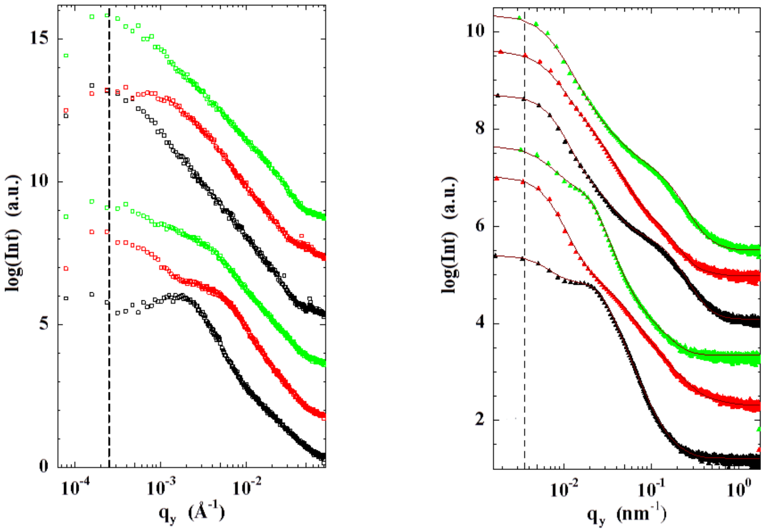

(a)

(b)

Figure 4.2:
(a) PSD curves of the AFM data of all the samples and (b) Out-of-plane cuts from the GISAXS 2d data. The used solvents CB (black), DB (red) and TB (green) without and with DIO (from bottom to top). All curves are shifted along the y-axis for more clarity.

To probe the inner film morphology, GISAXS is performed on all the samples made out of different solvents. By analyzing the out-of-plane cuts of the 2D GISAXS data via fitting them in the framework of the so-called effective surface approximation (see Figure 4.2b.) the specific structural information is obtained. It can be seen that the surface structures for all the samples are bigger than the inner film structures. Moreover, the domain sizes decrease from hundred nanometer length scale close to the excition diffusion length (20 nm), both on the film surface and inside the films due to the addition of solvent DIO. Correspondingly, the structural peaks shift to higher q values. The extracted structure sizes for the different solvents used in the preparation of the active layer are in good agreement with the performance of the corresponding solar cell devices: The DIO including samples give rise to relatively higher efficiency due to the evident minimized structure size. Among the three investigated solvents, chlorobenzene-based solar cells shows the most promising efficiency (3.6%), matching with the most homogenous and best optimized domain size (at about 75 nm). [3] Further analysis is still undergoing, as well as the optimization of solar cell device performance.

[1] M. A. Green, K. Emery, Y. Hishikawa, W. Warta, E. D. Dunlop, *Prog. Photovolt: Res. Appl.* **20**, 606-614 (2012)

[2] A. C. Arias, J. D. Mackenzie, R. Stevenson, J. J. M. Halls, M. Inbasekaran, E. P. Woo, D. Richards, R. H. Friend, *Macromolecules* **34**, 6005-6013 (2001)

[3] S. Guo, A. Naumann, E. M. Herzig, G. Tainter, J. Perlich, P. Müller-Buschbaum, in preparation

4.2 Light induced aging of thin polymer-fullerene blend films for organic photovoltaics

C. Schaffer, G. Santoro[1], S. V. Roth[1], P. Müller-Buschbaum

[1] HASYLAB at DESY, Hamburg, Germany

With their potential application as a cheap and versatile source of electricity, organic photovoltaics provide a promising technology with a vast variety of applications due to their potential mechanical flexibility. Thus, research has focussed on the increase of the power conversion efficiency of organic solar cells, which has by now been reported as high as 10% [1], making this technology comparable to common state-of-the art thin film solar cells. In contrast, less effort has been spent on understanding the mechanisms responsible for degradation of organic photovoltaic devices. As a major factor, (photo-) oxidation of the light absorbing layer, which typically consists of a blend of an organic semiconductor and a fullerene, turned out to limit the lifetime of OPV strongly. Accordingly, encapsulation techniques that suppress this pathway of degradation have been developed. Thus, lifetimes for organic solar cells of up to seven years have been reported meanwhile [2]. Nevertheless, even this is not yet comparable to the lifetime of their inorganic counterpart and not achieved for every system. Therefore, additional pathways of degradation and aging need to be considered. The morphological alteration of the active layer as a consequence of illumination is the subject of the present work.
Other than in inorganic solar cells, the energy of absorbed photons cannot be directly used to generate free charge carriers in inorganic solar cells. It needs to be transported as an exciton to an interface between conducting polymer and fullerene domains where free charge carriers can consequently be generated. As the range of an exciton is limited by the exciton diffusion length, which is typically in a range of several up to few ten nanometers in a polymer, it is crucial that the morphology of the polymer-fullerene blend layer matches to the exciton diffusion length. Therefore, the alteration of the inner morphology of bulk-heterojunction organic solar cells as an effect of aging is expected to severely affect the power conversion efficiency.It is well known that the degradation process of polymer films can be accelerated by illumination [3]. Therefore, a series of identical blend films consisting of P3HT:PCBM (poly(3-hexylthiophen-2,5-diyl):[6,6]-phenyl-C61-butyric acid methyl ester) and PCPDTBT:PC[71]BM (poly[2,1,3-benzothiadiazole-4,7-diyl[4,4-bis(2-ethylhexyl)-4H-cyclopenta[2,1-b:3,4-b′]dithiophene-2,6-diyl]] : [6,6]-phenyl-C71-butyric acid methyl ester) on PEDOT:PSS have been prepared and illuminated with light of a high pressure metal halide lamp.

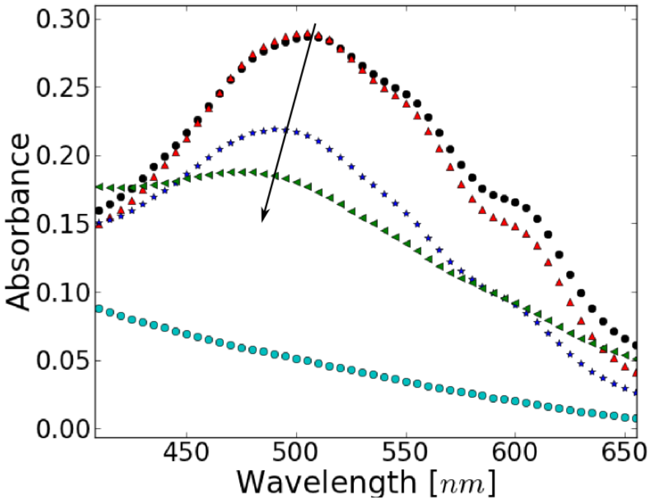

Figure 4.3:
UV/Vis spectra of P3HT:PCBM films after different illumination times between 1 min and 48 h and a non-illuminated reference.

These films have been characterized in terms of UV/Vis spectroscopy. Fig. 4.3 shows a selection of UV/Vis spectra of the P3HT:PCBM films in different aging stages. The absorbance was corrected for variations in the film thickness. As depicted with the arrow, the absorbance of the film decreases with increasing illumination time after the first 30 minutes of illumination. Moreover, the peak absorption wavelength shows a blue shift of roughly 30 nm as a consequence of illumination. After 48 h of illumination, the film is bleached to a state where no more characteristic features can be identified. Both findings can be explained by the (photo-) oxidation of the absorbing polymer which also leads to a loss of conjugation length causing the blue shift of the absorption peak. This loss of conjugation length has been formerly correlated to the alteration of the polymer's chemical structure [3], suggetsting that also the morphological structure of the active blend film might be altered as a consequence of illumination. This is of special interest since the inner structure of the active film is expected to strongly correlate to the solar cells' characteristics.

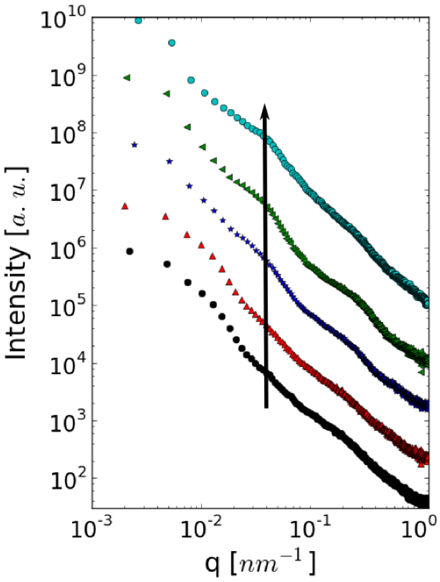

Figure 4.4:
Out-of-plane cuts for thin P3HT:PCBM blend films after different times of illumination with a metal halide arc lamp. Light exposure times were 0 min, 1 min, 30 min, 10 h, 48 h (bottom to top)

In order to determine the effect of light on the inner morphology of the polymer blend film, grazing incidence small angle x-ray scattering (GISAXS) has been performed on the films presented earlier. Fig. 4.4 shows the out-of-plane cuts from the GISAXS data of the same P3HT:PCBM blend films that have been presented in terms of UV/Vis spectroscopy. As depicted by the arrow, the illumination leads to the appearance of structures with sizes of more than 25 nm which were not found in the initially prepared P3HT:PCBM films [4]. Finally, it could be shown that the illumination of active polymer-blend films for organic photovolatics leads not only to a change in their optical characteristics but also to a variation in their bulk nano-morphology.

[1] M. A. Green,K. Emery,Y. Hishikawa,W. Warta, E. D .Dunlop , *Prog. Photovolt. Res. Appl.* **20**, 12-20 (2012)

[2] C. H. Peters, I. T. Sachs-Quintana, J. P. Kastrop, S. Beaupré, M. Leclerc, M. D. McGehee, *Adv. Energy Mater.* **1**, 491-494 (2011)

[3] T. Tromholt, M. Manceau, M. Helgesen, J. E. Carlé, F. C. Krebs, *Sol. Energy Mater. A. Solar Cells* **95**, 1308-1314 (2010)

[4] M. A. Ruderer, S. Guo, R. Meier, H.-Y. Chaing, V. Körstgens, J. Wiedersich, J. Perlich, S. V. Roth, P. Müller-Buschbaum, *Adv. Funct. Mater.* **21**, 3382-3391 (2011)

4.3 The influence of processing additives on the morphology of bulk heterojunction films

W. Wang, M. Philipp, D. Magerl, J.-F. Moulin[1], P. Müller-Buschbaum

[1] FRM II, Garching, Germany

Photoactive polymers used in bulk heterojunctions (BHJ) and their applications in organic photovoltaics have attracted tremendous attention. Compared to standard inorganic solar cells, plenty of promising advantages exist for these materials. Currently the main drawback of organic photovoltaics is still the low efficiency. The morphology of the BHJ film plays an important role for the performance of organic solar cells. Thermal annealing or solvent annealing can optimize the morphology of BHJ films. Recently, it was observed that by incorporating a few volume percent of alkanedithiols in the solution of BHJs, the power conversion efficiency of photovoltaic cells can be increased a lot. Alkanedithiols selectively dissolve [6,6]-phenyl C_{61}-butyric acid methyl ester (PCBM), whereas the semi-conducting polymer poly(3-hexylthiophene) (P3HT) is not soluble [1]. Because of the different selectivity, the morphology of BHJ films can be tuned. In our investigation, the semi-conducting polymer P3HT is used as donor material and PCBM is chosen as acceptor material. P3HT and PCBM are dissolved in toluene with the ratio of 1:0.8. The 1,8-octanedithiol , which is used as processing additive, is added in toluene with the volume fraction of 5%. The P3HT:PCBM solution is deposited on a silicon substrate via spin coating. Then the films are heated at 140 °C for 20 min. The resulting surface structure is investigated by optical microscopy (OM) and atomic force microscopy (AFM). The absorbance of the film is probed by an ultraviolet-visible absorption spectroscopy. TOF-GISANS experiments are performed to investigate the inner structure of the film on mesoscopic scale.

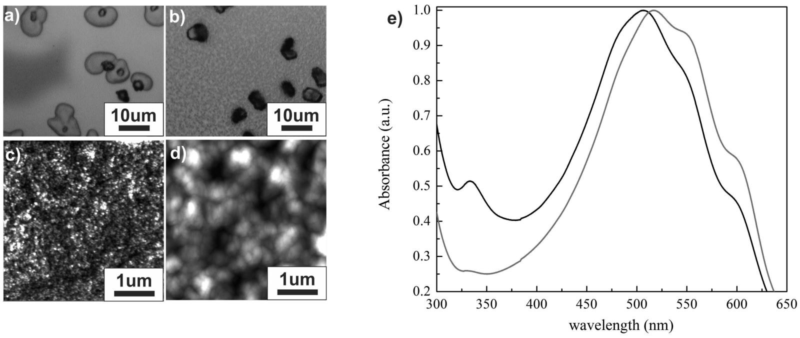

Figure 4.5:
OM images of P3HT:PCBM films without (a) and with (b) 1,8-octanedithiol; AFM images of P3HT:PCBM films without (c) and with (d) 1,8-octanedithiol; absorbance data (e) of films without (dark curve) and with (grey curve) 1,8-octanedithiol

In OM images (Fig. 4.5a and b), the P3HT:PCBM film with 1,8-octanedithiol shows better grown PCBM crystal clusters as compared to the one without 1,8-octanedithiol. Furthermore, the P3HT:PCBM film with 1,8-octanedithiol shows prominent features of phase separation, which is critical for exciton dissociation in organic photovoltaic devices. AFM results (Fig. 4.5c and d) give additional information about the surface morphology of films on nanometer scale. The P3HT:PCBM film with 1,8-octanedithiol shows more elongated structures and continuous networks as compared to the one without 1,8-octanedithiol, which is beneficial to charge transport in organic photovoltaic devices. The P3HT:PCBM film with 1,8-octanedithiol also shows phase separation on larger length scales. Fig. 4.5e presents normalized absorption spectroscopy images of the P3HT:PCBM films without and with 1,8-octanedithiol, respectively. The absorption band of P3HT in the film with 1,8-octanedithiol is red-shifted by 10 nm as compared to the one without 1,8-octanedithiol, which indicates an increased conjugation length of P3HT. Thus the P3HT crystallinity is improved by adding this processing additive to the solution.

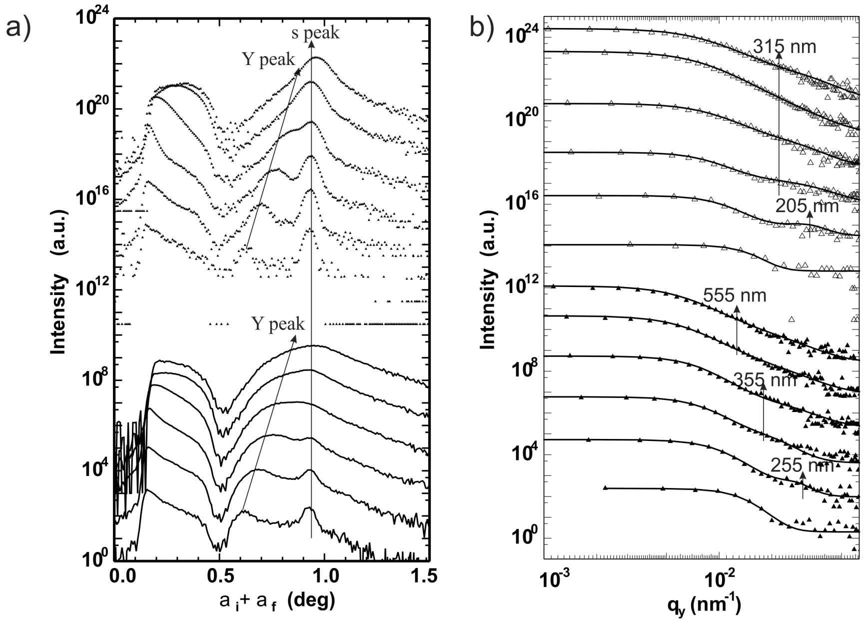

Figure 4.6:
Vertical (a) and horizontal cuts (b) of 2D TOF-GISANS data for P3HT:PCBM films with 1,8-octanedithiol (top, hollow symbols) and without 1,8-octanedithiol (bottom, solid symbols); all curves are vertically shifted for presentation; the neutron wavelength increases from bottom to top 0.324 nm, 0.475 nm, 0.624 nm, 0.664 nm, 0.924 nm and 1.074 nm.

For the investigation of inner film morphologies on mesoscopic scales, time-of-flight grazing incidence small angle neutron scattering (TOF-GISANS) measurements were performed at the REFSANS instrument. The corresponding line cuts of the TOF-GISANS data for the films with and without additive are shown in Fig. 4.6. As visible in the vertical line cuts (see Fig. 4.6a), with increasing wavelength, the Yoneda peak approaches the specular peak, which is due to the wavelength dependence of the critical angle. In addition, the curves of the P3HT:PCBM film without 1,8-octanedithiol show more prominent Yoneda scattering as compared to the ones with 1,8-octanedithiol, due to larger roughness. Fig. 4.6b) shows horizontal line cuts together with model fits. As seen in the fitting results, the characteristic lateral structure size increases and gets more broadly distributed with increasing neutron wavelength. When the incident angle is smaller than the critical angles of the polymer film, the neutron beam cannot penetrate the full film anymore. Thus, as the neutron wavelength increases, progressively surface sensitivity is gained. As a consequence, the fitting results show that near the film surface larger structures exist as compared to the film bulk. In general, without processing additive the lateral structures are larger and increase more is size towards the film surface as compared to the film with the addition of 1,8-octanedithiol.

In summary, adding 1,8-octanedithiol to the solution of P3HT:PCBM gives rise to more ordered structures on the molecular level of the P3HT phase and more homogenous structures on the mesoscopic scale due to less strong demixing of P3HT and PCBM.

[1] J. K. Lee, W. L. Ma, C. Brabec, J. Yuen, J. S. Moon, J. Y. Kim, K. Lee, G. Bazan, A. Heeger, *J. Am. Chem. Soc.* **130**, 3619-3623 (2008)

4.4 Influence of annealing temperature on ternary system

E. M. Herzig, C. M. Palumbiny, W. Wang, S. V. Roth[1], P. Müller-Buschbaum

[1] HASYLAB at DESY, Hamburg, Germany

Organic Photovoltaics (OPV) has recently gained a lot of attention, particularly since power conversion efficiencies have exceeded 10% in 2012. [1] During the last years the interdisciplinary research has brought some important understanding on charge creation and transport properties in OPV devices. It is well established that the nano-morphology of the active layer is closely linked to solar cell performance. [2]

The model system poly(3-hexylthiophene-2,5-diyl):phenyl-C61-butyric-acid-methyl-ester (P3HT:PCBM) is widely used to investigate the basic working principles of organic solar cells. A standard procedure to maximize the performance of this binary system is temperature annealing. This annealing results in adequately sized domains in the thin film and increases crystallization of the polymer component facilitating charge transport. Kim et al. [3] have found that the addition of a third component can also increase the performance of the binary P3HT:PCBM system.

To fully understand the influence of a third component, the internal structure of the active layer of organic solar cells the system needs to be examined on various length scales. In the present investigation we focus on the length scales in the nanometer range obtained from grazing incidence small angle x-ray scattering (GISAXS) found in the ternary system P3HT:PCBM with polystyrene sulfonate (PSS). GISAXS can reveal information on the size and the distribution of regions with different electron densities within the examined thin P3HT:PCBM:PSS films. In a ternary system with two low electron density polymers (P3HT and PSS) and higher electron density fullerene (PCBM) the contrast will change depending on the intermixing of the components. It is therefore not straight forward to interpret single measurements and it is of advantage to be able to examine a set of measurements where one parameter is ideally continuously changed.

For temperature annealing this can be achieved by producing a sample that is annealed on a temperature gradient. While keeping the composition and annealing time constant, the annealing temperature can hence be varied from around room temperature to above the melting point of P3HT. Fig. 4.7 shows how such a gradient sample is obtained. A homogeneous thin film on a rectangular silicon substrate is heated on the one end while it is cooled on the other end. This approach allows the formation of a constant temperature gradient throughout the sample once the thin film is placed on the heating stages. After a fixed amount of time the sample is removed, is brought back to room temperature and subsequently examined. The P03 high flux, micro-focus beamline at HASYLAB facilitates fast measurements and therefore allows the lateral scanning of a gradient resulting in measurements with a continuous set of different annealing temperatures. The left hand side of figure 4.7 shows a selection of the several hundred measurements depicting the dominant changes with temperature. The most dominant change is the growing large scale structure that disappears into the resolution limit for very high temperatures. Similarly to measurements with different PSS contents this large scale structure is attributed to a PSS-rich phase. The pronounced peak at this low q-regime requires the fitting with a well-defined size distribution before it approaches too close to the resolution limit. The good contrast that is necessary for such a clear peak further indicates that it is unlikely that larger amounts of PCBM are present in the amorphous polymer.

Another clear structure size is found (few nanometers) in the 2D plot of the out-of-plane cuts in figure 4.7. The fits show that the increasing intensity in the 2D plot is dominantly due to the growing contribution of this length scale of around 6 nm, while the 2D plot nicely shows the continuous nature of this increase with annealing temperature up to around 140°C.

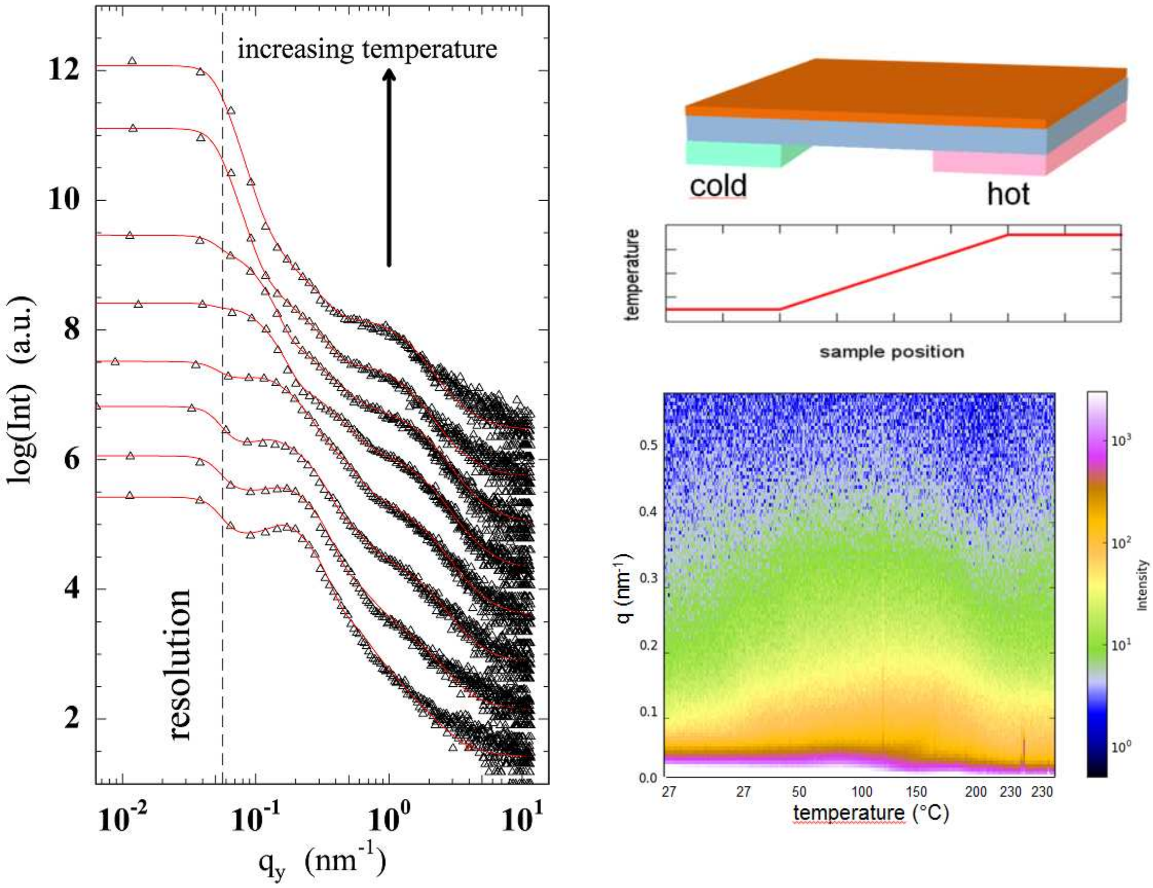

Figure 4.7:
Left: Out-of-plane cuts for increasing temperature from bottom to top. The largest length scale increases at all temperatures while intermediate and lower length scales remain constant up to very high temperatures. Top right: Sketch of experimental setup to obtain a gradient sample. The sample is heated on one end and actively cooled on the other end to obtain constant annealing conditions. Bottom right: 2D plot of all measured out-of-plane-cuts for various temperatures. Intensity is depicted in color.

For higher temperatures this length scale increases to around 8 nm. As shown previously [4] this feature can be attributed to PCBM domains.
A third intermediate structure size is necessary to fit the data. However, due to the fact that particularly for the lower temperatures this feature is not well defined, the size cannot be uniquely defined and no trend deviating from a constant value can be observed. For higher temperatures the sizes change from 40 to 65 nm.
This experiment shows that the segregation of the third component is significantly influenced over the whole tested temperature range while the remaining system still shows typical length scales of the binary system.

[1] M. A. Green, K. Emery, Y. Hishikawa, W. Warta, E. D. Dunlop, *Prog. Photovoltaics* **20**, 606-614 (2012)

[2] M. A. Ruderer, P. Müller-Buschbaum, *Soft Matter* **7**, 5482-5493 (2011)

[3] K. C. Kim, J. H. Park, O. O. Park, *Sol. Energ. Mat. Sol. Cells* **92**, 1188-1191 (2008)

[4] M. A. Ruderer, R. Meier, L. Porcar, R. Cubitt, P. Müller-Buschbaum, *J. Phys. Chem. Lett.* **3**, 683-688 (2012)

4.5 Influence of PSS on the morphology of P3HT:PCBM solar cells

A. Naumann, E. M. Herzig, J. Perlich[1], P. Müller-Buschbaum

[1] HASYLAB at DESY, Hamburg, Germany

Concerning the topical question on the future energy supply organic photovoltaic devices have attracted the worldwide interest over the last decades. Though still comprising lower efficiencies and lifetimes compared to their inorganic counterparts, an intense improvement of the performance of organic solar cells has been accomplished due to the research over the last years. As a consequence, world record efficiencies have overcome the limit of 10 %. Furthermore, organic photovoltaic devices present novel advantages, like light weight, mechanical flexibility and the potential to fabricate solar cells on a mass production scale at low costs.

Today, the best investigated system for the active layer of organic solar cells is the combination of the fullerene-derivative PCBM as the n-type material and poly(3-hexylthiophene) (P3HT) as the p-type material. Different approaches to optimize this system are accomplished in worldwide research, as properties, like the blend morphology, the conductivity or absorption can be varied by multiple ways. One possibility to optimize these characteristics is the implementation of a ternary system by addition of a third component. Thereby, a great variety of possibilities arises, as a much wider range of parameters can be varied in comparison to the original binary system. In the present investigation the aim is the understanding of the influence of the addition of poly(styrenesulfonate) (PSS) to the binary P3HT:PCBM system. PSS was used as third component by other research groups already. For example, Kim et al. have found an increased solar cell performance in such system [1].

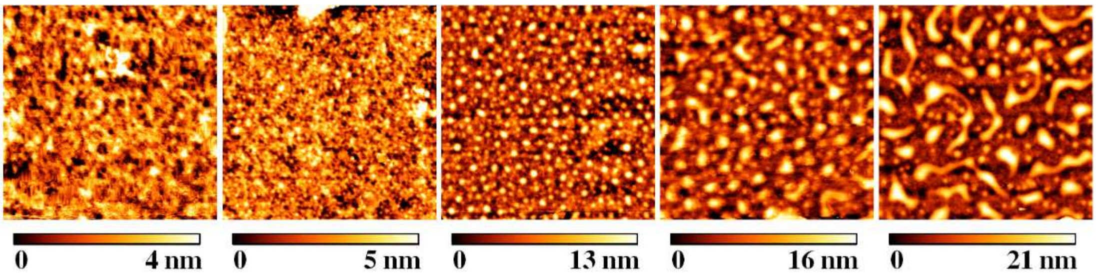

Figure 4.8:
8×8 μm^2 AFM images of P3HT:PSS:PCBM films with 0, 5, 10, 15 and 20 wt% PSS (left to right).

One of the main focuses of the investigation is the effect of PSS on the film morphology, as the morphology is crucial for the solar cell efficiency [2]. To probe the film surface on a micron scale atomic force microscopy (AFM) is used. Figure 4.8 shows AFM images of films with increasing amount of PSS. The pure P3HT:PCBM blend film shows a surface roughness, but no explicit surface structure. However, when PSS is added, a well defined surface structure is present. Spherical structures, which are elevated compared to the residual surface, appear. They grow larger and higher with increasing amount of PSS. For 15 and 20 wt% PSS they even merge into elongated structures. The surface structure is an indication for phase separation between PSS and the residual materials. However, AFM only gives topographic information of a small area. Therefore grazing incidence X-ray scattering (GISAXS) measurements are performed at beamline BW4 of HASYLAB in Hamburg to investigate the inner film morphology. To obtain statistical values of lateral structures, so-called out-of-plane cuts of the 2d scattering images are performed at the critical angles of the film materials [3]. The corresponding cuts at the critical angle of PCBM are shown in figure 4.9 (a). Each peak or shoulder-like feature represents a

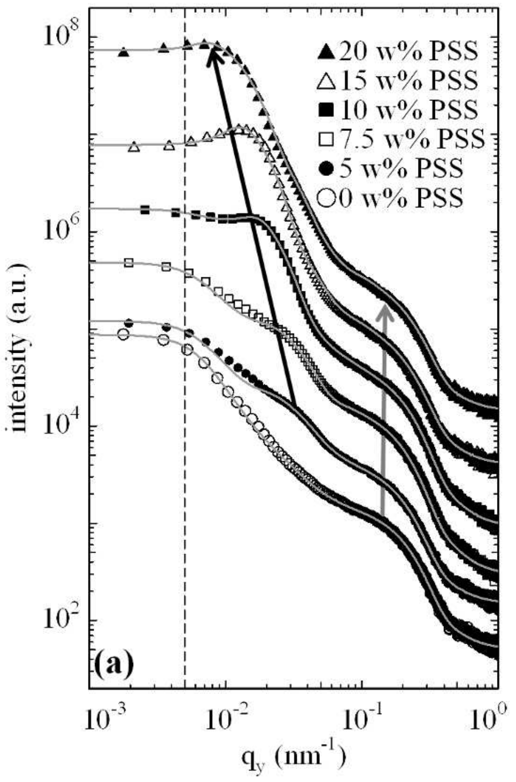

Figure 4.9:
(a) Double-logarithmic plot of GISAXS out-of-plane cuts with gray lines indicating the fit and the dashed line showing the resolution limit. From the fit the structure sizes are obtained, which are shown in (b) for the structure indicated by the black and in (c) by the gray arrow.

characteristic lateral structure, in this case one observes a bigger structure, indicated with the black arrow, which is growing upon adding PSS and a smaller structure, indicated with the gray arrow, which is constant for all PSS contents. To obtain the structure sizes the out-of-plane cuts are fitted with an appropriate model. The resulting structure radii are shown in figure 4.9 (b), (c). The big objects are changing severely in size upon adding PSS. By comparing these bigger objects with the AFM images (figure 4.8) it is found that they are consistent with the structures observed via AFM. Therefore these structures are PSS domains resulting from phase separation, which are located at the surface. The small objects with an average radius of about 7.5 nm on the other hand are not influenced by PSS. They can be identified as PCBM structures and are not observable in the AFM, therefore they are inner structures.

In conclusion, it is important to compare different measurements in order to get an idea of the film morphology. Furthermore, the investigation of different characteristics, like film morphology, absorption and crystal orientation are necessary to fully understand the influence of PSS on the P3HT:PCBM blends.

[1] K. C. Kim, J. H. Park, O. O. Park, *Sol. Energy Mater. Sol. Cells* **92**, 1188-1191 (2008)

[2] M. A. Ruderer, P. Müller-Buschbaum, *Soft Matter* **7**, 5482-5493 (2011)

[3] P. Müller-Buschbaum, *Anal. Bioanal. Chem.* **376**, 3-10 (2003)

4.6 Influence of PSS on the degradation properties of P3HT:PCBM films

P. Schreiber, C. Schaffer, E. M. Herzig, P. Müller-Buschbaum

The study of degradation processes that can take place within polymer solar cells is one of the key elements in their development. It is needed in order to make polymer solar cells competitive as compared to inorganic solar cells. Especially the active layer of a polymer solar cell is prone to chemical and physical degradation. The active layer in an organic solar cell is the part where photons are absorbed and as a consequence of this absorption, bound electron-hole-pairs (excitons) are generated.

For the conversion of the energy of photons into usable electrical energy these excitons need to be dissociated. In order to simplify this dissociation the active layer is often a blend of electron donating and accepting materials. One such blend system that has been studied intensively is P3HT (poly(3-hexylthiophene)):PCBM ([6,6]-phenyl-C_{61}butyric acid methyl ester), where the polymer P3HT acts as electron donor and the fullerene derivative PCBM as electron acceptor. The addition of PSS (poly(styrene sulfonic acid)) to this binary system has shown to be promising in terms of organic solar cell efficiency. [1]

In the present investigation the influence of PSS on the degradation of the ternary system P3HT:PSS:PCBM is focussed. To study the ageing of the active layer accelerated testing is used where the decay is artificially accelerated by increasing a parameter that influences the degradation. Here, acceleration is achieved by exposing samples of the ternary system to UV light. For the investigation of the effect of PSS on degradation of P3HT:PSS:PCBM films, annealed P3HT:PCBM(1:1) and P3HT:PSS:PCBM(4:1:5) blend films are studied using optical microscopy, UV-vis spectroscopy as well as atomic force microscopy (AFM). AFM measurements of fresh and irradiated samples (see figure 4.10) reveal not only an alteration in surface structure but also a decrease in film thickness.

These modifications are also visible on a macroscopic scale when analyzing the degraded sample surfaces by optical microscopy. The spectroscopic results eventually allow to determine an enhanced stability for P3HT and a lowered stability for PCBM towards degradation when PSS is added to P3HT:PCBM. λ_{max} is the wavelength and I_{max} the intensity at which the absorption maximum for P3HT and PCBM occurs. $\Delta\lambda_{max}$ is a better measure for the degradation grade of the material than ΔI_{max} because the change in intensity is not only due to degradation induced change in electronic material structure but also superimposed by the decrease in film thickness. Figure 4.11 shows that $\Delta\lambda_{max}$ exhibits in both cases a blue shift.

Since temperatures during sample illumination are comparatively low, physical degradation is assumed to happen only to a minor extent. Among chemical degradation oxidation through

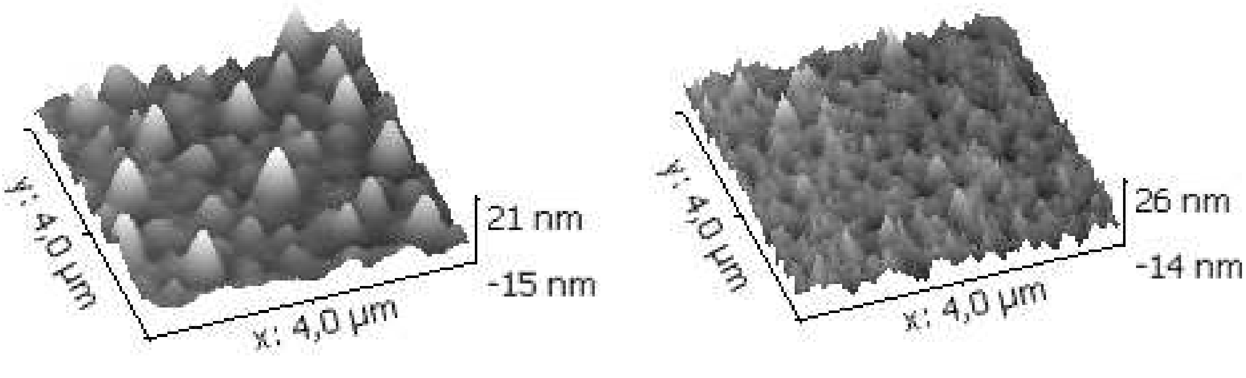

Figure 4.10: AFM images of a fresh sample (left) and an about 70 h irradiated sample (right).

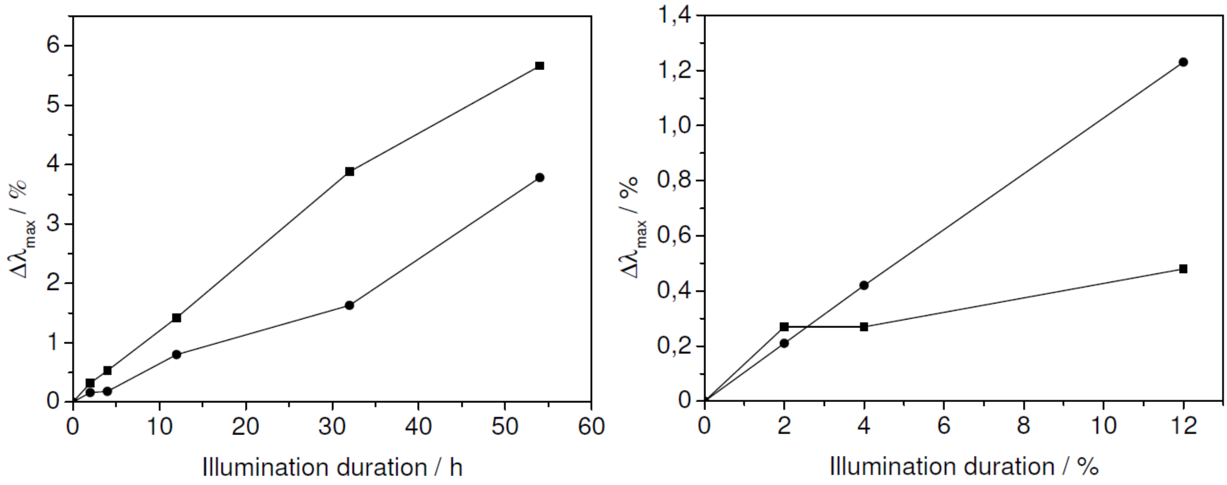

Figure 4.11:
Development of $\Delta\lambda_{max}$ ($\Delta\lambda_{max}$=(($\lambda_{max,fresh}$-$\lambda_{max,sample}$)/$\lambda_{max,fresh}$)·100) with time (P3HT left, PCBM right). P3HT:PCBM (squares), P3HT:PSS:PCBM (dots).

ambient oxygen or ozone, which forms upon UV irradiation, should be the dominant cause for the ageing of the polymer blend films. Because of too low temperatures thermally induced oxidation by ambient oxygen should only marginally account for degradation in this investigation.
Photo-induced oxidation by ambient oxygen is the main reason for degradation since in regard of P3HT it leads to the formation of volatile low-molecular-weight carboxylic acids, whose migration out of the samples is favored by heating, [2] whereby the decrease in film thickness is explainable.
Although photo-induced oxidation of PCBM and P3HT by ozone is reported, ozone cannot be the cause for the decrease in film thickness because even under illumination it only slowly reacts with P3HT while no volatile species of the kind mentioned above are produced. [3, 4]
Furthermore, the concentration of ozone might be too low for a significant oxidation of the polymer blend films. In respect of P3HT there is also a photooxidatively induced reduction in conjugation length. This explains the increasing blue shift and decreasing absorption the longer the material is oxidized. Photo-induced oxidation lowers the LUMO of PCBM. [3]
The reason for the effect of PSS on stability, mentioned above, is very likely due to its influence on the density of the two other components: Domains of P3HT become more dense whereas regions of PCBM become less dense. [5]
In general, molecular oxygen can diffuse more easily through less dense zones and thus there is more oxidation taking place in such parts of the active layer. Component density seems to be the key element when considering photo-oxidation by molecular oxygen.

[1] K. C. Kim, J. H. Park, O. O. Park, *Sol. Energ. Mat. Sol. Cells* **92**, 1188-1191 (2008).

[2] A. Dupuis, P. Wong-Wah-Chung, A. Rivaton, J. Gardette, *Polym. Degrad. Stabil.* **97**, 366-374 (2012)

[3] M. O. Reese, A. M. Nardes, B. L. Rupert, R. E. Larsen, D. C. Olson, M. T. Lloyd, S. E. Shaheen, D. S. Ginley, G. Rumbles, N. Kopidakis, *Adv. Funct. Mater.* **20**, 3476-3483 (2010)

[4] H. Hintz, H. J. Egelhaaf, H. Peisert, T. Chassé, *Polym. Degrad. Stabil.* **95**, 818-825 (2010).

[5] K. Wagenbauer, *Bachelor thesis at TUM* (2011)

4.7 Investigation of ternary polymer blends with spectroscopy and GIWAXS

P. Deimel, E. M. Herzig, J. Perlich[1], W. de Jeu[2], P. Müller-Buschbaum

[1] HASYLAB at DESY, Hamburg, Germany
[2] DWI at RWTH, Aachen, Germany

Today's most extensively investigated system in organic photovoltaics is the binary blend of the photoactive polymer poly(3-hexylthiophene-2,5-diyl) (P3HT) and the fullerene derivative phenyl-C61-butyric-acid-methyl-ester (PCBM). In the blend P3HT functions as an electron donor and PCBM as an electron acceptor. Within the P3HT phase an electron-hole pair can be generated by the absorption of light. This so-called exciton is then separated at the donor-acceptor interface. As a consequence, the interpenetration of P3HT and PCBM phases - i.e. the morphology of the active layer - strongly influences the device performance. In 2007, Kim et al. observed that by adding a third component, namely partially sulfonated polystyrene (PSP), to the standard P3HT:PCBM system, the device efficiency was improved by almost 30% for a certain ratio of the components. [1] Inspired by that, Wagenbauer investigated the effect of polystyrene-sulfonate (PSS) on the standard system in order to understand how PSS takes influence on the morphology of the active layer. [2] He found that PSS has an effect on the molecular order and the crystal orientation of the P3HT fraction. In the presented investigation the effects of adding the third component polystyrene (PS) - PS is not electrolytic and contains no sulfonate group - to the standard P3HT:PCBM system shall be outlined. The aim is to understand how PS influences the morphology and order within such a ternary blend layer.

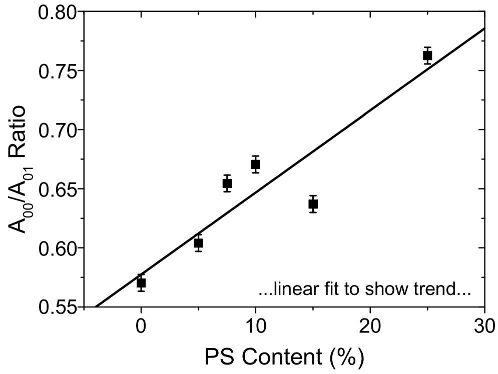

Figure 4.12:
P3HT absorption peak ratio A_{00}/A_{01} from UV/Vis absorption measurements as a function of the PS mass-fraction (weight%) in the ternary blend samples (error bars reflect variation of fit parameters).

To investigate the influence of PS on the P3HT:PCBM system thin ternary blend films with different weight ratios of the components are spin-coated on glass and silicon substrates. In this way the mass-fractions of P3HT and PS are varied while the PCBM mass-fraction is kept constant at 50 wt%. Via X-ray reflectivity (XRR) measurements a film thickness of 91 nm for the respective ternary blend layers is determined. Ultraviolet-visible spectroscopy (UV/Vis) measurements show that the absorption intensity attributed to P3HT decreases with decreasing amount of photoactive P3HT inside the blend. However, for a simultaneously increasing mass-fraction of PS the vibronic A_{00} and A_{01} shoulders on the absorption pattern are more pronounced. These shoulders arise from P3HT absorption that is assumed to consist of a superposition of absorption peaks - e.g. A_{00} and A_{01} - with equal peak widths. Regarding P3HT as weakly coupled H-aggregate, as introduced by Frank C. Spano [3] and referring to J. Clark et al. [4], the molecular order of P3HT can be described by the absorption peak ratio of its A_{00} and A_{01} absorption peaks (see Fig. 4.12). This ratio increases for increasing PS content and is related to conjugation length and crystalline quality of P3HT. It is followed that with an increasing PS content the order of P3HT is increased, most likely leading to an enhanced self-stacking and the formation of P3HT lamellae plane structures [5] inside the blend layers. This would mean an enhanced degree of crystallinity for the P3HT fraction inside the ternary blends.

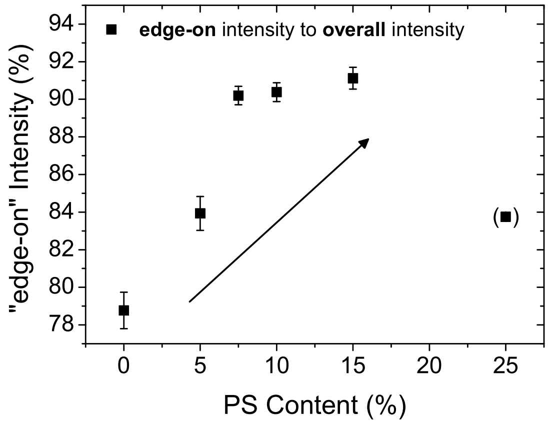

Figure 4.13:
Scattered intensity from edge-on oriented P3HT lamellae plane structures referred to the overall scattered intensity in GIWAXS tube-integrals along (100) P3HT reflex as a function of the PS mass-fraction (wt%) in the ternary blend layers (error bars reflect variation of background correction; 25% PS value neglected due to decomposition pattern in ternary blend layer).

To further investigate the order of P3HT inside the blends grazing incidence wide angle X-ray scattering (GIWAXS) is applied. This technique allows for the investigation of crystalline or semi-crystalline structures inside the ternary blend films. It appears that P3HT lamellae plane structures inside the films are - as expected - mostly oriented edge-on to the surface of the substrate. With increasing PS content, however, a weak scattered signal from face-on oriented P3HT in the standard P3HT:PCBM sample tends to disappear increasingly. By relating the sum over the whole scattered intensity along the (100) P3HT Bragg-fringe to the sum of the scattered intensity that was defined - in an angular manner - to come predominantly from edge-on oriented P3HT one obtains Fig. 4.13. An increasing PS content inside the ternary blend layers seems to enhance the overall edge-on orientation of P3HT lamellae plane structures.

To conclude, the degree of crystallinity within the P3HT fraction in the observed ternary blend layers of P3HT:PS:PCBM can be increased by simply varying the PS content. This might be beneficial for the application in organic photovoltaic devices as it allows for improving charge carrier mobility. Nevertheless, it also appears that with increasing PS content the portion of edge-on P3HT lamellae plane structures increases and the portion in face-on orientation has the tendency to disappear. For the application in organic photovoltaic devices this could be disadvantageous as face-on P3HT offers vertical charge transport. However, the observed effects might be interesting for applications in organic field effect transistors (OFET).

[1] K. C. Kim, J. H. Park, O. O. Park, *Sol. Energ. Mat. Sol. Cells* **92**, 1188-1191 (2008)

[2] K. Wagenbauer, Technische Universität München (2011)

[3] F. C. Spano, *J. Chem. Phys.* **122**, 2347015 (2005)

[4] J. Clark, C. Silva, R. H. Friend, F. C. Spano, *Phys. Rev. Lett.* **98**, 206406 (2007)

[5] A. J. Moulé, K. Meerholz, *Adv. Mater.* **20**, 240-245 (2008)

4.8 Systematic investigation on ternary bulk heterojunction solar cells based on PTB7:PC$_{70}$BM

C. Jendrzejewski, S. Guo, S. V. Roth[1], P. Müller-Buschbaum

[1] HASYLAB at DESY, Hamburg, Germany

Organic solar cells hold great promise for future applications in photovoltaics as they have potentially lower production costs, much lower weight and high flexibility in comparison to inorganic solar cells. In the past decades there have been great progresses in the development of the active layer for organic solar cells. With the appearance of the new electron donor polymer poly[[4,8-bis[(2-ethylhexyl)oxy]benzo[1,2-b:4,5-b']dithiophene-2,6-diyl][3-fluoro-2-[(2-ethylhexyl)carbonyl] thieno[3,4-b]thiophenediyl]] (denoted PTB7), an efficiency of 9.2 % has been reported, when it is blended with PC$_{70}$BM. [1]
In the present work, the effect of a third component 1,8-diiodooctane (DIO) is investigated to further tailor the film morphology. Ternary systems have shown very promising results due to the combined advantages of the host material and the third component, and therefore improve the final power conversion efficiencies. DIO is often used to improve the efficiency of the chlorobenzene based PTB7: PC71BM bulk heterojunction solar cell, but the changes in morphology are just partially known today. [2]
To exploit the effect of different DIO concentrations (0, 3, 6, 9 %vol), optical microscopy and grazing incidence small angle X-ray scattering (GISAXS) are applied.

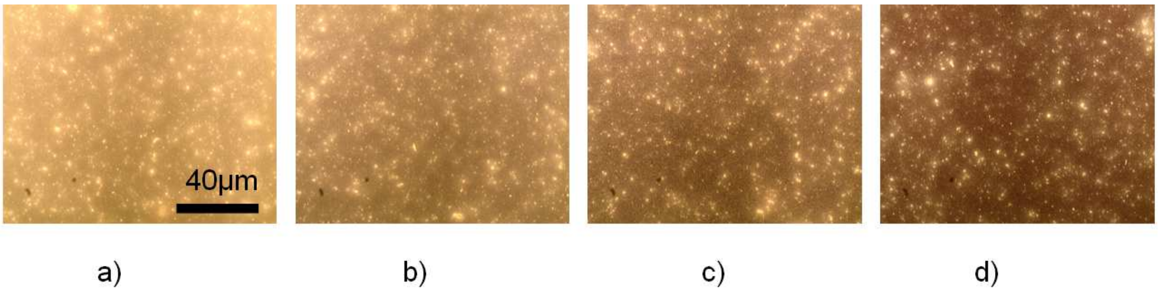

Figure 4.14:
Optical microscopy images of a PTB7:PC$_{70}$BM film with different DIO concentrations (from left to right: 0, 3, 6, 9 %vol), spin-coated on a PEDOT:PSS modified Si-substrate.

In Fig. 4.14 optical microscopy images of the active layers are presented. Homogeneous films with small bright dots are observed. The bright spots are most likely aggregated PC$_{70}$BM clusters. Among the four pictures color changes of background are observed, resulting from different layer thicknesses. As the morphology on optical scale seems rather similar, GISAXS is used to further investigate the nano-morphology. GISAXS is an excellent method to investigate the inner film morphology with high statistics, and structure sizes from a few to hundreds of nanometer can be resolved. Figure 4.15 shows two dimensional (2D) GISAXS data, which were measured at a sample-detector distance of 3.6 m. By analyzing these 2D data information about the inner structure of the film, both normal and parallel to the sample surface can be obtained.

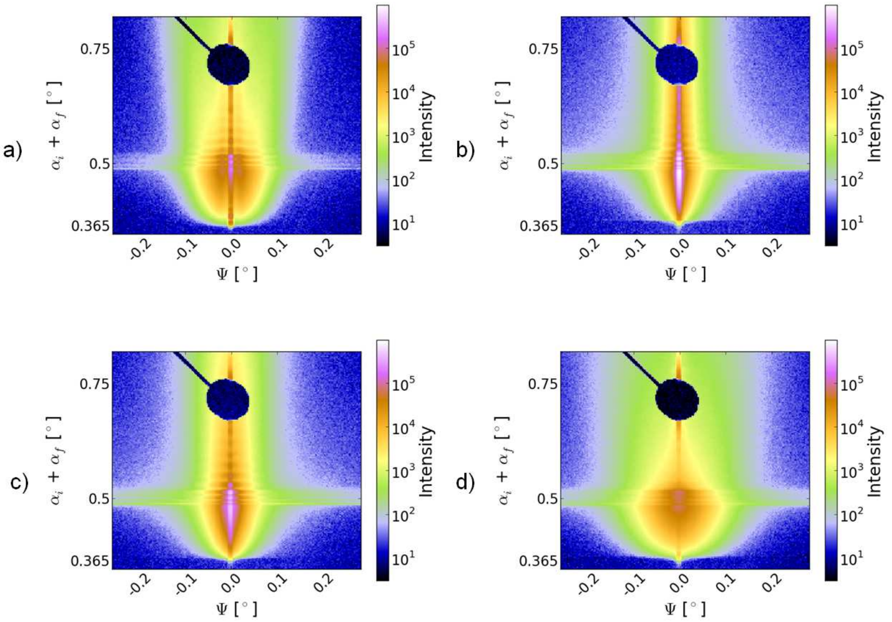

Figure 4.15:
2D GISAXS data of a PTB7:PC$_{70}$BM film with different DIO concentrations (from a) to d): 0, 3, 6, 9 %vol), taken at the P03 beamline. Changes of vertical and lateral scattering pattern are observed. By increasing the concentration from 0 to 3 %vol the scattering pattern gets more defined to the center. Further addition of DIO (picture c) and d)) leads to a broader and less defined scattering pattern.

In Fig. 4.15 tremendous changes are observed in the scattering patterns. For samples with low DIO concentrations there are signs of correlated roughness, visible by modulated intensity between the Yoneda peak and the beamstop region. For samples with higher DIO concentrations the characteristic signature of correlated roughness disappear slowly, observed as much less pronounced intensity modulation. This phenomenon can be explained by the higher mobility of the polymer chains introduced by a higher DIO concentration, which evaporates much more slowly than the host solvent chlorobenzene. Therefore, the polymers have more time to rearrange themselves and avoid the energetically unfavorable conformation of correlated roughness, resulting into a smoother surface.

Moreover, morphological changes along the horizontal scattering direction are observed. From 0 %vol to 3 %vol of DIO the structure sizes increase, seen by the increase of intensity at very low q_y-values. The intensity peak around $q_y \sim 0$ gets more pronounced and well-defined. A different phenomenon is observed at higher concentrations of DIO (6 % and 9 % vol). The Yoneda peak gets less defined, indicating that the structures size decrease and varies more. However, detailed analysis, e.g. detector and out-of-plane cuts need to be performed and fitted to see the morphology evolution. The evolution of structure size in the films, increased structure sizes from 0 % to 3 % vol and then decreased till 9 % vol, contradicts the theoretical improvement of the solar cell performance. Therefore, the preparation of solar cells with the given amount of DIO is ongoing to better correlate all the results.

[1] Z. He, C. Zhong, S. Su, M. Xu, H. Wu, Y. Cao, *Nat. Photonics* **6**, 591-595 (2012)

[2] B. A. Collins, Z. Li, J. R. Tumbleston, E. Gann, C. R. McNeill, H. Ade , *Adv. Energy Mater.* **3**, 65-74 (2013)

4.9 Increased conductivity of PEDOT:PSS for ITO free solar cells

C. Heller, C. M. Palumbiny, P. Müller-Buschbaum

Organic solar cells (OSCs) are promising alternatives for energy production especially for mobile applications. Due to low cost materials and the possibility of cheap large scale manufacturing a fast payback can be achieved. One of the most outstanding properties, which is quite promising for new fields of application, is the possibility to manufacture flexible devices due to the elastic properties of organic materials. Although one major advantage of OSCs compared to regular inorganic solar cells is its flexibility, in research predominantly rigid indium tin oxide (ITO) coated glass substrates are used with the drawback of non desirable mechanical properties and relatively high costs. In those devices ITO is used as an electrode with good electrical properties. Although an ITO coating of PET foil is possible, ITO itself loses its good conductive properties upon bending. [1] In this context poly(3,4-ethylenedioxythiophene):poly(styrenesulfonate) (PEDOT:PSS) has attracted considerable interest among the various conducting polymers, due to its excellent electrical and optical properties. It is one of the most promising alternatives for ITO as a transparent electrode for flexible OSCs and other electronic devices such as organic light emitting diods (OLEDs), organic field effect transistors (OFETs) or electronic paper. However, commercially available PEDOT:PSS has still a low electrical conductivity compared to indium tin oxide. Although there are ways of increasing the conductivity (e.g. doping), a further increase is crucial for the overall device performance.

In our study, the conductivity of PEDOT:PSS films has been increased dramatically from about 1 S/cm to 950 S/cm using a post treatment method which is different to conventional doping as shown before in literature. [2] With this method we were able to get conductivity values reaching the conductivity range of commonly used ITO covered glass substrates (1000 S/cm). Fig. 4.16 shows the influence of the post treatment on non doped (0 mg/ml) and doped PEDOT:PSS films. The used dopant is glycerol as it is known for increasing the conductivity by several orders of magnitude. [3] Fig. 4.16 clearly shows the conductivity increase with increasing glycerol content, which is well known in literature, reaching saturation at 40 mg/ml. However, the additional post treatment increases the conductivity further. Our investigations clearly indicate that this leads to similar values in conductivity independent of the doping prior the post treatment.

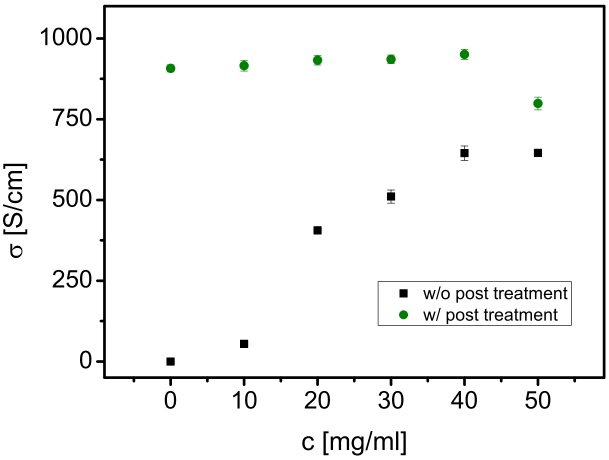

Figure 4.16:
Conductivity of PEDOT:PSS thin films for various glycerol doping concentrations (black squares) and post treated films (green circles), respectively.

Reaching similar conductivity as indium tin oxide coated glass substrates, high conductive PEDOT:PSS allows the production of ITO free solar cells. For implementation in OSCs various possible device architectures are investigated in the following. Fig. 4.17 shows the IU-curves and architectures for four different solar cells: reference cell (black, a), ITO with high conductive electron blocking PEDOT:PSS layer (red, b), ITO free solar cell with high conductive PEDOT:PSS layer as electrode substitute (blue, c), ITO free solar cell with an additional layer of normal PEDOT:PSS on top of the high conductive PEDOT:PSS layer (green, d). The latter architecture is hence mimicking the exact design of the reference solar cell replacing the ITO layer with a high conductive PEDOT:PSS layer. As active layer a polymer blend of poly(3-hexylthiophen-2,5-diyl) (P3HT) and [6,6]-phenyl-C61-butyric acid methyl ester (PCBM) in a ratio of 1:1 is spin coated and aluminum contacts are evaporated on top of the cell.

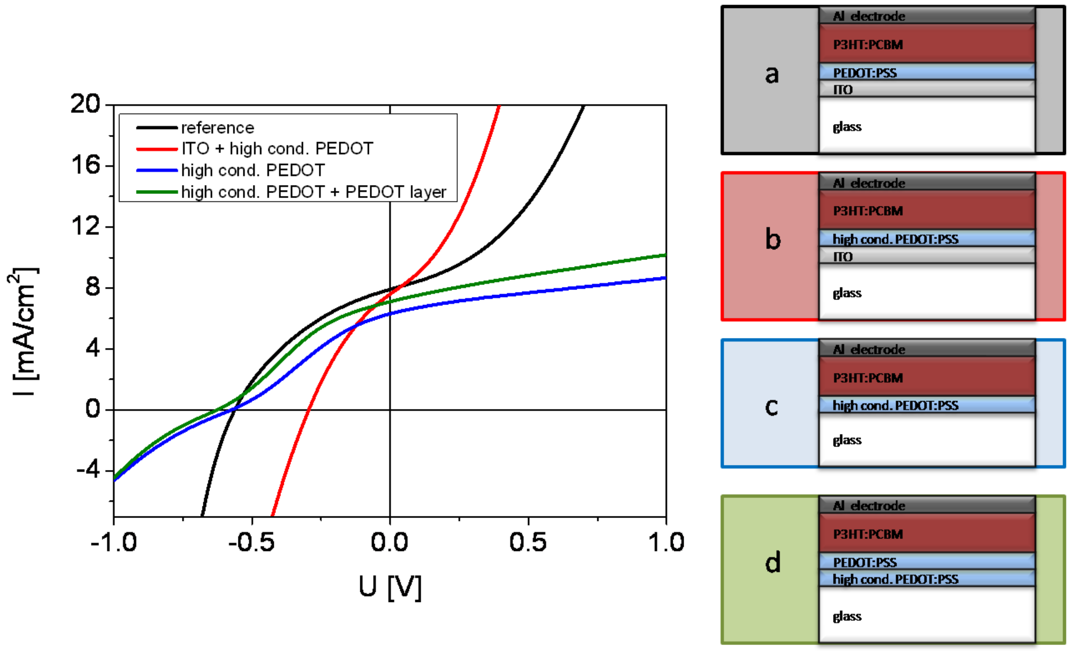

Figure 4.17:
IU-characteristic of four different organic solar cell set ups. The set ups are depicted on the right.

Investigation of the IU-characteristics shows that the mimicked ITO free cell (d) reaches with 1.43 % efficiency almost the efficiency of the reference cell (a) of 1.66 %. The lower efficiency of the ITO free solar cell is most likely due to the still higher resistance of the PEDOT:PSS layer compared to ITO. This is indicated by a lower short circuit current and a ten times higher serial resistance compared to the reference solar cell. Optimization of the device architecture and the layer thickness will lead to further increase in performance of the ITO free solar cell. Here, we are able to show the possibility of ITO free solar cells without a huge loss of performance. Furthermore, the higher open circuit voltage and higher shunt resistance of ITO free solar cells are very promising for the application in flexible electronic devices.

[1] V. Zardetto, T. M. Brown, A. Reale, A. Di Carlo, *J. Polym. Phys.* **49**, 638-648 (2011)

[2] Y. H. Kim, C. Sachse, M. L. Machala, C. May, L. Müller-Meskamp, K. Leo, *Adv. Funct. Mater.* **21**, 1076-1081 (2011)

[3] B. D. Martin, N. Nikolov, S. K. Pollack, A. Saprigin, R. Shashidhar, F. Zhang, P. A. Heiney, *Synthetic Metals* **142**, 187-193 (2004)

4.10 Structural analysis of highly conductive PEDOT:PSS for ITO-free flexible solar cells

C. M. Palumbiny, C. Heller, G. Santoro[1], S. V. Roth[1], P. Müller-Buschbaum

[1] HASYLAB at DESY, Hamburg, Germany

Solar cells based on organic materials offer a wide variety of new applications in the field of renewable energy conversion. Their transparency, translucency and especially their potential to manufacture flexible electronic devices provide numerous smart design opportunities and roll to roll mass production. However, there are still some drawbacks. The high cost of indium tin oxide (ITO) which is used as transparent electrode and its brittleness still limits the wide range of applications for electronic devices[1]. For this purpose several attempts using metal grids, carbon nanotubes, graphene or conducting polymers have been made to respond to these needs. Among the latter is Poly(3,4-ethylenedioxythiophene):poly(styrenesulfonate) (PEDOT:PSS) with its promising properties (transparency, cost-efficiency, hole conductivity and flexibility) which is widely used as selective intermediate electrode in flexible organic electronics. For replacing the ITO electrode however, it is lacking three orders of magnitude in conductivity to replace the ITO electrode. Many attempts have been made to improve the conductivity of PEDOT:PSS, first of all the addition of solvents such as ethylene glycol (EG)[2,3] or dimethyl sulfoxide (DMSO) improving the conductivity as much as 2-3 orders of magnitude. Further improvement by a factor of two has been achieved by post treatment in solvents[4].

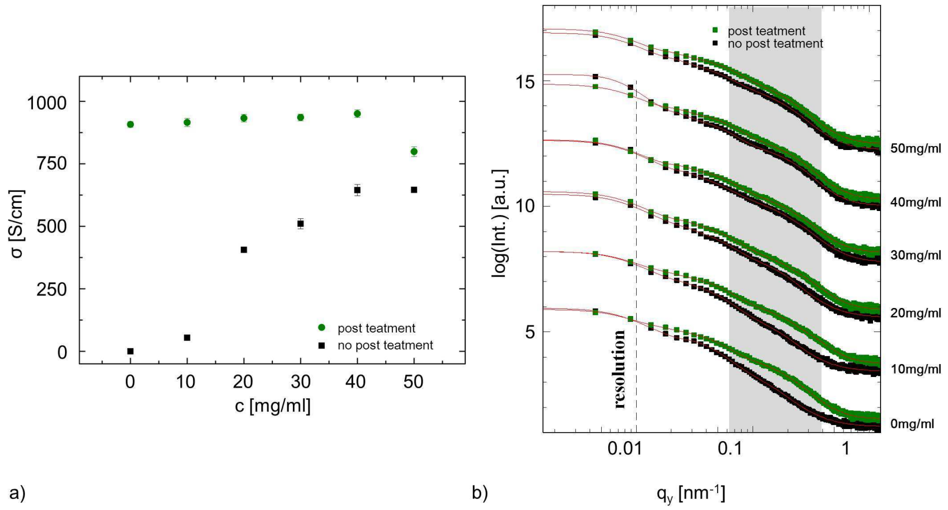

Figure 4.18: (a) Conductivity of PEDOT:PSS thin films for different glycerol doping concentrations (black points) and post treated films (green points), respectively. (b) GISAXS out of plane cuts together with their fits for all glycerol concentrations.

Here, we investigate and refine a recently developed post treatment method for enhancing the conductivity of PEDOT:PSS reaching the order of ITO as shown before in literature[4]. As Figure 0.1 a) clearly shows this method of doping and post treatment is well suited to enhance the conductivity of PEDOT:PSS to the range of commonly used ITO. For a deeper understanding of the induced changes by the solvent treatment, the surface morphology has been investigated with scanning electron microscopy (SEM) and moreover the inner morphology has been addressed with grazing incident small angle x-ray scattering (GISAXS). Figure 0.1 b) shows the out of plane cuts of the GISAXS measurements for various glycerol concentrations with and without equivalent post treatment together with their fitting curves. As the out of plane cuts already indicate, the difference between no post treatment and post treatment is gradually decreasing with increasing glycerol doping. The trend is the same as observed for conductivity (Figure 0.1 a)). Kim et al. attribute the enhancement of conductivity by solvent treatment to the removal of the non-conducting PSS from the conducting PEDOT:PSS layer[4].

Owing to the conductivity differences of PEDOT and PSS we were able to performed SEM measurements for topographical characterization of the differently treated PEDOT:PSS layers as exemplarily shown in Figure 0.2 a).

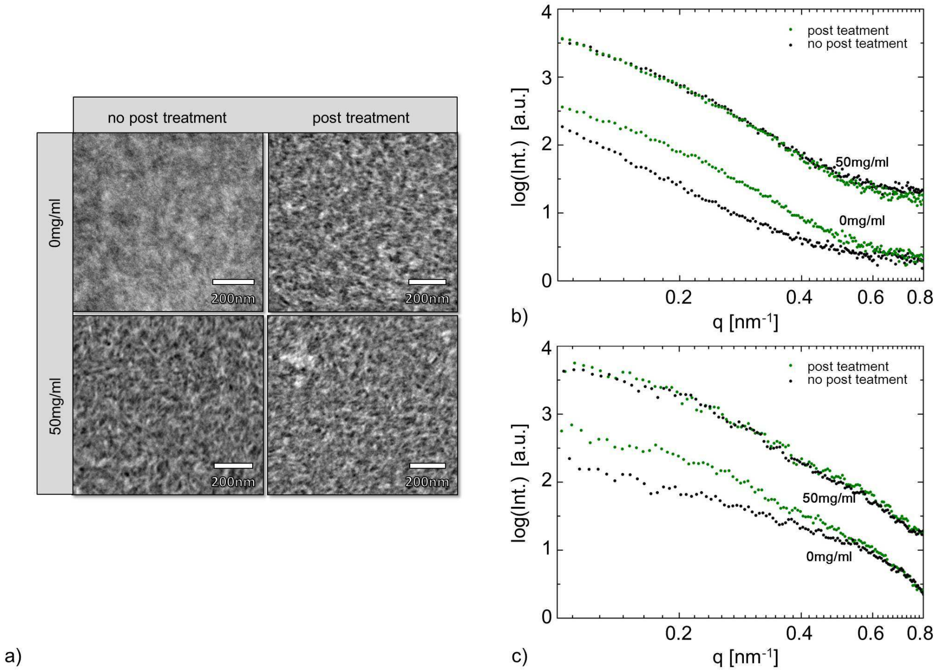

Figure 4.19:
(a) SEM measurements of 0 mg/ml and 50 mg/ml glycerol doped PEDOT:PSS and the corresponding post treated films. (b,c) Comparison of the GISAXS out of plane cuts (b) and the extracted PSDF from the SEM measurements (c) for the q-range of intrest (highlighted in gray color in Figure 0.1 b)).

By fourier transformation and radial integration, the power spectral density function (PSDF) (Figure 0.2 c)) is extracted and compared to the corresponding GISAXS cuts (Figure 0.2 b)). As for the conductivity and the GISAXS measurements, the trend of the decreasing difference between non post treated and post treated layers remains. Note that the slight difference in the curve shape can be referred to the difference between inner film and surface morphology.

In conclusion, we could show that the morphological changes induced by the solvent treatment to the surface morphology can be correlated to the changes induced to the inner morphology. Moreover, the results are in good agreement with the electronic changes of the PEDOT:PSS layer with doping and/or solvent treatment supporting the work of Kim et al. The results reveal new paths for ITO-free flexible solar cells. The profound understanding of the changes induced by the solvent treatment concerning the inner and surface morphology gives directions for further targeted application.

[1] V. Zardetto, T.M. Brown, A. Reale, A. Di Carlo, *J. Polym. Phys.* **49**, 638-648 (2011)

[2] B.D. Martin, N. Nikolov, S.K. Pollack, A. Saprigin, R. Shashidhar, F. Zhang, P.A. Heiney, *Synthetic Metals* **142**, 187-193 (2004)

[3] R. Meier, C. Birkenstock, C. M. Palumbiny and P. Müller-Buschbaum *Phys. Chem. Chem. Phys.* **14**, 15088-15098 (2012)

[4] Y.H. Kim, C. Sachse, M.L. Machala, C. May, L. Müller-Meskamp, K. Leo, *Adv. Funct. Mater.* **21**, 1076-1081 (2011)

5 Polymer-hybrid systems

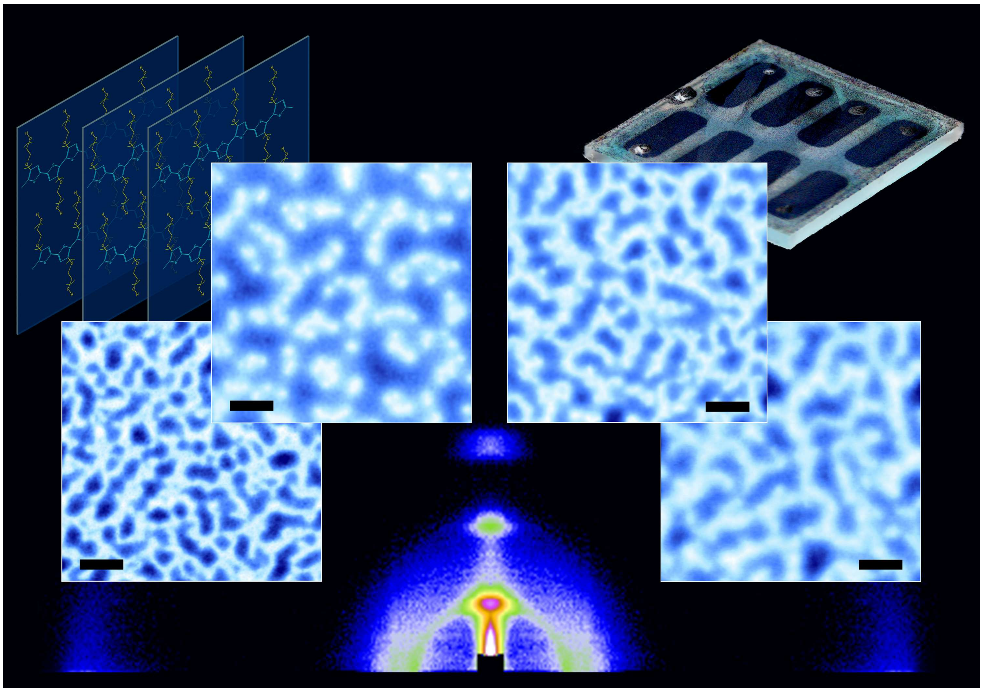

5.1 Low temperature sol-gel route for nanostructured polymer/titania hybrid films based on custom made poly(3-alkoxy thiophene)

M. A. Niedermeier, M. Rawolle, P. Lellig[1], V. Körstgens, E. M. Herzig, A. Buffet[2], S. V. Roth[2], J. S. Gutmann[3], T. Fröschl[4], N. Hüsing[4], P. Müller-Buschbaum

[1] Max-Planck-Institut für Polymerforschung, Mainz, Germany
[2] HASYLAB at DESY, Hamburg, Germany
[3] Institut für Physikalische Chemie, Universität Duisburg-Essen, Essen, Germany
[4] Materialchemie, FB Materialforschung und Physik, Salzburg, Austria

In the fast developing field of photovoltaics, the so-called hybrid solar cells, consisting of an inorganic matrix combined with an organic hole conductor, have received a lot of attention in the recent years. Typically, the inorganic matrix is formed in a separate step, which involves elevated temperatures well above 200 °C. This matrix is subsequently backfilled with the organic hole conductor. But this route of fabrication is not ideal, since the task of backfilling is complicated and there are several problems which have to be overcome, e.g. an air layer in the bottom which blocks incoming material, and thus prevents a complete backfilling.

A workaround to these problems is promised by a low-temperature sol-gel process, in which the polymer and the inorganic semiconductor network are fabricated simultaneously. This approach, however, poses several challenges. Firstly, a semiconducting titania matrix which has a reasonable degree of crystallinity has to be fabricated without the typical sintering or calcination processes at high temperatures. And secondly, the conductive polymer needs to establish a proper interface with the inorganic material and, thereby, maintain the role of the structure directing agent. To meet these challenges, in the present work a poly(3-alkoxy thiophene) polymer is used in a novel low-temperature sol-gel synthesis combined with an ethylene glycol modified titanate (EGMT) as the titania precursor. EGMT allows for tuning the crystal phase of the titania by changes of the pH value, and thus avoiding the typical high temperature treatments. The poly(3-alkoxy thiophene) is derived from poly(3-hexyl thiophene) (P3HT), where the hexyl side chains are substituted by a poly(ethylene oxide) side chain. We hence name it in the following poly(3-ethylene oxide thiophene), in short P3EOT. Ethylene oxide containing polymers are widely used for structuring titania films, since it is known that metal oxides selectively coordinate to the ethylene oxide.

Films prepared with the pure P3EOT are compared to hybrid films, fabricated by combining P3EOT with the EGMT precursor. Additionally, an annealing step in nitrogen atmosphere was performed for both types of films for 15 minutes at 140 °C.

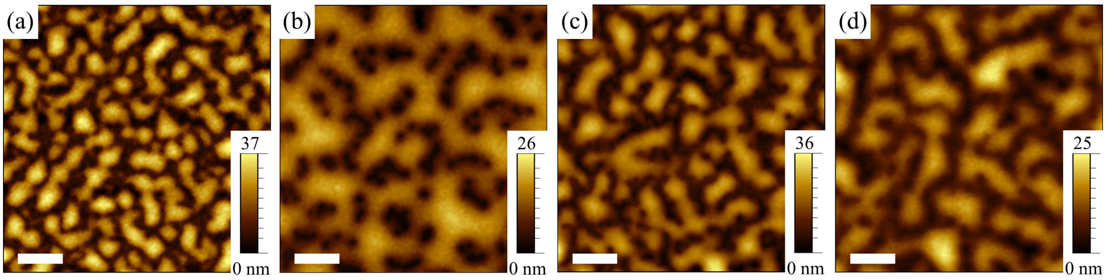

Figure 5.1:
Topography AFM images of the P3EOT films as prepared (a) and after annealing (b), hybrid film as prepared (c) and after annealing (d) are shown. The scale bar in every image corresponds to 1 μm, so each AFM image shows a section of the sample surface of 5x5 μm^2.

Figure 5.1 shows atomic force microscopy (AFM) topography images of the pure P3EOT and the hybrid films before (a), (c) and after (b), (d) annealing, respectively. Before annealing both, the pure P3EOT and the hybrid film show a defined surface structure typical for block copolymers with a similar rms-roughness of roughly 6 nm. Upon annealing the rms-roughness is lowered to roughly 4 nm for both films. However, the surface morphology of the pure P3EOT and the hybrid film now show notable differences. For the pure polymer film a smoothing of the surface is observed and the defined surface structures get smeared out. In the case of the hybrid film, the topology still resembles the state of the non-annealed film. This behavior is attributed to the titania network which is present inside the polymer matrix. As already mentioned, the titania coordinates to the ethylene oxide block of the polymer. Therefore, the titania network which is bound to the P3EOT hinders the polymer mobility and thus limits changes in the surface topography, as observed in the AFM measurements. This observation is supported by scanning electron microscopy images of samples where the polymer matrix was removed from the hybrid films via a high temperature step. An interconnected network of small titania granules with sizes ranging from 5 to 15 nm is visible in these samples [1].

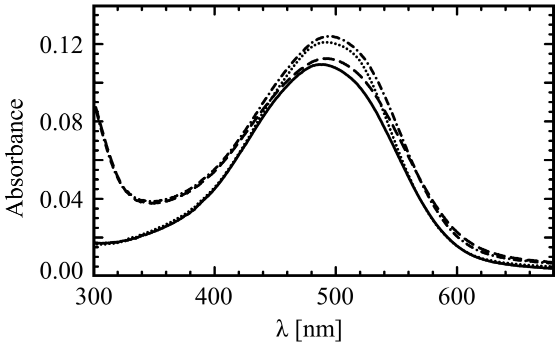

Figure 5.2:
Absorbance of the films in the wavelength region from 300 to 680 nm, measured with UV/Vis-spectroscopy. The solid and dotted lines correspond to the pure P3EOT film before and after the annealing, respectively. The dashed and dashed-dotted lines correspond to the hybrid film before and after annealing, respectively.

UV/Vis spectroscopy is used to probe the optical properties of the pure P3EOT and the hybrid films. Figure 5.2 shows the absorbance spectra of the different films. The solid and dotted line correspond to the pure P3EOT film before and after annealing, respectively. For both curves, a maximum in absorption is visible at 500 nm. This is similar to the behavior of P3HT which has a typical absorption maximum at around 530 nm. Upon annealing of the pure P3EOT film, an increase in absorbance is visible along with a slight shift of the maximum towards higher wavelengths, which is again similar to P3HT films. This shift is assigned to an increase of the conjugation length, indicating a better ordering of the polymer chains, and thus, an increased crystallinity. The absorbance curves of the hybrid films before and after annealing are represented by the dashed and dash-dotted line, respectively. Similar to the pure P3EOT film, a maximum in absorption is visible at 500 nm, which shifts slightly after annealing the film. However, for wavelengths below 420 nm the hybrid films both show a strong increase in absorption. As observed in the AFM measurements, the hybrid films have a titania network embedded in the polymer matrix. Titania being a wide-band gap semiconductor, is known as strong photoabsorber for UV-light. The increase of the absorption at about 400 nm corresponds to an energy of about 3.0 eV, which matches the band gap of rutile TiO_2, indicating the presence of crystalline titania in our hybrid films. The crystallinity of the titania and the P3EOT is further verified by grazing incidence wide angle X-ray scattering. For titania a (110)-Bragg peak is present at $q = 19.4\ nm^{-1}$ which corresponds to the rutile phase. And for P3EOT a π-stacking distance of 0.37 nm is found, which is again similar to P3HT, showing that the substitution of the side chain leaves the optical and crystallographic properties unchanged.

[1] M. A. Niedermeier, M. Rawolle, P. Lellig, V. Körstgens, E. M. Herzig, A. Buffet, S. V. Roth, J. S. Gutmann, T. Fröschl, N. Hüsing, P. Müller-Buschbaum, *ChemPhysChem*, **14**, 597-602 (2013)

5.2 Characterization of oxygen plasma-treated titanium dioxide surfaces with a foam like structure

B. Su, M. A. Niedermeier, M. Rawolle, P. Müller-Buschbaum

Due to their high surface to volume ratio and their bi-continuous morphology, foam-like nanostructures of titania are very interesting for applications in photovoltaics, for example in hybrid solar cells or dye-sensitized solar cells (DSSC). The nanoporous titania layers are responsible for the electron transport and directing dye layers' structure. In our studies, the morphology of titania films is investigated with respect to a possible incorporation into hybrid solar cells. Plasma treatment, which is an environmentally friendly physical surface modification technology, is a suitable method to change the wetting characteristics of polymers [1]. In this report, we focus on the effect of oxygen plasma treatment on the foam like structure of titanium dioxide.

To gain the foam like nanostructure of titanium dioxide, we use sol-gel synthesis in combination with block copolymer micro-phase separation. Silicon wafers were used as the substrate, which were cleaned in the acidic bath for 15 minutes at $80°C$ before spin-coating [2]. Poly (styrene-*block*-ethylene oxide), denoted P(S-*b*-EO), is an amphiphilic block copolymer which was used as a structure directing agent. Firstly, P(S-*b*-EO) (48.91 mg) was dissolved in 1,4-dioxan (2.265 ml), which is a good solvent for both polymer blocks. Afterwards, HCl (37%, 13.1 μl), as a bad solvent for the PS block, and titanium tetraisopropoxide (TTIP, 242.8 μl) as titania precursor, were added to the polymer solution and stirred for 1 hour. In the next step, the mixed solution was deposited on pre-cleaned Si(100) substrates via spin-coating at $19.0°C$ and 41% humidity, at a rotating speed of 2000 r/min. To obtain crystalline TiO_2 films, the samples were put into a furnace and heated to $400°C$ for 4 hours.

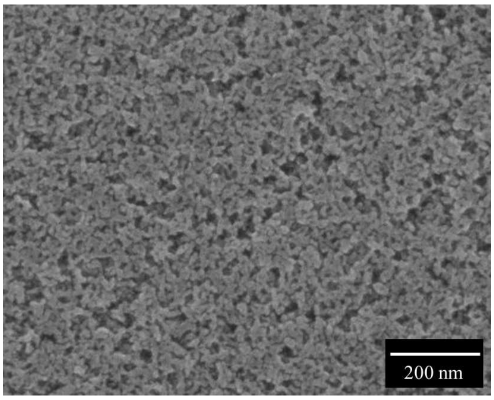

Figure 5.3:
SEM image of titanium dioxide films after calcination at $400°C$ for 4 hours, as obtained by combination of sol-gel chemistry and P(S-*b*-EO) as a block copolymer template.

Fig. 5.3 shows the top view of titanium dioxide film after calcination with a foam like structure measured with scanning electron microscopy (SEM). The sample contains a large quantity of small-size structures. However, mesopores are distributed in the film homogeneously, with an average diameter of the pores of 22.5 nm.

Plasma treatment was performed with oxygen at the pressure of 0.4 Pa and a power of 240 W. The titania foam structures were treated for 5 min, 10 min, 15 min, 25 min, and 40 min in the oxygen plasma, respectively. After the treatment, the water contact angle of the samples was measured directly with a Dataphysics system. A droplet of 1μl was dropped on the sample and recorded by "uEye" camera. Each picture was taken after 5 s (time was started to record when the water drop was deposited on the sample) and fitted with the "SCA20" software (from "Data Physics Corporation"). Figure 5.4 shows the different contact angles for the different plasma etch times. The contact angle changed tremendously for 5 and 15 minutes of oxygen plasma treatment. After 40 minutes oxygen plasma treatment, the contact angle was reduced drastically from 19.65° to 3.5°. However, there is only a slight change between 25 minutes and 40 minutes oxygen plasma treatment, from 3.75° to 3.5°. It has been reported in literature that the contact angle is determined by the balance of surface forces. Thus, after oxygen plasma treatment surface forces are changed. To obtain the change of thickness of titanium oxide films, samples are measured in the Filmetrics F20 ThinFilm Measurement System (Filmetrics Inc., San Diego). The results show that the thickness of the titanium oxide films is nearly unchanged: Before the oxygen plasma treatment (86.9 ± 2.67 nm) and after the oxygen plasma treatment (87.92 ± 2.75 nm).

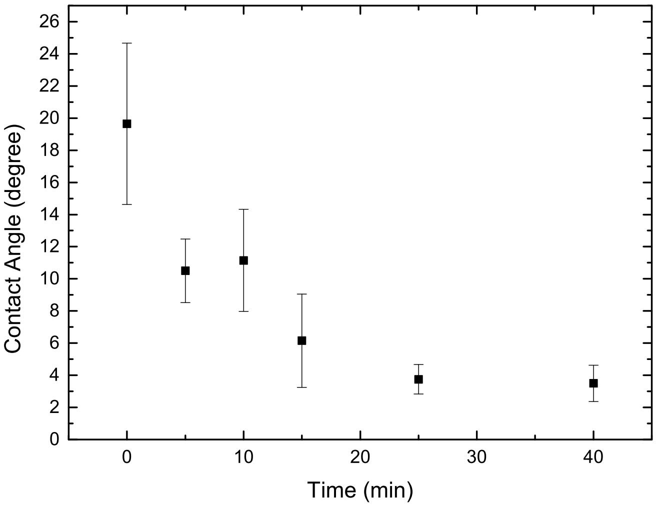

Figure 5.4:
Water contact angle of titania foam samples, which were treated in oxygen plasma for 5 min, 10 min, 15 min, 25 min, and 40 min, respectively.

In conclusion, the study revealed that oxygen plasma treatment could make the foam like structure of titanium dioxide extremely hydrophilic. The major modification effects by oxygen plasma can be depicted as following [3]: (a) cross-linking of near-surface molecules, (b) introduction of new functional groups, (c) degradation of polymer molecules, (d) etching. In the condition of low power, the wetting behavior of oxygen plasma treated titanium oxide films is largely depended on the cross-linking of near-surface molecules, which can balance the surface force. The etching effect was not observed in this work.

[1] M. Morra , E. Occhiello , F. Garbassi, *Langmuir* **5**, 872-876 (1989)

[2] P. Müller-Buschbaum, N. Hermsdorf, S.V. Roth, J. Wiedersich, S. Cunis, R. Gehrke, *Spectrochim. Acta* **59**, 1789-1797 (2004)

[3] B. L. Johansson , A. Larsson, A. Ocklind, A. Ohrlund, *J. Appl. Polym. Sci.* **86**, 2618-2625 (2002)

5.3 Fabrication of sponge-like titania nanostructures by sol-gel synthesis with different structure-directing agents

L. Song, M. A. Niedermeier, P. Müller-Buschbaum

Titania nanostructures have a huge application potential in photovoltaics due to their morphology with a large surface area and an interconnected network. The morphology is vital, as it influences charge transfers routes and the charge separation takes place at the interface of the titania and the dye in case of dye sensitized solar cells (DSSC).
Several techniques have been developed to fabricate thin nanostructured titania films, such as spray pyrolysis, magnetron sputtering, and spin coating from solution. In the last method the film thickness is controllable via the concentration of the solution and the used spin coating parameters. In the present investigation, the titania nanostructures are prepared from sol-gel synthesis in combination with block copolymer templating as follows: a certain amount of polystyrene-block-polyethyleneoxide, denoted P(S-b-EO), is dissolved in 1,4-dioxane, then concentrated HCl and titanium tetraisopropoxide (TTIP) are added slowly under constant stirring. After this process completes, the whole solution continues to stir for 50 min. Next it is deposited on the silica substrates by spin coating. The obtained films are calcined at 400 ^{o}C in an ambient condition to combust the polymer matrix. By this final step, titania is transformed from amorphous phase to anatase phase. In this experiment, the P(S-b-EO) was used as a structure-directing agent; the 1,4-dioxane is the good solvent for both PS and PEO blocks; the concentrated HCl is a catalyst for hydrolysis and also a poor solvent for the PS block, but a good solvent for PEO block; the TTIP is the titanium source.
Two different block copolymers P(S-b-EO) were used. One with a molecular weight of 2300 g/mol for the PS block and 700 g/mol for the PEO block (denoted as P_{3000}(S-b-EO)) and one with the PS and PEO molecular weights being 1500 g/mol and 600 g/mol, respectively (denoted as P_{2100}(S-b-EO)). Using different relative weight fractions of 1,4-dioxane, concentrated HCl, and TTIP can result in different morphologies of the titania films. Sponge-like structures can be formed with following weight fractions: 1,4-dioxane:HCl:TTIP=0.92:0.005:0.075 [1].
The morphology of the different titania films has been investigated by scanning electron microscopy (SEM) and the effect of UV light irradiation on the films' hydrophilicity has been determined by water contact angle measurements.

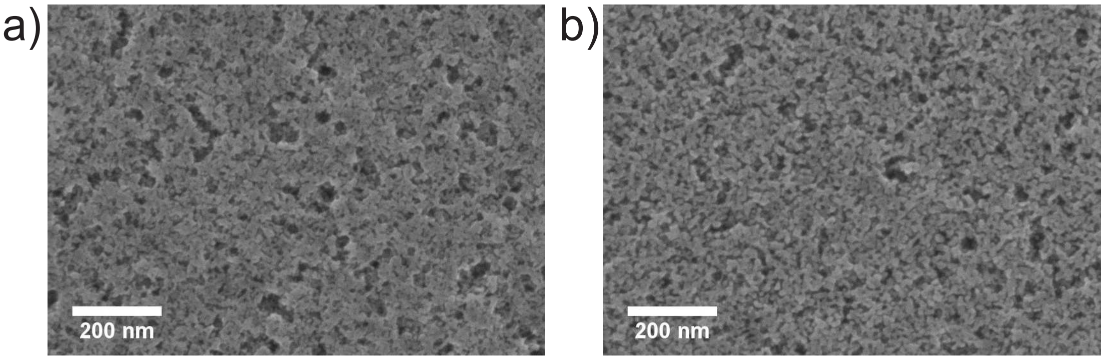

Figure 5.5:
SEM images of the sponge-like titania surface nanostructure as using two different structure-directing agents: a) P_{3000}(S-b-EO) and b) P_{2100}(S-b-EO).

Fig. 5.5 a) and b) show top views of these two titania films using different P(S-b-EO)s. Both images demonstrate the porous sponge-like morphologies. The structures are homogeneous on the large scale and there are no obvious defects in the surfaces. The morphologies of these two

titania films are very similar despite they used different chain lengths P(S-b-EO)s as templating agents. Therefore, it is convinced that the chain length of diblock polymer have little effect on the film's morphology when compared with the relative weight fractions of 1,4-dioxane, concentrated HCl, and TTIP [1]. However, the average pore sizes visible in Fig. 5.5 a) are slightly bigger than those in Fig. 5.5 b). The long-chain P(S-b-EO) tends to form bigger micelles in the solution and this difference in micelle size causes the different pore sizes.
In solid-state DSSC a dye layer is necessary for the change generation. Thus the titania network structure needs to be covered with such dye layer. [2] thus the adhesive ability of titania with respect to the dye is crucial, which links closely with its hydrophilicity. The hydrophlicity was characterized by water contact angle measurements and improved by the illumination with UV light.

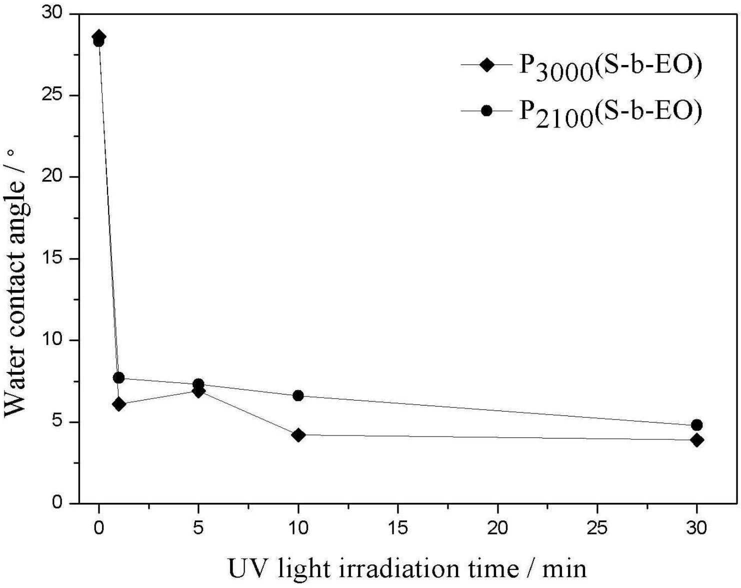

Figure 5.6:
Variations of water contact angle as two films were exposed under the UV light irradiation for different times.

The UV light irradiation induced changes of the water contact angle of the titania films are illustrated in Fig. 5.6. Illuminated by the UV light irradiation for 1 minute, the water contact angle of the film using P_{3000}(S-b-EO) drops from 28.6° to 6.1°; that of the film using P_{2100}(S-b-EO) also shows a dramatic downward trend (from 28.3° to 7.7°). Both films show a rapid and strong improvement of their hydrophilicity, which can be explained by chemisorption of water. Specifically, the UV light irradiation induces the generation of the Ti^{3+} at the surface of titania films, and the Ti^{3+} chemisorbs water molecules from the air. [3] Both water contact angles remain unchanged for increased UV exposure time, which indicates that the exposure time has little influence.

[1] Y. J. Cheng, J. S. Gutmann, *J. Am. Chem. Soc.* **128**, 4658-4674 (2006)

[2] S. Ito, P. Liska, P. Comte, R. L. Charvet, P. Pechy, U. Bach, L. Schmidt-Mende, S. M. Zakeeruddin, A. Kay, M. K. Nazeeruddin, M. Grätzel, *Chem. Commun.* **34** , 4351-4353 (2005)

[3] R. Wang, N. Sakai,A. Fujishima,T. Wanabe,K. Hashimoto, *J. Phys. Chem.* **103**, 2188-2194 (1999)

5.4 Probing the nanostructure of titania in a small droplet sample with GISAXS tomography

M. Rawolle, M. A. Ruderer, J. M. Feldkamp[1], A. Timmann[2], C. G. Schroer[1], P. Müller-Buschbaum

[1] TU Dresden, Dresden, Germany

[2] HASYLAB at DESY, Hamburg, Germany

Titanium dioxide, also known as titania, has interesting optoelectronic properties. Therefore, titania is widely applied for example in gas sensing, photocatalysis and photovoltaics [1]. The nanostructure of titania is of high importance for all the mentioned applications, as a large surface-to-volume ratio is necessary for the most efficient functionality. Possibilities to direct the titania nanostructure are numerous, where one possible route to tailor the titania nanostructure is based on block copolymer templates which are applied in the sol-gel synthesis of titania [2]. As the sol-gel synthesis is a wet-chemical process, droplet samples are of high interest. In industrial application, the solution-based preparation can be applied for example in ink-jet printing, which enables very cheap processing.

Grazing incidence small angle x-ray scattering (GISAXS) is performed in order to investigate the nanostructure not only on the surface of a sample but also in the volume with a statistical relevance. To probe the structure of a small droplet with the resolution of different structures, GISAXS is combined with tomography. GISAXS micro-tomography was introduced successfully to probe the nanostructure in a droplet of nanoparticles in 2009 [3].

In order to tailor the titania nanostructure in a small droplet, the structure directing template consisting of the block copolymer poly(dimethyl siloxane-*block*-methyl methacrylate (poly ethylene oxide)) P(DMS-*b*-MA(PEO)) is dissolved in a mixture of good solvents for both blocks of the amphiphilic block copolymer, tetrahydrofuran and 2-propanol. The sol-gel synthesis is started in the template solution by the addition of the titania precursor titanium tetra isopropoxide (TTIP) and hydrochloric acid (HCl), which acts both as a selective solvent and as catalyst to start the sol-gel reaction. All the components are mixed in one glass vial, as described in reference [4] along with the refinement of the structure direction by introducing micro-fluidics for mixing of the sol-gel components. After stirring of the sol-gel for 60 min, a single droplet of the sol-gel with a volume of 0.1 μL is deposited with a needle on a pre-cleaned silicon wafer. After drying for 17 hours under ambient conditions, the titania-polymer composite droplet is calcined at 450 °C for 4 hours to combust the polymer and to crystallize the titania. The optical microscopy image of the calcined titania droplet in figure 5.7 reveals a droplet with a diameter of 1.25 mm.

The GISAXS microtomography measurements have been performed at the synchrotron beamline BW4 at HASYLAB, DESY, Hamburg. The titania droplet is scanned with GISAXS tomog-

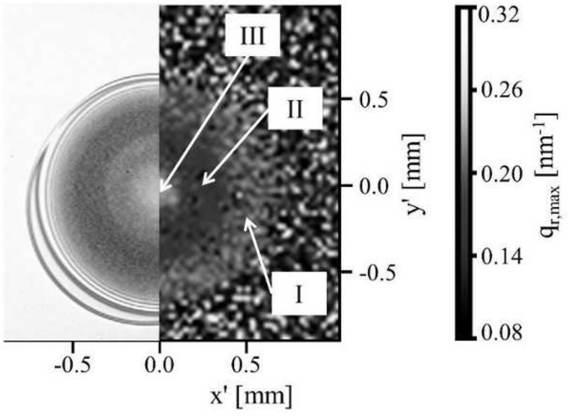

Figure 5.7:
Optical microscopy (left) and tomography map (right) of a structured droplet of titania. In the reconstructed tomography map, the maximum in the scattering in q_r is plotted as a function of x' and y' of the sample coordinate system used in tomography. Three different regions, labeled with (I), (II) and (II), can be distinguished according to the maximum $q_{r,max}$ of 0.21, 0.16 and 0.25 nm^{-1}, depicted in gray scale.

raphy measurements with a counting time of 3 s per image, an incident angle of $0.3°$ at 74 translational positions with a step width of 25 μm and at 114 rotational positions with a step width of $1.6°$. The tomographic reconstruction is successful for $q_r > 0$, where q_r is the radial component of the scattering vector in cylindrical coordinates.

A maximum is observed in the scattered intensity as a function of q_r. The reconstructed tomography map is shown along with the optical micrograph in figure 5.7, where the 2d map of different positions of the maximum in q_r are represented in gray scale. Three distinct regions of different titania nanostructures in the droplet are observed. Representative scanning electron microscopy (SEM) images and the reconstructed scattering patterns for the three different regions are shown in figure 5.8.

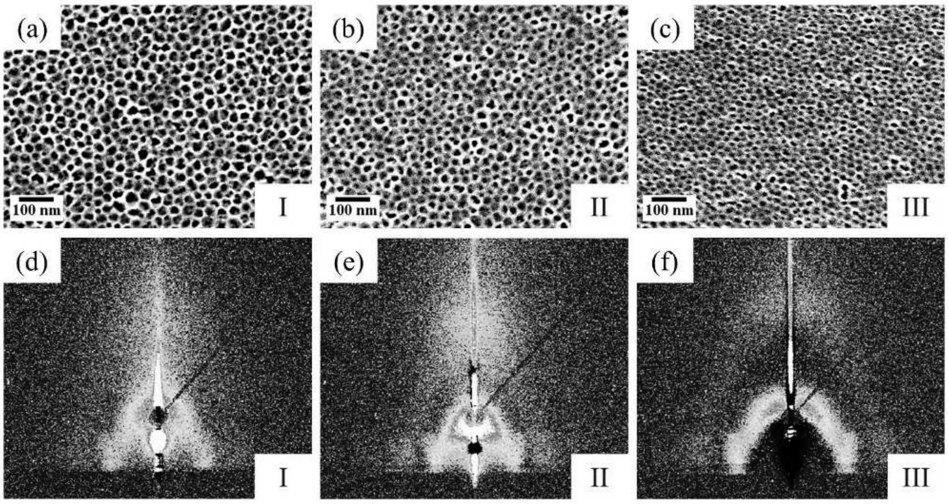

Figure 5.8:
Representative SEM images (a-c) and reconstructed GISAXS patterns (d-f) for the three different regions (I-III) in the structured droplet of titania.

In the rim of the drop, the surface of the titania nanostructure consists of mesopores with a diameter of around 27 nm as probed with SEM. In an intermediate rim, pores with a diameter of 21 nm are observed and in the center of the drop, the diameter of the observed pores is just 17 nm. In addition, the structured titania in the center of the droplet is thicker. In the reconstructed scattering patterns, a change of the most prominent lateral structure size from 30 nm in the outer rim to 39 nm in the intermediate rim and to 25 nm in the center of the droplet is determined. Consequently, the structure in the volume of the titania droplet differs from the structure at the surface. Furthermore, the scattering pattern in the outer rim resembles the scattering pattern of a homogeneous thin film of structured titania when deposited by spin coating [4].

In conclusion, the structures in the rim of the droplet resemble the structures in a homogeneous film best. The rim of the droplet dries fastest, the inner parts of the droplet dry slower. Consequently, the structures collapse more in the center parts of the droplet.

[1] O. Carp, C. L. Huisman, A. Reller, *Prog. Solid State Chem.* **32**, 33-177 (2004)

[2] M. Rawolle, M. A. Niedermeier, G. Kaune, J. Perlich, P. Lellig, M. Memesa, Y.-J. Cheng, J. S. Gutmann, P. Müller-Buschbaum, *Chem. Soc. Rev.* **41**, 5131-5142 (2012)

[3] M. Kuhlmann, J. M. Feldkamp, J. Patommel, S. V. Roth, A. Timmann, R. Gehrke, P. Müller-Buschbaum, C. G. Schroer, *Langmuir* **25**, 7241-7243 (2009)

[4] M. Rawolle, M. A. Ruderer, S. M. Prams, Q. Zhong, D. Magerl, J. Perlich, S. V. Roth, P. Lellig, J. S. Gutmann, P. Müller-Buschbaum, *Small* **7**, 884-891 (2011)

5.5 Morphology studies of titania nanoparticle films for hybrid photovoltaic applications

S. Pröller, V. Körstgens, T. Geue[1], H. Iglev[2], P. Müller-Buschbaum

[1] PSI, Villigen, Switzerland
[2] TU München, Department Physik E11, Garching, Germany

Thin films containing titania nanoparticles have a variety of possible applications. For applications in photovoltaics a high absorption coefficient and a large surface area are desirable. Blends of organic and inorganic semiconductors are used in hybrid solar cells. Advantage of those hybrid solar cells is the combination of inorganic semiconductors with the film-forming polymer. Properties of inorganic nanoparticles are size tunability, high absorption coefficients and high mobilities. Today hybrid solar cells have not yet reached very high efficiencies due to problems such as uncontrolled aggregation and insulating ligands at the nanoparticle surface. However, hybrid solar cells have the potential to provide low cost electricity. [1]
Studies by Baeten et al. [2] lead to efficiencies of 0.2% for drop cast poly(3-[potassium-6-hexanoate]thiophene-2,5-diyl) (P3KHT) in combination with rutile titanium(IV) oxide nanorod arrays. The water solubility of P3KHT provides the possibility to produce fully 'green' hybrid solar cells. This safe and environmentally friendly processing of P3KHT circumvents the drawback of the conventionally used poly(3-hexylthiophene-2,5-diyl) (P3HT), namely the use of toxic organic solvents like chlorobenzene or chloroform.

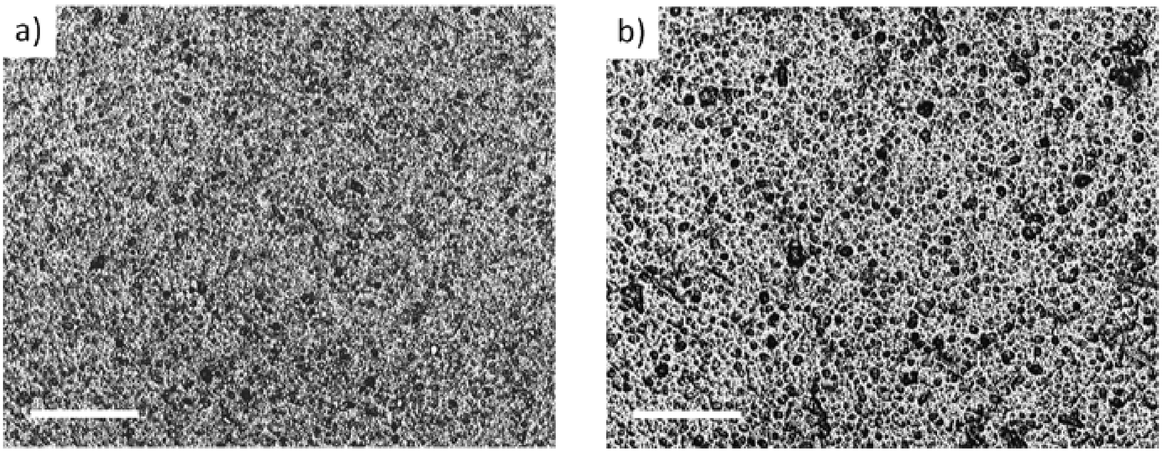

Figure 5.9:
Microscopy images with 10-fold magnification of the thin films (a) with 5 μm titanium(IV) oxide particles (b) with titanium(IV) oxide particles with a particle size distribution smaller than 5 μm. The scale bar indicates 200 μm.

For our experiments, we use P3KHT supplied by Rieke Metals as polymer and rutile titanium(IV) oxide powder with an average grain size of 5 μm by Sigma-Aldrich to produce the hybrid films. For investigations, 0.33 wt% of the water soluble P3KHT is dissolved in deionized water by stirring at room temperature. Three samples are prepared, one containing 0.16 wt% of the 5 μm titanium(IV) oxide particles with a particle, one containing 0.16 wt% titanium(IV) oxide particles with a particle size distribution smaller than 5 μm and one without titanium particles, respectively. Silicon wafers are acid cleaned in a solution of 54 ml deionized water, 84 ml hydrogen peroxide and 198 ml sulforic acid for 15 minutes at room temperature as described previously [3]. A microscopy image with 10-fold magnification of the P3KHT film with 5 μm titanium(IV) oxide particles can be seen in figure 5.9a. The P3KHT film with titanium(IV) oxide

particles with a particle size distribution smaller than 5 μm is shown in figure 5.9b. Both show a homogeneous mixture whereas the second one has a rather coarse distribution.
In order to investigate the internal structure of the samples, time-of-flight neutron reflectometry measurements are performed. [4] The results are shown in figure 5.10 for both, the sample with 5 μm titanium(IV) oxide particles and the sample without particles respectively. The P3KHT curve shows the silicon edge at $q_z = 0.01\mathring{A}^{-1}$ whereas the reflectivity curve for P3KHT with the 5 μm titanium(IV) oxide particles shows the edge at slightly higher $q_z = 0.012\mathring{A}^{-1}$. Data analysis is in progress.

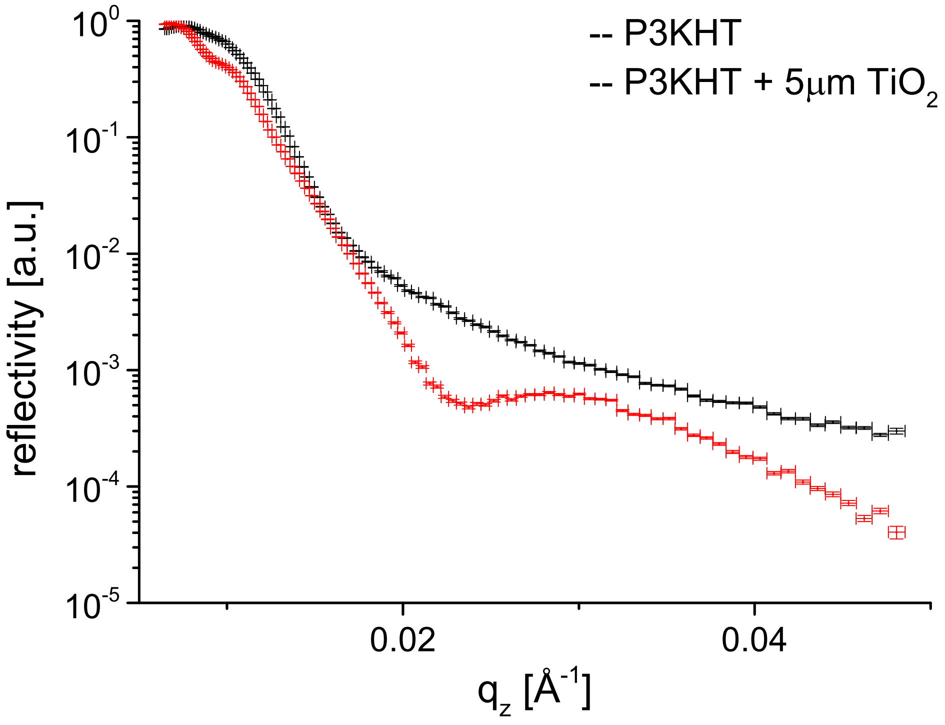

Figure 5.10:
Neutron reflectivity data of a hybrid composite film consisting of P3KHT with 5 μm titanium(IV) oxide particles and pure P3KHT, respectively.

Further investigations will compare photovoltaic performances of the P3KHT and titanium(IV) oxide blends with solid-state dye-sensitized solar cells as described by Snaith et al. [4]. We will use different blend ratios and titanium particles of different sizes. The optical properties will then be studied by UV/Vis spectroscopy. Furthermore we are looking for possibilities to influence the particle size and its distribution, respectively.

[1] B. R. Saunders, *J. Colloid Interface Sci.* **369**, 1-15 (2012)

[2] L. Baeten, B. Conings, J. D'Haen, A. Hardy, J. V. Manca, M. K. Van Bael, *Sol. Energy Mater. Sol. Cells* **107**, 230-235 (2012)

[3] P. Müller-Buschbaum, *Eur. Phys. J. E* **12**, 443-448 (2003)

[4] J. Penfold, *Curr. Opin. Colloid Interface Sci.* **7**, 139-147 (2002)

[5] H. J. Snaith, R. Humphry-Baker, P. Chen, I. Cesar, S. M. Zakeeruddin, M. Grätzel, *Nanotechnology* **19**, 1-12 (2008)

5.6 Morphology evolution of ZnO nanostructures upon solvent vapor treatment

K. Sarkar, J. Perlich[1], P. Müller-Buschbaum

[1] HASYLAB at DESY, Hamburg, Germany

ZnO nanostuctures are synthesized in the present study using a sol-gel technique coupled with the structure directing property of an amphiphilic diblock copolymer, P(S-*b*-4VP) in which a commercial ZnO precursor, i.e. zinc acetate dihydrate (ZAD), has been incorporated. The diblock copolymers respond to the external fields such as temperature and solvent vapor. [1] Among the various morphologies synthesized, the grid-like morphology shown in Fig. 5.11 has been chosen to study the morphological evolution under the influence of tetrahydrofuran (THF) vapor for different annealing times. Solvent annealing is only responsible for the reorganization of the diblock copolymer. Hence, a final calcination step is performed at a high temperature to ensure the effect of solvent annealing on the final ZnO morphology.

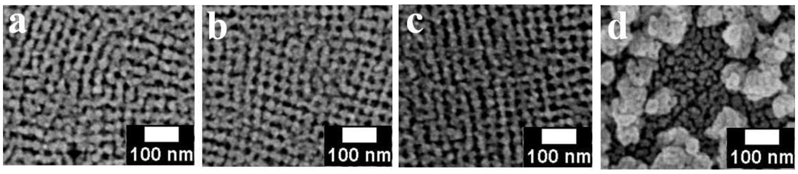

Figure 5.11:
SEM images of calcined ZnO grid-like morphology after THF solvent treatment times of (a) 3 hours (b) 9 hours (c) 12 hours and (d) 48 hours.

As seen from the SEM images of the calcined samples in Fig. 5.11, there is significant difference in the ZnO morphology observed after 48 hours of solvent treatment. Although the SEM images of sample annealed for shorter times look similar, an in-depth investigation is needed to understand the structural evolution going on in the volume of the film. To serve the need, grazing incidence small angle x-ray scattering (GISAXS) has been performed in the P03 beamline of the PETRA III storage ring in HASYLAB, DESY, Hamburg on both the as-annealed and calcined samples. Horizontal cuts at the Yoneda position have been performed from the 2D scattering images (not shown) and are plotted in Fig. 5.12 (a).

All the cuts are analyzed with a model fit (shown as solid lines) considering cylindrical form factor and the structure factor from a one-dimensional paracrystal. A single structure and form factor have been used to fit the data for all the samples. All other peaks in the corresponding curves are due higher orders. It is noteworthy that the best fit with the above mentioned model has been obtained for the sample without any solvent treatment. Whereas, the fit for the same sample after calcination shows a poor agreement in the lower q region, indicating the presence of some defects which are introduced in the sample post calcination giving rise to domains of larger structural length scales in the volume of the films, which are not accessible by SEM. In case of the solvent treated samples, it is observed that the fit using the same model, does not fit so well as for the as-annealed samples. In contrast, for the calcined samples, these defects are healed and the fits obtain are in a good agreement with the data. For the sample with the longest solvent annealing time, a structural collapse is observed which results in the loss of all the higher orders. The resulting fits yield the correlation distance between the objects and the average size of the objects visualized as pore size of the grid in the present case. These values are plotted as a function of annealing time in Fig. 5.12 (b) and (c) to obtain a more quantitative overview of the processes occurring in the volume of the films.

In Fig. 5.12 (b) a reduced correlation distance is observed for all samples after calcinations, which points to shrinkage of the structure due to the removal of the polymer template from the films. After solvent treatment a gradual increase in the pore size is observed, which is seen more

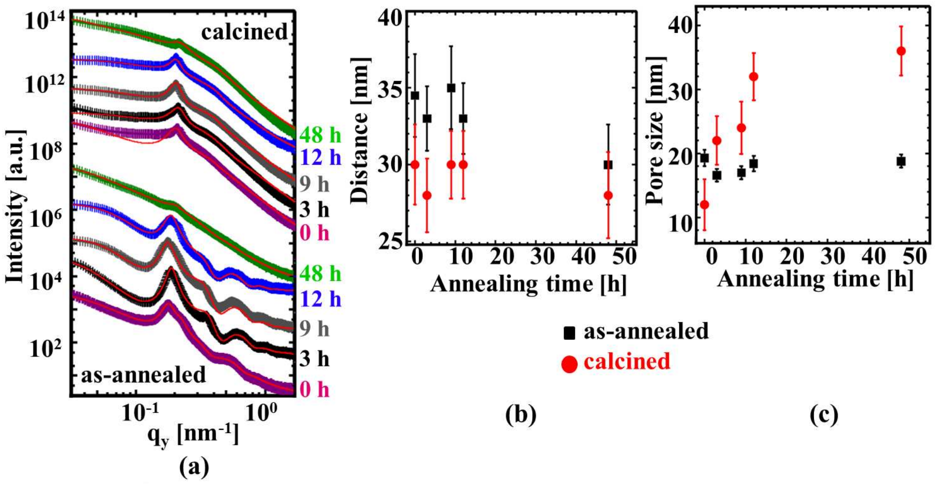

Figure 5.12:
Horizontal cuts shifted along the intensity axis of the 2D GISAXS data at the q_z-value of the Yoneda peak of the spin coated as-annealed and calcined ZnO films for different solvent annealing time scales indicated on the right axis of the graph. The solid lines are the fit to the data (a), average correlation distance (b) and pore size (c) of the objects in the film volume as obtained from the fits for the as-annealed and the calcined samples plotted against different solvent annealing time.

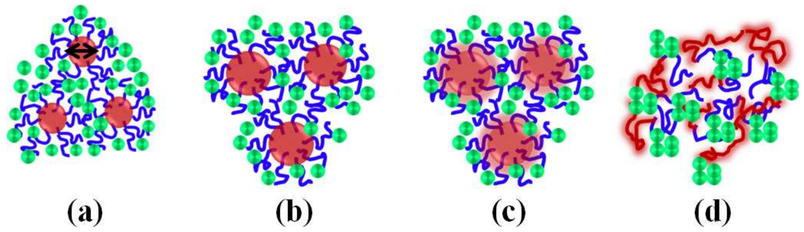

Figure 5.13:
Schematic of structural evolution kinetics upon THF solvent vapor treatment of the ZnO spin coated films after (a) 3 hours (b) 9 hours (c) 12 hours and (d) 48 hours.

prominently for the calcined samples, Fig. 5.12 (c). The mechanism of the structural evolution hence studied by GISAXS is summarized using a schematic representation in Fig. 5.13. In this sketch the red core of the micelle represents the hydrophobic part of the block copolymer template, whereas the blue chains denote the hydrophilic block in which ZAD (depicted by green spheres) is preferably incorporated. THF is chosen so that it is slightly preferable to the PS, the core forming block of the copolymer. Hence, with time the solvent penetrates the shield of ZnO and tries to swell the PS block as a result of which the ZnO in the corona block are pushed away from each other. After calcination, when the copolymer is entirely removed from the system, the ZnO network is left behind with increasing pore size upon increasing the solvent treatment time. However, if the solvent treatment is carried out for sufficient long time, the PS block is fairly dissolved, resulting in a collapse of the micelle structure and thereby forming ZnO aggregates as also observed from the SEM images. Hence, the solvent treatment plays an important role in deciding the morphology of the final ZnO films synthesized by a suitable diblock copolymer.

[1] T. H. Kim, J. Huh, J. Hwang, H. -C. Kim, S. H. Kim, B. -H. Sohn, C. Park, *Macromolecules* **42**, 6688-6697 (2009)

5.7 Effect of high temperature annealing and UV irradiation on zinc oxide nanostructures

N. Paul, M. Niedermeier, K. Sarkar, C. Palumbiny, J. Perlich[1], A. Paul[2], P. Müller-Buschbaum

[1] HASYLAB at DESY, Hamburg, Germany
[2] Physics Department E21, TUM, Garching, Germany

Zinc oxide is a II-VI compound semiconductor having a direct band gap of 3.37 eV. As it has a large exciton binding energy of 60 meV, it yields high UV emission at room temperature. Due to its unique optical and electronic properties, it has attracted extensive fundamental research interest and is used in several technological applications such as photovoltaics, light emitting diodes, piezoelectric devices and spintronics. [1] In the photovoltaic industry, it is used as an anti-reflection window, a textured active part of the p-n-junction, or a hole blocking layer. Each of these applications requires different structural morphologies of the ZnO to work effectively. For example, as an active n-type semiconductor, a high surface-to-volume ratio is necessary for an effective charge separation, which takes place at the p-n type interface. In this application, larger structures are also necessary to enhance light harvesting properties. On the other hand, as a hole blocking layer, the ZnO film morphology should be homogeneous, dense and well connected.

We report on the effect of different post-treatments on the structural morphology of ZnO nanostructures synthesized by sol-gel technique. Structural templating is also attempted by block copolymer micro-phase separation process. In the present investigation, Pluronic F127, having a molecular weight of 12,600 daltons, is used as the structure directing agent. Pluronic F127 is a triblock copolymer of poly(ethylene oxide) (PEO) and poly(propylene oxide) (PPO) with an approximate molecular formula $(PEO)_{100}$ $(PPO)_{70}(PEO)_{100}$.

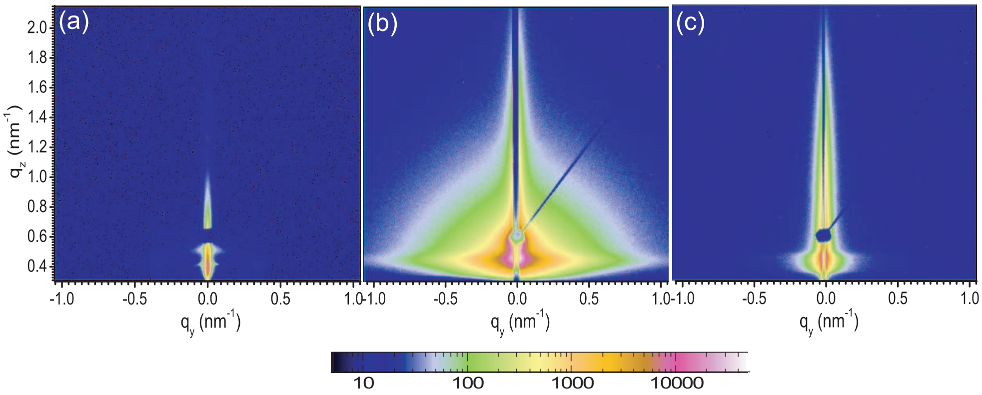

Figure 5.14:
2D GISAXS data of the (a) as-prepared, (b) calcined and (c) UV irradiated samples with ZnO morphologies. The circular beamstop is installed to shield the specular peak. The intensity scale bar for all the images is the same as shown at the bottom.

The triblock copolymer is dissolved in a good-poor solvent pair, containing hydrochloric acid and ethanol to induce micro-phase separation. To this solution, the zinc acetate precursor solution is added and the sol-gel process starts. The solution is kept at 50 ° C under constant stirring for 3 hours. After this time, the nanocomposite solution is transferred to a substrate via spin-coating. The thin film is aged for 2-3 days in a constant humidity chamber to allow a controlled evaporation of the solvent from the film. One of these films is furnace annealed (FA) / calcined at 450 °C for one hour. Recently, Nilsson et al. reported that a 24 h UV light treatment to a

similar synthesis procedure can be used to achieve similar results as a calcination treatment at high temperatures, in case of titania. [2] Therefore, we subjected a second film to UV irradiation in a closed chamber for 2 days to see if a similar effect can also be seen for ZnO.
To probe the inner morphologies of the ZnO films, grazing incidence small angle X-ray scattering (GISAXS) measurements were carried out at beamline BW4 at HASYLAB in Hamburg. The as-prepared sample shows a well-defined narrow structure as shown in Fig. 5.14. The calcined sample shows a broad structure which indicates a distribution over different length scales of the structures in the films compared to the as-prepared sample. For UV irradiated samples, the structures collapse.
In order to quantify the information about the structures installed in the sample plane, horizontal line cuts of the 2D GISAXS data are performed at the characteristic q_z value, corresponding to the observed Yoneda peak position. The horizontal cuts for as prepared, calcined and the UV irradiated samples are shown in Fig. 5.15. The horizontal cut for the as prepared sample show a prominent structure factor peak. However, after calcination, there is a broadening of the structural peak indicating a distribution over different length scales of the structures in the films. After UV treatment, no structural peak can be seen.

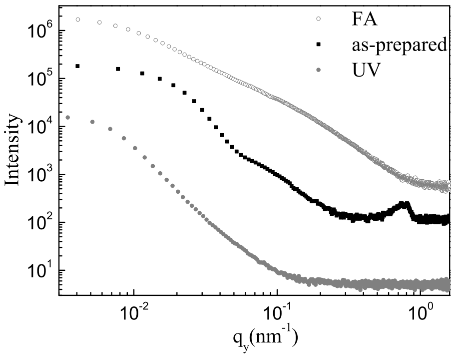

Figure 5.15:
Horizontal line cuts of the 2D GISAXS data at the q_z-value of the Yoneda peak of the spin coated ZnO films for as-prepared (squares), calcined (hollow circles) and UV irradiated (filled circles) samples with ZnO morphologies. All the data are shifted along the intensity axis for clarity.

Moreover, the crystallinity differs for the different post-treatment protocols as well. The x-ray diffraction (XRD) patterns of the calcined and UV irradiated sample are shown in Fig. 5.16. The observed diffraction peaks for the calcined sample is in agreement with those of the hexagonal polycrystalline ZnO with wurtzite structure. No peaks of any other phase were detected. In contrast, the XRD pattern of the UV irradiated sample shows peaks which do not correspond to hexagonal ZnO with wurtzite structure.

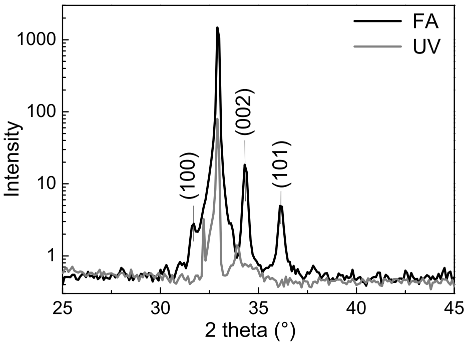

Figure 5.16:
XRD data of the calcined (black) and UV irradiated (gray) samples. The observed diffraction peaks for the calcined sample corresponds to the hexagonal polycrystalline ZnO with wurtzite structure.

[1] J. Huang, Z. Yin and Q. Zheng, *Energy Environ. Sci.* **4**, 3861-3877 (2011)

[2] E. Nilsson, Y. Sakamoto, and A. E.C. Palmqvist, *Chem. Mater.* **23**, 2781-2785 (2011)

5.8 Dispersions of polymer-modified carbon nanotubes: A small-angle scattering investigation

A. A. Golosova, J. Adelsberger, A. Sepe, M. Niedermeier, P. Lindner[1], S. S. Funari[2], R. Jordan[3,4], C. M. Papadakis

[1] Institut Laue-Langevin, Grenoble, France
[2] HASYLAB at DESY, Hamburg, Germany
[3] TU München, Department Chemie, Garching, Germany
[4] TU Dresden, Department Chemie, Dresden, Germany

Nanocomposites from carbon nanotubes (CNTs) display interesting mechanical properties. However, mixing of CNTs with polymers requires strong mechanical forces and, in many cases, agglomeration is observed at later times. Chemical modification of CNTs with polymers has been found to improve the dispersibility of CNTs in polymers [1].

We have used self-initiated photografting and photopolymerization to form stable polystyrene (PS) grafts on single- (SW) and multi-walled (MW) CNTs. The effect of modification on the structure and agglomeration behavior of the CNTs in solution was studied using small-angle neutron and X-ray scattering (SANS, SAXS) [2]. Whereas SAXS gives overall information, SANS together with the use of deuterated solvents highlights the polymer shells or the CNTs. The focus was on the influence of the polymerization time, i.e. the amount of grafted PS on both SW and MWCNTs.

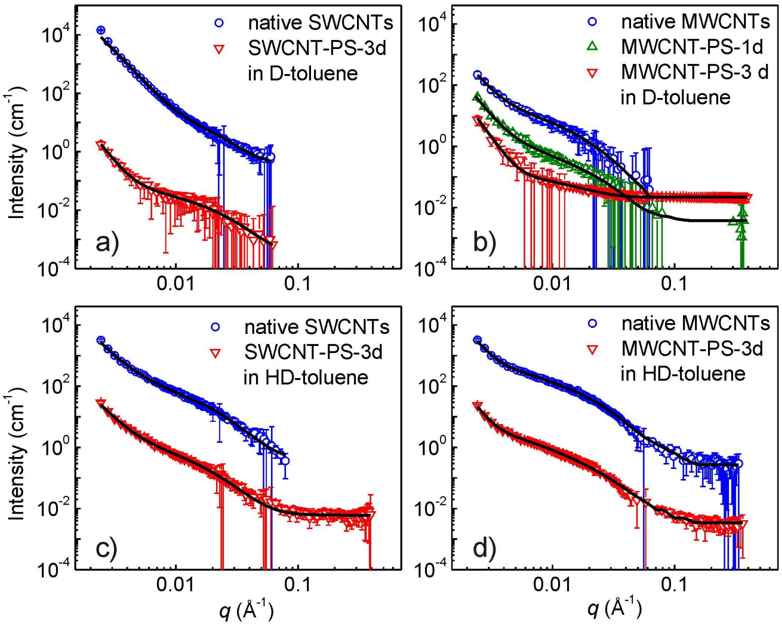

Figure 5.17: SANS curves in D-toluene (a,b) and in HD-toluene (c,d) at 0.5 mg/ml. The lines are model fits. The curves were shifted vertically.

Dispersions of SW and MW CNTs modified with PS grafts for 1 or 3 days and of native SW and MWCNTs were prepared by ultrasonication in toluene. Measurements were started immediately at D22, ILL, or at beamline A2, HASYLAB at DESY. SANS experiments were carried out in a wide range of momentum transfers q, whereas SAXS revealed details of the local structures at high q-values. In SANS, the polymer shell or the bare CNTs were highlighted by using deuterated toluene (C_7D_8, D-toluene) or the mixture C_7D_8/C_7H_8 =11/89 vol.% (HD-toluene) as a solvent. Representative curves are shown in Fig. 5.17. Modelling was carried out assuming fractal aggregates of homogeneous cylinders (SWCNTs) or hollow cylinders (MWCNTs) (Fig. 5.18a,b). Fitting parameters were the inner and outer cylinder radii, the cylinder length resp. the mesh size, the agglomerate size and the scattering length densities.

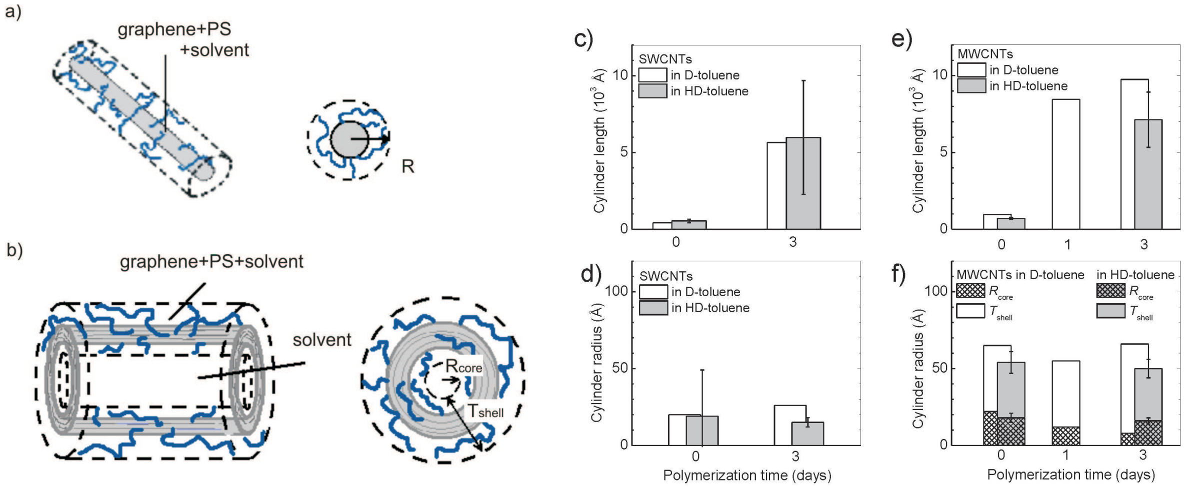

Figure 5.18:
Left: (a) Homogeneous cylinder model for the modified SWCNTs and (b) core-shell cylinder model for the modified MWCNTs. Right: Cylinder dimensions in dependence on polymerization time. Length of the SWCNTs (c) and MWCNTs (e). Cylinder radius of the SWCNTs (d). Core radius and shell thickness of the MWCNTs (f).

In spite of the poor statistics due to the very low CNT concentrations and of the broad distributions of the CNTs' dimensions, good fits (Fig. 5.17) and a consistent set of parameters could be obtained (Fig. 5.18c-f). The fractal dimension turns out to be 3 in all cases, and the aggregate size remains at ca. $10^4 - 10^5$ Å, i.e. the CNTs stay agglomerated in the dispersion with unchanged agglomerate size. Nevertheless, on smaller length scales, the PS modification does affect their dispersion ability: The length of the cylindrical segments increases significantly for all samples (Fig. 5.18c,e), i.e. the mesh size in the fractal aggregate increases significantly. The aggregates are thus much more loosely packed for the PS-modified CNTs than in the native ones.

Moreover, in D-toluene, changes in the core and shell radii of the modified MW CNTs are observed compared to the native ones (Fig. 5.18d,f). For instance, for MW CNTs modified for 3 days, the shell thickness is with 58 Å larger than for the native MWCNTs (43 Å) which is due to the PS grafts. The core radius of the MWCNTs is 18.0-19.5 Å. From these values together with the known number of graphene layers in the MWCNT, we conclude that the thickness of the PS shell is 10-20 Å upon modification for 3 days. The core radius decreases, i.e. PS grafts are also present inside the CNT. The (modified) SWCNTs are found to form ropes consisting of several CNTs. For all samples, the CNT dimensions together with the scattering length densities and the weight fractions of PS from thermogravimetric analysis, the thickness of the graphene layers could be determined.

The SAXS curves could be fitted by the model curves as well, however, deviations indicate that the model is too simple to describe small-scale features. To conclude, SANS and SAXS experiments gave detailed insight into the structures of PS-modified and native SW and MW CNTs in toluene. The modification of the CNTs with PS grafts results in thicker PS shells along with a significant increase of the mesh size of the aggregates.

The project has been funded by the International Graduate School of Science and Engineering (IGSSE).

[1] M. Burghard, K. Balasubramanian, *Small* **1**, 180-192 (2005)

[2] A. A. Golosova, J. Adelsberger, A. Sepe, M. A. Niedermeier, P. Lindner, S. S. Funari, R. Jordan, C. M. Papadakis, *J. Phys. Chem.* **116**, 15765-15774 (2012)

5.9 Dynamic study of metal nanoparticle growth on solid surfaces

E. Metwalli, V. Körstgens, K. Schlage[1], S. V. Roth[1], R. Röhlsberger[1], P. Müller-Buschbaum

[1] HASYLAB at DESY, Hamburg, Germany

The growth of metal films on solid supports has crucial consequences on the structure and physical properties of the film. Therefore, manipulating the film growth by controlling the growth conditions is an effective pathway to control the film properties for many potential applications. In order to understand and eventually manipulate such properties, one must first be able to characterize the film structures as a function of film formation. In situ grazing incidence small-angle x-ray scattering (GISAXS) is an excellent approach to investigate metal growth on solid surfaces and enables real time observation of the nanoparticles formation/growth and hence it can yield insight into the underlying film formation mechanisms.

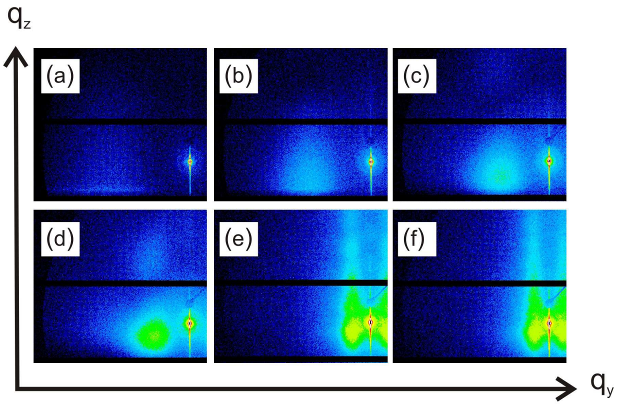

Figure 5.19:
Composite image showing selected 2D GISAXS images during gold sputtering on silicon surface at different sputtering time viz. a) 6, b) 10.5, c) 15, d) 22.5, e) 90, and f) 150 *s*. In about 150 *s*, we have collected 10000 images while Au is deposited on the surface in a real time mode. With increasing the sputtering deposition time a side scattering peak appears and moves inwards towards the in-plane scattering (q_y = 0). The intensity of the overall scattering pattern increases with increasing the metal upload. Also one observes that the scattering peak is initially very broad and gets narrower upon further metal upload.

In the present investigation we used the DC sputtering technique [1-4] to investigate the deposition of Au metal onto two energetically different surfaces, namely hard (silica) and soft (polystyrene thin film) surfaces. Utilizing a portable DC magnetron sputtering deposition system mounted at a GISAXS beamline, we have investigated the formation and growth kinetics of Au nanoparticles on these surfaces. The deposition was performed at an argon pressure of 1.6 x 10^{-2} mbar and at a rate of 11.6 nm/min. The in situ GISAXS measurements were carried out at beamline P03 of PETRA-III storage ring at HASYLAB (DESY, Hamburg). The sample inside the sputtering chamber was placed horizontally at an incidence angle α_i = 0.5° to the incidence x-ray beam. The incidence angle is well above the critical angle of both the polymer film and the silicon substrate (α_c(PS) = 0.154°, α_c(Si) = 0.22°). GISAXS 2D images were collect with a noise-free high resolution Pilatus-300k detector in a real time mode every fifteen-milliseconds (Fig. 5.19).

As seen in Fig. 5.20, the metal particles characteristic peak shifts along the q_y direction towards lower values as a function of time for both the silicon and the homopolymer film. The side-peak intensity is increasing with time because of the high scattering power of the metal atoms. The latter peak is a characteristic of the inter-particle distance as a function of metal load. Eventually, under the same sputtering conditions the metal particle migration seems to be much faster on the silicon substrate compared with the polymer film as indicated by the slope of the q_y decay with time. For both surfaces, the metal growth is much slower at time larger than 30 *s* that corresponds to time after a quasi uniform film layer formation. From FWHM of these characteristic metal peaks, the particle size distribution is found to be much broader on the homopolymer PS film compared with the silicon substrate (data not shown). From these results it is obvious that the adatom migration on the substrate surface is one of the most important mechanisms that control the film growth. As the metal atoms arrive at the substrate surface, they migrate on the surface and when two of them are near neighbors, they form a stable nucleus and remain on the surface. If an atom does not combine with another one, it evaporates back in the gas phase instead. With increasing the metal upload on the surface, many random nucleation sites are formed. When the distance between the two neighboring islands are less than the diffusion length of the atoms on the substrates, the density of nuclei reaches saturation. After that, all arriving adatoms are captured by the islands either directly or after diffusion along the substrate surface to minimize their energy. The three dimensional growing of the islands with increasing the metal upload would lead to forming cap-shaped clusters. With a neck between two clusters, the coalescence process is followed by neck growth and a physical continuity of the metal film is created. As a conclusion, the in situ real time GISAXS investigation is essential for understanding how the metal layer growth correlates with the surface energy of solid support.

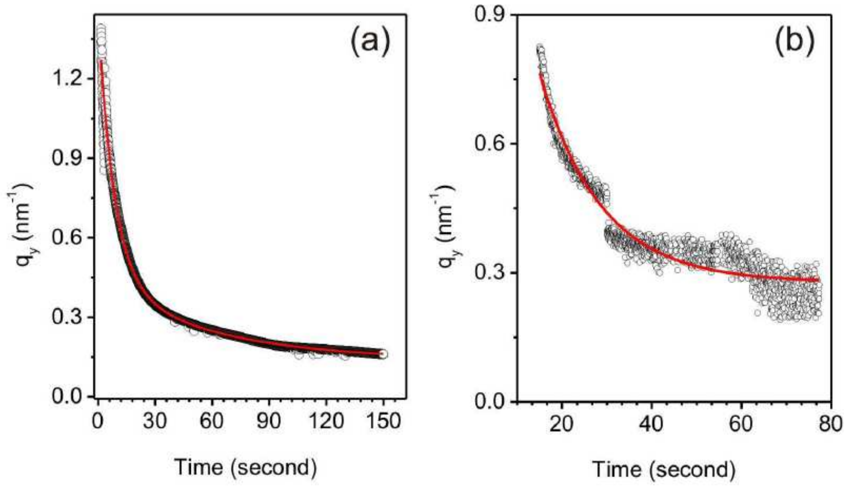

Figure 5.20:
The time evolution of the position of the primary GISAXS side-peak along the q_y direction as quantitatively determined using Lorentzian function with the help of the software package DPDAK on both pre-cleaned silicon surface (a) and on the thin polystyrene film (b).

[1] E. Metwalli, S. Couet, K. Schlag, R. Röhlsberger, V. Körstgens, M. Ruderer, W. Wang, G. Kaune, S. V. Roth, P. Müller-Buschbaum, *Langmuir* **24**, 4265-4272 (2008)

[2] T. Diederich, S. Couet, R. Röhlsberger, *Phys. Rev. B* **76**, 054401 (2007)

[3] A. Buffet, M. M. Abul Kashem, K. Schlage, S. Couet, R. Röhlsberger, A. Rothkirch, G. Herzog, E. Metwalli, R. Meier, G. Kaune, M. Rawolle, P. Müller-Buschbaum, R. Gehrke, S.V. Roth, *Langmuir* **27**, 343-346 (2011)

[4] G. Kaune, E. Metwalli, R. Meier, V. Körstgens, K. Schlage, S. Couet, R. Röhlsberger, S. V. Roth, P. Müller-Buschbaum, *ACS Appl. Mater. Interfaces* **3**, 1055-1062 (2011)

5.10 Temperature effects on the kinetics of metal nanoparticle growth on polymer films

S. Brunner, E. Metwalli, J. Perlich[1], S. Yu[1], G. Santoro[1], S. V. Roth[1], P. Müller-Buschbaum

[1] HASYLAB at DESY, Hamburg, Germany

Metal-polymer interfaces play a key role for many important applications such as solar cells and energy storage devices. Analysis of the formation of metal layers on polymer surfaces is crucial for the understanding of these interfaces. In the present report, the deposition, formation and growth of metal nanoparticles on thin polymer films is observed in real-time utilizing in situ grazing incidence small angle X-ray scattering (GISAXS). Temperature and metal source are varied to investigate their influence on growth rate and growth mechanism.

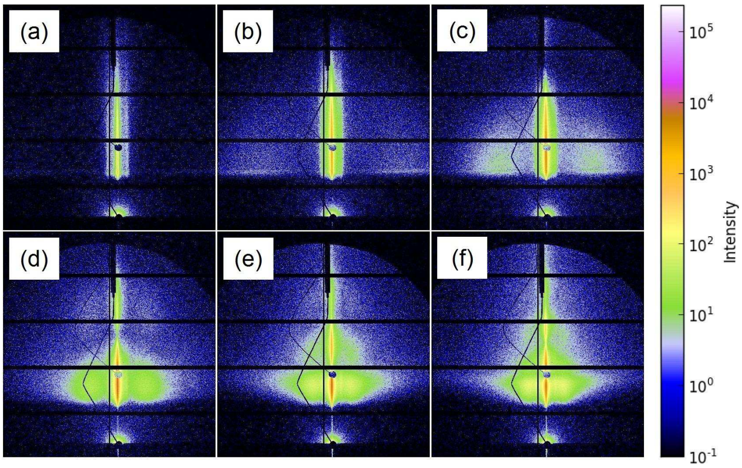

Figure 5.21:
Selected 2D GISAXS data taken during in situ sputter deposition of gold on P(S-*b*-B) DBC at sputtering times of (a) 10, (b) 50, (c) 100, (d) 200, (e) 400 and (f) 600 *s*, respectively. With increasing sputtering time, while an increasing load of Au is deposited on the polymer surface, the intensity of the scattering pattern increases. A side peak can be observed that moves with increasing metal load towards the $q_y = 0$ position.

Thin films (60 nm) of poly(styrene-*block*-butadiene) diblock copolymer (DBC), with a number average molar mass of M_n =88 kg/mol and a polydispersity of M_w/M_n =1.19, were prepared by spin coating. The molar fraction of the polystyrene block $f_{(PS)}$ =31.8% suggests the formation of a cylindrical morphology with a periodic distance of approximately 50 nm (calculated according to GISAXS data). In situ GISAXS utilizing the DC sputtering technique [1-2] allowed the investigation of the formation and growth of metal nanoparticles on thin polymer films at different temperatures. The measurements were performed at beamline P03 of the PETRA storage ring at HASYLAB (DESY, Hamburg) and were carried out for Au and Ag, each at room temperature and at approximately 70 $°C$. It has to be stated that the temperature in the sputtering chamber could be kept constant only to a low extent and fluctuated in the range of $+/-5\ °C$. The sputter deposition occurred in argon atmosphere at a pressure of 1.5×10^{-2} mbar for a total time period of 600 s and 1000 s for Au and Ag, respectively. For data acquisition, 0.095 s time-scale 2D GISAXS images were collected in real-time using a noise-free Pilatus 1M detector (see Fig. 5.21). From these data, one can observe a side peak that appears and grows in intensity with increasing sputter time. The q_y position of this side peak is a measure for the inter-particle distance. Therefore its migration with increasing metal load provides information on the characteristics of metal particle growth and layer formation. To determine the impact of temperature on the metal deposition, the position of the primary side peak has been determined by fitting Lorentzian functions to the peaks in the out-of-plane cuts (along q_y direction). The evolution of the peak position with sputter time is shown in Fig. 5.22. The initial slope of the decay with time is steeper for higher temperatures, which indicates faster metal particle migration and film growth. This observation is backed-up by fitting of the curves using a exponential decay function of second order. Large decay constants for the high temperature deposition process are observed, 18% and 22% larger compared to the room temperature deposition process for Au and Ag, respectively. After approximately 200 seconds, the metal growth becomes significantly slower and reaches saturation in a similar way for room temperature as well as for higher temperatures. At this time, a uniform metal layer has already been formed. The observed behavior is qualitatively the same for both silver and gold, while the peak position decay slope is generally much steeper for silver deposition compared to gold. These results show that increased temperature leads to enhanced kinetics of metal particle assemblies and faster metal film growth on polymer surfaces. This can be explained by faster migration of metal atoms on the surface due to their higher internal energy. However, the basic growth mechanism of nucleation and layer formation seems to be largely unaffected, as the general behavior and shape of the out-of-plane cuts and the resulting peak position over time graphs are very similar for all regarded temperatures. As a conclusion, the growth of metal films on polymer surfaces can be affected by increased temperature in terms of faster kinetics. The effect of temperature during the sputter deposition step on the film properties is yet to be investigated.

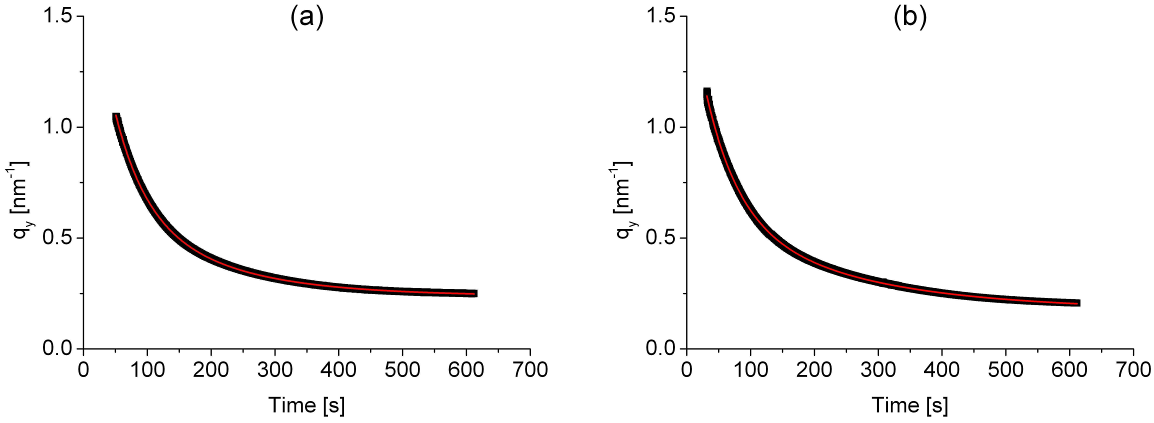

Figure 5.22:
q_y position of the primary side peak and its evolution with increasing sputtering time as determined by fitting of Lorentzian functions using the software package DPDAK. The selected graphs represent gold on P(S-*b*-B) DBC at room temperature (a) and approx. 70 $^\circ C$ (b). The lines are the exponential fits to the data points.

[1] E. Metwalli, S. Couet, K. Schlage, R. Röhlsberger, V. Körstgens, M. Ruderer, W. Wang, G. Kaune, S. V. Roth, P. Müller-Buschbaum, *Langmuir* **24**, 4265-4272 (2008)

[2] T. Diederich, S. Couet, R. Röhlsberger, *Phys. Rev. B* **76**, 054401 (2007)

5.11 IsGISAXS simulation of gold growth on spiro-OmeTAD

W. Lu, M. A. Niedermeier, P. Müller-Buschbaum

Deposition of the metal electrode to contact the cell with a load is the final and an important step in the production of a hybrid solar cell. Commonly, the metal is directly deposited on the polymer surface and as a consequence a polymer-metal interface is established. The quality of this interface influences not only the transported of electrons and therefore the solar cell performance, but also the surface adhesion of the cathode and therefore its stability.

Two points are important for the interface characteristics: 1) the growth behavior of the metal layer on the polymer surface and 2) the interaction between the polymer and the metal. In the present investigation we focus on the structural development of the metal on the polymer surface. We have used grazing incidence small angle x-ray scattering (GISAXS) to observe the development of the metal layer. In addition to a high surface sensitivity, GISAXS enables us to gain information about the inner structures, hidden inside the thin film. As GISAXS is non-destructive, GISAXS is a suitable method to follow the structural development in-situ. From a thorough analysis of the scattering data we get detailed structural parameters which describe the growing metal film, such as shapes, sizes and arrangement. From the temporal evolution of these parameters we can derive growth laws for the metal layer.

The GISAXS measurements were performed at the BW4 beamline of the DORIS III storage ring at HASYLAB/DESY in Hamburg. The selected wavelength was set to 0.138 nm. The Instrument is normally used in transmission geometry. With the installation of a two-circle goniometer with a z-translation table we employed a reflection geometry to realize diffuse x-ray scattering under the conditions of small angel scattering with a set-up of high quality entrance slits and a completely evacuated pathway. The beam divergence in and out of the plane of reflection was set by two entrance cross-slits. The scattered intensity was recorded with a 2-dimensional detector which has a 512×512 pixel resolution. A sample-detector distance of 2.7 m was chosen to resolve large in-plane structures. At the fixed incident angle of 0.487°, the two-dimensional intensity distribution can be cut in several vertical and horizontal slices with respect to the sample surface. These cuts are called in-plane cut and out-of-plane cut respectively.

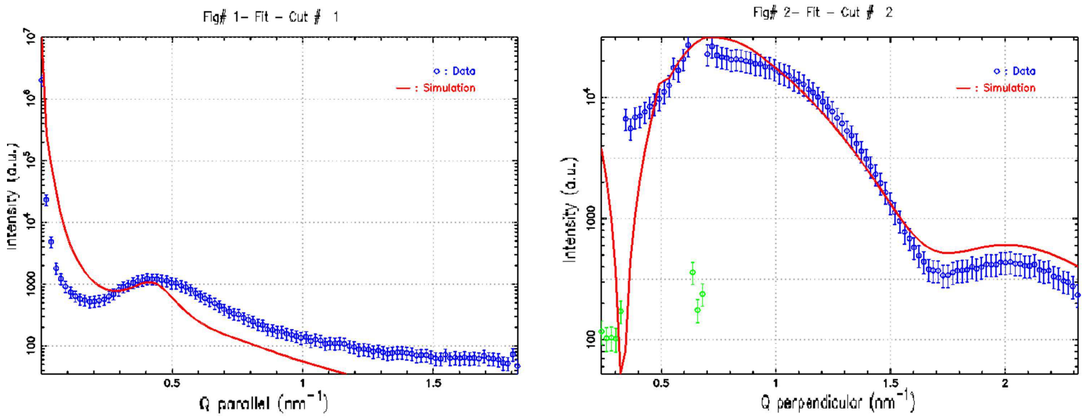

Figure 5.23: left: out-of-plane cut; right: in-plane cut

In Fig. 5.23 the in-plane cut and the out-of-plane cut for the example of a sputter time of 90 seconds is shown. The out-of-plane cut was taken at maximum intensity and the in-plane cut was taken at $q_y = 2.85 \times 10^{-5} \AA^{-1}$ correspond to $\Psi = 0.0004^\circ$.

Modeling is done with the software package IsGISAXS. Different models for the metal particles were tested to gain the level of agreement between data and simulation as shown in Fig. 5.23.

In selecting the model we were guided by scanning electron microscopy (SEM) data. The 2D model from the SEm data was translated into a potential 3D model for the GISAXS data (see Fig. 5.24). It turned out that only one type of metal particle on the polymer surface was not sufficient to explain the GISAXS data. Thus a second particle type (full-spheroid) was added to the first one (cylinder).

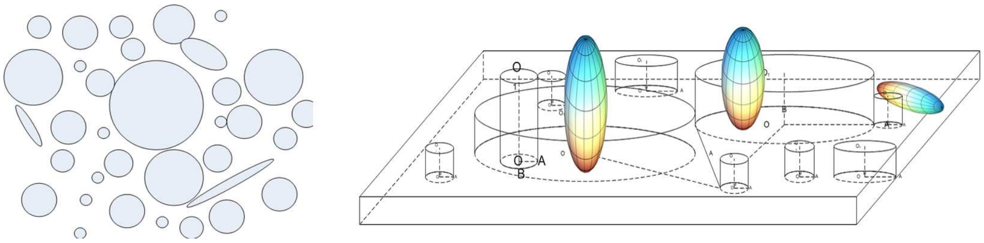

Figure 5.24: left: 2D model from SEM; right: used 3D model with 2 particles

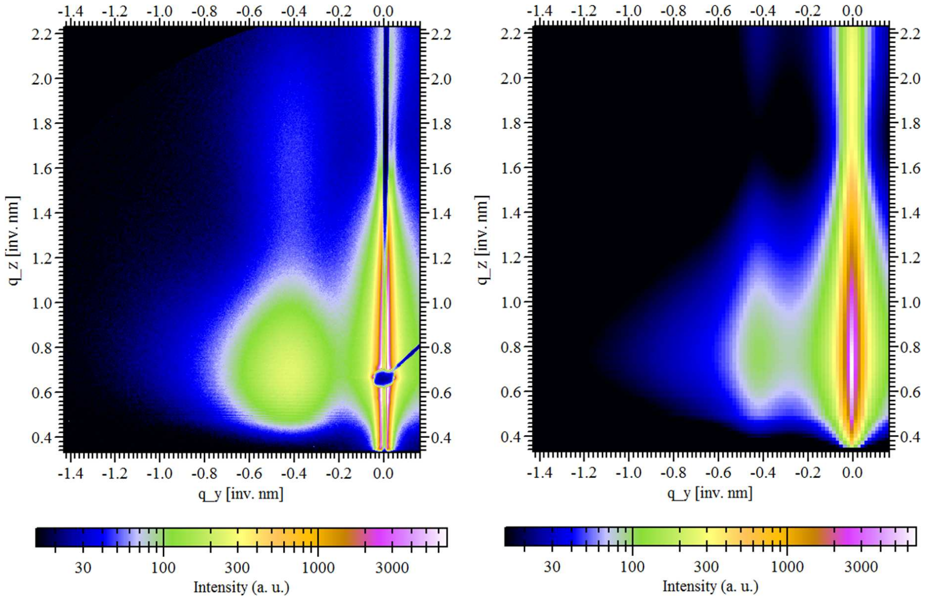

Figure 5.25: left: measured 2D GISAXS data; right: modeling using IsGISAXS

Finally, with the parameters the full 2D GISAXS data sets have been simulated. An example is shown in Fig. 5.25. The parameters of the simulation are summarized in table 1 .

particle type	full spheroid	cylinder
frequency	1	9
radius (nm)	5	40
Distribution	Gaussian	Gaussian
SigmaR/R	0.5	0.5
Height/R	0.95	0.1
Width	2	2
Peak position D (nm)	13.2	
Wide (nm)	3.7	

Table 1: List of parameters used in IsGISAXS simulation

5.12 Early stages of gold nanoparticle attachment to polyelectrolyte surfaces investigated with a combination of micro-fluidics and GISAXS

V. Körstgens, M. Philipp, N. Paul, D. Magerl, S. V. Roth[1], P. Müller-Buschbaum

[1] HASYLAB at DESY, Hamburg, Germany

Grazing incidence small angle x-ray scattering (GISAXS) in combination with a special designed micro-fluidic cell offers wide-spread opportunities for the investigation of nanostructures at the solid-liquid interface [1, 2]. With the micro-focusing of a highly brillant x-ray beam of a third generation synchrotron source the kinetics of growth and attachment processes of nanostructures are accessible. In the present study a beamsize of 10 μm x 8 μm has been chosen as at the incident angle of 0.45° the footprint of the beam matches the width of the micro-fluidic channel of 1 mm. The attachment of negatively charged gold nanoparticles of 10 nm diameter to different polyelectrolyte layers is probed.

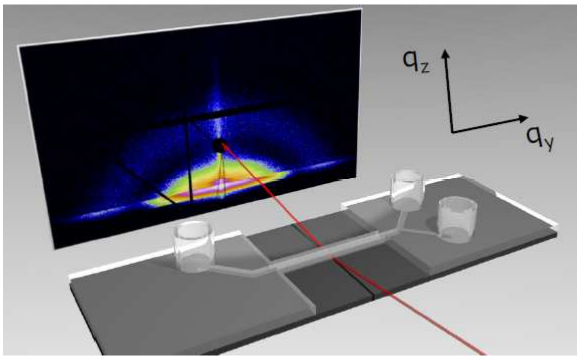

Figure 5.26:
GISAXS set-up with micro-fluidic cell. In the sketch the incoming x-ray beam (in red) is specularly reflected. Within a micro-fluidic experiment the cell is scanned in the x-ray beam.

In Fig. 5.26 the general set-up of a micro-fluidic GISAXS experiment is shown. The scattering pattern on the 2D plane for a flow experiment with 0.02 ml min^{-1} gold nanoparticles attaching to a positively charged polyelectrolyte film. Films have been produced by subsequential dipping of acid cleaned silicon into polymer solutions as described by Paul et al. [3].

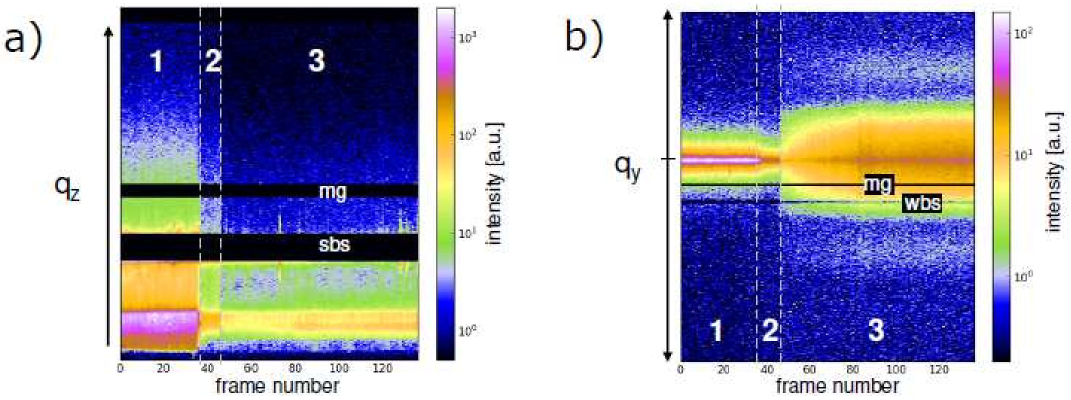

Figure 5.27:
Attachment of gold nanoparticles to positively charged polyelectrolyte surface: a) composite image of vertical (detector) cuts for 140 consecutive frames scanning the micro-fluidic channel, regions without scattered intensity are marked "sbs" for specular beamstop and "mg" for the inter module gap of the Pilatus detector; b) composite image of out-of plane cuts, line marked with "wbs" with reduced intensity due to shadowing of the wire holding the direct beamstop. White numbers in both composite images indicate regimes in the micro-fluidic experiment as explained in the text.

For a positively charged polyelectrolyte layer represented by poly(allylamine) hydrochloride composite images of vertical (detector) cuts and horizontal cuts are shown in Fig. 5.27a) and 5.27b) for a micro-fluidic experiment. As the initially dry channel is filled with nanoparticle dispersion with 0.02 ml min^{-1} the micro-fluidic cell is scanned through the micro-sized x-ray beam. Three different regimes can be distinguished in the experiment. 1) the scattering pattern of the dry film, 2) a pre-cursor of liquid wets the surface and 3) the channel is completely filled and the attachment process of nanoparticles can be followed. The transition from region 2 to 3 due to the decrease of intensity by absorption of the dispersion filled channel is sharp and serves as a reference point. Because the flow velocity as well as the scanning velocity in opposite direction are known, for each position along the micro-fluidic channel the contact time with the nanoparticle dispersion can be assigned. In the horizontal cuts (Fig. 5.28a) an increase in intensity of a peak originating from the form factor of spheres (marked with black arrow in Fig. 5.28a is observable. The onset of nanoparticle attachment after complete filling of the channel is marked with a green arrow. For clarity the scattering curves of several measurements have been added up in Fig. 5.28a. In Fig. 5.28b a comparison of the early stages of nanoparticle attachment to positively and negatively charged surface (represented by poly(styrenesulfonate)) is given with peak intensities extracted from the individual scattering curves.

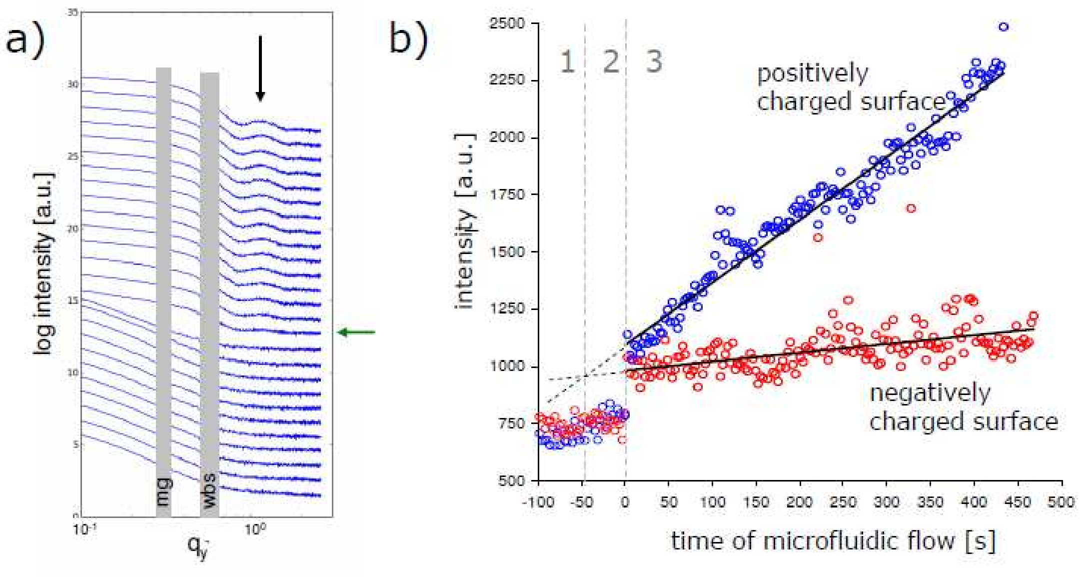

Figure 5.28:
a) Out of plane cuts for in-situ micro-fluidic experiment attachment to positively charged surface and b) peak intensities as obtained from the GISAXS measurement. The time gives the individual contact time with nanoparticle dispersion as explained in the text. The attachment of particles to positively charged surface (blue circles) is compared to the attachment to a negatively charged surface (red circles).

This work has been financially supported by the BMBF (grant number 05K10WOA).

[1] J.-F. Moulin, S. V. Roth, P. Müller-Buschbaum, *Rev. Sci. Instrum.* **79**, 015109 (2008)

[2] E. Metwalli, J.-F. Moulin, J. Perlich, W. Wang, A. Diethert, S. V. Roth, P. Müller-Buschbaum, *Langmuir* **25**, 11815-11821 (2009)

[3] N. Paul, A. Paul, R. Steitz, M. Kreuzer, M. C. Lux-Steiner, *J. Phys. Chem. B* **116**, 4492-4499 (2012)

5.13 Tack of different metals in contact with the pressure sensitive adhesive poly(etyhlhexyl-stat-methylmethacrylate)

G. Gümüssoy, M. Schindler, P. Müller-Buschbaum

Pressure sensitive adhesives (PSAs) are still spreading to more and more fields of application due to their superiority compared to other joining methods. The established bonds are of low weight and cheap in production. Moreover, they also allow for residual-free removal and high bonding energies compared to the force needed to establish the bond. Furthermore many different kinds of materials can be joined using PSAs, such as paper, wood, metal, glass and many more. The class of adhesives under study is for example used in vibration damping and noise abatement techniques in the aircraft industry. [1]

In this study, the adhesive performance of different metals in contact with the well-established PSA poly(ethylhexyl-stat-methylmethacrylate) is investigated. The strength of an adhesive bond is affected by many different influences. Diethert et al. have shown that the PSA at hand establishes enrichment layers depending on its preparation and its environment, which severely affect the performance of the adhesive. [2] The near-surface compositional evolution in this statistical copolymer has also been investigated by Schindler et al., where a complete inversion of the initial composition was shown. [3] Not only the adhesive itself, but also the adherent's properties play an important role. In the present study we focus on different metals. The surface energy of the different metals was determined, being a crucial component for the wetting behavior during the contact of adherent and adhesive. For these measurements the Owens-Wendt-technique was applied, where the contact angles of small droplets of liquids with different polar and dispersive contributions is monitored over time. [4] Fig. 5.30 shows Owens-Wendt plots for aluminum, stainless steel and titanium from which the polar and dispersive parts of the surface energy can be extracted.

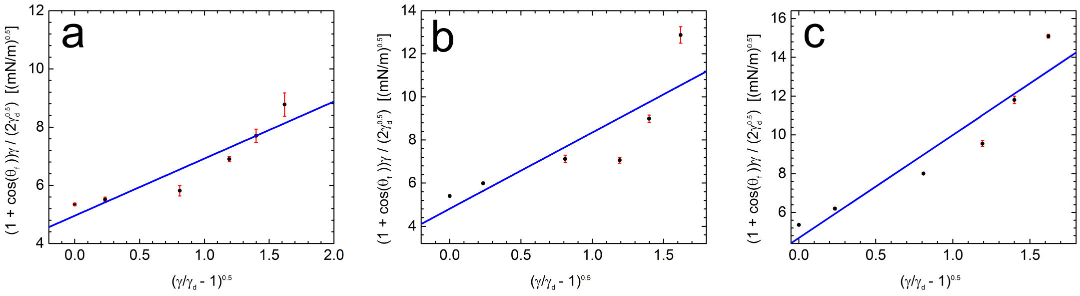

Figure 5.29:
Owens-Wendt plots for different metals: a) aluminum, b) stainless steel, c) titanium. The slope and intersection of each fit represent the polar and dispersive surface energy, respectively.

The method of choice to address the adhesive properties of PSAs is the well-established tack measurement. A metal punch, representing the adherent, approaches the adhesive film until full contact is reached. As soon as a defined force is applied to the surface, the position of the punch stays constant to allow for relaxation in the polymer film. After a chosen time of 10 *s* the punch is retracted, while the force needed for debonding is measured as a function of the distance from the adhesive. Meanwhile a camera follows the appearance and evolution of cavities through the backside of the adhesive. From these measurements the tack energy (the total energy needed to break the bond) and the maximum force can be extracted. Fig. 5.30 shows tack measurements for aluminum, stainless steel and titanium.

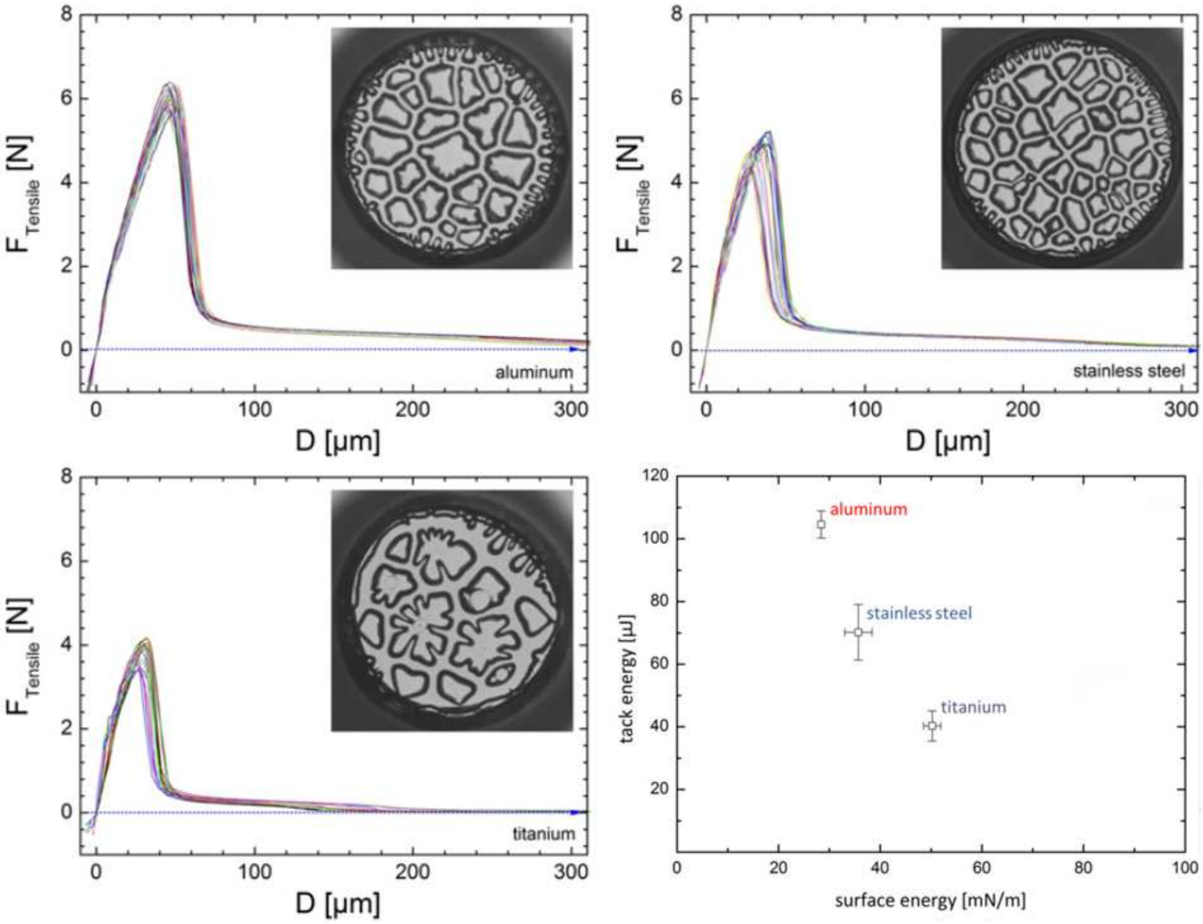

Figure 5.30:
Tack measurements for aluminum, stainless steel and titanium: Several force-distance curves are shown together with an inset of the cavity morphology for each adherent. The maximum force decreases from aluminum to titanium. The obtained tack energy is shown together with the surface energies in the lower right.

Also surface chemistry and surface roughness severely affect the shape and number of cavities and are to be addressed in terms of their influence on the tack performance. From Fig. 5.30 it can clearly be seen that both, the maximum force and the tack energy, strongly decrease with increasing surface energy of the adherent.

[1] Published patent application, *USA Patent and Trademark Office*, Patent no: **20090184200**, (2009)

[2] A. Diethert, K. Ecker, Y. Peykova, N. Willenbacher, P. Müller-Buschbaum, *ACS Appl. Mater. Interfaces* **3**, 2012-2021 (2011)

[3] M. Schindler, A. Kriele, P. Müller-Buschbaum, *J. Adhes.* **88**, 684-698 (2012)

[4] D. K. Owens, R. C. Wendt, *J. Appl. Polym. Sci.* **13**, 1741-1747 (1969)

6 Dynamics

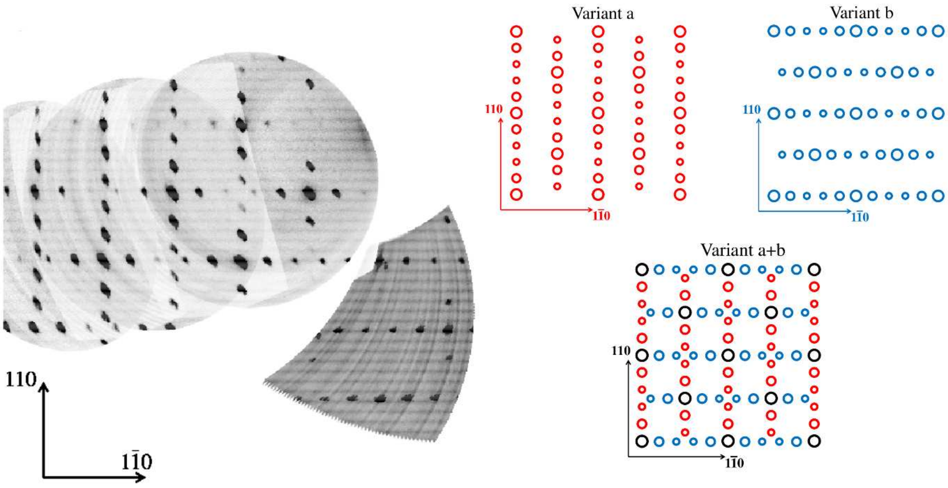
Variant a
Variant b
Variant a+b
110
1$\bar{1}$0
110
1$\bar{1}$0
110
1$\bar{1}$0
110
1$\bar{1}$0

6.1 Elastic nature of the demixing transition of semi-dilute aqueous poly(N-isopropylacrylamide) solutions

M. Philipp, U. Müller[1], R. Aleksandrova[1], R. Sanctuary[1], P. Müller-Buschbaum, J. K. Krüger[1]

[1] University of Luxembourg, Luxembourg, Luxembourg

Stimuli-responsive polymers, which undergo reversible demixing transitions when subjected to external stimuli, like changes of temperature, pH or ionic strength have great potential in various fields of application, like biomedicine and biotechnology (e.g. [1]). Amongst the stimuli-responsive polymers, poly(N-isopropylacrylamide) (PNIPAM) has attracted attention because of its sharp and reversible molecular collapse transition in aqueous media at about 32 °C. On a microscopic level, while heating the aqueous PNIPAM solution above its demixing transition temperature T_c, the conformation of the flexible linear PNIPAM chain changes from a swollen coil to a collapsed globule as the solvent quality passes from good to poor. This molecular collapse is followed by aggregation of PNIPAM chains, leading to PNIPAM-rich aggregates with diameters of several 100 nm.

Basic research has focused on different aspects of this complex coil-to-globule transition, like the critical fluctuations arising in the low temperature phase while approaching T_c or the laws governing the growth of PNIPAM-rich aggregates in the high temperature phase [2]. Several macroscopic properties were investigated at the demixing transition of PNIPAM systems with the aim to provide a bridge towards the micro- to mesoscopic structure formation.

Due to the immense volume changes observed at the demixing transition of manifold PNIPAM systems, this transition is often denominated as a volume phase transition. However, for PNIPAM hydrogels it turned out that the isothermal compressibility, but not the mass density, is the order parameter susceptibility of the demixing transition [3]. We here adress for the first time the elastic nature of the demixing transition of semi-dilute aqueous PNIPAM solutions. Stress-strain experiments, which are commonly applied to access the elastic properties of solids, are not a feasible alternative in case of liquids. In contrast, Brillouin spectroscopy allows probing thermally induced sound waves at GHz frequencies propagating within liquids. Due to the high probed frequencies, this technique permits interferences with viscoelastic properties to be overcome and determines high frequency clamped elastic properties. That Brillouin spectroscopy is an appropriate technique to elucidate the mechanical instabilities accompanying the demixing transition of PNIPAM systems is supported by the only existing Brillouin data on chemically cross-linked PNIPAM hydrogels [3]. Our Brillouin spectroscopic investigations are complemented by measurements of mass density in order to be able to compare the two alternative facets of this demixing transition of semi-dilute aqueous PNIPAM solutions.

The Brillouin spectroscopic investigations were performed on a modified six-pass tandem Brillouin spectrometer of the Sandercock type in collaboration with the group of Prof. Krüger at the University of Luxembourg. The vacuum laser wavelength of the frequency-doubled Nd-YAG laser equals to λ_0 = 532 nm, leading in the used backscattering geometry to an acoustic wavelength of $\Lambda \approx 200$ nm. A self-built aluminum thermostat allowed for achieving an average heating rate of 5 °C/h at the sample position. The evolution of mass density was determined by means of a DMA 5000 M densitometer from Anton Paar, Austria. The PNIPAM homopolymer (M_n = 20 - 25 kg/mol) was purchased from Sigma-Aldrich Chemie GmbH, Taufkirchen.

Details of the experimental investigations, the evaluation of the Brillouin spectra and the interpretation of the data are given in [4]. The hypersonic velocity v_L determined from the Brillouin spectra permits calculating the longitudinal elastic modulus according to $c_{11} = \rho v_L^2$, where ρ denotes the mass density. The corresponding data are represented versus temperature in Fig. 6.1(a) and versus mass density in Fig. 6.1(b) for three semi-dilute PNIPAM solutions and pure water.

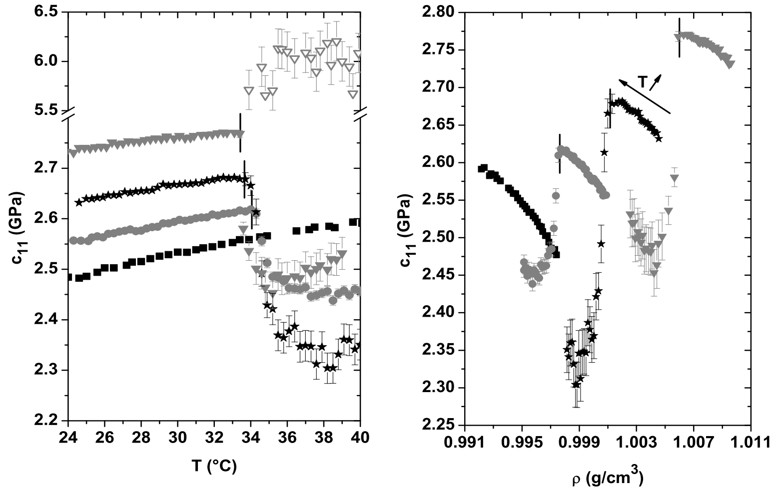

(a)

(b)

Figure 6.1:
Evolution of the longitudinal elastic modulus c_{11} versus (a) temperature T and (b) mass density ρ for pure water (squares), the 3 mass% (dots), the 6 mass% (stars) and the 10 mass% (triangles) PNIPAM solutions across the demixing transition. The vertical bars indicate the demixing temperature T_c of the PNIPAM solutions.

The main outcome of this study is as follows. For the solution with the highest PNIPAM concentration, Brillouin spectroscopy reveals that the size of compact PNIPAM-rich agglomerates is larger than 200 nm (corresponding to data points given as open triangles above T_c in Fig. 6.1(a)). These agglomerates possess a sharp distribution of the elastic moduli, which can be attributed without any doubt to a material with gel-like mechanical consistency. This experimental finding is in contradiction to the assumptions made by several authors, who assume that PNIPAM-rich agglomerates are in the glassy state. Furthermore, according to Fig. 6.1(b), the relative change of the longitudinal modulus at T_c for the PNIPAM solutions is much more pronounced, in some cases by a factor of 100, compared to that of the mass density. This representation indeed evidences the governing role of linear elasticity in the mechanical instability related to the demixing transition of PNIPAM systems. These investigations demonstrate the similarity in terms of the role played by the longitudinal modulus for the demixing transition in aqueous PNIPAM solutions and in chemically cross-linked PNIPAM hydrogels.

M.P. thanks the Fonds National de la Recherche (Luxembourg) for the receipt of a Marie Curie cofunded AFR Postdoc grant.

[1] M. A. Cole, N. H. Voelcker, H. Thissen, H. J. Griesser, *Biomaterials* **30**, 1827-1850 (2009)

[2] A. Meier-Koll, V. Pipich, P. Busch, C. M. Papadakis, P. Müller-Buschbaum, *Langmuir* **28**, 8791-8798 (2012)

[3] S. Hirotsu, I. Yamamoto, A. Matsuo, T. Okajima, H. Furukawa, T. Yamamoto, *J. Phys. Soc. Japan* **64**, 2898-2907 (1995)

[4] M. Philipp, U. Müller, R. Aleksandrova, R. Sanctuary, P. Müller-Buschbaum, J. K. Krüger, *Soft Matter* **8**, 11387-11395 (2012)

6.2 Competition between crystal electrical field shift and Kondo screening in CeNi$_9$Ge$_{4-x}$Si$_x$

C. Gold[1], G. G. Simeoni[2], W. Scherer[1], E.-W. Scheidt[1]

[1] CPM, Institut für Physik, Universität Augsburg, Augsburg, Germany
[2] FRM II, Garching, Germany

CeNi$_9$Ge$_4$ is an outstanding Fermi liquid compound which is positioned at the borderline to a non Fermi-liquid state. So far it exhibits the largest ever recorded Sommerfeld coefficient $\gamma = 5.5\,\mathrm{J/mol/K^2}$ at 0.08 K among paramagnetic Ce compounds [1]. This behavior is mainly driven by local magnetic fluctuations. The $J = 5/2$ ground state of the Ce^{3+} ion splits in a tetragonal crystal field, generated by the square-antiprismatic environment, into three Kramer's doublets. The two lowest doublets reveal a minute energetic separation of $\Delta_1 \simeq 6\,\mathrm{K}$ and are energetically well separated from the higher one ($\Delta_2 \simeq 128\,\mathrm{K}$) [2]. Due to the fact that the Kondo energy $T_\mathrm{K} = 3.5\,\mathrm{K}$ is of the same order of magnitude as Δ_1, the first excited doublet contributes significantly to the Kondo ground state. As the splitting of the two Kondo broadened low lying doublets is neither resolved in specific heat nor by cold neutron inelastic scattering we denote the crystal field ground state as a quasi-quartet (effectively fourfold degenerate N) [3]. Recently, we reported for CeNi$_{9-x}$Cu$_x$Ge$_4$ that the change of N by shifting the first excited doublet to higher energies enforces the system towards a quantum critical point [2], [4].

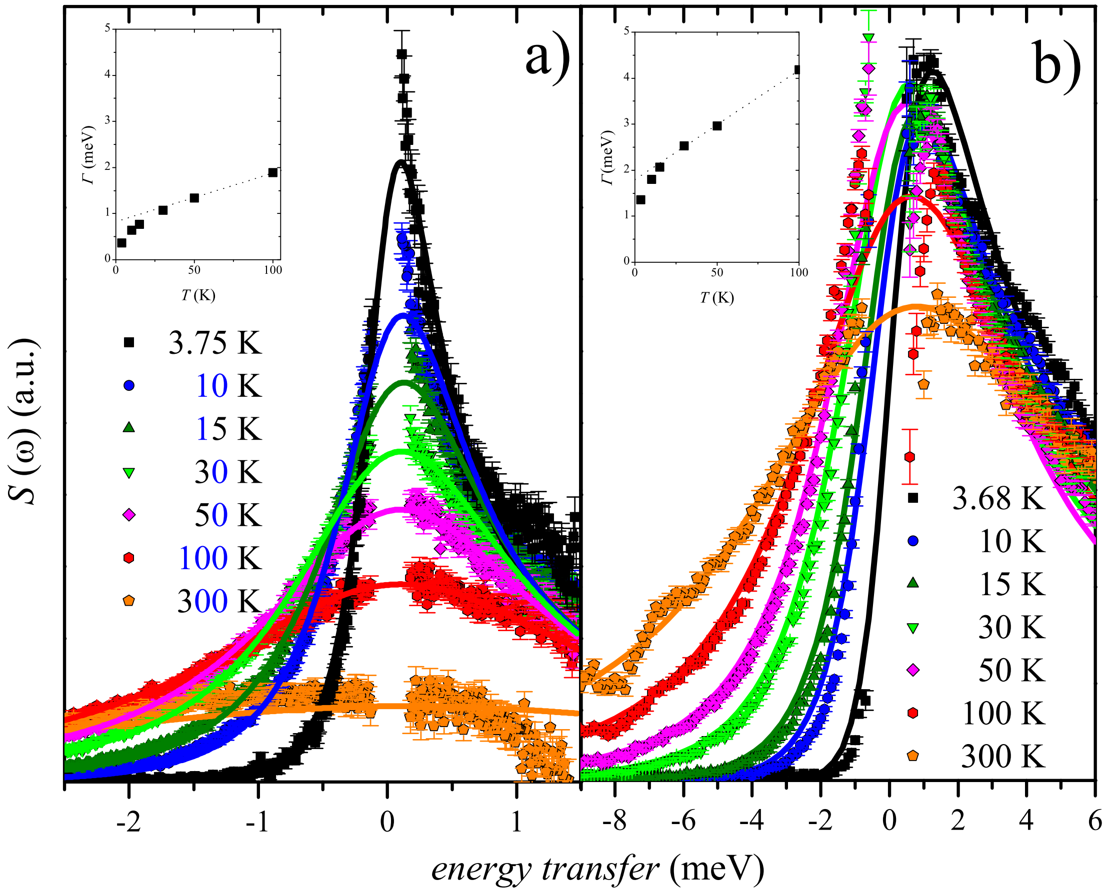

Figure 6.2:
The magnetic correlation function $S(\omega)$ at selected temperatures as labelled for a) CeNi$_9$Ge$_{3.9}$Si$_{0.1}$ and b) CeNi$_9$Ge$_3$Si (the lines represent Lorentzian fits). The inserts show the T dependence of the line widths, $\Gamma(T)$ obtained from the Lorentzian fits[5]

To gain more insight into the fluctuation spin dynamics of the $\mathrm{CeNi_9Ge_4}$ ground state we studied the $\mathrm{CeNi_9Ge_{4-x}Si_x}$ substitution serie [5]. $\mathrm{CeNi_9Si_4}$ is a model-type Kondo lattice system ($\gamma = 155\,\mathrm{mJ/mol/K^2}$) which can be well described by a sixfold degenerate Coqblin-Schrieffer model [6]. A strong volume decrease of about 5.6 % by the substitution of Ge for Si indicates an increasing $T_\mathrm{K}(x)$ in the Doniach picture. In contrast to this, specific heat $C(T)$ and resistivity $\rho(T)$ studies indicate, that below the Si-concentration $x = 0.5$, T_K decreases with increasing x, while this trend is reversed for $x > 0.5$. To clarify this unusual scenario, inelastic neutron scattering measurements were performed. From the quasi-elastic correlation function $S(\omega)$ (Fig.1) and the resulting temperature dependent line widths $\Gamma(T)$ (inserts in Fig.1) the Kondo temperatures are determined for $\mathrm{CeNi_9Ge_{3.9}Si_{0.1}}$ $T_\mathrm{K} = 4.2\,\mathrm{K}$ and $\mathrm{CeNi_9Ge_3Si}$ $T_\mathrm{K} = 13.7\,\mathrm{K}$. As plotted in Fig.2 these temperatures are in agreement with those Kondo temperatures determined from single crystal susceptibility data ($x = 0$) and specific heat investigations using the Coqblin-Schrieffer model [6]. These results support a continuous increases of $T_\mathrm{K}(x)$. Therefore we conclude that the observed discontinuity of $T_\mathrm{K}(x)$ is due to the interplay between the Kondo screening and the change of the CF scheme, which initially leads to an incipient reduction of the quasi-fourfold ground state degeneracy towards a lower ($N < 4$) interstitial state on the Ge-rich side, finally followed by an ensuing increase to a sixfold one [5].

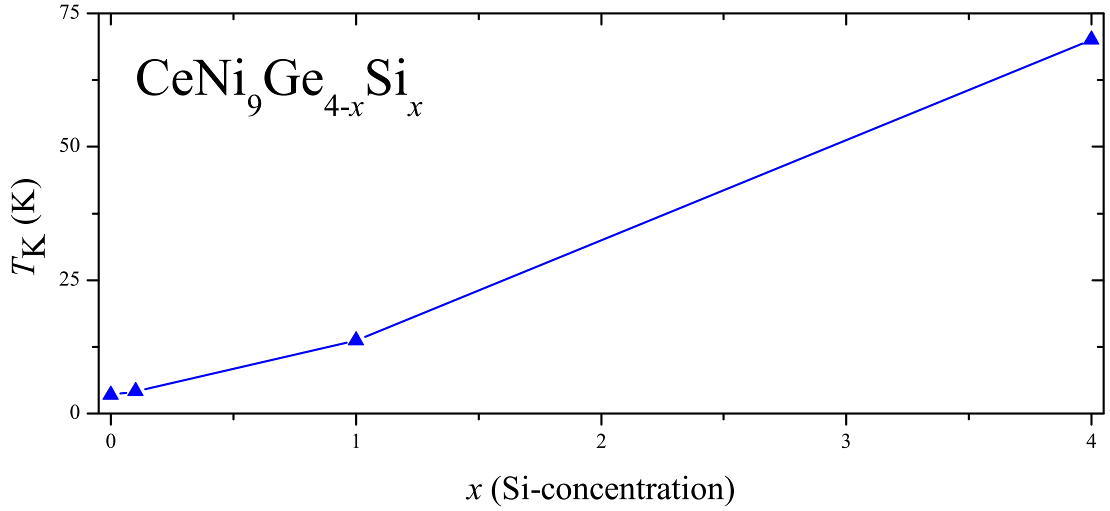

Figure 6.3: The Si-concentration x dependent Kondo temperature

[1] U. Killer, E.-W. Scheidt, G. Eickerling, H. Michor, J. Sereni, T. Pruschke, S. Kehrein, *Phys. Rev. Lett.* **93**, 216404 (2004)

[2] L. Peyker, C. Gold, W. Scherer, H. Michor, T. Unruh, G. G. Simeoni, A. Senyshyn, D. T. Adroja, O. Stockert, E.-W. Scheidt, *EPL* **93**, 37006 (2011)

[3] E.-W. Scheidt, F. Mayr, U. Killer, W. Scherer, H. Michor, E. Bauer, S. Kehrein, T. Pruschke, F. Anders, *Physica B* **378-380**, 154-156 (2006)

[4] L. Peyker, C. Gold, E.-W. Scheidt, W. Scherer, J. G. Donath, P. Gegenwart, F. Mayr, V. Eyert, E. Bauer, H. Michor, *J. Phys.: Condens. Matter* **21**, 235604 (2009)

[5] C. Gold, P. Gross, L. Peyker, G. Eickerling, G. G. Simeoni, O. Stockert, E. Kampert, F. Wolff-Fabris, H. Michor and E.-W. Scheidt, *J. Phys.: Condens. Matter* **24**, 355601 (2012)

[6] H. Michor, S. Berger, M. El-Hagary, C. Paul, E. Bauer, G. Hilscher, P. Rogl, G. Giester, *Phys. Rev. B* **67**, 224428 (2003)

6.3 Hydrogen motion in $LiBH_4$

W. Lohstroh[1], L. Silvi[1]

[1] FRM II, Garching, Germany

The complex hydride $LiBH_4$ is intensely studied as potential hydrogen storage material due to its high volumetric and gravimetric storage density of 121.3 kg/m^3 and 18.4 mass %[1], respectively. Hydrogen desorption typically only occurs above the $LiBH_4$ melting temperature (553 K) and numerous studies have been conducted in order to make the material a viable option for hydrogen storage systems. Rehydrogenation of $LiBH_4$ is possible although under harsh pressure and temperature conditions. The material forms an ionic crystal lattice of $[BH_4]^-$ complexes and Li^+ ions with an orthorombic LT-structure. At 383K, a structural phase transition to a hexagonal HT-phase occurs. The phase transition is accompanied by extreme dynamical disorder of the $[BH_4]^-$ tetraedra [2]. The rotional motion of $[BH_4]^-$ in $LiBH_4$ across the structural phase transition has been studied using quasielastic neutron scattering at the time-of-flight spectrometer TOFTOF.

Prior to use, $LiBH_4$ (Sigma Aldrich, 95%) was ball milled for 27 h in a high energy planetary mill (Retsch PM400). Approximately 61 mg of the powder were filled into an Aluminum flat cell resulting in an estimated neutron transmission of 0.85. The incoming wavelength was 2.5 $\mathring{A}$ which gave an energy resolution of 400μeV (FWHM) at the elastic peak and an accessible Q-range of 0.5-4.5 $\mathring{A}^{-1}$. Measurements were taken at temperatures between 343 and 413 K.

The rotational motion of the $[BH_4]^-$ tetraedra can be described as jump rotations of hydrogen atoms between different equilibrium positions. The scattering function $S(Q,\omega)_{rot}$ is given by:

$$S_{rot}(Q,\omega) = A_0\delta(\omega) + \sum A_n L_n(\frac{1}{\Gamma_n},\omega) \tag{6.1}$$

where

$$EISF = A_0 = \frac{I_{el}}{I_{el} + I_{inel}} \tag{6.2}$$

is the elastic inelastic structure factor (EISF) and $L_n(\Gamma_n,\omega)$ Lorentzian functions with $\Gamma_n = 1/\tau_n$. τ_n is the average residence time between successive jumps (while the jump itself is assumed to be instantaneous). Different types of motion can be identified from the Q-dependence of the EISF. For this however, it is necessary to cover a large range of energy transfer values, ω, to capture all of the quasielastic contributions as well as a sufficient Q-range.

The results for the QENS measurements at three different temperatures are shown in Fig. 6.4. With increasing temperature a strong quasielastic signal appears around the elastic peak which results from the increased hydrogen motion. For the analysis, the data have been fitted using a δ-function and one or two Lorentzians which were numerically convoluted with the (gaussian) resolution function. From Γ_1 the medium residence times τ_1 have been estimated to be in the range from 3 to 30 ps, similar to the values that have been reported previously for $LiBH_4$ [3,4]. From the fitted data, the EISF has been calculated and the results are shown in Fig. 6.5. The most likely rotational motions for the $[BH_4]^-$ tetraedron are: (i) 120 deg rotations around the C_3 symmetry axis (with one H-atom fixed) (ii) tumbling motion, i.e. 120 deg rotations that occur with equal probality around all 4 C_3 axis and (iii) free rotations of the H-atom on a sphere (with the $r = d_{B-H}$). The theoretical EISF [5] for each type of these motion is also plotted in Fig. 6.5. Obviously, the EISF at 413 K is well described by isotropic rotation of the H-atoms on a sphere with radius $r_{B-H} = 1.26\mathring{A}$ however, the data obtained at lower temperatures do not agree with any of the simple models. In general, the EISF describes the long time average position of a H-atom, i.e. it is the fourier transform of the probability density of finding the atom at the position **r** [5]. From this, a generalized EISF has been determined, basically describing a situation where

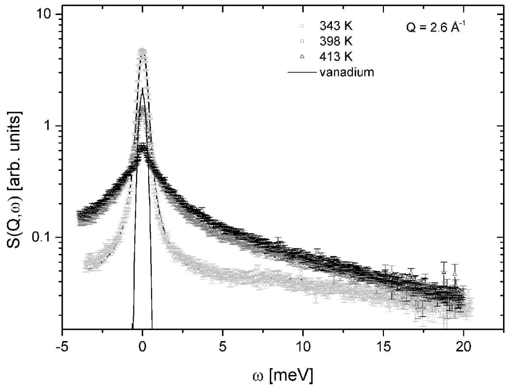

Figure 6.4:
$S(Q, \omega)$ of $LiBH_4$ at 343 (□), 398 (◯), and 413 K (△) together with the resolution function (vanadium standard). The solid lines are fits to the data (for details see text).

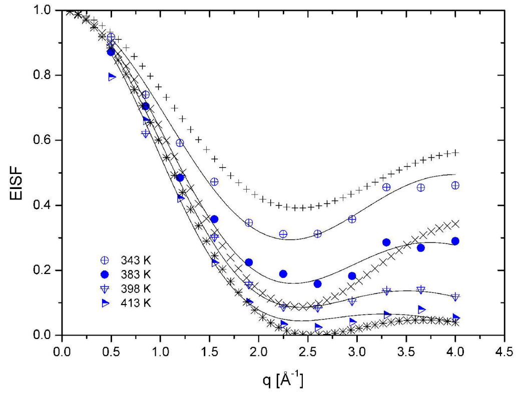

Figure 6.5:
The elastic-inelastic structure factor EISF for 343, 383, 398, and 413 K. Theoretical model functions for 120deg rotations (+), tumbling motion (×) and isotropic rotation (∗) are shown. The solid lines are fits of the EISF to a generalized model (for details see text).

120 deg rotations around the various C_3 axis occur with two different median residence times with $\tau_2 = \rho\tau_1$. Using this model, the EISF data of the 343 K measurement are well described ($\rho = 4.6$, see Fig. 6.5, solid line). For higher temperatures, ρ approaches 1, i.e. the tumbling motion (ii) as described above. This rotational motion is additionally superposed by diffusion of hydrogen inside a sphere and the EISF of the convoluted scattering functions for this case are also shown in Fig. 6.5 (373, 398 and 413K measurements). Using the model described above, the $[BH_4]^-$ motion can be consistently described in the entire temperature range investigated. At low temperatures (343 K) mainly 120 deg rotations around a preferred axisd are present with the occasional tumbling of the $[BH_4]^-$. With increasing temperature, the tumbling motions occur more frequently, simulateneously the $[BH_4]^-$ motion around its lattice site become larger. These motions that can be considered as a precursor of the structural phase transition. Finally, in the HT-phase, free rotation of the $[BH_4]^-$ tetraedra at the lattice site is obtained.

[1] A. Züttel, P. Wenger, S. Rentsch, P. Sudan, Ph. Mauron and C. Emmenegger, *J. Power Sources* **118**, 1-7 (2003)

[2] F. Buchter, Z. Lodziana, Ph. Mauron, A. Remhof, O. Friedrichs, A. Borgschulte, A. Züttel, D. Sheptyakov, Th. Straessle, A. J. Ramirez-Cuesta, *Phys. Rev. B* **78**, 094302 (2008)

[3] N. Verdal, T. J. Udovic, J. J. Rush, *J. Phys. Chem. C* **116**, 1614-1618 (2011)

[4] A. Remhof, Z. Lodziana, P. Martelli, O. Friedrichs, A. Züttel, A. Skripov, J. P. Embs, Th. Straessle, *Phys. Rev. B* **81** 214304 (2010)

[5] R. Hempelmann, *Quasielastic Neutron Scattering and Solid State Diffusion*, Clarendon Press, Oxford (2000)

6.4 The onset of self-diffusion in short-chain molecular melts

H. Morhenn[1,2], T. Unruh[2]

[1] FRM II, Garching, Germany
[2] LS für Kristallographie und Strukturphysik, FAU Erlangen-Nürnberg, Germany

The observed dynamics in molecular liquids strongly depend on the observation time one looks at the motions: At very short times the atoms move ballistically until they feel the bonds to their neighbors. This connectivity gives rise to a characteristic subdiffusive behavior, and at long timescales the freely diffusive regime is reached and the molecules show Fickian diffusion behavior.

The understanding of the subdiffusive behavior is essential in order to describe the transport mechanism in molecular melts, since the initial steps of molecular self-diffusion take place on this timescale. It is conceivable that these short-time dynamics are quite complex due to the interplay of intra- and intermolecular interactions.

To probe these dynamics, quasielstic neutron scattering (QENS) experiments and molecular dynamics (MD) simulations were performed on a short- ($C_{16}H_{34}$) and long-chain ($C_{100}H_{202}$) n-alkane system. MD simulations are based on force field parameters, which model the bonded and non-bonded interactions between the atoms. With QENS one can probe the atomic motions on a pico- to nanosecond timescale on a molecular length scale, providing a unique tool to test the force fields used in the simulations.

In order to validate the simulated trajectories, intermediate scattering functions were calculated and compared with the measured data. As can exeplarily be seen in figure 6.6, the simulated dynamics perfectly represent the measured ones over the whole temperature-, time- and length-scale studied.

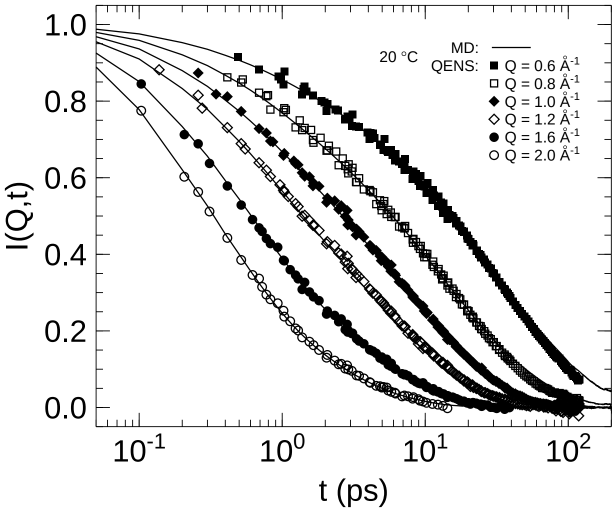

Figure 6.6:
Intermediate scattering functions of $C_{16}H_{34}$ as measured with quasielastic neutron scattering (QENS) at TOFTOF (symbols) and calculated from the molecular dynamics (MD) simulations for several values of momentum transfer Q at $T = 20\,°C$ [1].

Previous studies showed that the dynamics observed with QENS are faster than the long-time long-range diffusion coefficients [2,3]. The analysis of the MD simulations now prove that one does not observe self-diffusion of the molecules, but rather local chain dynamics. Three basic relaxation processes for these chain dynamics can be saparated [1,4]:

1. On very short times of some picoseconds a rotation of the dihedrals is observed. This reorientation is faster at the ends of the chains, due to the locally increased degrees of freedom. The average activation energy of this process is $14.7\,\mathrm{kJ\,mol^{-1}}$ for $C_{16}H_{34}$.

2. Next the atoms start to see their intermolecular neighbors, which leads to a collective flow-like motion of atoms in large clusters, giving rise to a non-gaussian behavior of the motions. This effect was observed in the $C_{100}H_{202}$ system, where the molecules are far more immobile than the $C_{16}H_{34}$ chains.
3. On a longertime scale the whole molecules rotate, just before the self-diffusive regime is reached. As illustrated in figure 6.7 the non-gaussian behavior of the molecules' displacement reaches a maximum.

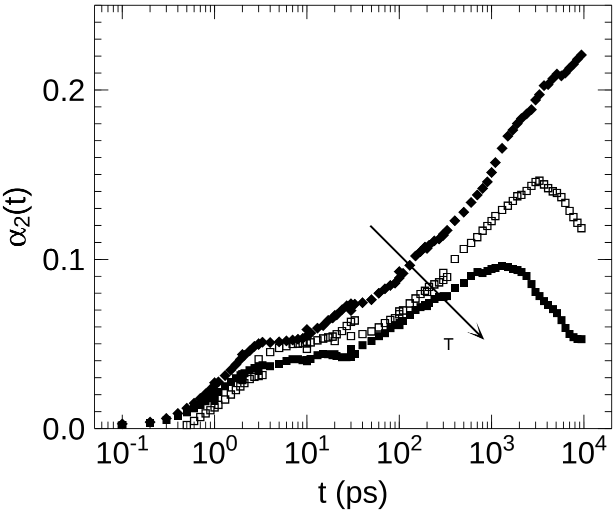

Figure 6.7:
Non-gaussianity of displacement of the center-of-mass coordinates of $C_{100}H_{202}$ calculated from the MD simulations. The maximum of $\alpha_2(t)$ conincides with the timescale of molecular rotation.

Polyethylene oxide (PEO) is of similar structure as n-alkanes, but every third methylene group is substituded by an oxygen atom. The short time dynamics observed with QENS show no dependence of the molecular weight, and only a small dependence can be detected on an increased observation time (see fig. 6.8). Comparing these findings to the n-alkane dynamics shows that the small modification of the molecular backbone results in a massive slowdown of the PEO chains.

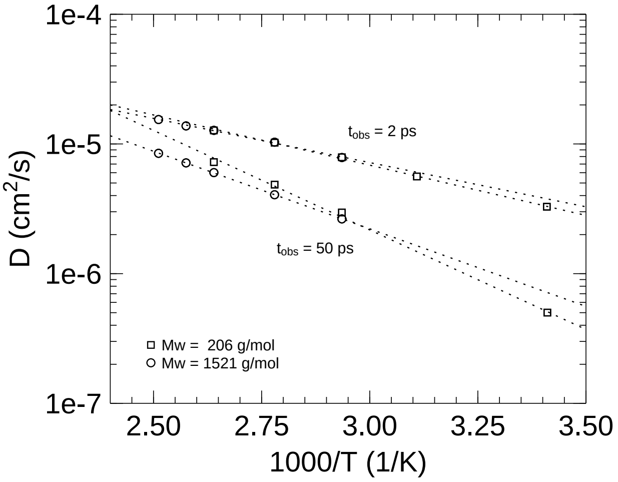

Figure 6.8:
Apparent diffusion coefficients extracted from QENS experiments for two PEO samples, roughly matching the molecular weight of $C_{16}H_{34}$ ($M_w = 224\,\mathrm{g/mol}$) and $C_{100}H_{202}$ ($M_w = 1405\,\mathrm{g/mol}$). Two different instrumental resolutions were set, resulting in two observation times t_{obs}.

[1] H. Morhenn, S. Busch, T. Unruh, *J. Phys.: Condens. Matter.* **24**, 375108 (2012)

[2] C. Smuda, S. Busch, G. Gemmecker, T. Unruh *J. Chem. Phys.* **129**, 14513 (2008)

[3] H. Morhenn, S. Busch, T. Unruh, *LS Funktionelle Materialien, Annual Report,* 96–97 (2011)

[4] H. Morhenn, S. Busch, D. Richter, W. Petry, T. Unruh *submitted*

6.5 Vibrational properties of Ni-Mn-Ga in the five-layer modulated martensite phase

S. Ener, J. Neuhaus[1], B. Pedersen[1] W. Petry

[1] FRM II, Garching, Germany

Ni-Mn-Ga magnetic shape memory materials show a magneto-structural transition, which leads to large strains of 6% and 10% for off-stoichiometric compositions with 5-layered and 7-layered martensite structures, respectively [1,2]. The ferromagnetic shape memory effect can be observed in two different ways - magnetic field induced structural transition (MIT) and magnetic field induces variant reorientation (MIR). For the observation of the MIT, material has to be cycled around the structural transition temperature and the structural transition temperature change has to be strongly coupled to the external magnetic field. In the case of MIR, the crystallographic structure of the material stays in the modulated martensite phase with ferromagnetic ordering. In the martensite phase of the Ni-Mn-Ga, the crystallographic short axis and the easy axis of the magnetization are magneto-structurally coupled. So they move together. If the energy barrier for the twin boundary mobility is low enough or in other words, if the magnetic stress is bigger than the twinning stress, it is possible to move the twin boundaries just by applying an external magnetic field in the range of 0.5–1 Tesla. This mobility of the twin boundaries allows the minimization of the Zeeman energy which is created by the external magnetic field [3].

In this study we investigate the vibrational properties of five-layer modulated (5M) martensite which is a good candidate for MIR applications. The crystallographic properties of the 5M single crystal has been investigated in detail by neutron diffraction at the thermal single crystal diffractometer (RESI) at the Forschungsneutronnenquelle Heinz Maier-Leibnitz (FRM II) in Garching, Germany. Room temperature diffraction measurements are carried out on an Eulerian cradle with k_i = 1.039 Å. Fig.6.9 shows the double variant modulated structure of 5M. Red and blue circles indicate perpendicular oriented modulated structures along [110] and [$1\bar{1}0$]-directions, respectively.

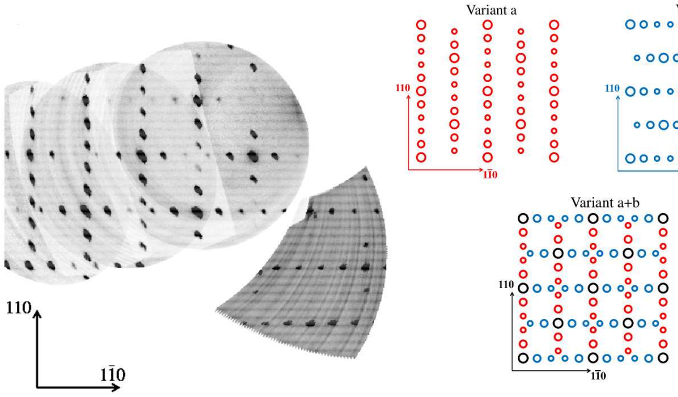

Figure 6.9: Reconstructed hk0-plane of five-layer modulated martensite phase with variant representation. Black spots are the Bragg intensities of different scattering planes.

Fig.6.10 shows the measured modes in high symmetry directions of the 5M modulated martensite at room temperature. Due to the low crystallographic symmetry of the martensite phase phonon dispersion exhibits six high symmetry directions. [$\xi\xi0$]-direction indicates both [$\xi\xi0$] and [$\xi\bar{\xi}0$] directions which are coming from the perpendicular modulated structures. Transversal modes of [$\xi\xi0$] direction are shown as squares and transversal mode of [$\xi\bar{\xi}0$] is shown as stars. First-principles calculations of 5M martensite for the stoichiometric composition [4] perfectly reproduces the measurement results except the transversal modes of [$\xi\bar{\xi}0$] as expected.

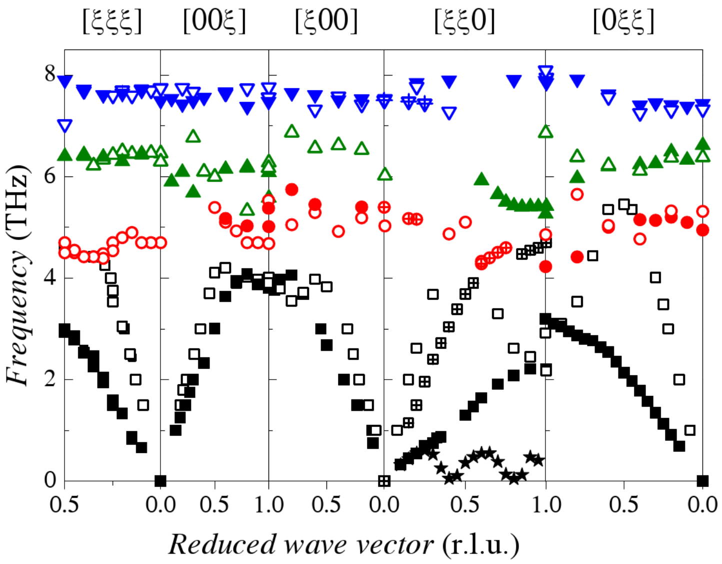

Figure 6.10:
Phonon dispersion of five-layer modulated martensite along the high symmetry directions. Different symbols and colors represent different phonon polarizations.

The comparison of measurements with the first-principles calculations is shown in Fig. 6.11. Measurements and calculation fit remarkably. The energy bands for the optical modes are caught correctly by the calculations. Also the smoothed dip at the TA_2-mode is reproduced.

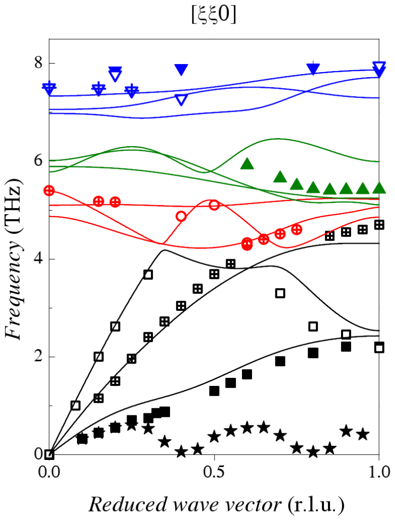

Figure 6.11:
Phonon dispersion of 5M martensite measured along [ξξ0] (symbols) and compared to first-principles calculations [4] for stoichiometric martensite.

Our measurement results show that, the low lying excitations which are observed along [ξξ0] direction are related to the acoustic modes of [$\xi\bar{\xi}$0] and differ from the phason observed by Shapiro *et al.* [5].

[1] S. J. Murray, M. Marioni, S. M. Allen, R. C. O'Handley, T. A. Lograsso, *Appl. Phys. Lett.* **77**, 886 (2000)

[2] A. Sozinov, A. A. Likhachev, N. Lanska, K. Ullakko, *Appl. Phys. Lett.* **80**, 1746 (2002)

[3] M. Acet, Ll. Mañosa, A. Planes, *Handbook of Magnetic Materials*, 231-289 (2011)

[4] P. Entel, V. D. Buchelnikov, M. E. Gruner, A. Hutch, V. V. Khovalio, S. K. Nayak, A. T. Zayak, *Materials Science Forum* **583**, 21 (2008)

[5] S. M. Shapiro, P. Vorderwisch, K. Habicht, K. Hradil, H. Schneider *Europhys. Lett.* **77**, 56004 (2007)

7 Methodological and instrumental developments

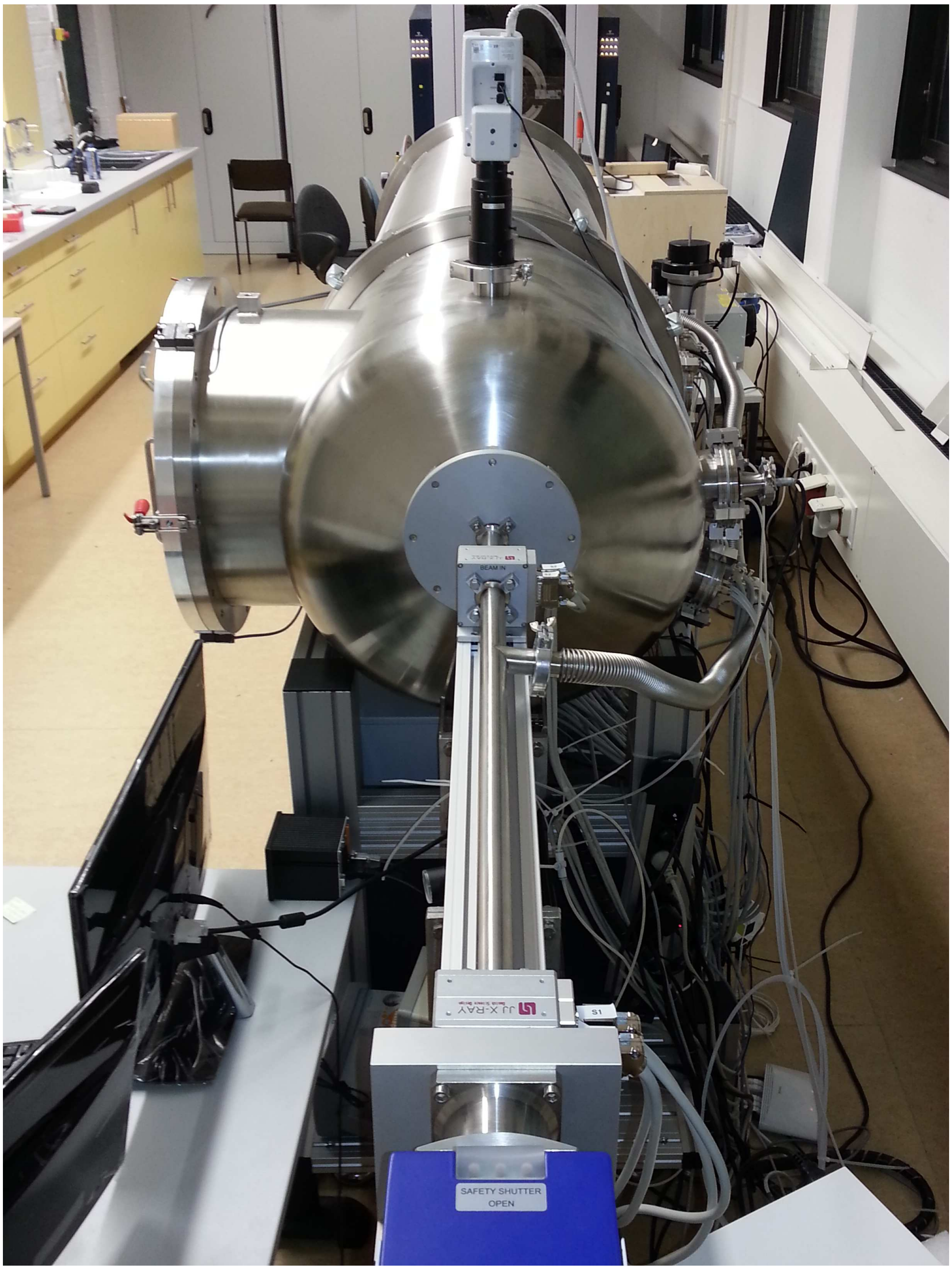

7.1 A cold chopper spectrometer for the European Spallation Source

L. Silvi[1], W. Lohstroh[1], G. G. Simeoni[1], J. Neuhaus[1], W. Petry

[1] FRM II, Garching, Germany

The long pulse of the European Spallation Source (ESS) will provide a high integral neutron flux, comparable to the best existing steady state reactors. Taking advantage of the time structure of the neutron beams considerable gains in the measurable signal are expected. The proposed cold direct time-of-flight spectrometer is a versatile instrument to address important scientific cases, ranging from soft matter and biological samples to magnetic and functional materials. Examples of scientific cases can be summirized from these fields: magnetism, soft matter, material science, strongy correlated systems, functional materials.

The cold chopper spectrometer forsees a total instrument length of 120.4 m (moderator–detector distance). The long pulse from the source (2.86 ms, $\nu_{\text{ESS}} = 14$ Hz) will be chopped in different times, allowing the energy resolution to vary between "high resolution mode" (5-10 μeV at $9\ \AA$), to a "relaxed resolution mode" (100 μeV at $5\ \AA$) where most of the experiments are expected to take place.

For a clean resolution function the source pulse has to shaped to 1000 μs maximum length and the layout of the spectrometer is based on the "balanced spectrometer" conditions. The instrument length allows a useful wavelength of 2.6 $\AA$, leading to a possibility to use a single pulse or Rate Repetition Multiplication (RRM) options.

For obtaining a clean resolution function, a total number of 6 choppers are used:

- counter rotating chopper pair as a Pulsing chopper (P), placed at 7 m from the source, and rotating at $N_1\times$ 14 Hz. It leads to a triangular pulse shape (in time) with a FWHM τ_P.
- Frame Overlap chopper (FO) rotating with a $\nu_{\text{ESS}} = 14$ Hz frequency, placed at 6 m from the P chopper, avoiding overlap between two subsequent source pulses in the time T = 71400 μs but not restricting the natural wavelength band width.
- counter rotating chopper pair as the Monochromating chopper (M), placed at 108 m from the P chopper (rotatation speed $N_2\times$ 14 Hz).
- a single chopper, just located in front of the M chopper pair as a second frame overlap chopper: it adjusts the number of pulses impinging on the sample during the source pulse time frame (Rate Repetition Mode, RRM). Moreover the observation time windows between adjacent RRM pulses can be adjusted. Depending on the used ratio, the number of RRM pulses can be chosen from 1 to N_2, where $N_2 \times 14$ Hz is the M chopper rotating speed.

The instrument will use neutrons from the cold moderator, and the guide system will be optimized for cold neutrons, taking special care to avoid the direct view to the source (line-of-sight). It is composed of three sections: the first is a straight guide with a supermirror coating $m = 2$ up to the FO chopper, the second and s-shape ballistic guide with $m = 4$ and a last focussing parabolic shape part with variable coating (from $m = 3$ to $m = 6$). The s-shape guide allows a homogeneous beam profile and a defined cut-off for short wavelength, depending on guide dimensions and supermirror coating. The last part is used for focussing at the sample position, especially required by small samples. A collimator can be inserted before the last section obtaining a $5 \times 5\ mm^2$ spot on the sample, and avoiding the "halo" coming from high divergence neutrons.

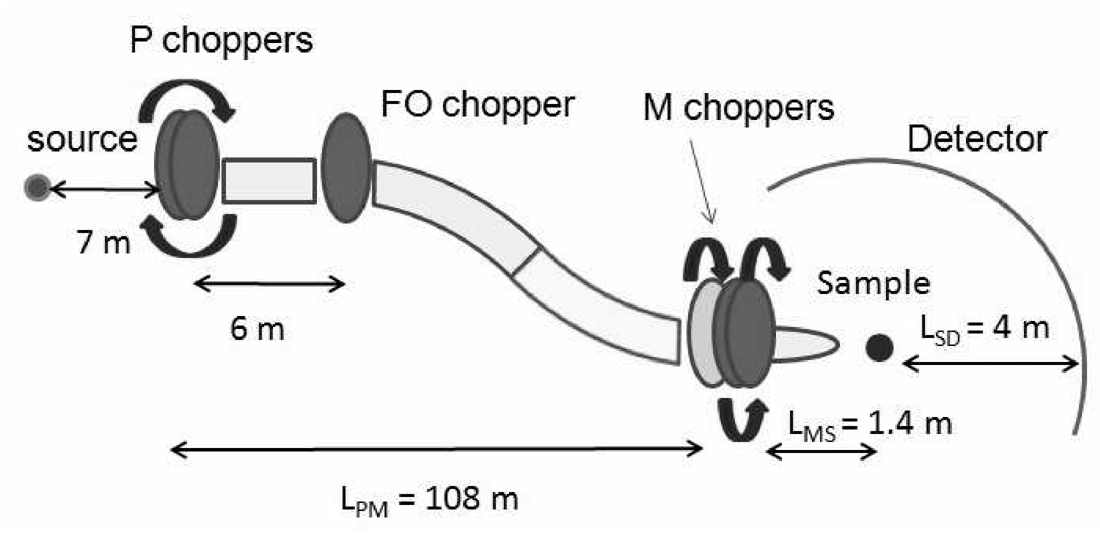

Figure 7.1: Instrument layout as described above

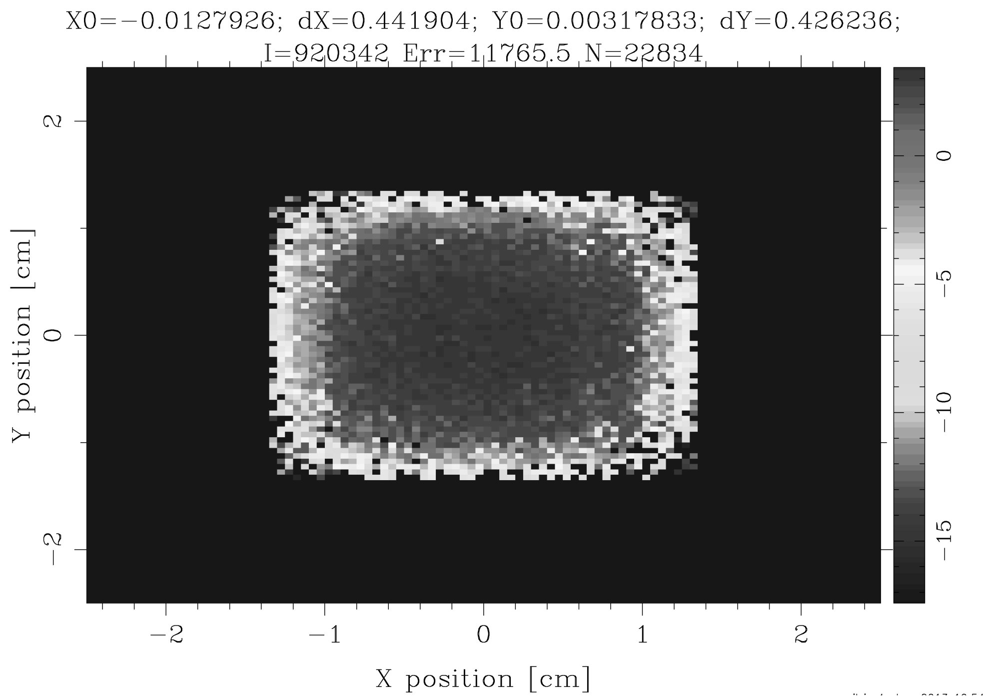

Figure 7.2: Example of simulation using McStas, measuring the flux at the sample position.

[1] R. E. Lechner, *Proceedings Workshop on Neutron Scattering Instrumentation for SNQ* **J1-1954**, p. 202 (1984)

[2] S. Roth, Ph.D. Thesis, *Technische Universität München*, München (2001)

[3] T. Unruh, J. Neuhaus, W. Petry, *Nucl. Instrum. Meth. A* **580**, 1414-1422 (2007)

[4] P. Willendrup, E. Farhi and K. Lefmann, *Physica B* **350**, E735-E737 (2004)

7.2 Eliminating spatial distortions in Anger-type gamma cameras

M. Leitner, H. Ceeh[1], J.-A. Weber[1]

[1] E21, Physik Department, TU München

Two-dimensional position sensitive gamma detectors of the Anger type are standard tools in diverse fields of physics and even more widely deployed in nuclear medicine. In such cameras the incident gamma photon generates a localized flash of light in the scintillation crystal, which is detected by an array of photo-multiplier tubes. The read-out position is the center of mass of the nonlinearly amplified responses of the respective photo-multipliers. It is clear that these positions will be subject to systematic distortions due to both the regular hexagonal arrangement of the photo-multipliers and inevitable deviations from ideal behaviour of the analog circuits.

In 2012, a spectrometer for Angular Correlation of Positron Annihilation Radiation (ACPAR) was set up and put into operation in Garching. This method allows to determine the electron momentum density (specifically the Fermi surface) of single-crystalline samples. The obtained amount of information critically depends on the position resolution of the used Anger cameras. Here we give a short report on how we optimized the performance by correcting the experimental data for distortions determined from a calibration pattern, a thorough account of which has already been published [1].

For determining the distortions we placed an 8 mm stack of perforated sheet metal with a hexagonal arrangement of circular holes with 3 mm diameter and 5 mm distance directly in front of the detectors and exposed it to 511 keV gamma radiation from a distant point source. In order to enhance the pattern we passed the images through a spatial band-pass filter, which suppresses both long-range response inhomogeneities and pixel-to-pixel Poisson noise. A detail of the resulting calibration pattern is given in the left panel of Fig. 7.3. The holes in the mask show up as peaks in the calibration image, and the presence of distortions is clearly visible by eye as deviations from the ideal hexagonal arrangement.

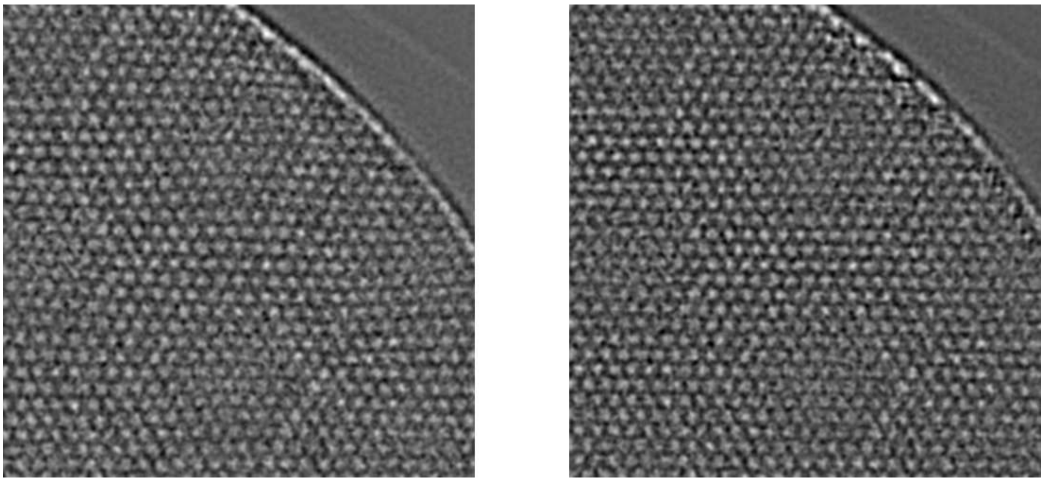

Figure 7.3: Detail of a calibration pattern image: before (left) and after distortion correction (right).

With the present statistical quality of the calibration data the single peak positions are still affected by Poisson noise. However, the typical length scale of the distortions is obviously larger than the resolution of the pattern, which allows us to model the displacement vector field as a smooth function. We therefore implemented the distortion correction as the problem of optimal overlap between the calibration pattern and a set of Gaussian peaks subject to a regularization on the nearest-neighbour distances (which can be thought of as springs connecting the Gaussians). This problem is solved incrementally by first assigning the central peak, and then iteratively enlarging the array of fitted peaks by an outer layer and relaxing the peak positions according to the overlap and spring forces. In this way local optimization leads to the global optimum, as the newly-added peaks are already in the correct basin of attraction. Consequently, the algorithm requires hardly any human guidance in assigning the approximately 6000 peaks. Thanks to the spring forces, the obtained peak positions display practically no noise. They correspond to displacements on the order of 3 mm, compared to a detector diameter of 41.5 cm. Apart from seemingly random distortions due to miscalibrations or degradation of the analog components in the circuitry, they display systematic features due to the photo-multiplier arrangement: directly over a photo-multiplier tube an infinitesimal area on the detector is contracted by 30% in the image compared to the regions between the tubes (giving apparently higher illuminations over the tubes).

For correcting the data for these distortions, we generated a look-up matrix of shifts that move a given read-out position to the correct physical location. The correction happens on an event-by-event basis in 32 bit integer arithmetic and is therefore very efficient (running with negligible CPU load in on-line correction and being limited by the data transfer rate from disk in off-line correction). The calibration pattern after distortion correction is given in the right panel of Fig. 7.3. Obviously, distortion correction recovers the ideal hexagonal pattern.

The real criterion of merit is the resolution gain in ACPAR spectra. An experiment on crystalline quartz constitutes one of the most sensitive tests: When a positron is injected into this system, it captures an electron and forms a positronium state. In defect-free quartz this state delocalizes, and, due to the very low concentration of positronium, follows a thermal Boltzmann distribution. The momentum distribution of the annihilation radiation will therefore display peaks at the reciprocal lattice vectors (corresponding to the Fourier coefficients of the delocalized state) for intra-positronium annihilations, superimposed on a broad background when the positron annihilates with a bound electron. The width of the peaks is given by the thermal momentum, convolved with the instrumental resolution.

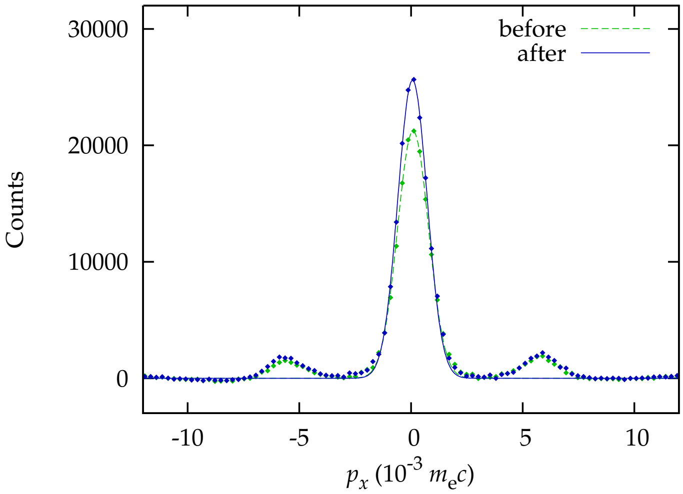

Figure 7.4:
Cut through momentum density after subtraction of the background, before and after distortion correction. Points are data and lines are Gaussian fits to the central peak. The satellite peaks are the higher-order components at the reciprocal lattice positions at $5.70 \cdot 10^{-3}\ m_e c$.

Fig. 7.4 gives the spectra before and after distortion correction. The gain in resolution corresponds to a contribution of distortions to the point spread function of 2.2 mm. Comparing this to the residual statistical component of the point spread function of 1.64 mm shows that distortion correction leads to an improvement of the instrumental resolution by a factor of 1.7.

Funding of this project by the DFG via the Transregio 80 “From Electronic Correlations to Functionality” is gratefully acknowledged.

[1] M. Leitner, H. Ceeh, J.-A. Weber, *New J. Phys.* **12**, 123014 (2012)

7.3 Manufacturing cylindrical LEU Mo-99 targets by sputtering

T. Hollmer[1], B. Baumeister[1], C. Steyer[1]

[1] FRM II, Garching, Germany

The decay product of molybdenum-99 (Mo-99), technetium-99m (Tc-99m), is the most widely used diagnostic medical isotope. It is used for a variety of medical investigations such as the detection of diseases or the study of organ structures and functions. Tc-99m decays to Tc-99 by emission of a 140keV photon, which can be detected by scintillator devices and thereby used for medical imaging.The main production route of Mo-99 is the nuclear fission of uranium-235 (U-235). Approximately 6% of its fission products result in Mo-99. Currently, production involves irradiating small amounts of highly-enriched uranium (HEU) in an intense neutron flux.

Due to proliferation concerns, a great deal of effort has been made in recent years to convert the production to low-enriched uranium targets (LEU, enrichment below 20%). The reduction in enrichment leads to a lower particle density of U-235 and an increased neutron capture due to U-238. One approach to compensating for this is to increase the total uranium in the irradiation targets, which can be achieved by using pure metallic uranium foils instead of a uranium dispersion in aluminum. One important advantage of metallic uranium is its mechanical separability from the cladding material after irradiation. This results in significantly less highly radioactive waste and, therefore, lower production costs.

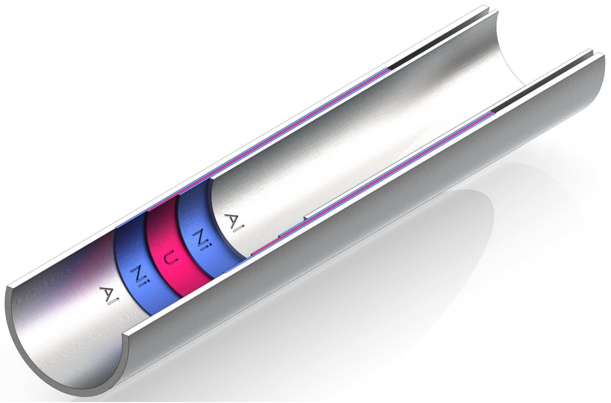

Figure 7.5: Sectional drawing of a cylindrical Mo-99 target

A promising target design is the cylindrical target, which was developed by Argonne National Laboratory (ANL) together with other institutes [Figure 7.5]. This target consists of a thin metallic LEU foil (approx. 130 μm thick) wrapped in a diffusion barrier (e.g. nickel), which is then encapsulated between two concentric aluminum cylinders. It is approx. 160 mm in length and has an outer diameter of approx. 30 mm. The cylindrical design guarantees good structural integrity and heat transfer. The diffusion barrier prevents bonding of the uranium and the cladding made of aluminum during irradiation and, therefore, allows easy disassembly of the target afterwards [1].

Currently, the foils used in these targets are either produced by hot and cold rolling (Argonne National Laboratory) or by a direct casting method (Korea Atomic Energy Research Institute). Both methods have their specific assets and drawbacks. The rolling process is labor intensive, but is able to produce foils of high and homogenous quality. The direct casting method, on the other hand, is economical but the foils produced show surface irregularities and an uneven thickness [2, 3].

Based on our experience of coating uranium [4] we are currently investigating a third way of producing cylindrical LEU targets. Our approach is the physical vapor deposition (PVD) of the diffusion barrier and the uranium directly on the inside of the outer aluminum cylinder. In this way, the material is evaporated by the bombardment of argon ions from a glow plasma discharge. This process offers several advantages over the traditional methods. Due to the sputtering geometry, the uranium sputter target will be almost fully utilized. This, together with the elimination of a preceding foil production step, will lead to lower manufacturing costs. Given an adequate sputtering reactor, it is possible to apply coatings of uniform thickness and establish good thermal contact between the layers. This meets the essential safety requirements for these targets.

The challenge here is the small geometry of the target, which is far below conventional PVD set-ups. This made it necessary to develop a completely new sputtering reactor. To this end, several concepts were developed and thermal and electromagnetic simulations were performed. The most promising concept is currently set up in a test assembly. The ongoing tests show very promising results. First targets were successfully coated with copper, as a non-radioactive surrogate [Figure 7.6]. Currently, the process parameters are optimized to achieve the desired layer properties in a reasonable coating time.

Based on the results obtained using surrogate materials, a final sputtering reactor will be installed in our uranium laboratory within the year. The reactor will be built in an argon glove box, which allows for safe handling of uranium under condition of the highest purity.

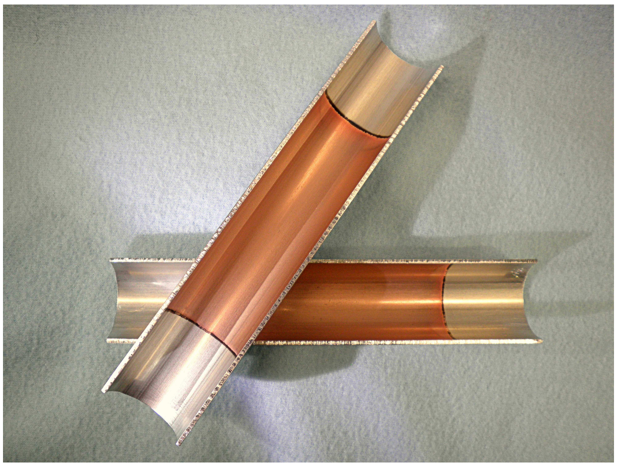

Figure 7.6: Inside of a copper-coated target cylinder

[1] NATIONAL RESEARCH COUNCIL, "Medical isotope production without highly enriched uranium", p. 92, The national academic press, Washington D.C. (2009).

[2] T. C. WIENCEK, "Status and Progress of foil and target fabrication activities for the production of 99Mo from LEU", ANL, Proceedings of the RERTR International Meeting 2008.

[3] A. BAKEL, "Overview of progress related to implementation of the LEU-modified Cintichem process", ANL, Proceedings of the RERTR International Meeting 2008.

[4] W. Schmid, "Construction of a sputtering reactor for the coating and processing of monolithic U-Mo nuclear fuel", FRM II (2011).

7.4 The effect of external stress on irradiation induced <c>-loop formation in Zircaloy-4

R. M. Hengstler-Eger, P. B. Hoffmann[1], M. A. Kirk[2]

[1] AREVA NP GmbH, Erlangen, Germany
[2] Argonne National Laboratory, Lemont (IL), USA

In the past years, unexpectedly high fuel assembly growth has been observed in some pressurized water reactor (PWR) plants, which was not predicted by the fuel assembly (FA) codes that are based on the operational experience and the theoretical knowledge of irradiation deformation. To explain this unexpected phenomenon, to improve the FA codes and to facilitate the development of advanced deformation resistant alloys, a better understanding of the microstructural processes in the FA structural components, like guide tubes and spacer grids, during neutron irradiation is necessary. The objective of this work was to contribute to such better understanding by specifically studying the influence of external stress on the irradiation behavior of PWR guide tube alloys, a parameter whose effect on the observed unexpected growth is unclear. Irradiation induced macroscopic component deformation at high fluences is reported to be governed by a process of enhanced material growth (”breakaway growth”), which is associated by many authors with the formation of c-component vacancy-type dislocation loops. Therefore, the main focus during the conducted microstructural studies was on the formation and characteristics of those <c>-loops.

As compared to direct in-pile neutron irradiation in a power plant or test reactor, this work is based on an out-of-pile method: heavy ion irradiation, coupled with in-situ transmission electron microscopy (TEM). The huge advantages of heavy ion irradiation as compared to in-pile neutron irradiation are the vastly reduced irradiation times in the range of several hours, the absence of target activation, the easy experimental accessibility which allows to control and measure the experimental parameters with accuracy, and the capability to isolate single parameters. The unique asset of in-situ TEM is the possibility to observe defined material regions from their unirradiated state up to highest damage levels, to study the microstructural processes dynamically and to document the microstructural developments as a function of the damage level in the form of movies.

We showed in previous work that heavy ion irradiation in combination with in-situ TEM is suitable for the simulation of all major aspects of in-pile irradiation damage. Specifically, both <a>- and <c>-loops can be produced, with their characteristics corresponding to the loop structures produced in Zry-4 by in-pile neutron irradiation [1].

Thus, the successfully applied ion irradiation parameters were used to study the effect of external tensile stress on TEM tensile samples. The irradiations were conducted at 300 °C, which corresponds to typical PWR guide tube temperatures during operation. As projectile, 1 MeV Kr was chosen, due to its mass being close to Zirconium which leads to similar displacement cascades; also, with Kr being chemically inert, the occurrence of chemical reactions with the target is assumed to be insignificant. The sample was irradiated to an ion fluence of $5 \cdot 10^{15}\mathrm{cm}^{-2}$, corresponding to a dose level of 25 displacement per atom (dpa), which is at the higher end of typical PWR guide tube end-of-life dose levels. The chosen stress level was the yield strength level (175 MPa at 300 °C for Zry-4), as the point of yield strength is a defined state in the sample under strain which can be clearly recognized by the onset of dislocation channel formation, indicating the transition to plastic deformation.

External tensile stress showed a very significant and direct correlation with the irradiation induced <c>-loop structure. In the Zry-4 sample under irradiation at yield strength level, the <c>-loop linear density decreased continuously with an increase of the component of the tensile stress parallel to the c-axis, and the stress applied parallel to the c-axis suppressed the <c>-loop formation entirely. Such a dependence of the <c>-loop structure on the tensile stress direction can be explained by theory in a straightforward way, but has been verified experimentally for the first time. The effect is surprising in both its clarity and its magnitude. It has thus been shown that tensile stress has a most significant effect on <c>-loop formation in Zr-based alloys, and the effect is highly dependent on the orientation of the stress direction towards the grains' orientation.

While the applied stress in the range of the yield strength is clearly higher than in-pile component stress levels during operation, is seems a valid conclusion that the observed effect should also occur for lower stress levels, with a respectively lower magnitude. Based on the known typical guide tube textures and the elastic properties of α-Zr, it can be deduced that, in theory, an increase of the hold-down spring forces should lead to a reduction of <c>-loop formation in the majority of the grains, which could in turn lower the guide tubes' axial growth. Any such measures would, however, have to be taken in compliance with the known effect of stronger hold-down forces on creep and the resulting increase in fuel assembly bow.

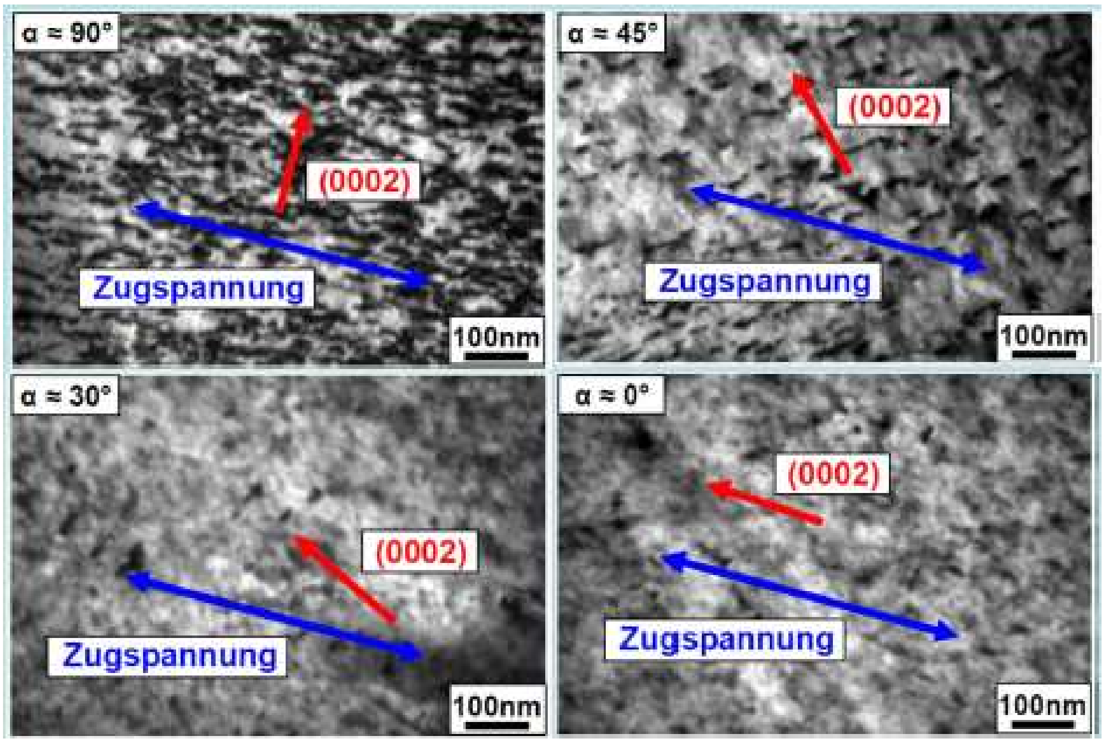

Figure 7.7: <c>-loops in Zry-4 at yield strength level, after 25 dpa; grain thicknesses are comparable.

[1] R. M. Hengstler-Eger, P. Baldo, L. Beck, J. Dorner, K. Ertl, P. B. Hoffmann, C. Hugenschmidt, M. A. Kirk, W. Petry, P. Pikart, A. Rempel, *J. Nucl. Mat.* **423**, 170-182 (2012)

7.5 Measurement capabilities of the newly installed SAXS instrument

E. Metwalli, P. Müller-Buschbaum

A state of the art in-house small-angle x-ray scattering (SAXS) instrument from SAXSLAB ApS-Denmark is installed in our x-ray laboratory. With this new machine (Fig. 7.8) we are capable of measuring SAXS/WAXS and GISAXS/GIWAXS of various types of materials in both, bulk and thin film format. The new instrument is equipped with a GENIX 3D micro-focus x-ray source (λ = 0.1542 nm), optics, a three-slit collimation system, a fully evacuated sample chamber and beam path, and a movable 2D Pilatus 300K detector. Sample-to-detector distance can vary between 106 mm and 1400 mm for WAXS, MAXS and SAXS measurements. The easy moving detector in a large evacuated tube allows us to make measurements over a very large q-range. The complete motorization of the system allows for ease of use and a high degree of automation in alignment and experiment execution [1].

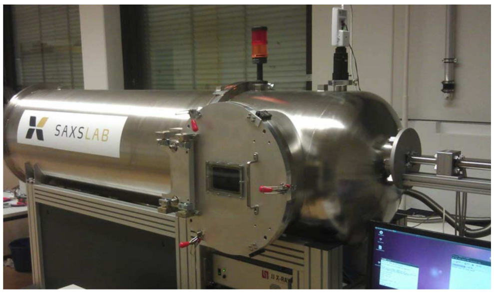

Figure 7.8: Photograph of the newly installed SAXS-WAXS instrument.

In the present report we demonstrate experiments on both, bulk and thin film polymer samples using SAXS/WAXS and GISAXS/GIWAXS, respectively. For the SAXS/WAXS measurements, the bulk sample was prepared using a 25 mg/mL solution of a P(S-*b*-EO) diblock copolymer (DBC) with $f_{(EO)}$ = 0.25. The bulk sample solution was brought on a thin mica window, where it was allowed to dry. After the complete drying of the sample, another mica window was used to sandwich it. The whole assembly was brought together using a stainless steel metal holder. This sample assembly allows x-ray transmission experiments (SAXS/WAXS). Fig. 7.9 shows two WAXS diffraction peaks of the DBC sample located at 13.7 nm^{-1} and 16.7 nm^{-1}. These peaks were observed at temperatures below 60 °C, which indicates that PEO is in the crystalline state. Additionally, the SAXS data (Fig. 7.9 b) indicate a lamellar morphology at temperatures below 60 °C; two ordered peaks at q/q^* = 1 and 2 with a related periodic distance of about 48 nm, are seen. Because the crystalline peaks vanish at temperatures above 60 °C , it is assumed that the PEO crystals melt at this temperature (Fig. 7.9 a). Correspondingly, the SAXS data indicate a micro-phase separation of the DBC at 60 °C (Fig. 7.9 b). The strong shift of the main SAXS characteristic peak to 0.21 nm^{-1} indicates a transition to cylindrical morphology with a periodic distance of about 30 nm (Fig. 7.9 b).

The GISAXS/GIWAXS measurements were performed on thin films (Fig. 7.10). The GISAXS image of the benzene vapor annealed P(S-*b*-EO) DBC thin film is presented in Fig. 7.10 b. The GISAXS data of the DBC film were collected at different beam sizes (vertical slits at 0.1, 0.2 and 0.5 mm). With decreasing slit size the resolution of the characteristic peak improves (see Fig. 7.10 c). The data from both, the SAXSLAB instrument (data acquisition time 20 h) and the P03 beamline of PETRAIII (DESY, Hamburg), are compared in Fig. 7.10 d) and indicate a fairly good resolution of our in-house system. The GIWAXS image (Fig. 7.10 a) of a thermally post-treated P3HT:PCBM blend film shows the (100) and (200) P3HT Bragg peaks with a low-intensity ring associated with PCBM, indicating that the PCBM content suppress the possible in-plane (010) P3HT reflections.

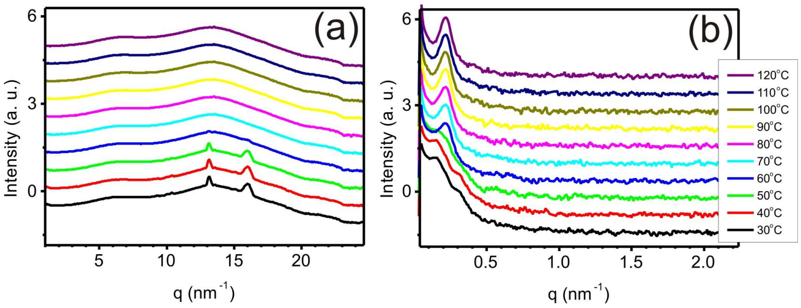

Figure 7.9:
(a) WAXS and (b) SAXS profiles of the bulk P(S-*b*-EO) DBC sample at different temperatures. The WAXS data show two diffraction peaks at temperatures below 60 °C. Correspondingly, in the SAXS data the position of the first order peak is abruptly shifted from 0.13 nm^{-1} to 0.21 nm^{-1} at 60 °C. This is a result of the melting PEO-crystals, establishing a micro-phase separation from lamellar to hexagonal morphology. Curves are shifted for clarity.

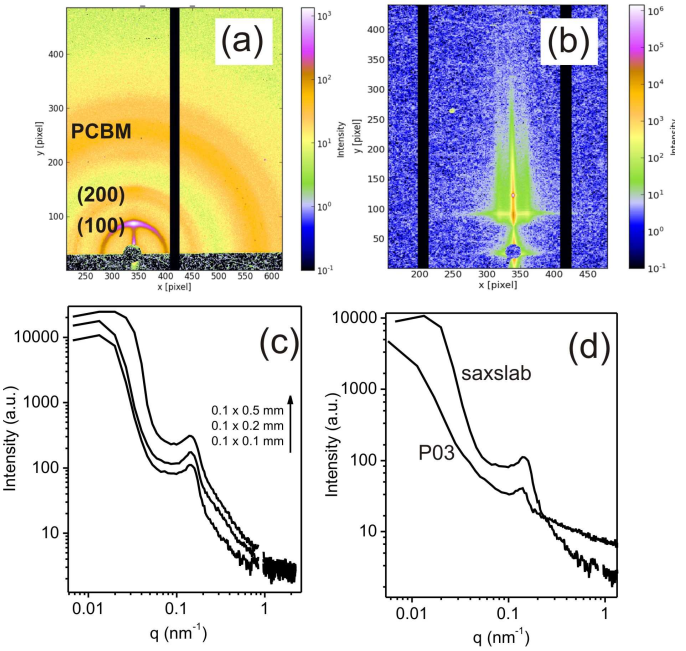

Figure 7.10:
(a) The GIWAXS data of the thermally post-treated P3HT:PCBM film; the grazing angle was 0.2°, SD distance 106 mm and exposure time 3 h, (b) GISAXS data of benzene vapor annealed P(S-*b*-EO) DBC thin film; the grazing angle was 0.45°, SD distance 1056 mm and exposure time 20 h, (c) horizontal line cuts of the 2D GISAXS data of the DBC film measured at different slit sizes; vertical slit is parallel to the sample surface, (d) Line cuts of the DBC film from both the SAXSLAB instrument and the P03 beamline (PETRA-III, DESY); incidence angle of 0.45°, SD distance 2080 mm and exposure time 3 s.

In summary, with our new instrument SAXS/WAXS and GISAXS/GIWAXS measurements are feasible with high quality, which allows for a good in-house characterization.

[1] Operator Manual: Ganesha 300XL SAXS-WAXS system (SAXSLAB ApS, Denmark)

7.6 Annealing of colloidal polystyrene thin films

G. Herzog[1], G. Benecke[1,2], A. Buffet[1], R. Gehrke[1], J. Perlich[1], M. Schwartzkopf[1], V. Körstgens, R. Meier, M. A. Niedermeier, M. Rawolle, M. A. Ruderer, P. Müller-Buschbaum, W. Wurth[3], S. V. Roth[1]

[1] DESY, Hamburg, Germany
[2] MPIKG Golm, Potsdam, Germany
[3] University Hamburg, Hamburg, Germany

The installation of colloidal thin films plays an important role in many areas of technology and science. Its range of applications stretches from paints [1] to sensors [2]. The most commonly used method to install such films is solution casting. However, in technological applications, the working temperature might exceed room temperature. Hence it is very important to investigate the structural stability of such colloidal thin films at elevated temperatures, for polymers typically around the glass transition temperature.

In recent studies we have extensively investigated in-situ the film formation using microbeam grazing incidence small angle x-ray scattering (GISAXS) in combination with nanofocus [3] or imaging ellipsometry [4,5]. Here we combine imaging ellipsometry [6] and annealing to investigate the thermal stability of polystyrene (PS) colloidal thin films with different end groups.

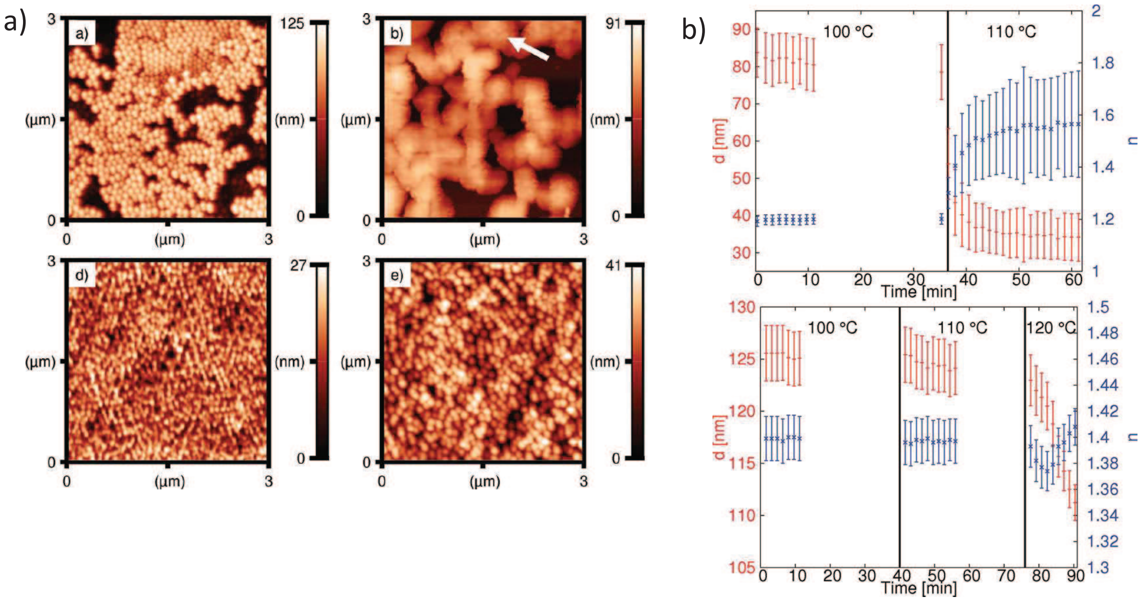

Figure 7.11:
Reprinted with permission from Herzog et al., Langmuir, 2012, 28 (21), pp 8230-8237, DOI: 10.1021/la3007348. Copyright 2012 American Chemical Society. a) AFM images of carboxylated (cPS) and pure (PPS) polystyrene colloidal thin films before and after crossing the glass transition temperature of PS. b) Colloidal height d and refractive index n obtained by imaging ellipsometry. The temperatures and annealing times are indicated.

The experiments presented here [7] were performed at the beamline BW4 of DESY, Hamburg, Germany. The wavelength was λ=0.138nm at a sample-to-detector distance of 1982mm and an incident angle of α_i=0.37°. The standard CCD detector (2048x2048 pixels, pixel size of 79.1μm) of BW4 was used. To obtain optical data in-situ an imaging ellipsometer - surface probe ellipsometric microscope (SPEM) by Accurion GmbH - was installed at the beamline in GISAXS geometry. The LASER wavelength was 532nm, the field of view 201x205 μm^2. In order to investigate the thermal stability temperatures upto 120°C were used, being well above the glass transition temperature of the PS films used. In addition, the thin films were investigated by atomic force microscopy prior and after thermal annealing. As sample we used carboxylated PS colloids as well as pure PS colloids (Kisker) having a nominal diameter of 96 nm. The thin films were installed by spin-coating on pre-cleaned Si wafer pieces.

Fig. 7.11a) shows AFM images obtained prior and after annealing of pure (PPS) and carboxylated PS (cPS) thin films (110°C and 120°C respectively). Clearly, a change in structure is visible. For PPS, the individual PS colloids seem to have merged in domains with sizes of some 100 nm. However, for cPS still individual colloids are visible. GISAXS pattern (not shown) taken during annealing show a loss of order by vanishing structural and form factor peaks. This change is accompanied by a decrease in height d of the colloids as seen by imaging ellipsometry. Fig. 7.11b) shows the height d and the refractive index n of the colloidal thin films. remarkably, when crossing the glass transition temperature (105°C) both samples show a decrease of d and an increase in n, being much more pronounced in the case of PPS. This proves clearly the influence of the end group of the colloids on the thermal stability.

To summarize, we have combined GISAXS, annealing and in-situ imaging ellipsometry to observe the temperature stability of PS films with different end-groups. While optical microscopy showed no difference, the nanoscopic methods including AFM clearly reveal drastic changes during temperature treatment.

[1] S. Hu, J. Rieger, S. V. Roth, R. Gehrke, R. J. Leyrer, Y. Men, *Langmuir* **25**, 4230-4234 (2009)

[2] R. Elghanian, J. J. Storhoff, R. C. Mucic, R. L. Letsinger, C. A. Mirkin, *Science* **277**, 1078 (1997)

[3] S. V. Roth, T. Autenrieth, G. Grübel, C. Riekel, M. Burghammer, R. Hengstler, L. Schulz, P. Müller-Buschbaum, *Appl. Phys. Lett.* **91**, 091915 (2007)

[4] S. V. Roth, G. Herzog, V. Körstgens, A. Buffet, M. Schwartzkopf, J. Perlich, M. M. Abul Kashem, R. Döhrmann, R. Gehrke, A. Rothkirch, K. Stassig, W. Wurth, G. Benecke, C. Li, P. Fratzl, M. Rawolle, P. Müller-Buschbaum, *J. Phys: Cond. Matter* **23**, 254208 (2011)

[5] V. Körstgens, J. Wiedersich, R. Meier, J. Perlich, S.V. Roth, R. Gehrke, P. Müller-Buschbaum, *Anal. Bioanal. Chem.* **396**, 139-149 (2010)

[6] V. Körstgens, R. Meier, M. A. Ruderer, S. Guo, H.-Y. Chiang, J. Perlich, S. V. Roth, R. Gehrke, P. Müller-Buschbaum, *Rev. Sci. Instrum.* **83**, 076107 (2012)

[7] G. Herzog, M. Abul Kashem, G. Benecke, A. Buffet, R. Gehrke, J. Perlich, M. Schwartzkopf, V. Körstgens, R. Meier, M. Niedermeier, M. Rawolle, Monika, M. Ruderer, P. Müller-Buschbaum, W. Wurth, S. V. Roth, *Langmuir* **28**, 8230-8237 (2012)

7.7 Ordering during directional drying in organic thin films: An in-situ grazing-incidence X-ray scattering study

J. Perlich[1], V. Körstgens, M. Schwartzkopf[1], G. Santoro[1], S. Yu[1], P. Müller-Buschbaum, S. V. Roth[1]

[1] DESY, Hamburg, Germany

The dip-coating technique is one of the commonly applied methods for the preparation of thin films or the patterning of templates from polymer solutions and particle suspensions [1]. The coating principle is based on the withdrawal of a solid substrate out of a liquid solution. The withdrawal and supposed deposition of a specific material are mainly governed by the withdrawal speed and the physical as well as chemical sample surface properties [1]. Hence these parameters determine whether the deposition yields the desired patterning result. In this regard, Ghosh et al. prepared stripe-like pattern and demonstrated the dependence of the deposition as a function of particle diameter, withdrawal speed and entrained film thickness to come up with different deposition modes [2]. The technique is based on a drying process, the so-called directional drying, involving the natural propagation of drying fronts across the liquid film. Solidification starts from the film edge and progresses towards the middle, whereas three distinct transitions are identified: ordering, aggregation and dewetting [3]. Roth et al. investigated recently the air-water-substrate boundary of a horizontally drying droplet of colloidal solution obtaining a quantitative view of the solidification and ordering [4]. However, the directional drying during dip-coating involves the drawing speed as additional parameter. For a full understanding of the drying process, several parameters are of interest, i.e. film height, particle concentration and structure height at any given time during drying at a fixed spot on the sample surface are of interest. Based on this complex knowledge, the evaporation profile over the liquid film and occurring flows could be extracted.

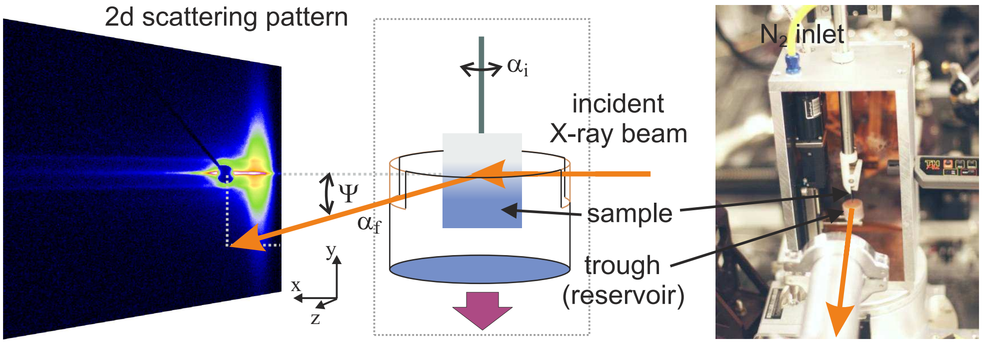

Figure 7.12:
Experimental GISAXS geometry and setup photograph. During the in situ real-time dip-coating study the trough moves vertically, whereas the sample exhibits a stationary position.

The investigation of the vertical drying process during dip-coating is performed by microbeam grazing incidence small angle X-ray scattering (μGISAXS) as non-destructive, surface sensitive probe revealing the structure at the vicinity of the drying fronts as shown in the scheme in Fig. 7.12. With the selected measurement configuration, a fixed spot on the sample surface is probed and the structural information at the time the drying fronts pass through the beam-illuminated area is obtained [5].

Recent experiments have been performed at beamline P03 MiNaXS of the PETRA III storage ring using a micro-focused beam ($\lambda = 0.096$ nm) with a size 6×4 μm^2 (h × v) enabling improved lateral resolution [6]. The distance between the sample and detector was set to $D_{SD} = 4590$ mm.

Fig. 7.13 presents the results of the simultaneous GISAXS measurements of the dip-coating process of a model system of polystyrene nanoparticles ($2R$ = 194 nm) in an aqueous suspension with a drawing speed of 2.25 mm/min at 10 frames per second (fps). The final scattering pattern at time $t = \tau$ in Fig. 7.13(a) clearly indicates the successful deposition of the thin colloidal film with a highly ordered hexagonal array of PS nanoparticles.

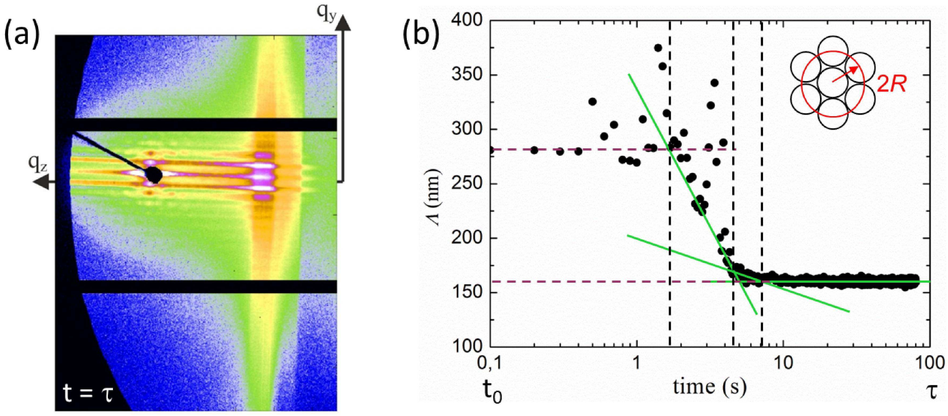

Figure 7.13:
(a) 2d GISAXS data of the final dip-coated thin film of PS nanoparticles. (b) Extracted characateristic in-plane length scale Λ as a function of the drying time t.

The evolution ($t_0 \to \tau$) to the final particle arrangement is represented by the extracted characateristic in-plane length scale Λ as a function of the drying time t as shown in Fig. 7.13(b). The appearing peak at q = 0.0224 nm^{-1} becomes more pronounced and shifts towards q' = 0.0395 nm^{-1} (hor. dashed lines), hence decreasing the characateristic in-plane length scale Λ from 280 nm down to 159 nm. Furthermore, distinct transition regions (vert. dashed lines) upon solvent evaporation are clearly identified by the change in slope of $\Lambda(t)$ [7].

The successful experiments at MiNaXS on the pattern formation of drying colloidal suspensions illustrate strikingly the very high potential of advanced scattering experiments in grazing incidence. The experimental setup provides the required high precision for gracing incidence sample alignment and enables real-life conditions under controlled environment. Due to the improved time-resolution by a factor of 100 (0.1 fps → 10 fps), the identification of distinct transition regions is possible [5, 7]. However, further analysis, i.e. peak heights and widths, yields concentration profile is required and a more detailed investigation of the process key parameters will be performed with purely colloidal suspensions as well as the successive patterning of these prepared colloidal templates with different species of nanoparticles.

[1] L. E. Scriven, *Mater. Res. Soc. Symp. Proc.* **121**, 717-729 (1988)

[2] M. Ghosh, F. Fan, K. J. Stebe, *Langmuir* **23**, 2180-2183 (2007)

[3] J. Li, B. Cabane, M. Sztucki, J. Gummel, L. Goehring, *Langmuir* **28**, 200-208 (2012)

[4] S. V. Roth, A. Rothkirch, T. Authenrieth, R. Gehrke, T. Wroblewski, M. Burghammer, C. Riekel, L. Schulz, R. Hengstler, P. Müller-Buschbaum, *Appl. Phys. Lett.* **91**, 091915 (2007)

[5] J. Perlich, M. Schwartzkopf, V. Körstgens, D. Erb, J. F. H. Risch, P. Müller-Buschbaum, R. Röhlsberger, S. V. Roth, R. Gehrke, *phys. stat. sol. RRL* **6**, 253-255 (2012)

[6] A. Buffet, A. Rothkirch, R. Döhrmann, V. Körstgens, M. M. Abul Kashem, J. Perlich, G. Herzog, M. Schwartzkopf, R. Gehrke, P. Müller-Buschbaum, S. V. Roth, *J. Synchr. Rad.* **19**, 647-653 (2012)

[7] J. Perlich, V. Körstgens, M. Schwartzkopf, G. Santoro, S. Yu, P. Müller-Buschbaum, S. V. Roth, *in preparation*

7.8 Detachment of model biofilms in micro-fluidic systems investigated with GISAXS

V. Körstgens, S. V. Roth[1], P. Müller-Buschbaum

[1] HASYLAB at DESY, Hamburg, Germany

Biofilms are films of microbial origin found at solid-liquid interfaces mostly in aqueous environments. In these films microorganisms are dispersed in a matrix of extracellular substances (e.g. proteins and polysaccharides). Biofilms one may experience in daily life are dental plaque or the detrimental coatings which build up in water and waste water systems. These films have in common that they have a gel-like character with a certain mechanical stability [1]. Biofilms lead to problems in macroscopic aqueous systems such as industrial or household water distribution and heat exchanger systems as well as in aqueous micro-fluidic systems. For the removal of these biofilms it is essential that the right strategy is chosen. It is possible that the most detrimental effects of biofilms are initiated by a wrongly chosen cleaning procedure. For example if the chosen cleaning method leads to a dispersion of viable microorganisms, the microbial biofilm may spread. Also the detachment of comparable large patches of biofilm from the surface is not helpful as e.g. filters in macroscopic water systems may block. The blocking problem applies to micro-fluidic systems in particular. The in-situ investigation of model biofilms with grazing incidence small angle x-ray scattering (GISAXS) offers the opportunity for a better understanding of detachment processes.

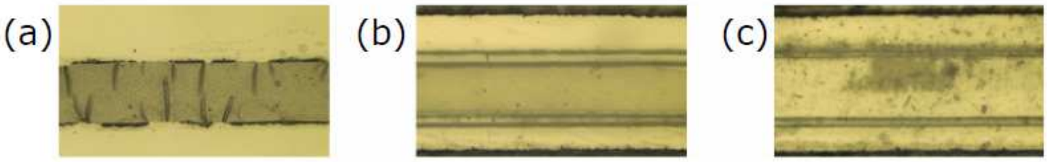

Figure 7.14:
Investigated films in top view a) stripe of film on glass substrate b) film in micro-fluidic cell after flow of water c) desintegrated film with remaining patches after longer flow

In this study films consisting of sodium alginate and dispersed spherical polystyrene nanoparticles of 105 nm diameter were put onto pre-cleaned glass slides by blade coating. The films are produced as small stripes of 2 cm length with a width below 1 mm that they fit exactly in the channel of our micro-fluidic cell design developed for GISAXS measurements in our group [1, 2]. In Fig. 7.14a such film is shown after cross-linking with calcium ions by rinsing with $CaCl_2$. The film shows some wrinkles after gelation, which disappear after the exposure to water in the micro-fluidic channel (Fig. 7.14b). After running the micro-fluidic experiment with a solution of a complexing agent for calcium ion a disintegration of the film with some remaining patches can be observed (Fig. 7.14c). Whereas the information gained with the microscope is more or less restricted to the basic information if the surface is still covered with a film or not, structural information about the film is accessible with GISAXS. For the GISAXS experiment a micro-focused x-ray beam hits the surface under a shallow angle resulting in a footprint slightly larger than the width of the micro-fluidic channel. The micro-focused beam allows for scanning along the y-direction of the channel while water flows through the channel with 0.01 ml min^{-1}. The fluid flow direction is opposite to the scanning direction of the channel. For the investigation shown in Fig. 7.15 subsequent measurements of 1 s in 125 μm distance are recorded with a Pilatus detector. From these 2d GISAXS data composite images out of individual vertical (Fig. 7.15a) and horizontal line cuts (Fig. 7.15b) clearly show the first complete filling of the channel (marked with a red arrow in Fig. 7.15). The individual frames before the red arrow ($n < 15$) correspond to the dry film. The respective q_y-scattering curves representing lateral structures show two distinct shoulders. With water contact one shoulder transforms into a more prominent peak whereas the shoulder at larger q_y-values disappears. With ongoing flow of water the scattering curve indicate the presence of larger structures. The experiment shown here covers the first minutes of micro-fluidic flow only, at which the structure changes but a mechanically stable film remains as shown in Fig. 7.14b.

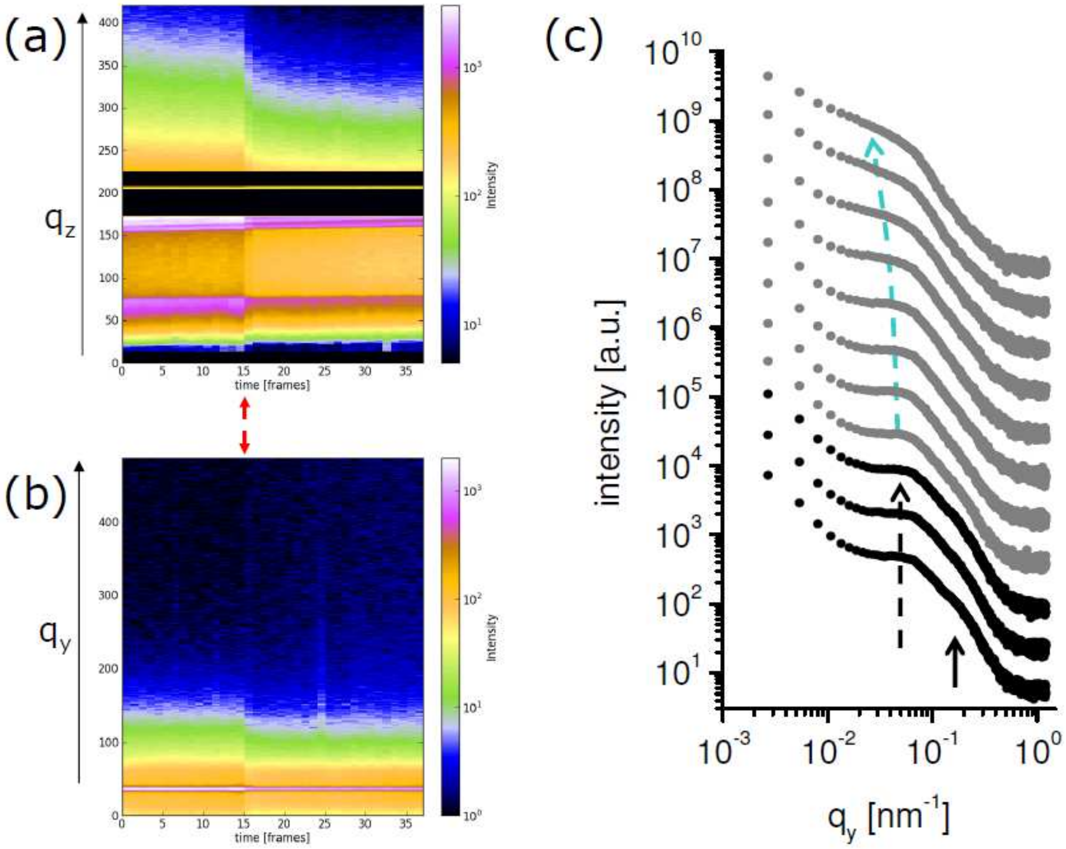

Figure 7.15:
Micro-fluidic experiment with a calcium cross-linked alginate film with dispersed polystyrene spheres a) composite image of vertical (detector) cuts b) composite image of horizontal (out of plane) cuts c) out of plane cuts with sum of 3 measurements in juxtaposition; the grey curves mark the measurements at which the channel is completely filled with liquid

Based on this study the detachment processes of model biofilms in micro-fluidic systems are accessible. The aim of future investigations is the variation of the flow rates and the experimental observation for longer times. Furthermore a closer adaptation of the model films to natural biofilms regarding the cohesive and adhesive properties is desired. With a conclusive biofilm model also the investigation of the effect of cleaning agents becomes of interest.

This work has been financially supported by the BMBF (grant number 05K10WOA).

[1] V. Körstgens, H. C. Flemming, J. Wingender, W. Borchard, *J. Microbiol. Meth.* **46**, 9-17 (2001)

[2] J.-F. Moulin, S. V. Roth, P. Müller-Buschbaum, *Rev. Sci. Instrum.* **79**, 015109 (2008)

[3] E. Metwalli, J.-F. Moulin, J. Perlich, W. Wang, A. Diethert, S. V. Roth, P. Müller-Buschbaum, *Langmuir* **25**, 11815-11821 (2009)

7.9 Ultrananocrystalline diamond - a grazing-incidence small-angle X-ray scattering study

I. Staudinger, A. Sepe, J. Perlich[1], S.V. Roth[1], S. Ghodbane[2], D. Steinmüller-Nethl[2], H. Sternschulte[3], C. M. Papadakis

[1] HASYLAB at DESY, Hamburg, Germany
[2] KOMET rhoBeSt GmbH, Innsbruck, Austria
[3] nanoTUM, TU München, Garching, Germany

Ultra nanocrystalline diamond (UNCD) films feature crystallites smaller than 10 nm and a smooth surface; thus, they represent a homogeneous and isotropic material (Fig. 7.16, [1]). Furthermore, both p- and n-type doped UNCD films are available with high carrier concentrations, a requirement for applications in sensing-devices based, for instance, on electrochemistry. UNCD films are grown in a chemical vapour deposition process with a high secondary nucleation rate. The obtained films are composed of separated single crystal diamond grains with rounded shapes which are embedded randomly oriented in an amorphous carbon-hydrogen matrix. To obtain information about the grain size and the distance of the grains in the matrix, UNCD films are usually studied by transmission electron microscopy (TEM), which, however requires a highly sophisticated preparation. An alternative method to obtain information about the structural film properties is grazing-incidence small-angle X-ray scattering (GISAXS). This technique allows the determination of the shape of the grains, their size and size distribution as well as the distances between the grains without any sample preparation. Furthermore, due to the much larger probe area defined by the spot size of the X-rays on the sample surface, the data have excellent sampling statistics. For the first time, we studied UNCD films with GISAXS [2]. For the analysis of the GISAXS data, information about the scattering length density (SLD) and the surface roughness of the UNCD film are required. Both parameters have been determined independently by X-ray reflectometry (XRR) measurements.

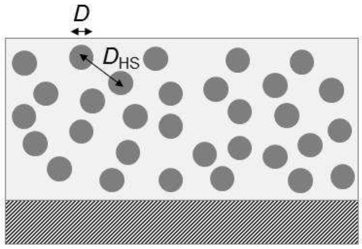

Figure 7.16:
Model used for calculating the scattering from UNCD films. The spheres indicate the cystallites in the amorphous film. D denotes the sphere diameter, D_{HS} the center-to-center distance between spheres.

An undoped UNCD film with homogeneous film thickness of 3.8 μm was deposited on pre-cleaned (2 cm $\times$ 3 cm) cm^2 Si(001) substrates by using a modified hot filament technique with a precursor gas mixture of pure CH$_4$ and H$_2$. To obtain a plane sample, the substrate temperature had to remain in the range of 760-770°C all along the diamond growth process. XRR measurements were carried out using a D5000 diffractometer (Siemens). The XRR curve was fitted with a model of a homogeneous film on a substrate. This way, the surface roughness as well as the scattering length density and the absorption of the film were determined. GISAXS measurements were performed at beamlines BW4 and P03, both at HASYLAB, DESY, Hamburg. As detectors, a MarCCD camera or PILATUS 300k were used. Incident angles α_i were chosen both below and above the critical angles of the UNCD film. All measurements were taken at pristine spots to avoid potential effects of beam damage. The GISAXS images were modelled using the FitGISAXS software [3] which is based on the distorted-wave Born approximation. The scattering length densities and the absorption values measured by XRR were used as input parameters. The diamond nanoparticles were modeled as monodisperse spheres of diameter D

(Fig. 7.16). Their correlation within the film plane was approximated as a two-dimensional liquid. As a fitting parameter, the ratio of the centre-to-centre distance between the spheres, D_{HS}, and D, was used. The hard-sphere volume fraction, η_{HS}, was fixed at 0.1. Since the refractive index values of all layers are similar, the model "Buried layer" was used, i.e. the spheres are homogeneously distributed between the film surface and a depth of 3 μm, and the refractive index of the matrix of the film matrix was assumed to be equal to the one of the substrate.

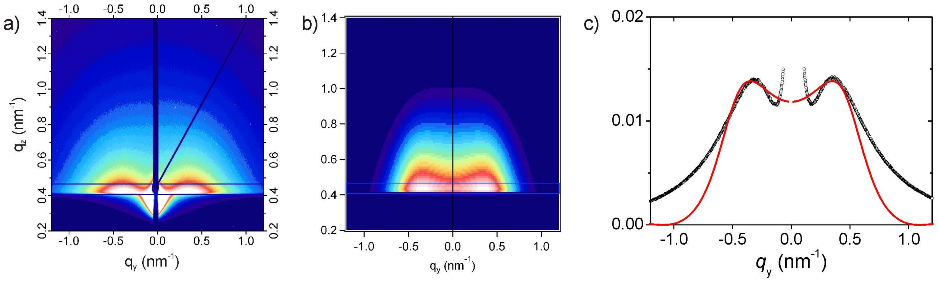

Figure 7.17:
(a) Measured GISAXS images at the incident wave vectors having a z-component $k_{iz} = 0.239$ nm^{-1}. The blue lines parallel to q_y denote the regions over which was integrated to obtain the profiles in (c). (b) Corresponding simulated image and (c) intensity profile (black circles) and model curve (red line).

A representative 2D image is shown in Fig. 7.17a. Intensity maxima are visible at $q_y = 0.28-0.36$ nm^{-1} which have a round shape and extend from the horizon to higher q_z values. Their intensity decays towards high q_z values due to the scattering geometry in grazing incidence. These maxima are caused by the scattering from the diamond nanocrystallites which have an electron density different from the surrounding amorphous matrix and a certain average distance from each other. The model resulted consistently in the 2D image showing scattering of similar shape as the experimental one (Fig. 7.17b). The sphere diameter, D, and the average centre-to-centre distance of the spheres, D_{HS}, were determined from 1D line profiles summed over a stripe narrow in q_z and extending along q_y (Fig. 7.17c). It is positioned such that it includes the region of strong intensity at $q_z = 0.4 - 0.5$ nm^{-1}, depending on k_{iz}. In these profiles, the q_y positions and the peak heights were matched by varying the parameters. At this, the increasing intensity towards $q_y = 0$ was not taken into account. Then, the 2D GISAXS image was generated and the overall shape of the intensity maxima in the 2D images was verified.

This procedure resulted for all images in $D = 8.0-8.5$ nm and $D_{HS} = 10.4-11.9$ nm. With these values, the model used describes the 2D images in a satisfactory way. Only at high q_y values (above ca. 0.5 nm^{-1}), the model curve decays too steeply. This may be due to the monodisperse approximation. Moreover, the TEM images from similar UNCD samples suggest that the crystallites are slightly elongated with a random orientational distribution. Such a distribution can, however, not be modelled in the present version of the FitGISAXS software.

We conclude that the diamond crystallites are close to spherical and do not touch each other but there is a minimum distance between them of $2-4$ nm. GISAXS gave statistically relevant information in a non-destructive way.

[1] D.M. Gruen, *Annu. Rev. Mater. Sci.* **29**, 211-259 (1999)

[2] H. Sternschulte, I. Staudinger, A. Sepe, C. M. Papadakis, J. Perlich, S. V. Roth, S. Ghodbane, D. Steinmüller-Nethl, submitted

[3] D. Babonneau, *J. Appl. Crystallogr.* **43**, 929-936 (2010)

8 Teaching and outreach

8.1 Lectures, seminars and lab courses

Spring semester 2012

Prof. Dr. Peter Müller-Buschbaum, *Experimentalphysik 2 für Maschinenwesen*
Prof. Dr. Peter Müller-Buschbaum, *Angewandte Physik: Polymerphysik 2*
Prof. Dr. Christine M. Papadakis, *Grundlagen der Experimentalphysik 2 (LB-Technik)*
Prof. Dr. Christine M. Papadakis, *Nanostructured Soft Materials II*
Prof. Dr. Peter Müller-Buschbaum, Prof. Dr. Christine M. Papadakis, *Seminar über Struktur und Dynamik kondensierter Materie*
Prof. Dr. Peter Müller-Buschbaum, Prof. Dr. Christine M. Papadakis, *Studentenseminar: Grundlegende Phänomene der Physik der weichen Materie*
Prof. Dr. Peter Müller-Buschbaum, Prof. Dr. Christine M. Papadakis, *Seminar: Polymere*
Prof. Dr. Peter Müller-Buschbaum, Prof. Dr. Christine M. Papadakis, *Bachelor-Seminar: Funktionelle weiche Materialien*
Prof. Dr. Peter Müller-Buschbaum, *Tutorenseminar zur Vorlesung Experimentalphysik 2 für Maschinenwesen*
Prof. Dr. Winfried Petry, Prof. Dr. Peter Böni, Prof. Dr. Wolfgang Häußler, Prof. Dr. Klaus Schreckenbach, *Seminar über Neutronen in Forschung und Industrie*
Prof. Dr. Winfried Petry, *Blockseminar Erasmus Mundus MaMaSELF Summerschool*

Fall semester 2012/2013

Prof. Dr. Peter Müller-Buschbaum, *Angewandte Physik: Polymerphysik 1*
Prof. Dr. Christine M. Papadakis, *Grundlagen der Experimentalphysik 1 (LB-Technik)*
Prof. Dr. Christine M. Papadakis, *Nanostructured Soft Materials 1*
Prof. Dr. Peter Müller-Buschbaum, Prof. Dr. Christine M. Papadakis, *Seminar über Struktur und Dynamik kondensierter Materie*
Prof. Dr. Peter Müller-Buschbaum, Prof. Dr. Christine M. Papadakis, *Studentenseminar: Grundlegende Phänomene der Physik der weichen Materie*
Prof. Dr. Peter Müller-Buschbaum, Prof. Dr. Christine M. Papadakis, *Seminar: Polymere*
Prof. Dr. Winfried Petry, Prof. Dr. Peter Böni, Prof. Dr. Wolfgang Häußler, Prof. Dr. Klaus Schreckenbach, *Seminar über Neutronen in Forschung und Industrie*

Lab courses 2012

Theoretische und praktische Einführung in AFM (Fortgeschrittenenpraktikum)
Thermische Analyse (Fortgeschrittenenpraktikum)
Neutronenstreuung am FRM II (Fortgeschrittenenpraktikum)
JCNS Laboratory Course - Neutron Scattering (Forschungspraktikum)

8.2 Conferences and public outreach

C. M. Papadakis
Tag der Physikerin
Garching, 15 Feb 2012

Tag der Physikerin

Mittwoch, 15. Februar 2011, 15.00-17:30 Uhr
Physik-Department, TU München, Garching
Hörsaal 3

15.00 h Begrüßung
Dekan Prof. Dr. Martin Stutzmann

15.15 h High Energy Neutrinos
from the South Pole
Prof. Dr. Elisa Resconi
Excellenzcluster „Universe“,
TU München

16.00 h Postersitzung im Foyer
Imbiss und Gespräch

Eine Veranstaltung des Dekanats,
der Frauenbeauftragten des Physik-Departments
und des TUM Gender-Zentrums.

Eingeladen sind Studentinnen und Studenten,
Wissenschaftlerinnen und Wissenschaftler,
Schülerinnen und Schüler und andere Interessierte.

P. Müller-Buschbaum, W. Petry
Lehrerfortbildung 'Elektromobilität: Grundlagen, Konzepte'
36. Edgar-Lüscher-Seminar
Zwiesel, 20 – 22 Apr 2012

Programm

Freitag, 20. April 2012

13.00 - 14.30	Studienberatung der TUM
15.00 - 15.30	Begrüßung
15.30 - 16.45	**Grundlagen der Elektromobilität** *Prof. Dr. Hartmut Schneck, KIT*
16.45 - 17.00	Diskussion
17.00 - 18.15	**Schlüsseltechnologie Batteriespeicher - Stand der Technik und Entwicklungsprognosen** *Prof. Dr. Andreas Jossen, TUM*
18.15 - 18.30	Diskussion
ab 19.30	Empfang der Stadt Zwiesel (Rathaus)

Samstag, 21. April 2012

09.00 - 10.15	**Elektromobilität aus der Sicht der Energieinformatik** *Dr. Martin Sachenbacher, TUM*
10.15 - 11.00	Diskussion und Kaffeepause
11.00 - 12.15	**Brennstoffzellentechnologie** *Prof. Dr. Hubert Gasteiger, TUM*
12.15 -12.30	Diskussion
14.30 - 15.45	**Exergieanalyse und die thermodynamische Bewertung von Energiewandlungsprozessen** *Prof. Dr. Katharina Krischer*
15.45 - 16.30	Diskussion und Kaffeepause
16.30 - 17.45	**Das MUTE-Projekt der TUM** *Dipl.-Ing. Thomas Hierlinger, TUM*
17.45 - 18.00	Diskussion

Sonntag, 22. April 2012

09.00 - 10.15	**Das Shell Eco-marathon-Fahrzeug der Hochschule München** *Prof. Dr. Jochen Melzer, Hochschule München* **Vergleich von Wasserstoff- und Methanolbrennstoffzellen für den mobilen Einsatz im Fahrzeug** *Erika Schwab, Hochschule München*
10.15 - 11.00	Diskussion und Kaffeepause
11.00 - 12.15	**E-WALD: Elektromobilität Bayerischer Wald** *Prof. Dr. Peter Sperber, Hochschule Deggendorf*
12.15 - 13.00	Diskussion, Themenfindung für das 37. Seminar

Organisation

Prof. Dr. Peter Müller-Buschbaum
TUM

Prof. Müller-Buschbaum befasst sich in seiner Forschungsarbeit mit der Entwicklung polymerbasierter Materialien mit neuartigen Struktur-Eigenschaftsbeziehungen. Strukturen aus leitfähigen Polymeren und deren Anwendungen für die Photovoltaik sind ein Schwerpunkt der Arbeiten.

Prof. Dr. Winfried Petry
TUM

Prof. Petry ist Ordinarius am Lehrstuhl E13 des Physik-Departments, Leiter des Prüflabors für Technische Physik, wissenschaftlicher Direktor der Forschungsneutronenquelle Heinz Maier-Leibnitz (FRM-II), Betreuungsprofessor des Physik Departments für die Bayerische Elite-Akademie und Vorsitzender der Arbeitsgemeinschaft Metall- und Materialphysik der Deutschen Physikalischen Gesellschaft.

Organisatorische Hinweise

Organisation vor Ort:

OStD Hans-Werner Janda,	*Gymnasium Zwiesel*
StD Wolfgang Achatz,	*Gymnasium Zwiesel*
StR Claus Starke,	*Gymnasium Zwiesel*
StR Christian Stoiber,	*Gymnasium Zwiesel*

Email:
sekretariat@gymnasium-zwiesel.de

Hinweise:

- Alle Veranstaltungen finden in der Aula des Gymnasiums Zwiesel statt. Die Teilnehmer erhalten am Ende des Seminars für 5,- € eine CD mit sämtlichen Vorträgen.
- Die Mensa des Gymnasiums ist während des Seminars geöffnet (Mittagessen, Kaffeepausen).
- Buch- und Lehrmittelausstellung in der Aula.

Titelfoto: © Torsten Rempt / PIXELIO

36. Edgar-Lüscher-Seminar

am Gymnasium Zwiesel
Freitag, 20. April, bis Sonntag, 22. April 2012

Elektromobilität: Grundlagen, Konzepte

Schirmherr:
Prof. Dr. Dr. h.c. mult. Wolfgang Herrmann,
Präsident der TUM

Veranstalter:
Ltd. OStD Klaus Drauschke,
Ministerialbeauftragter für die Gymnasien in Niederbayern

Wissenschaftliche Leitung:
Prof. Dr. Peter Müller-Buschbaum, *TUM*
Prof. Dr. Winfried Petry, *TUM*

P. Müller-Buschbaum, C. M. Papadakis
E13 Summer School
Rudolfshütte, Uttendorf/Weißsee, Austria, 12 – 15 Jun 2012

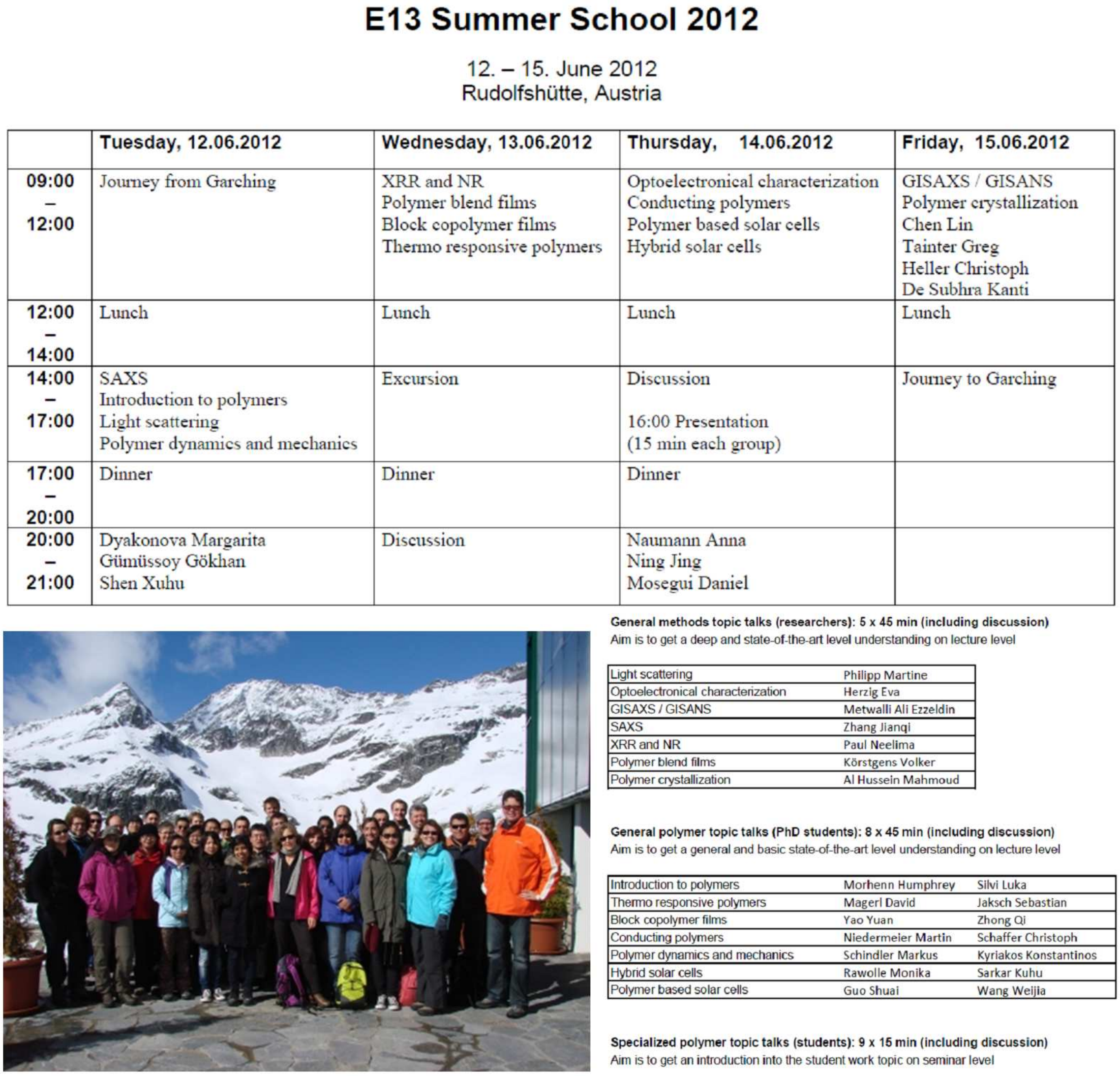

E13 Summer School 2012

12. – 15. June 2012
Rudolfshütte, Austria

	Tuesday, 12.06.2012	**Wednesday, 13.06.2012**	**Thursday, 14.06.2012**	**Friday, 15.06.2012**
09:00 – 12:00	Journey from Garching	XRR and NR Polymer blend films Block copolymer films Thermo responsive polymers	Optoelectronical characterization Conducting polymers Polymer based solar cells Hybrid solar cells	GISAXS / GISANS Polymer crystallization Chen Lin Tainter Greg Heller Christoph De Subhra Kanti
12:00 – 14:00	Lunch	Lunch	Lunch	Lunch
14:00 – 17:00	SAXS Introduction to polymers Light scattering Polymer dynamics and mechanics	Excursion	Discussion 16:00 Presentation (15 min each group)	Journey to Garching
17:00 – 20:00	Dinner	Dinner	Dinner	
20:00 – 21:00	Dyakonova Margarita Gümüssoy Gökhan Shen Xuhu	Discussion	Naumann Anna Ning Jing Mosegui Daniel	

General methods topic talks (researchers): 5 x 45 min (including discussion)
Aim is to get a deep and state-of-the-art level understanding on lecture level

Light scattering	Philipp Martine
Optoelectronical characterization	Herzig Eva
GISAXS / GISANS	Metwalli Ali Ezzeldin
SAXS	Zhang Jianqi
XRR and NR	Paul Neelima
Polymer blend films	Körstgens Volker
Polymer crystallization	Al Hussein Mahmoud

General polymer topic talks (PhD students): 8 x 45 min (including discussion)
Aim is to get a general and basic state-of-the-art level understanding on lecture level

Introduction to polymers	Morhenn Humphrey	Silvi Luka
Thermo responsive polymers	Magerl David	Jaksch Sebastian
Block copolymer films	Yao Yuan	Zhong Qi
Conducting polymers	Niedermeier Martin	Schaffer Christoph
Polymer dynamics and mechanics	Schindler Markus	Kyriakos Konstantinos
Hybrid solar cells	Rawolle Monika	Sarkar Kuhu
Polymer based solar cells	Guo Shuai	Wang Weijia

Specialized polymer topic talks (students): 9 x 15 min (including discussion)
Aim is to get an introduction into the student work topic on seminar level

C. M. Papadakis, S. Jaksch
Workshop 'Gummibärchen, volle Windeln und tanzender Matsch – physikalische und chemische Gele'
in the framework of the program 'Innovative Naturwissenschaften TUM-WHG',
Werner-Heisenberg-Gymnasium Garching
19 Jun 2012

"Dancing mud and full diapers - physical and chemical gels" - this was the motto of the lesson held by Prof. Christine Papadakis and her coworkers in the compulsory optional subject Chemisty. The pupils prepared investigated gels from superabsorbers as they are used in diapers or concrete. Then, they made gummi bears from gelatine and syrup and put them in the fridge over night. Finally, they prepared mud from starch and water and made it dance on a loud speaker. This way, the pupils saw different examples for chemically cross-linked, thermoreversible and physical gels. They were enthusiastic and discovered that physics is not necessarily dry and boring! The day after, they tried the gummi bears which actually tasted quite good. This lesson was part of the cooperation program between TUM and the WHG in which pupils of the 8th grade learn about the different research directions present at TUM.

W. A. Herrmann, W. Lang, M. Lienkamp, P. Müller-Buschbaum, H. Spliethoff, U. Stimming
Colloqium 'Energy Challenges Germany 2050'
2nd Colloquium of the Munich School of Engineering
28 Jun 2012

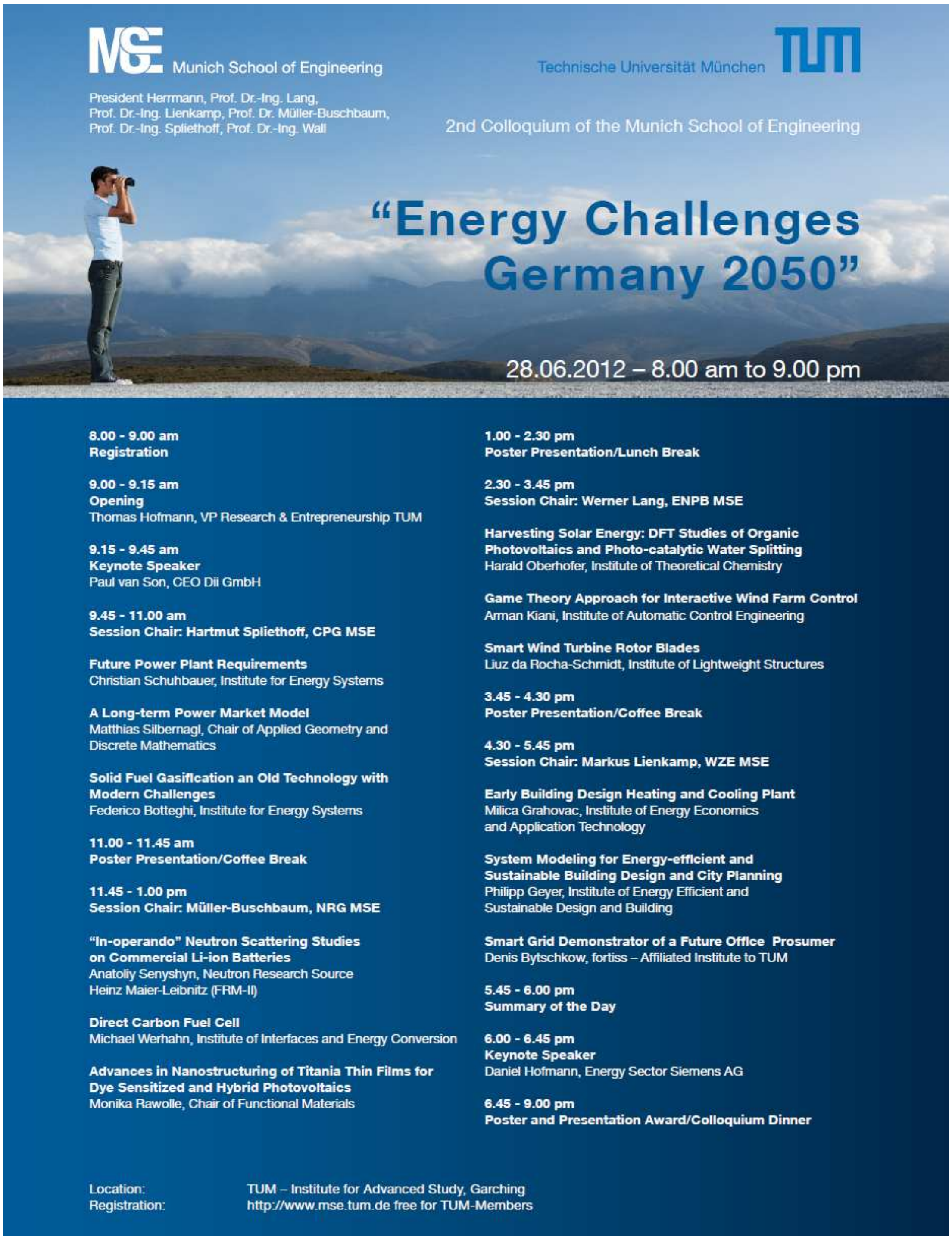

Munich School of Engineering

President Herrmann, Prof. Dr.-Ing. Lang,
Prof. Dr.-Ing. Lienkamp, Prof. Dr. Müller-Buschbaum,
Prof. Dr.-Ing. Spliethoff, Prof. Dr.-Ing. Wall

Technische Universität München

2nd Colloquium of the Munich School of Engineering

"Energy Challenges Germany 2050"

28.06.2012 – 8.00 am to 9.00 pm

8.00 - 9.00 am
Registration

9.00 - 9.15 am
Opening
Thomas Hofmann, VP Research & Entrepreneurship TUM

9.15 - 9.45 am
Keynote Speaker
Paul van Son, CEO Dii GmbH

9.45 - 11.00 am
Session Chair: Hartmut Spliethoff, CPG MSE

Future Power Plant Requirements
Christian Schuhbauer, Institute for Energy Systems

A Long-term Power Market Model
Matthias Silbernagl, Chair of Applied Geometry and Discrete Mathematics

Solid Fuel Gasification an Old Technology with Modern Challenges
Federico Botteghi, Institute for Energy Systems

11.00 - 11.45 am
Poster Presentation/Coffee Break

11.45 - 1.00 pm
Session Chair: Müller-Buschbaum, NRG MSE

"In-operando" Neutron Scattering Studies on Commercial Li-ion Batteries
Anatoliy Senyshyn, Neutron Research Source Heinz Maier-Leibnitz (FRM-II)

Direct Carbon Fuel Cell
Michael Werhahn, Institute of Interfaces and Energy Conversion

Advances in Nanostructuring of Titania Thin Films for Dye Sensitized and Hybrid Photovoltaics
Monika Rawolle, Chair of Functional Materials

1.00 - 2.30 pm
Poster Presentation/Lunch Break

2.30 - 3.45 pm
Session Chair: Werner Lang, ENPB MSE

Harvesting Solar Energy: DFT Studies of Organic Photovoltaics and Photo-catalytic Water Splitting
Harald Oberhofer, Institute of Theoretical Chemistry

Game Theory Approach for Interactive Wind Farm Control
Arman Kiani, Institute of Automatic Control Engineering

Smart Wind Turbine Rotor Blades
Liuz da Rocha-Schmidt, Institute of Lightweight Structures

3.45 - 4.30 pm
Poster Presentation/Coffee Break

4.30 - 5.45 pm
Session Chair: Markus Lienkamp, WZE MSE

Early Building Design Heating and Cooling Plant
Milica Grahovac, Institute of Energy Economics and Application Technology

System Modeling for Energy-efficient and Sustainable Building Design and City Planning
Philipp Geyer, Institute of Energy Efficient and Sustainable Design and Building

Smart Grid Demonstrator of a Future Office Prosumer
Denis Bytschkow, fortiss – Affiliated Institute to TUM

5.45 - 6.00 pm
Summary of the Day

6.00 - 6.45 pm
Keynote Speaker
Daniel Hofmann, Energy Sector Siemens AG

6.45 - 9.00 pm
Poster and Presentation Award/Colloquium Dinner

Location:	TUM – Institute for Advanced Study, Garching
Registration:	http://www.mse.tum.de free for TUM-Members

P. Müller-Buschbaum, S. V. Roth
Colloquium 'The polymer metal interface'
3rd TUM – HASYLAB Colloquium
Garching, 10 – 11 Sep 2011

3rd Colloquium TUM-HASYLAB "The polymer metal interface"
date: Monday, 10. September to Tuesday, 11. September 2012
venue: Physik-Department, Seminarraum E13
Technische Universität München

Program

Monday, 10. 09. 2012
13:00 – 13:15 Peter Müller-Buschbaum (TUM)
Welcome

13:15 – 13:45 Stephan V. Roth (HASYLAB)
Recent upgrades of the MiNaXS beamline P03

13:45 – 14:15 Monika Rawolle (TUM)
Titania thin films: a low temperature route to crystalline nanostructures

14:15 – 14:45 Eva M. Herzig (TUM)
Changes in Ternary OPV blends due to temperature

14:45 – 15:15 Sebastian Bommel (HASYLAB)
Growth-study of the fullerene C60 on mica using real-time and in-situ x-ray scattering

15:15 – 15:45 coffee break

15:45 – 16:15 Martine Philipp (TUM)
Microfluidic studies of the swelling behavior of hydrogels

16:15 – 16:45 Jan Perlich (HASYLAB)
Ordering during directional drying in organic thin films

16:45 – 17:15 Claudia Palumbiny (TUM)
Structured Interfaces for Organic Photovoltaics

17:15 – 17:45 Kuhu Sarkar (TUM)
Hybrid films based on ZnO network structures for applications in organic photovoltaics

17:45 – 18:30 discussion on future projects – part I

18.30 dinner in Garching

Tuesday, 11. 09. 2012
09:45 – 10:15 Gonzalo Santoro (HASYLAB)
In-situ RF-sputter chamber at P03: Status and planned upgrades

10:15 – 10:45 Ezzeldin Metwalli (TUM)
Real time GISAXS investigation of metal deposition on hard and soft surfaces

10:45 – 11:15 Matthias Schwartzkopf (HASYLAB)
Growth kinetics of Au on Si: From atoms to layers

11:15 – 11:45 Yuan Yao (TUM)
Comparison study of Gold and Aluminum deposition on polymer surfaces

11:45 – 12:15 Shun Yu (HASYLAB)
Al-sputter deposition on AlQ3

12:15 – 13:15 lunch break

13:15 – 13:45 Martin Niedermeier (TUM)
In-situ GISAXS characterization of metal electrode formation on a solid hole conductor

13:45 – 14:15 Gerd Herzog (HASYLAB)
Spray deposition of colloids

14:15 – 14:45 Christoph Schaffer (TUM)
In-Situ GISAXS experiments on (PCPDTBT:PC70BM) bulk heterojunction polymer solar cells

14:45 – 15:15 Jianqi Zhang (TUM)
Structural evolution in diblock copolymer thin films with perpendicular lamellar structure during solvent vapor treatment

15:15 – 15:45 discussion on future projects – part II

15:45 – 16:00 Peter Müller-Buschbaum (TUM)
Closing remarks

P. Müller-Buschbaum
Lehrerfortbildung 'Astrophysik'
Edgar-Lüscher-Lectures
Dillingen, 17 – 19 Sep 2012

EDGAR–LÜSCHER–LECTURES DILLINGEN/DONAU 2012
Thema: Astrophysik
Datum: Montag, 17. September bis Mittwoch, 19. September 2012
Tagungsort: Akademie für Lehrerfortbildung Dillingen
Veranstalter: Akademie für Lehrerfortbildung Dillingen und TU München
wissenschaftliche Leitung: Prof. Dr. Peter Müller-Buschbaum,
mit Unterstützung durch den Exzellenzcluster „Universe“
Technische Universität München.

Programm

Montag, 17. 09. 2012
15:00 – 15:30 Prof. Dr. Peter Müller-Buschbaum (Physik-Department TUM)
Begrüßung

15:30 – 17:00 Prof. Dr. Stephan Paul (Physik-Department TUM)
Entwicklung des Universums

18:30 – 20:00 Prof. Dr. Thomas Preibisch (Universitäts-Sternwarte München)
Sternentstehung und interstellares Medium

Dienstag, 18. 09. 2012
8:30 – 10:00 Dr. Sadegh Khochfar (Max-Planck-Institut für extraterrestrische Physik)
Galaxien und Dunkle Materie

10:00 – 10.30 Kaffeepause

10:30 – 12:00 NN
tba

15:30 – 17:00 Dr. Peter Aufmuth (MPI für Gravitationsphysik)
An der Schwelle zur Gravitationswellen-Astronomie

18:30 – 20:00 PD Dr. Frank Eisenhauer (Max-Planck-Instituts für extraterrestrische Physik)
Riesenteleskope und Weltraumastronomie

Mittwoch, 19. 09. 2012
8:30 – 10:00 Nora Lützgendorf (ESO)
Schwarze Löcher

10:00 – 10.30 Kaffeepause

10:30 – 12:00 PD Dr. Hans-Thomas Janka (Max-Planck-Institut für Astrophysik))
Sternentwicklung und Supernovae

Ab 12:00 Prof. Dr. Peter Müller-Buschbaum / StD Werner Ettinger
Lehrgangsabschluss

W. Petry, A. Magerl
Ferienakademie 'Medizinphysik'
Sarntal, Italy, 23 Sep – 05 Oct 2012

Homepage Ferienakademie Sarntal, Kurs 6: Medizinphysik

Jeden Herbst veranstalten die Technische Universität München zusammen mit der Friedrich-Alexander-Universität Erlangen-Nürnberg und der Universität Stuttgart eine Ferienakademie im Südtiroler Sarntal mit dem Ziel, begabte und besonders interessierte Studenten zu fördern und noch weiter zu motivieren. Die Kosten für die Akademie werden aus Spenden gedeckt, d.h. die Teilnahme ist für Studenten kostenlos. Erwartet wird von den ausgewählten Teilnehmern im Gegenzug eine aktive Beteiligung bei der Vorbereitung und Durchführung der Kurse. Durch Vorträge und Diskussionen, auch über Kursgrenzen hinweg, sollen die vielfältigen Problemstellungen und insbesondere die Lösungsansätzen in möglichst großer Breite verdeutlicht werden.

In einer ausgewogenen Mischung aus Freizeit (Ferien) und Studium (Akademie) werden Studenten verschiedener Fachrichtungen und Universitäten in entspannter Atmosphäre für einen Gedankenaustausch zusammengebracht. Die Auswahl der Teilnehmer erfolgt aufgrund ihrer Qualifikation durch den Direktor der Akademie und die Beauftragten der jeweiligen Universitäten in Abstimmung mit den Dozenten der jeweiligen Kurse.

Als Rahmenprogramm gibt es Bergwanderungen im Sarntal, Ausflüge in die Umgebung (z.B. nach Bozen), Sportturniere, Törgelen und vieles mehr. Es bietet sich auch insbesondere die Gelegenheit, wertvolle Kontakte zu Professoren, zu Gästen aus der Industrie und zu Kommilitonen aus anderen Universitäten und Studiengängen zu knüpfen.

Ferienakademie 2012:

Sarntal, Südtirol, Italien, Sonntag 23. September bis Freitag 5. Oktober 2012

Kurs 6: Medizinphysik

Dozenten:

- Prof. Dr. Winfried Petry, Forschungs-Neutronenquelle Heinz-Maier-Leibnitz und Lehrstuhl für Funktionelle Materialien, Technische Universität München
- Prof. Dr. Andreas Magerl, Lehrstuhl für Kristallographie und Strukturphysik, Universität Erlangen-Nürnberg

Gastdozenten:

- Prof. Dr. Alois Herkommer, Institut für Technische Optik, Universität Stuttgart

Assistenten:

- Dr. Harald Breitkreutz, Forschungs-Neutronenquelle Heinz-Maier-Leibnitz, Technische Universität München

Kursinhalt:

Die Medizinphysik bewegt sich im Grenzgebiet zwischen Medizin, Physik und der dazugehörigen Technik. Dementsprechend bildet sie die physikalischen Grundlagen der Medizintechnik ab und hat mit dem Medizinphysiker ein eigenes Berufsbild und seit einiger Zeit auch einen eigenen Studiengang hervorgebracht. Mit zunehmender Komplexität der Medizintechnik und dem ebenfalls zunehmenden Anspruch der Mediziner an die Leistungsfähigkeit dieser Technik steigt der Bedarf an entsprechend interdisziplinär qualifiziertem Personal seit Jahren beständig an.

Computertomograph

Die Themengebiete der medizinischen Physik sind so vielfältig wie ihre Aufgaben. Am bekanntesten sind wohl die bildgebenden Verfahren wie die Computertomographie (CT), die Magnetresonanztomographie (MRT) oder das altbekannte Röntgen zur operationsfreien Diagnose verschiedenster Erkrankungen im Körperinneren. Neuere Entwicklungen umfassen die Kombinationen der bekannten Verfahren mit der Positronenemissionstomographie (PET), Phasenkontraströntgen, oder Diagnosen mit Kohärenter Anti-Stokes Raman Spektroskopie (CARS) oder Optischer Kohärenztomografie (OCT) u.v.m. Auch klassische Diagnoseverfahren wie Ultraschall oder physiologische Messverfahren wie Elektrokardiografie (EKG) und Elektorenzephalografie (EEG) fallen in dieses Gebiet.

OCT eines Sarkoms

Auf der therapeutischen Seite beschäftigt sich die medizinische Physik neben grundlegenden Fragestellungen zur Wechselwirkung von Radioaktivität mit Gewebe und den daraus resultierenden Konsequenzen unter anderem mit den diversen Strahlenbehandlungsmethoden gegen Tumoren, z.B. der Protonen-, Schwerionen- und Neutronentherapie, der Brachytherapie (Behandlung mit Radioaktivität von innen heraus) , der Radiochirurgie (Gamma-Knife) und interventioneller Radiochirurgie. Auch alltäglichere Behandlungen wie die Defibrillation, die Lasik zur Korrektur der Augenlinse oder andere nicht zwangsläufig krebsbezogene Verfahren wie fokussierter Ultraschall zur Zertrümmerung von Nierensteinen oder die Lichttherapie als Seitenzweig der Photomedizin fallen hierunter.

PET Scan eines Gehirns

Die oben genannten Punkte spiegeln nur einen kleinen Ausschnitt aus dem Spektrum der Medizinphysik wieder, zeigen aber bereits die Vielfältigkeit und den Anspruch dieses Aufgabengebietes. Tiefgehendes medizinisches und physikalisches Verständnis des Körpers und seinen Wechselwirkungsmechanismen wird gepaart mit hochpräziser Ingenieurskunst und ausgefeilter Algorithmik.

MR eines Knies

C. M. Papadakis, S. Ottinger, I. Staudinger

Herbstuniversität at the physics department ’Gummibärchen, Superabsorber und Schleimmonster’

in the framework of the ’Agentur für Mädchen in Wissenschaft und Technik’ of TU München
29 – 30 Oct 2012

The Physics Department wishes to facilitate the decision of young women to study physics. This way, we hope to increase the number of female physics students in our Faculty. At this, we offered a project for female high school students from 10th to 12th grade within the framework of the Herbstuniversität which offers projects all over TUM in the autumn break of the schools. The project offered focused on polymeric hydrogels. Five students participated. They made their own gummi bears, investigated superabsorbers and looked into the mechanical properties of starch solutions. Moreover, they got a guided tour over the campus, visited a physics lecture and the lab course, talked to physics students and had lunch in the canteen. Altogether, it was a lot of fun and some girls said that they can imagine to study physics.

C. M. Papadakis
Schnupperstudium für Abiturientinnen
Garching, 26 Nov 2012

The ”taster studies” is a new activity of the Physics Department: Girls which are on the brink of their Abitur and seriously consider to study physics at TU München, have on this day the opportunity to get an idea on the ground.

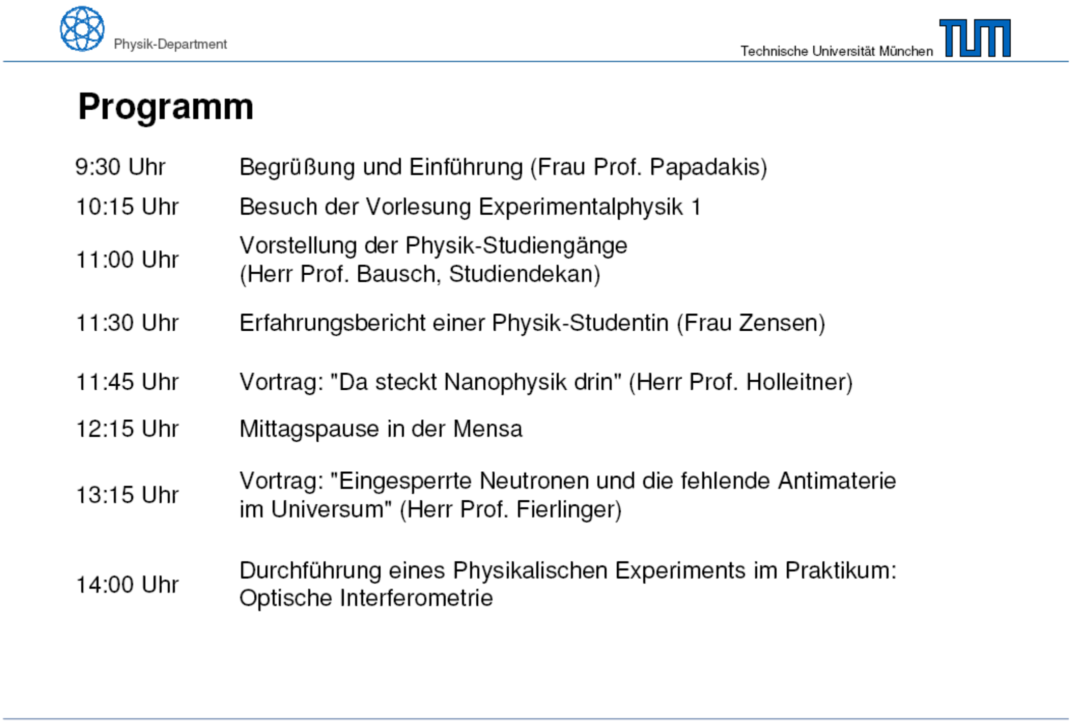

Physik-Department

Technische Universität München

Programm

9:30 Uhr	Begrüßung und Einführung (Frau Prof. Papadakis)
10:15 Uhr	Besuch der Vorlesung Experimentalphysik 1
11:00 Uhr	Vorstellung der Physik-Studiengänge (Herr Prof. Bausch, Studiendekan)
11:30 Uhr	Erfahrungsbericht einer Physik-Studentin (Frau Zensen)
11:45 Uhr	Vortrag: "Da steckt Nanophysik drin" (Herr Prof. Holleitner)
12:15 Uhr	Mittagspause in der Mensa
13:15 Uhr	Vortrag: "Eingesperrte Neutronen und die fehlende Antimaterie im Universum" (Herr Prof. Fierlinger)
14:00 Uhr	Durchführung eines Physikalischen Experiments im Praktikum: Optische Interferometrie

Prof. Dr. Peter Müller-Buschbaum:

- since 9/2012 Associate Editor of journal ACS Applied Materials & Interfaces of the American Chemical Society

- since 1/2012 Member of the Scientific Selection Panel of the Helmholtz-Zentrum Berlin für Materialien und Energie (HZB)

- since 2011 Mitglied im European Spallation Source (ESS) Scientific Advisory Panel (Reflectivity)

- since 2011 German representative at the European Polymer Federation (EPF) for polymer physics

- since 2011 elected member of 9th Committee Research with Synchrotronstrahlung (KFS), Section User Matters

- since 2010 spokesman of the regenerative engergies section (NRG) at the Munich School of Engineering (MSE) of TU Munich

- since 2010 member of TUMEnergie at TU Munich

- since 2010 spokesman of the energy section at the Physics Department/TU Munich

- since 2010 observer at the ESUO - European Synchrotron User Organization

- member of the scientific counsel at the "Institut für Biophysik und Nanosystemforschung" (Institute for Biophysics and Nanosystems research) of the Austrian Academy of Sciences IBN in Graz, Austria

- elected chairman of "HASYLAB User Committee (HUC)" at the synchrotron radiation laboratory HASYLAB in Hamburg

Prof. Dr. Christine Papadakis:

- member of the Project Review Panel 5: 'Soft Condensed Matter/Scattering' at HASYLAB, DESY, Hamburg

- member of the subcommittee "College 9: Structure And Dynamics Of Soft Condensed Matter" at the Institute Laue-Langevin (ILL), Grenoble, France

- women's representative of the Physics Department at TU München

Prof. Dr. Winfried Petry:

- since 1999 liaison professor of Bayerische Eliteakademie (Bavarian Leadership Academy) and since May 2011 member of the curatorium

- since 2007 member of the Steering Comittee of the Laue Langevin Institute and chairman of the instrumentation review panel of the CEA Leon Brillouin Laboratory

9 Publications, talks and funding

9.1 Publications

- J. Adelsberger, E. Metwalli, A. Diethert, I. Grillo, A. M. Bivigou-Koumba, A. Laschewsky, P. Müller-Buschbaum, C. M. Papadakis
  Kinetics of collapse transition and cluster formation in a thermoresponsive micellar solution of P(S-b-NIPAM-b-S) induced by a temperature jump
  Macromol. Rapid Commun. **33**, 254-259 (2012)

- R. A. Alaa, K. S. Virdi, R. Meier, M. Döblinger, P. Müller-Buschbaum, C. Scheu, P. Lugli, G. Scarpa
  Successive spray deposition of P3HT/PCBM organic photoactive layers: material composition and device characterization
  Adv. Funct. Mat. **22**, 4078-4086 (2012)

- M. M. Abul Kashem, D. Patra, J. Perlich, A. Rothkirch, A. Buffet, S. V. Roth, V. M. Rotello, P. Müller-Buschbaum
  Two- and three-dimensional network of nanoparticles via polymer mediated self-assembly
  ACS Macro. Lett. **1**, 396-399 (2012)

- B. Baumeister, W. Schmid, F. Kraus, W. Petry
  An alternative chemical chleaning procedure for blanc monolithic U-Mo foils
  Transactions of RRFM **March 2012**

- N. Boucharat, D. Wang, E. G. Bardaji, M. Fichtner, W. Lohstroh
  Effect of a Ti-Based Additives on the Desorption in Isotope Labeled 2 LiB(H,D)$_4$ *- Mg(H,D)*$_2$ *Nanocomposites*
  J. Phys. Chem. C **116**, 11877-11885 (2012)

- H. Breitkreutz, W. Petry
  Simulation of the time evolution of oxide layers surrounding cladding-meat contact faults (non-bonds) and their thermal-hydraulic implications
  Transactions of RRFM **March 2012**

- A. Buffet, A. Rothkirch, R. Doehrmann, V. Körstgens, M. M. Abul Kashem, J. Perlich, G. Herzog, M. Schwartzkopf, R. Gehrke, P. Müller-Buschbaum, S.V. Roth
  P03, the Microfocus and Nanofocus X-ray Scattering (MiNaXS) beamline of the PETRA III storage ring: The microfocus endstation
  J. Synchrotron Rad. **19**, 647-653 (2012)

- M. Däubler, H. Breitkreutz, W. Petry, R. Macian-Juan
  New reactors safety analysis of FRM II compact core using TRACE/PARCS
  Transactions of RRFM **March 2012**

- A. Diethert, V. Körstgens, D. Magerl, K. Ecker, J. Perlich, S. V. Roth, P. Müller-Buschbaum
  Structure and macroscopic tackiness of ultra-thin pressure sensitive adhesive films
  ACS Appl. Mater. Interfaces **4**, 3951-3958 (2012)

- S. Dullinger, A. Gattringer, W. Thuiller, D. Moser, N. E. Zimmermann, A. Guisan, W. Willner, Ch. Plutzar, M. Leitner, T. Mang, M. Caccianiga, T. Dirnböck, S. Ertl, A. Fischer, J. Lenoir, J.-Ch. Svenning, A. Psomas, D. R. Schmatz, U. Silc, P. Vittoz, K. Hülber
  Extinction debt of high-mountain plants under twenty-first-century climate change
  Nature Clim. Change **2**, 619-622 (2012)
- S. Ener, J. Neuhaus, W. Petry, R. Mole, K. Hradil, M. Siewert, M.E. Gruner, P. Entel, I. Titov, M. Acet
  Effect of temperature and compositional changes on the phonon properties of Ni-Mn-Ga shape memory alloys
  Phys. Rev. B **86**, 144305-144313 (2012)
- S. K. Filippov, P. Chytil, P. V. Konarev, M. Dyakonova, C.M. Papadakis, A. Zhigunov, J. Plestil, P. Stepanek, T. Etrych, K. Ulbrich, D. I. Svergun
  Macromolecular HPMA-based nanoparticles with cholesterol for solid-tumor targeting: Detailed study of the inner structure of a highly efficient drug delivery system
  Biomacromolecules **13**, 2594-2604 (2012)
- Y. Georgalis, M. Philipp, R. Aleksandrova, J. K. Krüger
  Light scattering studies on Ficoll PM70 solutions reveal two distinct diffusive modes
  J. Colloid Interface Sci. **386**, 141-147 (2012)
- C. Gold, P. Gross, L. Peyker, G. Eickerling, G. G. Simeoni, O. Stockert, E. Kampert, F. Wolff-Fabris, H. Michor, E.-W. Scheidt
  Interplay between crystal field splitting and Kondo effect in $CeNi_9Ge_{4-x}Si_x$
  J. Phys.: Condens. Matter **24**, 355601 (2012)
- A. A. Golosova, J. Adelsberger, A. Sepe, M. A. Niedermeier, P. Lindner, S. S. Funari, R. Jordan, C. M. Papadakis
  Dispersions of polymer-modified carbon nanotubes: a small-angle scattering investigation
  J. Phys. Chem. C **116**, 15765-15774 (2012)
- F. Gröstlinger, M. Rennhofer, M. Leitner, E. Partyka-Jankowska, B. Sepiol, B. Laenens, N. Planckaert, A. Vantomme
  Anisotropic diffusion in FePt thin films
  Phys. Rev. B **85**, 134302 (2012)
- R. M. Hengstler-Eger, P. Baldo, L. Beck, J. Dorner, K. Ertl, P. B. Hoffmann, C. Hugenschmidt, M. A. Kirk, W. Petry
  Heavy ion irradiation induced dislocation loops in AREVA's M5 alloy
  J. Nucl. Mater. **15**, 170-182 (2012)
- A. Heldmann, R. Jungwirth, H. Breitkreutz, W.Petry
  Energy and lattice damage distribution at the interface UMo-Al: Comparison of fission fragments and heavy-ions
  Transactions of RERTR **Oct 2012**
- G. Herzog, M. M. Abul Kashem, G. Benecke, A. Buffet, R. Gehrke, J. Perlich, M. Schwartzkopf, V. Körstgens, R. Meier, M. A. Niedermeier, M. Rawolle, M. A. Ruderer, P. Müller-Buschbaum, W. Wurth, S. V. Roth
  Influence of nanoparticle surface functionalization on the thermal stability of colloidal polystyrene films
  Langmuir **28**, 8230-8237 (2012)

- E. T. Hoppe, I. Hopp, M. Port, B. Menges, C. M. Papadakis
  Optical properties of polybutadiene in the bulk and near a gold interface
  Colloid Polym. Sci. **290**, 1731-1741 (2012)

- T. Huber, R. Jungwirth, A. Röhrmoser, W. Petry, D. Staicu, M. Ernstberger, H. Thiele, A. Zappia, D. W. Wachs, Ch. Jarousse, B. Stepnik, P. Lemoine, F. Charollais
  Thermal conductivity measurements of IRIS-TUM fuel plates (disperse U-8wt.%-Mo)
  Transactions of RRFM **March 2012**

- T. Huber, W. Petry, M. Fig, R. Kennedy, A. Robinson, D. Wachs
  First Results of Scanning Thermal Diffusivity Microscope (STDM) Measurements on Irradiated Monolithic and Disperse Fuel
  Transactions of RERTR **Oct 2012**

- R. Jungwirth, T. Zweifel, H.-Y. Chiang, W. Petry, F. Charollais, P. Lemoine, Y. Calzavara, H. Guyon, S. Van den Berghe, A. Leenaers, E. Koonen, B. Stepnik, C. Jarousse
  Ion irradiation of UMo/Al fuel samples with 7wt% and 12wt% Si inside the matrix (E-FUTURE II)
  Transactions of RRFM **March 2012**

- V. Körstgens, R. Meier, M. A. Ruderer, S. Guo, H.-Y. Chiang, J. Perlich, S. V. Roth, R. Gehrke, P. Müller-Buschbaum
  Note: Grazing incidence small and wide angle x-ray scattering combined with imaging ellipsometry
  Rev. Sci. Instrum. **83**, 076107 (2012)

- J. K. Krüger, U. Müller, B. Zielinski, M. Philipp, R. Sanctuary
  Competition between chemical network formation and physical adsorption and desorption processes in a silica-filled silicone rubber: calorimetry versus refractometry studies
  J. Adhes. **88**, 649-663 (2012)

- M. Leitner
  Absence of a trapping effect on the kinetic critical radius in nucleation and growth processes
  Acta. Mat. **60**, 6779-6783 (2012)

- M. Leitner
  Studying Atomic Dynamics with Coherent X-rays
  Springer (Heidelberg, 2012)

- M. Leitner, H. Ceeh, J.-A. Weber
  Eliminating spatial distortions in Anger-type gamma cameras
  New J. Phys. **14**, 123014 (2012)

- M. Leitner, S. Dullinger, F. Essl, G. Vogl
  The Spread of Ragweed as a Diffusion Process
  in: “Migrations: Interdisciplinary Perspectives”, M. Messer, R. Schroeder, and R. Wodak (eds.), pp. 267-274, Springer (Wien, Heidelberg, 2012)

- M. Leitner, B. Sepiol, L.-M. Stadler, B. Pfau
  Time-resolved study of the crystallization dynamics in a metallic glass
  Phys. Rev. B **86**, 064202 (2012)

- P. Lellig, M. A. Niedermeier, M. Rawolle, M. Meister, F. Laquai, P. Müller-Buschbaum, J. S. Gutmann
  Comparative study of hybrid and inorganic blocking layers for solid-state dye-sensitized solar cells
  Phys. Chem. Chem. Phys. **14**, 1607-1613 (2012)
- R. Meier, C. Birkenstock, C. M. Palumbiny, P. Müller-Buschbaum
  Efficiency-improved organic solar cells based on plasticizer assisted soft mmbossed PEDOT:PSS layers
  Phys. Chem. Chem. Phys. **14**, 15088-15098 (2012)
- R. Meier, H.-Y. Chiang, M. A. Ruderer, S. Guo, V. Körstgens, J. Perlich, S. V. Roth, P. Müller-Buschbaum
  In situ film characterization of thermally treated microstructured conducting polymer films
  J. Poly. Sci. Part B **50**, 631-641 (2012)
- A. Meier-Koll, V. Pipich, P. Busch, C. M. Papadakis, P. Müller-Buschbaum
  Phase-separation in semi-dilute aqueous poly(N-isopropylacrylamide) solutions
  Langmuir **8**, 8791-8798 (2012)
- A. Miasnikova, A. Laschewsky, G. De Paoli, C. M. Papadakis, P. Müller-Buschbaum, S. S. Funari
  Thermoresponsive hydrogels from symmetrical triblock copolymers poly(styrene-block-(methoxy diethylene glycol acrylate)-block-styrene)
  Langmuir **28**, 4479-4490 (2012)
- H. Morhenn, S. Busch, T. Unruh
  Chain dynamics in a hexadecane melt as seen by neutron scattering and identified by molecular dynamics simulations
  J. Phys.: Condens. Matter **24**, 375108 (2012)
- U. Müller, M. Philipp, J. C. Gaukler, W. Possart, R. Sanctuary, J. K. Krüger
  Dissolution, transport and reaction at a DICY/DGEBA interface
  J. Adhes. **88**, 253-276 (2012)
- M. A. Niedermeier, D. Magerl, Q. Zhong, A. Nathan, V. Körstgens, J. Perlich, S. V. Roth, P. Müller-Buschbaum
  Combining mixed titania morphologies into a complex assembly thin film by iterative block copolymer based sol-gel templating
  Nanotechnology **23**, 145602 (9p) (2012)
- H. Palancher, A. Bonnin, V. Honkimäki, P. Cloetens, T. Zweifel, R. Toucoulou, A. Rack, M. Voltolini
  Coating thickness determination in highly absorbent core-shell systems
  J. Appl. Chrystallogr. **45**, 906-913 (2012)
- H. Palancher, A. Bonnin, V. Honkimäki, T. Buslaps, M. Grasse, B. Stepnik, T. Zweifel
  Quantitative crystallographic analysis of as-fabricated full size U-Mo/Al(Si) nuclear fuel plates
  J. Alloy. Compd. **527**, 53-65 (2012)
- N. Paul, A. Paul, R. Steitz, M. Kreuzer, M. Ch. Lux-Steiner
  Selective self assembly of neurotransmitter molecules on polyelectrolyte multilayers
  J. Phys. Chem. B **116**, 4492-4499 (2012)

- A. Paul, N. Paul, C. Trautmann, J. Jutimooaik, R. Yimnirun, S. Rujirawat, B. Höpfner, I. Lauermann, M.Ch. Lux-Steiner, S. Mattauch, P. Böni
  Direct manipulation of the uncompensated antiferromagnetic spins in exchange coupled system by GeV ion irradiation
  Appl. Phys. Lett. **100**, 253102 (2012)

- A. Paul, C. Schmidt, N. Paul, A. Ehresmann, S. Mattauch, P. Böni
  Symmetric magnetization reversal in polycrystalline exchange coupled systems via simultaneous processes of coherent rotation and domain nucleation
  Phys. Rev. B. **86**, 094420 (2012)

- J. Perlich, M. Memesa, A. Diethert, E. Metwalli, W. Wang, S. V. Roth, J. S. Gutmann, P. Müller-Buschbaum
  Layer-by-layer fabrication of an anatase titania multilayer with gradual sponge-like morphology
  Colloid Polym. Sci. **290**, 119-126 (2012)

- J. Perlich, M. Schwartzkopf, V. Körstgens, D. Erb, J. F. H. Risch, P. Müller-Buschbaum, R. Röhlsberger, S. V. Roth, R. Gehrke
  Pattern formation of colloidal suspensions by dip-coating: An in situ grazing incidence x-ray scattering study
  phys. stat. sol.(RRL) **6**, 253-255 (2012)

- Y. Peykova, O. V. Lebedeva, A. Diethert, P. Müller-Buschbaum, N. Willenbacher
  Adhesive properties of acrylate copolymers: effect of the nature of the substrate and copolymer functionality
  Int. J. Adhes. Adhes. **34**,107-116 (2012)

- M. Philipp, U. Müller, R. Alexandrova, R. Sancturay, P. Müller-Buschbaum, J. K. Krüger
  On the elastic nature of the demixing transition of aqueous PNIPAM solutions
  Soft Matter **8**, 11387-11395 (2012)

- M. Philipp, U. Müller, P.-C. Gervais, C. Wehlack, W. Possart, R. Sanctuary, J. E. Klee, J. K. Krüger
  Influence of nanoparticles on the coupling between optical dipoles in epoxy-silica nanocomposites during network formation
  J. Adhes. **88**, 566-588 (2012)

- M.-T. Popescu, C. Tsitsilianis, C. M. Papadakis, J. Adelsberger, S. Balog, P. Busch, N. A. Hadjiantoniou, C. S. Patrickios
  Stimuli-responsive amphiphilic polyelectrolyte heptablock copolymer physical hydrogels: An unusual pH-response
  Macromolecules **45**, 3523-3530 (2012)

- Z. Di, D. Posselt, D.-M. Smilgies, R. Li, M. Rauscher, I. I. Potemkin, C. M. Papadakis
  Stepwise swelling of a thin film of lamellae-forming poly(styrene-b-butadiene) in cyclohexane vapor
  Macromolecules **45**, 5185-5195 (2012)

- M. Rawolle, E. V. Braden, M. A. Niedermeier, D. Magerl, K. Sarkar, T. Fröschl, N. Hüsing, J. Perlich, P. Müller-Buschbaum
  Low temperature route to crystalline titania network-structures in thin films
  ChemPhysChem **13**, 2412-2417 (2012)

- M. Rawolle, V. Körstgens, M. A. Ruderer, E. Metwalli, S. Guo, G. Herzog, G. Benecke, M. Schwartzkopf, A. Buffet, J. Perlich, S. V. Roth, P. Müller-Buschbaum
  Comparison of grazing incidence small angle x-ray scattering of a titania sponge structure at the beamlines BW4 (DORIS III) and P03 (PETRA III)
  Rev. Sci. Instr. **83**, 106104 (2012)

- M. Rawolle, M. A. Niedermeier, G. Kaune, J. Perlich, P. Lellig, M. Memesa, Y.-J. Cheng, J. S. Gutmann, P. Müller-Buschbaum
  Fabrication and characterization of nanostructured titania films with integrated function from inorganic-organic hybrid materials
  Chem. Soc. Rev. **41**, 5131 (2012)

- J. Repper, M. Hofmann, C. Krempaszky, B. Regener, E. Bernhuber, W. Petry, E. Werner
  Effect of macroscopic relaxation on residual stress analysis by diffraction methods
  J. Appl. Phys. **112**, 064906 (2012)

- A. Röhrmoser, H. Breitkreutz, W. Petry
  Extended study of FRM II core conversion with UMo disperse fuel at a prolonged fuel element
  Transactions of RRFM **March 2012**

- K. Rolfs, M. Chiemlus, J. M. Guldbakke, R. C. Wimpory, A. Raatz, W. Petry, P. Müllner, R. Schneider
  Key properties of Ni-Mn-Ga based single crystals grown with the SLARE-technique
  Adv. Eng. Mat. **14**, 614-635 (2012)

- M. A. Ruderer, R. Meier, L. Porcar, R. Cubitt, P. Müller-Buschbaum
  Phase separation and molecular intermixing in polymer-fullerene bulk heterojunction thin films
  J. Phys. Chem. Lett. **3**, 683-688 (2012)

- S. Salzinger, S. Huber, S. Jaksch, P. Busch, R. Jordan, C. M. Papadakis
  Aggregation behavior of thermo-responsive poly(2-oxazoline)s at the cloud point investigated by FCS and SANS
  Colloid Polym. Sci. **290**, 385-400 (2012)

- M. Schindler, A. Kriele, P. Müller-Buschbaum
  Reorganization of the near-surface composition in pressure sensitive adhesive films stored in nitrogen atmosphere
  J. Adhes. **88**, 684-698 (2012)

- K. Schlage, S. Couet, S. V. Roth, U. Vainio, R. Rüffer, M. M. Abul Kashem, P. Müller-Buschbaum, R. Röhlsberger
  The formation and magnetism of iron nanostructures on ordered polymer templates
  New J. Phys. **14**, 043007 (2012)

- R. Tscheliessnig, M. Zörnig, E. M. Herzig, K. Lückerath, J. Altrichter, K. Kemter, A. Paunel-Görgülü, T. Lögters, J. Windolf, S. Pabisch, J. Cinatl, H. F. Rabenau, A. Jungbauer, P. Müller-Buschbaum, M. Scholz, J. Koch
  Nano-coating protects biofunctional materials
  Materials Today **15**, 394-404 (2012)

- Q. Zhong, E. Metwalli, G. Kaune, M. Rawolle, A. M. Bivigou-Koumba, A. Laschewsky, C. M. Papadakis, R. Cubitt, P. Müller-Buschbaum
  Switching kinetics of thin thermo-responsive hydrogel films of poly(monomethoxy-diethylenglycol-acrylate) probed with in-situ neutron reflectivity
  Soft Matter **8**, 5241-5249 (2012)

- T. Zweifel, H. Palancher, A. Bonnin, F. Charollais, A. Leenaers, S. Van Den Berghe, R. Jungwirth, W. Petry, P. Lemoine
  Study of Si and ZrN coated UMo atomised particles using high energy XRD Transactions of RRFM **March 2012**

9.2 Talks

- J. Adelsberger, A. M. Bivigou-Koumba, A. Laschewsky, P. Müller-Buschbaum, C. M. Papadakis
  Self-assembled thermoresponsive hydrogels
  21th Polymer Networks Group Meeting, Jackson, WY, USA, 12 – 16 Aug 2012

- J. Adelsberger, E. Metwalli, A. Diethert, I. Grillo, A. M. Bivigou-Koumba, A. Laschewsky, P. Müller-Buschbaum, C. M. Papadakis
  Kinetics of collapse and aggregation in micellar solutions of thermoresponsive triblock copolymers - a time-resolved SANS investigation
  Trends and Perspectives in Neutron Scattering for Soft Matter and Biophysics JCNS Workshop, Tutzing, 08 – 11 Oct 2012

- S. Ener, J. Neuhaus, W. Petry
  Vibrational properties of Ni-Mn-Ga ferromagnetic shape memory alloys in the austenite phase
  DPG Frühjahrstagung, Berlin, 25 – 30 Mar 2012

- S. Filippov, J. Franklin, P. Konarev, P. Chytil, T. Etrych, A. Bogomolova, M. Dyakonova, C. M. Papadakis, K. Ulbrich, P. Stepanek, D. Svergun
  SAXS/SANS kinetic study of hydrolytically degradable polymer micelles for anticancer drug delivery
  SAS 2012, Sydney, Australia, 18 – 23 Nov 2012

- E. M. Herzig, A. Naumann, W. Wang, C. Palumbiny, S. Yu, S. V. Roth, P. Müller-Buschbaum
  Changes in ternary OPV blends due to temperature
  3rd TUM-HASYLAB Colloquium, Garching, 10 – 11 Sep 2012

- E. M. Herzig, A. Akthar, A. Naumann, G. Tainter, S. Guo, J. Perlich, S. V. Roth, P. Müller-Buschbaum
  Examination of crystalline structure in ternary photovoltaic polymer blends
  SPP 1355 Workshop, Würzburg, 18 Sep 2012

- E. M. Herzig, A. Naumann, W. Wang, C. Palumbiny, S. Yu, S. V. Roth, P. Müller-Buschbaum
  Deliberate tuning of crystal orientation in ternary photovoltaic polymer blend thin films
  GISAS 2012, Kyoto, Japan, 13 – 16 Nov 2012

- E. M. Herzig, A. Akthar, K. Wagenbauer, A. Naumann, G. Tainter, S. Guo, J. Perlich, S. V. Roth, P. Müller-Buschbaum
  Influence of a third component on the morphology of conducting binary polymer blends for photovoltaic applications
  SAS 2012, Sydney, Australia, 18 – 23 Nov 2012

- S. Jaksch
  Kinetics of the collapse transition of thermoresponsive poly(2-oxazoline)s
  26th Conference of the European Colloid and Interface Society, Malmö, Sweden, 02 – 07 Sep 2012

- S. Jaksch
  Kinetics of the collapse transition of thermoresponsive poly(2-oxazoline)s
  Trends and Perspectives in Neutron Scattering for Soft Matter and Biophysics JCNS Workshop, Tutzing, 08 – 11 Oct 2012

- S.Jaksch
  Kinetics of the collapse transition of thermoresponsive poly(2-oxazoline)s
  SAS 2012, Sydney, Australia, 18 – 23 Nov 2012

- V. Körstgens, S. V. Roth, P. Müller-Buschbaum
  Microfluidics and microGISAXS at P03/MiNaXS
  Satellite Meeting of the HASYLAB Users' Meeting "Status and Perspectives of Small Angle X-ray Scattering at DESY", Hamburg, 26 Jan 2012

- V. Körstgens, K. Sarkar, A. Buffet, M. Schwartzkopf, S. V. Roth, P. Müller-Buschbaum
  Microfluidics and microGISAXS – in situ characterization of nanostructures at the solid liquid interface
  ICCE-20, International Conference on Composites or Nano Engineering, Beijing, China, 22 – 28 Jul 2012

- J. K. Krüger, M. Philipp
  Wenn Licht auf Schall trifft: Eine Einführung in die Raster Brillouin Mikroskopie
  Session plénière ordinaire 2012, Institut Grand-ducal, Luxembourg, 27 Feb 2012

- M. Leitner, S. Ener, J. Neuhaus, W. Petry
  Correlated Electrons in Heusler Alloys
  TRR-80 Retreat Meeting, Freising, 13 – 14 Feb 2012

- W. Lohstroh, G. G. Simeoni, L. Silvi, J. Neuhaus, W. Petry
  A cold chopper spectrometer for ESS
  2nd In-kind contribution Meeting for ESS - IKON 2, Malmö, Sweden, 09 – 10 Feb 2012

- E. Metwalli
  Real-time GISAXS study of metal nanoparticles growth on nanostructured polymer films
  Satellite Meeting of the HASYLAB Users' Meeting SStatus and Perspectives of Small Angle X-ray Scattering at DESY", Hamburg, 26 Jan 2012

- E. Metwalli, H.E. Hermes, E. Calzada, A. Diethert, J. Adelsberger, R. Cubitt, U. Kulozik, J.F. Moulin, S.U. Egelhaaf, P. Müller-Buschbaum
  Thin film kinetics of soft materials under solvent vapor: prospects for time-resolved GISANS study
  ESS Science Symposium, Lund, 22 – 24 Feb 2012

- E. Metwalli, H. Hermes, E. Calzada , S.U. Egelhaaf, P. Müller-Buschbaum
  Neutron Radiography study of water migration into casein micellar films
  DPG Frühjahrstagung, Berlin, 25 – 30 Mar 2012
- D. Magerl, X.-P. Qiu, F. M. Winnik, P. Müller-Buschbaum
  A Comparison of the Morphology and Thermoresponsive Switching Behavior in Thin Films of Cyclic and Linear Poly(N-isopropylacrylamide)
  DPG Frühjahrstagung, Berlin, 25 – 30 Mar 2012
- D. Magerl
  IsGISAXS
  GISAXS Workshop, ALS User Meeting, Berkeley, CA, USA, 08 – 10 Oct 2012
- H. Morhenn, T. Unruh
  Short Time Dynamics of Molecular Liquids: Results from Neutron Scattering Experiments and Computer Simulations
  Assessment and Strategy Seminar LKS FAU Erlangen-Nürnberg, Flachau, Austria, 13 – 17 Feb 2012
- H. Morhenn, S. Busch, T. Unruh
  Chain dynamics of n-alkanes studied by neutron scattering
  DPG Frühjahrstagung, Berlin, 25 – 30 Mar 2012
- H. Morhenn, T. Unruh
  Dynamics in molecular liquids tackled by neutron scattering experiments and MD simulations
  Seminar of the Institute for theoretical physics I FAU Erlangen-Nürnberg, Erlangen, 5 Jun 2012
- H. Morhenn, S. Busch, T. Unruh
  The motions in liquid n-alkanes
  Deutsche Neutronenstreutagung, Bonn, 24 – 26 Sept 2012
- H. Morhenn, S. Busch, T. Unruh
  Short-time dynamics in molecular liquids
  10th International Conference on quasielastic neutron scattering, Nikko, Japan, 30 Sept – 04 Oct 2012
- H. Morhenn, T. Unruh
  Molecular dnymics explored with slow neutrons and fast computers
  Neutronen in Forschung und Industrie, Garching, 03 Dez 2012
- P. Müller-Buschbaum
  Fabrication of magnetic nanowire arrays on diblock copolymer films using external magnetic fields
  Nanomagnetic nanoTUM Workshop in Munich, 03 Feb 2012
- P. Müller-Buschbaum
  Polymer nanostructures at buried interfaces probed with time-of flight grazing incidence small angle neutron scattering
  FRMII Usermeeting workshop in Munich, 23 Mar 2012

- P. Müller-Buschbaum, M. A. Ruderer, S. Guo, R. Meier, H. Y. Chiang, V. Körstgens, J. Perlich, S. V. Roth
  Solvent induced morphology in polymer-based systems for organic photovoltaics
  DPG Frühjahrstagung, Berlin, 25 – 30 Mar 2012

- P. Müller-Buschbaum, E. Metwalli, V. Körstgens, A. Buffet, J. Perlich, S. V. Roth
  Millisecond time resolution GISAXS investigation of metal nanoparticle growth on soft and hard surfaces
  DPG Frühjahrstagung, Berlin, 25 – 30 Mar 2012

- P. Müller-Buschbaum
  Switching kinetics of thin thermo-responsive hydrogel films
  Talk at "Physics Seminar", University of Luxemburg in Luxemburg, 17 Apr 2012

- P. Müller-Buschbaum
  Polymer and small molecule nanostructures for applications in organic photovoltaics
  5th joint meeting of the nanocenters in the EuroTech Universities Alliance, University Copenhagen, Denmark, 01 Jun 2012

- P. Müller-Buschbaum
  Polymer- and hybrid-nanostructures for applications in organic photovoltaics
  Organic electronics group seminar, University Cambridge, U.K., 25 – 26 Jun 2012

- P. Müller-Buschbaum
  Polymer and small molecule nanostructures for applications in organic photovoltaics
  GdCH Kolloquium University Bielefeld, 12 – 13 Jul 2012

- P. Müller-Buschbaum, M. Rawolle, M. A. Niedermeier, K. Sarkar, J. Perlich, P. Lellig, J. S. Gutmann
  Tailoring Titania Nanostructures for Solar Cell Applications
  20th International Conference on Composites/Nano Engineering ICCE-20, Beijing, China, 22 – 28 Jul 2012

- P. Müller-Buschbaum
  Polymere für den Einsatz in der Photovoltaik
  Edgar-Lüscher-Fortbildungskurs für Physiklehrer, Dillingen, 17 – 19 Sep 2012

- P. Müller-Buschbaum, M. A. Ruderer, R. Meier, L. Porcar, R. Cubitt
  Phase Separation and Molecular Intermixing in Polymer-Fullerene Bulk Heterojunction Thin Films
  Deutsche Neutronenstreutagung, Bonn, 24 – 26 Sep 2012

- P. Müller-Buschbaum
  Polymer and Hybrid Films for Solar Cell Applications
  Opening EUROTECH Universities Interface Science for Photovoltaics, Bruxelles, Belgium, 11 – 12 Oct 2012

- P. Müller-Buschbaum
  Tailoring Titania Nanostructures for Solar Cell Applications
  Solar Technologies go Hybrid (SolTec), Munich, 17 – 19 Oct 2012

- P. Müller-Buschbaum
  Polymer and small molecule nanostructures for applications in organic photovoltaics
  Kolloquium at Technische Fakultät (TF) of Christian-Albrechts-University, Kiel, 22 Oct 2012

- P. Müller-Buschbaum
  Grazing Incidence Small Angle Neutron Scattering: Challenges and Possibilities
  Keynote Lecture at 2nd International GISAS Meeting - GISAS2012, Kyoto, Japan, 13 – 16 Nov 2012

- P. Müller-Buschbaum
  Determination of the inner morphology of organic solar cells with grazing incidence small angle neutron scattering
  Keynote Lecture at 15th International Small-Angle Scattering conference (SAS 2012), Sydney, Australia, Nov 18 – 23 2012

- M. A. Niedermeier, M. Rawolle, P. Lellig, V. Körstgens, E. M. Herzig, A. Buffet, S. V. Roth, J. S. Gutmann, T. Fröschl, N. Hüsing, P. Müller-Buschbaum
  Fabrication of polymer/titania hybrid thin films via low temperature sol-gel synthesis for application in photovoltaics
  ICCE-20, International Conference on Composites or Nano Engineering, Beijing, China, 22 – 28 Jul 2012

- M. A. Niedermeier, E. Metwalli, V. Körstgens, J. Perlich, A. Buffet, M. A. Kashem, K. Schlage, R. Röhlsberger, S. V. Roth, P. Müller-Buschbaum
  In-situ GISAXS study of metal electrode growth on semiconducting organic films
  3rd TUM-HASYLAB Colloquium, Garching, 10 – 11 Sep 2011 2012

- C. M. Palumbiny, K. Schaber, J. Anderson
  Energy independence in Bavarian villages: Local level solutions and their contribution to local and national sustainability targets
  United Nations Conference on Sustainable Development (Rio+20), 'Students for Sustainability', Sustainable Development Dialogues, Rio de Janeiro, 13 – 24 June 2012

- C. M. Palumbiny, D. Moseguí González, J. C. Heller, T. Pfadler, K. Sarkar, V. Körstgens, S. Yu, M. Al-Hussein, L. Schmidt-Mende, S. Roth, P. Müller-Buschbaum
  Structured interfaces for organic photovoltaics
  3rd TUM-HASYLAB Colloquium, Garching, 10 – 11 Sep 2012

- C. M. Papadakis
  Real-time, in-situ GISAXS experiments on block copolymer thin films during vapor treatment and drying
  Satellite Meeting of the HASYLAB Users' Meeting "Status and Perspectives of Small Angle X-ray Scattering at DESY", Hamburg, 26 Jan 2012

- C. M. Papadakis
  Structure and segmental dynamics of thermoresponsive block copolymers
  Faculty of Physics, National Technical University of Athens, Greece, 10 Feb 2012

- C. M. Papadakis
  Kinetics of structural changes in thermoresponsive blockcopolymer solutions
  DPG Frühjahrstagung, Berlin, 25 – 30 Mar 2012

- C. M. Papadakis, J. Adelsberger, E. Metwalli, A. Diethert, P. Busch, I. Grillo, A. M. Bivigou-Koumba, A. Laschewsky, P. Müller-Buschbaum
  Kinetics of collapse and aggregation in thermoresponsive micellar block copolymer solutions - a time-resolved SANS investigation
  SAS 2012, Sydney, Australia, 18 – 23 Nov 2012
- N. Paul, M. Ch. Lux-Steiner
  Fabrication, characterization and optimization of the glutamate switch using ATR-FTIR spectroscopy
  BMBF Project meeting, Reutlingen, 27 Feb 2012
- N. Paul, M. Müller, A. Paul, E. Guenther, I. Lauermann, P. Müller-Buschbaum, M. Ch. Lux-Steiner
  Molecularly imprinted conductive polymers for controlled trafficking of neurotransmitter at solid-liquid interface
  DPG Frühjahrstagung, Berlin, 25 – 30 Mar 2012
- N. Paul
  Selective self assembly of neurotransmitter molecules on polyelectrolyte multilayers
  Kolloquium des Leibniz Instituts für Analytische Wissenschaften ISAS, 18 Apr 2012
- J. Perlich, A. Buffet, M. Schwartzkopf, M. M. Abul Kashem, G. Herzog, K. Schlage, E. Metwalli, V. Körstgens, M. Rawolle, R. Röhlsberger, P. Müller-Buschbaum, S. V. Roth, R. Gehrke
  Fabrication of metamaterials by colloidal mask templating and glancing angle deposition: An in situ grazing incidence X-ray scattering study
  DPG Frühjahrstagung, Berlin, 25 – 30 Mar 2012
- J. Perlich
  Ordering during directional drying in organic thin films: An in situ grazing incidence X-ray scattering study
  3rd TUM-HASYLAB Colloquium, Garching, 10 – 11 Sep 2012
- J. Perlich, V. Körstgens, M. Schwartzkopf, G. Santoro, S. Yu, P. Müller-Buschbaum, S. V. Roth
  Ordering during directional drying in organic thin films: An in situ grazing incidence X-ray scattering study
  GISAS 2012, Kyoto, Japan, 13 – 16 Nov 2012
- J. Perlich, V. Körstgens, M. Schwartzkopf, G. Santoro, S. Yu, P. Müller-Buschbaum, S. V. Roth
  Ordering during directional drying in organic thin films: An in situ grazing incidence X-ray scattering study
  SAS 2012, Sydney, Australia, 18 – 23 Nov 2012
- W. Petry
  Update on Mo-99 at FRM II
  NEA-OECD-HLG on medical radioisotopes, Paris, France, 18 – 19 Jan 2012
- W. Petry
  Die Techneticum-Krise: Der Garchinger Forschungs-Reaktor wird Zentrum für die Versorgung von Patienten in ganz Europa
  SZ-Forum Gesundheit: Der Fukushima Effekt in der Medizin, Munich, 06 Mar 2012

- W. Petry
  Phonons in Martensite and Austenite NiMnGa – Its Relation to Ferromagnetic Shape Memory
  TMS (The Minerals, Metal and Materials Society) 2012, 14th Annual Meeting and Exhibition, Orlando Florida, USA, 11-15 Mar 2012

- W. Petry
  Heavy ion irradiation of E-FUTURE II fuel samples
  European Research Reactor Conference (RRFM), 18 - 22 Mar 2012, Prague, Czechia

- W. Petry
  Light in the Dark - neutrons for science, medicine and industry
  Visit to KAERI, Korea 26 Mar 2012

- W. Petry
  Licht im Dunkeln - Neutronen für Industrie und Medizin
  VDI TUM-Expertenforum 2012, 17 April 2012

- W. Petry
  Neutrons for science, medicine and industry
  Talk on the occasion of the visit of representatives of the European Nuclear Council, 26 Apr 2012

- W. Petry
  Neutronen für die Fertigungtechnik
  Invited talk on the occasion of the 70th birthday of Prof. Dr.-Ing. Hartmut Hoffmann, 21 Sep 2012

- W. Petry
  Energy and lattice damage distribution at the interface UMo-Al: Comparison of fission fragments and heavy-ions
  RERTR 2012 - International Meeting, 14 - 17 October, Prague, Czechia

- M. Philipp, U. Müller, R. Aleksandrova, J. K. Krüger, P. Müller-Buschbaum
  Linear and nonlinear elastic properties at the volume phase transition of aqueous PNIPAM solutions
  Colloquium of the SFB 755 Nanoscale Photonic Imaging, Georg-August-Universität Göttingen, Göttingen, 17 Apr 2012

- M. Philipp, V. Körstgens, D. Magerl, C. Heller, N. Paul, W. Wang, Y. Yao, G. Santoro, S. Yu, S. V. Roth, P. Müller-Buschbaum
  Micro-fluidics studies of the swelling behaviour of hydrogels
  3rd TUM-HASYLAB Colloquium, Garching, 10 – 11 Sep 2012

- M. Philipp
  Selbstorganisation von intelligenten Hydrogelen
  Cycle de conférence: Les chercheurs luxembourgeois à l'étranger. Institut Grand-ducal, Section des Sciences, Luxembourg, 15 Oct 2012

- M. Philipp, V. Körstgens, C. Heller, Y. Yao, W. Wang, S. V. Roth, P. Müller-Buschbaum
  Kinetic micro-fluidics study of the swelling behavior of hydrogels as probed by GISAXS
  GISAS 2012, Kyoto, Japan, 13 – 16 Nov 2012

- M. Philipp, K. Kyriakos, S. Jaksch, J. Adelsberger, I. Grillo, C. M. Papadakis, P. Müller-Buschbaum
  Cononsolvency of thermoresponsive polymer in binary solvents: a kinetic SANS study
  SAS 2012, Sydney, Australia, 18 – 23 Nov 2012

- M. Rawolle, in the frame of the presentation of the network "Solar Technologies Go Hybrid" by T. Bein
  Synthesis of titania nanostructures
  SolTech Kick-off Workshop, München, 17 – 19 Oct 2012

- M. Rawolle, C. Gebbe, E. V. Braden, M. A. Niedermeier, D. Magerl, K. Sarkar, V. Körstgens, E. Metwalli, Y. Yao, W. Wang, J. Perlich, A. Buffet, S. V. Roth, T. Fröschl, N. Hüsing, P. Müller-Buschbaum
  Titania thin films: a low temperature route to crystalline nanostructures
  3rd TUM-HASYLAB Colloquium, Garching, 10 – 11 Sep 2012

- M. Rawolle, M. A. Niedermeier, K. Sarkar, P. Lellig, J. S. Gutmann, T. Fröschl, N. Hüsing, J. Perlich, S. V. Roth, P. Müller-Buschbaum
  Advances in nanostructuring of titania thin films for dye-sensitized and hybrid photovoltaics
  2nd Colloquium of the Munich School of Engineering, Garching, 28 Jun 2012

- M. Rawolle, C. Gebbe, E. V. Braden, M. A. Niedermeier, D. Magerl, K. Sarkar, V. Körstgens, J. Perlich, A. Buffet, S. V. Roth, T. Fröschl, N. Hüsing, P. Müller-Buschbaum
  Low temperature route to nanostructured crystalline titania thin films
  DPG Frühjahrstagung, Berlin, 25 – 30 Mar 2012

- K. Sarkar, M. Rawolle, E. M. Herzig, W. Wang, P. Müller-Buschbaum
  Sol-gel templated zinc oxide films for solar cell application
  DPG Frühjahrstagung, Berlin, 25 – 30 Mar 2012

- K. Sarkar, M. Rawolle, E. M. Herzig, W. Wang, M. A. Niedermeier, C. Schaffer, C. M. Palumbiny, D. Moseguí González, A. Naumann, N. Paul, A. Buffet, J. Perlich, S. V. Roth, P. Müller-Buschbaum
  Hybrid films based on ZnO network structures for applications in organic photovoltaics
  3rd TUM-HASYLAB Colloquium, Garching, 10 – 11 Sep 2012

- K. Sarkar, C. Schaffer, D. Moseguí González, A. Naumann, J. Perlich, S. V. Roth, P. Müller-Buschbaum
  GISAXS study of morphology evolution of diblock copolymer based ZnO nanostructures upon solvent vapor treatment
  GISAS 2012, Kyoto, Japan, 13 – 16 Nov 2012

- K. Sarkar, M. Rawolle, M. A. Niedermeier, V. Körstgens, E. M. Herzig, W. Wang, C. Schaffer, D. Moseguí González, A. Naumann, J. Perlich, A. Buffet, S. V. Roth P. Müller-Buschbaum
  Mesoporous zinc oxide morphologies for applications in hybrid photovoltaics
  SAS 2012, Sydney, Australia, 18 – 23 Nov 2012

- M. Schindler, A. Kriele, P. Müeller-Buschbaum
  Influence of Interface Interactions on the Inner Structure of Pressure Sensitive Adhesive Films
  DPG Frühjahrstagung, Berlin, 25 – 30 Mar 2012

- A. Sepe, D. Posselt, J. Perlich, D.-M. Smilgies, C.M. Papadakis
  In-situ study of structural changes in lamellar diblock copolymer thin films during heat treatment
  DPG Frühjahrstagung, Berlin, 25 – 30 Mar 2012

- L. Silvi, W. Lohstroh, G. G. Simeoni, J. Neuhaus, W. Petry
  A cold chopper spectrometer for ESS
  IKON 3, Lund, Sweden, 19 – 21 Sep 2012

- G. G. Simeoni
  Neutron Scattering: new perspectives on high pressure investigations
  Gordon Research Seminar and Conference on High Pressure, University of New England, Biddeford, Maine, 23 – 29 Jun 2012

- Y. Yao, E. Metwalli, V. Körstgens, E. Herzig, W. Wang, A. Buffet, S. V. Roth, P. Müller-Buschbaum
  Magnetic nanoparticles in thin block copolymer films
  3rd TUM-HASYLAB Colloquium, Garching, 10 – 11 Sep 2012

- J. Zhang, A. Sepe, X. Shen, J. Perlich, D. Posselt, C. M. Papadakis
  Structural evolution in diblock copolymer thin films during solvent vapor treatment
  3rd TUM-HASYLAB Colloquium, Garching, 10 – 11 Sep 2012

- J. Zhang, A. Sepe, X. Shen, J. Perlich, D. Posselt, C. M. Papadakis
  Structural evolution in diblock copolymer thin films with perpendicular lamellar structure during solvent vapor treatment
  SAS 2012, Sydney, Australia, 18 – 23 Nov 2012

9.3 Posters

- P. P. Deen, K. H. Anderson, A. Hiess, D. N. Aggyriou, H. Bodallo, O. Kirstein, M. Sharp, K. Lefmann, A. Vickery, K. Kleno, W. Lohstroh, M. Monkenbusch, J. Voigt, Th. Brückel, M. Russina, H. Ronnow
  Spectroscopy at the European Spallation Source
  20th meeting on Collaboration of Advanced Neutron Sources, ICANS XX, Bariloche, Argentina, 04 – 09 Mar 2012

- M. Gruber, M. Rawolle, J. Wagner, D. Magerl, J. Perlich, S. V. Roth, A. Opitz, P. Müller-Buschbaum, W. Brütting
  Structure and morphology of organic donor-acceptor photovoltaic cells based on DIP and C_{60}
  DPG Frühjahrstagung, Berlin, 25 – 30 Mar 2012

- S. Guo, M. A. Ruderer, M. Rawolle, V. Körstgens, J. Perlich, S. V. Roth, P. Müller-Buschbaum
  A systematic X-ray scattering study on highly efficient bulk heterojunction P3HT:PCBM solar cell
  Tag der Physikerin, Garching, 15 Feb 2012

- S. Guo, M. A. Ruderer, M. Rawolle, V. Körstgens, J. Perlich, S. V. Roth, P. Müller-Buschbaum
  A systematic X-ray scattering study on highly efficient bulk heterojunction P3HT:PCBM solar cell
  DPG Frühjahrstagung, Berlin, 25 – 30 Mar 2012

- E. M. Herzig, K. Wagenbauer, M. Niedermeier, M. Rawolle, K. Sarkar, K. Scherer, J. Perlich, S. V. Roth, P. Müller-Buschbaum
  Three component organic photovoltaic systems
  Tag der Physikerin, Garching, 15 Feb 2012
- E. M. Herzig, K. Wagenbauer, V. Körstgens, W. Wang, Y. Yao, A. Buffet, S. V. Roth, P. Müller-Buschbaum
  Tuning of Crystal Orientation in Conducting Polymer Blends
  DPG Frühjahrstagung, Berlin, 25 – 30 Mar 2012
- S. Jaksch, S. Salzinger, S. Huber, J. Adelsberger, P. Busch, R. Jordan, C. M. Papadakis
  Switching Behavior of Thermoresponsive Poly(2-oxazoline) Copolymers
  DPG Frühjahrstagung, Berlin, 25-30 March 2012
- V. Körstgens, M. Rawolle, K. Sarkar, M. Trebbin, J. Thiele, S. With, F. J. de Jong, A. Buffet, J. Perlich, G. Benecke, G. Herzog, M. Schwartzkopf, S. V. Roth, M.Schlüter, S. Förster, P. Müller-Buschbaum
  Investigating microfluidics with microGISAXS at beamline P03
  HASYLAB User Meeting, Hamburg, 26 – 27 Jan 2012
- V. Körstgens, K. Sarkar, G. Herzog, M. Schwartzkopf, A. Buffet, F. J. de Jong, S. V. Roth, M. Schlüter, P. Müller-Buschbaum
  Flow induced surface attachment of gold nanorods as probed with microfluidics and in-situ GISAXS
  DPG Frühjahrstagung, Berlin, 25 – 30 Mar 2012
- V. Körstgens, K. Sarkar, M. Trebbin, M. Schwartzkopf, A. Buffet, S. V. Roth, S. Förster, P. Müller-Buschbaum
  Investigating microfluidics at interfaces with GISAXS
  DPG Frühjahrstagung, Berlin, 25 – 30 Mar 2012
- K. Kyriakos, M. Philipp, J. Adelsberger, S. Jaksch, A. Miasnikova, A. Laschewsky, I. Grillo, P. Müller-Buschbaum, C. M. Papadakis
  Cononsolvency in aqueous solutions of P(S-b-NIPAM) diblock copolymers
  DPG Frühjahrstagung, Berlin, 25 – 30 Mar 2012
- K. Kyriakos, M. Philipp, J. Adelsberger, S. Jaksch, A. Miasnikova, A. Laschewsky, I. Grillo, P. Müller-Buschbaum, C. M. Papadakis
  Cononsolvency in aqueous solutions of P(S-b-NIPAM) diblock copolymers
  JCNS Workshop 2012 ”Trends and Perspectives in Neutron Scattering for Soft Matter and Biophysics”, Tutzing, 08 – 11 Oct 2012
- W. Lohstroh, N. Boucharat, E. Gil Bardaji, M. Fichtner
  Gas Release from isotope labeled $2LiBH_4$ *-* MgH_2 *mixtures*
  6th International Symposium on Hydrogen & Energy, Stoos, Switzerland, 22 – 27 Jan 2012
- E. Metwalli, J.-F. Moulin, J. Perlich, W. Wang, A. Diethert, S.V. Roth, P. Müller-Buschbaum
  Progressive selective gold deposition on polymer templates using a flow-stream technique
  HASYLAB User Meeting, Hamburg, 26 – 27 Jan 2012
- E. Metwalli, W. Hefter, M. Nie, V. Körstgens, J. Perlich, S.V. Roth, P. Müller-Buschbaum
  Thin film membrane for solid-state micro-batteries
  2nd Colloquium of the Munich School of Engineering, Garching, 28 Jun 2012

- H. Morhenn, T. Unruh
  Revealing the dynamics leading to molecular self-diffusion by neutron scattering and MD simulations
  Second Annual NBIA Meeting on ESS Science, Copenhagen, Denmark, 25 – 29 Jun 2012

- A. Naumann, E. M. Herzig, P. Müller-Buschbaum
  Influence of PSS on the morphology of P3HT:PCBM solar cells
  Tag der Physikerin, Garching, 15 Feb 2012

- A. Naumann, E. M. Herzig, S. Guo, G. Tainter, J. Perlich, P. Müller-Buschbaum
  Influence of PSS on the morphology of P3HT:PCBM solar cells
  DPG Frühjahrstagung, Berlin, 25 – 30 Mar 2012

- M. A. Niedermeier, M. Rawolle, P. Lellig, V. Körstgens, E. M. Herzig, A. Buffet, S. V. Roth, J. S. Gutmann, T. Fröschl, N. Hüsing, P. Müller-Buschbaum
  Low temperature sol-gel synthesis of a polymer/titania hybrid films based on custom made poly(3-alkoxy thiophene)
  DPG Frühjahrstagung, Berlin, 25 – 30 Mar 2012

- M. A. Niedermeier, M. Rawolle, P. Lellig, V. Körstgens, E. M. Herzig, A. Buffet, S. V. Roth, J. S. Gutmann, T. Fröschl, N. Hüsing, P. Müller-Buschbaum
  Fabrication of custom tailored titania nanostructures and hybrid thin films for application in photovoltaics
  2nd Colloquium of the Munich School of Engineering, Garching, 28 Jun 2012

- C. M. Palumbiny, R. Meier, L. Schmidt-Mende, P. Müller-Buschbaum
  Micro- and nanostructuring of thin layers for the application in organic photovoltaics
  Tag der Physikerin, Garching, 15 Feb 2012

- C. M. Palumbiny, R. Meier, L. Schmidt-Mende, P. Müller-Buschbaum
  Micro- and nanostructuring of thin layers for the application in organic photovoltaics
  DPG Frühjahrstagung, Berlin, 25 – 30 Mar 2012

- C. M. Palumbiny, R. Meier, H. C. Hesse, R. Dunbar, L. Schmidt-Mende, P. Müller-Buschbaum
  Structured interfaces in organic photovoltaics
  2nd Colloquium of the Munich School of Engineering, Garching, 28 Jun 2012

- N. Paul, A. Paul, R. Steitz, M. Kreuzer, M. Ch. Lux-Steiner
  Selective adsorption of glutamate molecules by polyelectrolyte multilayers
  Tag der Physikerin, Garching, 15 Feb 2012

- N. Paul, A. Paul, S. Mattauch, P. Müller-Buschbaum, M. Ch. Lux-Steiner
  Interfacial engineering of polymer multilayers with polarized biomolecules: a new approach in growing supramolecular layer structures
  DPG Frühjahrstagung, Berlin, 25 – 30 Mar 2012

- J. Perlich, J. Rubeck, M. Schwartzkopf, S. V. Roth, R. Gehrke, V. Körstgens, M. A. Ruderer, P. Müller-Buschbaum
  The small angle scattering beamline BW4 of HASYLAB
  HASYLAB User Meeting, Hamburg, 26 – 27 Jan 2012

- M. Philipp, D. Magerl, R. Aleksandrova, U. Müller, O. Astasheva, M. König, C. Dawson, J. K. Krüger, P. Müller-Buschbaum
  Structural properties of poly(N-isopropylacrylamide)-based systems
  Tag der Physikerin, Garching, 15 Feb 2012

- M. Philipp, U. Müller, O. Astasheva, J. K. Krüger, P. Müller-Buschbaum
  Elastic anomalies at the volume phase transition of aqueous PNIPAM solutions
  DPG Frühjahrstagung, Berlin, 25 – 30 Mar 2012

- D. Posselt, Z. Di, A. Sepe, D.-M. Smilgies, C.M. Papadakis
  Structural changes in block copolymer thin films during solvent vapour treatment
  International Workshop on Soft Matter Physics and Complex Flows, Svolvaer, Lofoten, Norway, 22-25 May 2012

- M. Rawolle, M. A. Ruderer, S. M. Prams, Q. Zhong, D. Magerl, P. Lellig, J. S. Gutmann, J. Perlich, S. V. Roth, P. Müller-Buschbaum
  Nanostructuring of titania thin films by combination of micro-fluidics and block copolymer based sol-gel templating
  Tag der Physikerin, Garching, 15 Feb 2012

- M. Rawolle, K. Sarkar, M. A. Niedermeier, P. Lellig, J. S. Gutmann, P. Busch, J.-F. Moulin, M. Haese-Seiller, P. Müller-Buschbaum
  Nanoporous titania-ceramic nanocomposite films for applications in photovoltaics
  FRM II User Meeting, Garching, 23 Mar 2012

- M. Rawolle, M. A. Niedermeier, K. Sarkar, M. A. Ruderer, S. Guo, W. Wang, C. M. Palumbiny, C. Schaffer, E. M. Herzig, P. Müller-Buschbaum
  Structural investigation of thin polymer nanocomposite and blend films for photovoltaic applications
  SolTech Kick-off Workshop, München, 17 – 19 Oct 2012

- K. Sarkar, M. Rawolle, E. M. Herzig, W. Wang, P. Müller-Buschbaum
  ZnO nanostructures templated by a PS-b-PEO diblock copolymer via sol-gel route
  Tag der Physikerin, Garching, 15 Feb 2012

- K. Sarkar, M. Rawolle, E. M. Herzig, W. Wang, P. Müller-Buschbaum
  Hybrid films based on zinc oxide network structures for applications in organic photovoltaics
  2nd Colloquium of the Munich School of Engineering, Garching, 28 Jun 2012

- C. Schaffer, M. Ruderer, S. Guo, P. Müller-Buschbaum
  Degradation and aging in polymer solar cells
  2nd Colloquium of the Munich School of Engineering, Garching, 28 Jun 2012

- M. Schindler, J.-F. Moulin, R.A. Campbell, P. Müller-Buschbaum
  Self Assembly of Diblockcopolymers: GISANS at REFSANS
  FRM II User Meeting, Garching, 23 Mar 2012

- A. Sepe, E.T. Hoppe, D. Posselt, J.-F. Moulin, D.-M. Smilgies, C. M. Papadakis
  Solvent distribution in block copolymer thin films
  FRM II User Meeting, Garching, 23 Mar 2012

- A. Sepe, D. Posselt, K. Swiatek, D.-M. Smilgies, C. M. Papadakis
  Improvement of the structural order in block copolymer thin films by solvent vapour treatment - an in-situ XRR and GISAXS study
  SAS 2012, Sydney, Australia, 18 – 23 Nov 2012
- L. Silvi, G. G. Simeoni, W. Lohstroh, J. Neuhaus, W. Petry
  Design study of a cold neutron chopper spectrometer for the ESS
  Science and Scientist at ESS, Berlin, 19 – 20 Apr 2012
- H. Sternschulte, I. Staudinger, A. Sepe, C. M. Papadakis, J. Perlich, S. V. Roth, S. Ghodbane, D. Steinmüller-Nethl
  Grazing-incidence small-angle X-ray scattering study on ultra nanocrystalline diamond films
  International Conference on Diamond and Carbon Materials, Granada, Spain, 03 - 06 Sep 2012
- G. G. Simeoni, R. Valicu, G. Borchert, P. Boeni, W. Petry
  New scientific perspectives at TOFTOF at the FRM II
  FRM II User Meeting, Garching, 23 Mar 2012
- G. G. Simeoni
  Inelastic Neutron Scattering: Focusing Neutron Optics for High Pressure Experiments
  Gordon Research Conference on High Pressure, University of New England, Biddeford, Maine, 24 – 29 Jun 2012
- N. Violini, J. Voigt, Th. Brückel, ,M. Russina, K. Rolfes, G. G. Simeoni, W. Lohstroh, L. Silvi, P. P. Deen
  Development of Direct Geometry Chopper spectrometers for the European Spallation Souce
  DPG Frühjahrstagung, Berlin, 25 – 30 Mar 2012
- W. Wang, M. A. Ruderer, E. Metwalli, S. Guo, K. H. Scherer, S. V. Roth, J. Perlich, P. Müller-Buschbaum
  The Morphology of Flexible All Polymer Solar Cell
  Tag der Physikerin, Garching, 15 Feb 2012
- W. Wang, M. A. Ruderer, E. Metwalli, S. Guo, K. H. Scherer, S. V. Roth, J. Perlich, P. Müller-Buschbaum
  The Morphology of Flexible All Polymer Solar Cell
  DPG Frühjahrstagung, Berlin, 25 – 30 Mar 2012
- W. Wang, M. A. Ruderer, E. Metwalli, S. Guo, K. H. Scherer, S. V. Roth, J. Perlich, P. Müller-Buschbaum
  Modified surface of CNT electrodes for flexible all polymer solar cells
  2nd Colloquium of the Munich School of Engineering, Garching, 28 Jun 2012
- Y. Yao, E. Metwalli, H. Choe, M. Opel, P. Müller-Buschbaum
  Alignment of Magnetic Nanoparticles in Diblock Copolymer Films under External Magnetic Fields
  Tag der Physikerin, Garching, 15 Feb 2012
- Y. Yao, E. Metwalli, J. -F. Moulin, P. Müller-Buschbaum
  Magnetic nanoparticles embedded in thin block copolymer films
  FRM II User Meeting, Garching, 23 Mar 2012

- Y. Yao, E. Metwalli, V. Körstgens, E. Herzig, W. Wang, A. Buffet, S. V. Roth, M. Opel, P. Müller-Buschbaum
  Maghemite nanoparticles in thin block copolymer films
  DPG Frühjahrstagung, Berlin, 25 – 30 Mar 2012
- J. Zhang, A. Sepe, R. Steinacher, J. Perlich, D. Posselt, C.M. Papadakis
  Structural evolution in diblock copolymer thin films with perpendicular lamellar structure during solvent vapor treatment
  HASYLAB User Meeting, Hamburg, 26 – 27 Jan 2012
- J. Zhang, A. Sepe, R. Steinacher, J. Perlich, D. Posselt, C.M. Papadakis
  Structural evolution in diblock copolymer thin films with perpendicular lamellar structure during solvent vapor treatment
  DPG Frühjahrstagung, Berlin, 25 – 30 Mar 2012
- Q. Zhong, E. Metwalli, G. Kaune, M. Rawolle, A. M. Bivigou-Koumba, A. Laschewsky, C. M. Papadakis, R. Cubitt, P. Müller-Buschbaum
  Swelling and switching behaviors of novel thermo-responsive P(S-b-MDEGA-b-S) hydrogel films under vapor atmosphere
  DPG Frühjahrstagung, Berlin, 25 – 30 Mar 2012

9.4 Invited talks at LS Funktionelle Materialien

- Dr. Gerald Schneider, IFF FZ Jülich
  Dynamics of Polymers in Nanocomposites
  17 Jan 2012
- Prof. Dr. Igor Potemkin, Department of Physics, Moscow State University, Russia
  Micelle formation and interaction with colloidal particles of amphiphilic macromolecules: New approaches to 'old' problems
  19/20 Jan 2012
- Kai Scherer, University of Cambridge, U.K.
  Phase Behavior of P3HT/PCBM Blends
  01 Feb 2012
- Prof. Harald Ade, North Carolina State University, Raleigh, U.S.A.
  Organic devices: Insights provided by soft x-ray characterization methods
  04 Apr 2012
- Dr. Heide Götz, European Patent Office, Munich
  Patentsystem und Online-Recherchedienste
  24 Apr 2012
- Dr. Jyotsana Lal, University of Chicago, U.S.A.
  The behavior of polymer chains in confined geometries
  30 May 2012
- Dr. Jyotsana Lal, University of Chicago, U.S.A.
  Surface dynamics of polymer thin films
  27 Jun 2012

- Dr. Hadwig Sternschulte, TUM
  Growth and properties of CVD diamond
  20 Jun 2012
- Dr. Konstantinos N. Raftopoulos, National Technical University of Athens, Greece
  Nanoparticles in polymer chains. Effects on molecular mobility
  25 Jul 2012
- Dr. Robert Meier, Carl Zeiss Laser Optics GmbH, Oberkochen
  Tuning the optical surface of mirror systems for EUV-lithography
  31 Oct 2012
- Marco Laurati, Universität Düsseldorf
  Glasses of dynamically asymmetric colloidal mixtures: Structure, dynamics and mechanical response
  28 Nov 2012
- Dr. Zhenyu Di, Forschungszentrum Jülich
  The phase behavior of AB/BC diblock copolymer blends
  18 Dec 2012
- Dr. Alexander Hexemer, Advanced Light Source Advanced Light Source - Lawrence Berkeley National Laboratory, Berkeley, U.S.A.
  Next Generation Computing For GISAS
  19 Dec 2012
- Sebastian Eberle, Massachussetts Institute of Technology, U.S.A.
  Mechanical interactions between cells and electroactive polymers
  20 Dec 2012

9.5 Funding

Deutsche Forschungsgemeinschaft:

- Within DFG priority program SPP 1259:
  Struktur und Kinetik stimuli-responsiver, dünner Hydrogelfilme aus amphiphilen Blockcopolymeren
  Grant Number: MU 1487/8-3
  Project Leader: Prof. Dr. Peter Müller-Buschbaum

- *Beschaffung einer Anlage für die Röntgenklein- und -weitwinkelstreuung für den Lehrstuhl für Experimentalphysik IV, Physik-Department E13*
  Grant Number: INST 95/1112-1
  Project Leader: Prof. Dr. Peter Müller-Buschbaum

- Within DFG priority programm SPP 1239:
  Änderung von Mikrostruktur und Form fester Werkstoffe durch äußere Magnetfelder
  Grant Number: NE 1405/1-2
  Project Leader: Dr. Jürgen Neuhaus

- *Kinetik der Phasenumwandlung in Ausferritischem Gusseisen (ADI)*
  Grant Number: PE 580/11-1
  Project Leader: Prof. Dr. Winfried Petry

- *In-situ Eigenspannungsanalyse an Verbundgusskörpern mittels Neutronendiffraktometrie*
  Grant Number: PE 580/12-1
  Project Leader: Prof. Dr. Winfried Petry

- Within DFG priority program SPP 1259:
  Struktur und Kinetik stimuli-responsiver, dünner Hydrogelfilme aus amphiphilen Blockcopolymeren
  Grant Number: PA 771/4-3
  Project Leader: Prof. Dr. Christine Papadakis

- *Multicompartment systems based on poly (2-oxazoline)s*
  Grant Number: PA 771/6-2
  Project Leader: Prof. Dr. Christine Papadakis

- Within DFG priority program SPP 1369:
  Lokale Viskosität und Dichte in der Grenzphase von Polymeren an einer festen Grenzfläche - Fluoreszenz-Korrelationsspektroskopie und Neutronenreflektometrie
  Grant Number: PA 771/7-1
  Project Leader: Prof. Dr. Christine Papadakis

- *Structural changes in block copolymer thin films during solvent vapor treatment*
  Grant Number: PA 771/10-1
  Project Leader: Prof. Dr. Christine Papadakis

Bundesministerium für Bildung und Forschung:

- *Entwicklung und Aufbau des Mikrofluidik Messplatzes am Instrument MiNaXS am Synchrotron PETRA III*
  Grant Number: 05K10WOA
  Project Leader: Prof. Dr. Peter Müller-Buschbaum

Bayerisches Staatsministerium für Wissenschaft, Forschung und Kunst:

- Im Rahmen der Munich School of Engineering (MSE): Netzwerk Regenerative Energien
  Solar Technologies Go Hybrid
  Project Leader: Prof. Dr. Peter Müller-Buschbaum

Others:

- Im Rahmen des Internationalen Graduiertenkollegs: Material Science of Complex Interfaces (CompInt)
  Thin films of photoactive semiconducting polymers with incorporated nanoparticles
  Project Leader: Prof. Dr. Peter Müller-Buschbaum
- Im Rahmen des Internationalen Graduiertenkollegs: Material Science of Complex Interfaces (CompInt)
  Degradation und Alterung in Polymeren Mischungsfilmen für die Photovoltaik
  Project Leader: Prof. Dr. Peter Müller-Buschbaum
- Im Rahmen des Internationalen Graduiertenkollegs: Material Science of Complex Interfaces (CompInt)
  Strukturelle Änderungen in nanostrukturierten Blockcopolymerfilmen - Zeitaufgelöste in-situ-Untersuchungen mit Röntgenkleinwinkelstreuung unter streifendem Einfall
  Project Leader: Prof. Dr. Christine Papadakis
- Im Rahmen des Internationalen Graduiertenkollegs: Material Science of Complex Interfaces (CompInt)
  Responsive Hydrogele - Struktur, Dynamik und Kinetik
  Project Leader: Prof. Dr. Christine Papadakis
- Im Rahmen der International Graduate School of Science and Engineering (IGSSE)
  Interface Science for Photovoltaics - a EuroTech GreenTech Initiative
  Project Leader: Prof. Dr. Peter Müller-Buschbaum
- Im Rahmen des Fonds National de la Recherche Luxembourg: Forschungskooperation mit der Universität Luxemburg
  Marie Curie Cofunded, Aides à la formation recherche (AFR) Postdoc project: Volume phase transitions of PNIPAM-based aqueous bulk and thin film systems
  Project Leader: Prof. Dr. Peter Müller-Buschbaum; Co-Advisor: Prof. Dr. Dr. hc Jan Kristian Krüger

- Forschungskooperation mit dem Helmholtz-Zentrum Berlin für Materialien und Energie GmbH
  Organic and hybrid photovoltaic devices for energy and biomedical applications
  Project Leader: Prof. Dr. Peter Müller-Buschbaum; Co-Project Leader: Prof. Dr. Martha Ch. Lux-Steiner

- Forschungskooperation mit Kao Corporation, Japan
  Analysis of the near-surface composition profile of water-sensitive adhesive polymer films
  Project Leader: Prof. Dr. Peter Müller-Buschbaum

Outreach:

- Im Rahmen der Munich School of Engineering (MSE): Netzwerk Regenerative Energien
  Aufbau eines interdisziplinären Netzwerks aus Lehrstühlen der Technischen Universität München und anderen Forschungseinrichtungen zur Förderung der Forschungsaktivitäten im Bereich der regenerativen Energien
  Project Leader: Prof. Dr. Peter Müller-Buschbaum

10 The chair

10.1 Staff

Chair: Prof. Dr. Winfried Petry

Head: Prof. Dr. Peter Müller-Buschbaum

Professors

Prof. Dr. Christine M. Papadakis

Fellows

Dr. Ezzeldin Metwalli Ali
Dr. Eva Maria Herzig
Dr. Volker Körstgens
Dr. Joana Rebelo Kornmeier
Dr. Michael Leitner
Dr. Wiebke Lohstroh
Dr. Jürgen Neuhaus
Dr. Martine Philipp
Dr. Giovanna Giulia Simeoni
Dr. Tobias Unruh
Dr. Jianqi Zhang

PhD students

Joseph Adelsberger
Sebastian Busch
Hsin-Yin Chiang
Margarita Dyakonova
Semih Ener
Fabian Fuchs
Shuai Guo
Christian Hesse
Tobias Hollmer
Tilo Hoppe
Tanja Huber
Sebastian Jaksch
Konstantinos Kyriakos
David Magerl
Robert Meier
Humphrey Morhenn
Martin Niedermeier
Claudia Palumbiny
Monika Rawolle
Matthias Ruderer
Kuhu Sarkar
Christoph Schaffer
Robert Schenk
Markus Schindler
Martin Schmiele
Alessandro Sepe
Luca Silvi
Lin Song
Christian Steyer
Bo Su
Weijia Wang
Yuan Yao
Qi Zhong
Tobias Zweifel

Diploma students

Yvonne Boose
Simon Brunner
Miriam Däubler
Matthias Fuchs
William Hefter
Christoph Heller
Weiguo Lu
Daniel Moseguí González
Anna Naumann
Kai Hermann Scherer

Master students

Ammara Akhtar
Lin Chen
Subhra Kanti De
Margarita Dyakonova
Gökhan Gümüssoy
Christian Jendrzejewski
Sarah Lindner
Jing Ning
Stephan Pröller
Xuhu Shen
Gregory Tainter
Liu Wei

Bachelor students

Martin Baumann
Peter Deimel
Regina Eger
Karl-David Egger
Christian Gebbe
Felix Lang
Manuel Manlik
Korbinian Mechlem
Kai Hermann Müller
Sarah Ottinger
Sofia Ramirez
Patrick Schreiber
Isabella Staudinger

Students assistants

Erik Braden
Enzo Kopperger
Che-Hung Lin
Christina Psylla
Benjamin Stafford
Klaus Wagenbauer

Technical/administrative staff

Philipp Bork
Erik Faber
Susanna Fink
Reinhold Funer
Raffael Jahrstorfer
Josef Kaplonski
Dieter Müller
Jandal Ringe
Marion Waletzki

10.2 Graduations

- **Accomplished PhD theses**

Joseph Adelsberger
Struktur und Kinetik thermoresponsiver Hydrogele

Sebastian Busch
The Pico- to Nanosecond Dynamics of Phospholipid Molecules

Semih Ener
Lattice Dynamics in Ferromagnetic Shape Memory Alloy System Ni-Mn-Ga

Rosmarie Hengstler-Eger
Irradiation studies on the origin of pressurized water reactor fuel assembly deformation

Eicke Tilo Hoppe
Physikalische Eigenschaften von Polybutadienschmelzen am Polymer-Festkörper-Kontakt und im Volumen

Robert Meier
Novel Structuring Routines for Organic Photovoltaics

Andreas Meier-Koll
Neutronenkleinwinkelstreuung und Brillouinspektroskopie an thermoresponsiven Hydrogelen

Matthias A. Ruderer
Morphology of polymer-based films for organic photovoltaics

Alessandro Sepe
Structural ordering in block copolymer thin films

Roxana Valicu
Design and test adaptive focusing guide

Qi Zhong
Structure and transition behavior of novel thermo-responsive polymer films

- **Accomplished diploma theses**

  Yvonne Boose
  Spectral variations in thin film PV module performance under real conditions

  Matthias Fuchs
  Wärmeleitmessungen an UMo

  William Jean Hefter
  Polymere für Anwendungen in der Energiespeicherung

  Anna Naumann
  Ternary Polymer Blends for Applications in Organic Photovoltaics

  Kai Hermann Scherer
  Phase Behavior of P3HT/PCBM Blends

- **Accomplished master theses**

  Ammara Akhtar
  Polyethylene-induced structural modification in ternary polymer blends used in organic photovoltaics

  Margarita Dyakonova
  New polymeric systems for drug delivery

  Gökhan Gümüssoy
  Investigation of the metal-polymer interactions and their influence on the performance of pressure-sensitive adhesives

  Chen Lin
  Sol-Gel templated Zinc oxide films for application in hybrid photovoltaics

  Sarah Lindner
  Organic solar cells based on fullerenes and small molecules: device performance of flat and nanostructured interfaces

  Wei Liu
  Combination of micro-fluidics and sol-gel templating to tailor titania nanostructures for application in photovoltaics

  Jing Ning
  Influence of fluorine content in manipulating the nanomorphology of novel PTB7:PC71BM system

- **Accomplished bachelor theses**

  Martin Baumann
  Polymer-based thin films for new concepts of energy storage

  Peter Deimel
  Ternary Polymer Blends for Application in Organic Photovoltaics

  Regina Eger
  Nanostructured block copolymer films

  David Egger
  Smart thin films made of switchable polymers

Christian Gebbe
Herstellung von Titandioxid Nanostrukturen bei niedrigen Temperaturen für die Anwendung in der organischen Photovoltaik

Felix Lang
Nano-structuring of active layers for organic solar cells

Manuel Manlik
Automatisierung einer Probenzelle für die in-situ Dampfbehandlung dünner Polymerfilme

Korbinian Mechlem
Nanopartikel-basierte Solarzellen

Kai Müller
Synthesis of nanostructured zinc oxide morphologies using zinc acetate dihydrate as a precursor for applications in hybrid photovoltaics

Sarah Ottinger
Amphiphile Blockcopolymere: Einfluss der Architektur auf die Mizellbildung

Sofia Ramirez
Ternary polymer blends for applications in organic photovolatics

Isabella Staudinger
Charakterisierung ultrananokristalliner Diamantschichten mittels Kleinwinkelröntgenstreuung

10.3 Guests

- Prof. Igor I. Potemkin and Irina Neratova, Lomonosov Moscow State University, Russia
  19 – 20 Jan 2012

- Dr. Sergey Filippov, Institute of Macromolecular Chemistry, Academy of Sciences of the Czech Republic, Prague
  13 – 16 Feb 2012

- Dr. Markus Rauscher, Max Planck Institute for Intelligent Systems, Stuttgart
  24 Feb 2012, 02 Apr 2012, 23 Apr 2012, 17 Dec 2012

- Prof. Dorthe Posselt, Roskilde University, Denmark
  30 Apr – 04 May 2012

- Dr. Mahmoud Omar Mustafa Al-Hussein, University of Jordan, Amman, Jordan
  04 Jun – 31 Aug 2012

- Prof. André Laschewsky and Anna Miasnikova, Universität Postdam
  05 Jul 2012

- Dr. Konstantinos N. Raftopoulos, National Technical University of Athens, Greece
  25 Jul 2012

- Dr. Neelima Paul, Helmholtz-Zentrum, Berlin
  since 01 Oct 2011

- Rina Iikubo, Kao Corporation, Tokyo, Japan
  since 01 Sep 2012